

SEARCHING FOR LONG-LIVED DARK PHOTONS WITH THE HEAVY PHOTON SEARCH EXPERIMENT

A DISSERTATION
SUBMITTED TO THE DEPARTMENT OF PHYSICS
AND THE COMMITTEE ON GRADUATE STUDIES
OF STANFORD UNIVERSITY
IN PARTIAL FULFILLMENT OF THE REQUIREMENTS
FOR THE DEGREE OF
DOCTOR OF PHILOSOPHY

Matthew Reagan Solt
June 2020

¹²

© Copyright by Matthew Reagan Solt 2020
All Rights Reserved

¹³

I certify that I have read this dissertation and that, in my opinion, it is fully adequate in scope and quality as a dissertation for the degree of Doctor of Philosophy.

¹⁴

(Philip Schuster) Principal Adviser

I certify that I have read this dissertation and that, in my opinion, it is fully adequate in scope and quality as a dissertation for the degree of Doctor of Philosophy.

¹⁵

(John Jaros)

I certify that I have read this dissertation and that, in my opinion, it is fully adequate in scope and quality as a dissertation for the degree of Doctor of Philosophy.

¹⁶

(Dan Ackerib)

I certify that I have read this dissertation and that, in my opinion, it is fully adequate in scope and quality as a dissertation for the degree of Doctor of Philosophy.

¹⁷

(Pat Burchat)

Approved for the Stanford University Committee on Graduate Studies

¹⁸

¹⁹ **Abstract**

²⁰ A heavy photon (also called a dark photon or A') is a hypothetical vector boson that arises from a
²¹ massive $U(1)$ abelian gauge symmetry. Because of the ability of heavy photons to kinetically mix
²² with the Standard Model photon, they are connected to many of hidden sector models and are
²³ favored for a variety of dark sector scenarios, particularly for dark matter at the sub-GeV mass scale.
²⁴ The Heavy Photon Search Experiment (HPS) is a fixed target experiment at Jefferson Laboratory
²⁵ dedicated to searching for heavy photons in the MeV - GeV mass range and kinetic mixing strength
²⁶ $\epsilon^2 \sim 10^{-5} - 10^{-10}$. It does so through two distinct searches - a search for a narrow mass resonance
²⁷ and, for sufficiently small couplings, a search for secondary vertices beyond a large prompt QED
²⁸ background.

²⁹ In order to perform such searches, the HPS apparatus is a compact forward acceptance spectrometer
³⁰ that must be able to reconstruct particle masses and vertices with extreme precision. Heavy
³¹ photons are electro-produced from a continuous electron beam incident on a thin tungsten foil, and
³² HPS is able to reconstruct momentum of the subsequent decays to e^+e^- pairs through a silicon
³³ vertex tracker (SVT). HPS currently has three datasets - an Engineering Run in 2015 and 2016
³⁴ as well as a physics run with an upgraded detector in 2019 - all at different energies and beam
³⁵ currents. Presented in this dissertation are heavy photon physics and motivations, introduction to
³⁶ the HPS detector and reconstruction, upgrades and other models of interest, and the results from
³⁷ displaced vertex search from the HPS 2016 Engineering Run which was taken with a 2.3 GeV, 200
³⁸ nA continuous electron beam and collected a total of luminosity nb^{-1} (equivalent to days days of
³⁹ continuous uptime).

⁴⁰ This dissertation presents results...



Figure 1: This is my current placeholder figure.

⁴¹ Acknowledgments

⁴² I would like to thank a very long list of people...

43 Contents

<small>44</small>	Abstract	iv
<small>45</small>	Acknowledgments	vi
<small>46</small>	1 Introduction	2
<small>47</small>	2 Motivation	7
<small>48</small>	2.1 Observations	7
<small>49</small>	2.1.1 Galactic Rotation Curves	7
<small>50</small>	2.1.2 Weak Gravitational Lensing	9
<small>51</small>	2.1.3 Cosmic Microwave Background	10
<small>52</small>	2.1.4 Big Bang Nucleosynthesis and Type 1a Supernovae	11
<small>53</small>	2.1.5 Some Properties of Dark Matter	12
<small>54</small>	2.2 Theory Summary	13
<small>55</small>	2.3 Historical Motivations for A' s	15
<small>56</small>	2.4 Light Dark Matter	17
<small>57</small>	2.5 Signatures of A' s	21
<small>58</small>	2.6 Overview of Searches	23
<small>59</small>	2.6.1 Colliders	24
<small>60</small>	2.6.2 Beam Dumps	24
<small>61</small>	2.6.3 Thin Fixed Target	25
<small>62</small>	2.7 Heavy Photon Fixed Target Kinematics	28
<small>63</small>	2.8 Fixed Target Backgrounds	30
<small>64</small>	2.9 Overview of HPS	32
<small>65</small>	3 The HPS Detector	33
<small>66</small>	3.1 The Continuous Electron Beam Accelerator Facility (CEBAF)	34
<small>67</small>	3.2 Hall B and HPS Beamline	36
<small>68</small>	3.3 Silicon Vertex Tracker	41

69	3.3.1 Sensors and Readout	43
70	3.3.2 SVT Mechanicals	46
71	3.3.3 SVT Data Acquisition, Power, and Services	49
72	3.4 Electromagnetic Calorimeter and Trigger	52
73	3.5 Datasets	56
74	4 Event Reconstruction & Selection	57
75	4.1 HPS Coordinate Systems	57
76	4.2 Ecal Reconstruction	59
77	4.3 SVT Reconstruction	60
78	4.3.1 SVT Hit Reconstruction	60
79	4.3.2 SVT Cluster and 3D Hit Reconstruction	61
80	4.3.3 Track Reconstruction	62
81	4.4 Track Cluster Matching	64
82	4.5 Vertexing	65
83	4.6 Hit Efficiency	68
84	4.7 Tracker Alignment	70
85	4.8 Track-Truth Matching	72
86	4.9 Monte Carlo Samples	74
87	4.10 e^+e^- Preselection	78
88	4.11 Composition of the e^+e^- Sample & Normalization	87
89	4.11.1 MC Normalization	87
90	4.11.2 Radiative Fraction	87
91	4.11.3 HPS Rates	91
92	5 Search for A' Displaced Vertices	93
93	5.1 Previous Results from 2015 Engineering Run	94
94	5.2 Mass Resolution	97
95	5.2.1 Møller Event Selection	97
96	5.2.2 Mass Resolution	99
97	5.3 Hit Killing	103
98	5.3.1 A' Acceptance Effects	103
99	5.3.2 Hit Killing	105
100	5.4 Vertex Cuts	109
101	5.5 L1L1	109
102	5.6 L1L2	126
103	5.7 L2L2	135
104	5.8 Characterizing the Background	135

105	5.9 Results	144
106	5.10 Finding Signal Significance	146
107	5.11 Setting Limits	147
108	5.12 Combining Datasets	149
109	5.13 Systematics	150
110	5.14 Discussion of High z Backgrounds	151
111	5.15 A Machine Learning Approach	152
112	6 Upgrades & the Future of HPS	154
113	6.1 Layer 0 & Other Upgrades	154
114	6.2 Upgrade Performance	159
115	6.3 Preliminary 2019 Data	159
116	6.4 Reach Estimates	164
117	6.5 Generalized Displaced Vertices	165
118	6.5.1 Strongly Interacting Massive Particles (SIMPs)	165
119	6.5.2 SIMP Projections	166
120	7 Conclusions	169
121	Bibliography	170

¹²² List of Tables

¹²³	3.1 A summary of the basic parameters for different layers in the SVT.	42
¹²⁴	3.2 Summary of the pairs1 Trigger Selection from the 2016 Engineering Run.	55
¹²⁵	4.1 Basis for several different coordinate systems used in the HPS reconstruction and analysis.	57
¹²⁶	4.2 Requirements applied to V_0 particles during the reconstruction stage for data (i.e. MOUSE cuts).	65
¹²⁷	4.3 Requirements applied to V_0 particles during the reconstruction stage for MC (i.e. MOUSE cuts).	65
¹²⁸	4.4 Event generators and statistics for MC samples.	74
¹²⁹	4.5 Basic generator level physics requirements for different physics processes.	76
¹³⁰	4.6 Requirements applied to V_0 after reconstruction as an initial set to study. The time offset for data is 56 ns and the time offset for MC is 43 ns.	78
¹³¹	4.7 Requirements applied to V_0 after reconstruction as an initial set to study. The time offset for data is 56 ns and the time offset for MC is 43 ns.	80
¹³²	4.8 Table showing the efficiency of each cut on 10% of the 2016 data sample and on MC simulation for tridents, WABs and 80 MeV A' displaced samples. The trident sample contains both Bethe-Heitler and radiative events.	82
¹³³	4.9 Normalization parameters for the RAD, Tritrig, and WAB samples	87
¹³⁴	4.10 A list of cuts that are used to determine the radiative fraction and the number of e^+e^- events within a mass bin. The cuts are composed of the preselection cuts from Sec. ?? as well as the common cuts shared between L1L1, L1L2, and L2L2.	88
¹⁴⁴	5.1 Møller event selection for data on e^-e^- pairs. Since electron tracks are not required to match to Ecal clusters, the time difference is between track times and position differences are based on track extrapolations to the Ecal.	98
¹⁴⁵		
¹⁴⁶		
¹⁴⁷	5.2 Møller event selection for MC on e^-e^- pairs. Since electron tracks are not required to match to Ecal clusters, the time difference is between track times and position differences are based on track extrapolations to the Ecal.	98
¹⁴⁸		
¹⁴⁹		

150	5.3	A summary of the tight cuts for the L1L1 category.	113
151	5.4	Table showing the efficiency of each cut on 10% of the 2016 data sample and on	
152		MC simulation for tridents, WABs and 80 MeV A' displaced samples for the L1L1	
153		category. TODO: Update the cuts and numbers	126
154	5.5	A summary of the tight cuts for the L1L2 category.	127
155	5.6	Summary of systematics found to impact the displaced vertex search.	151
156	5.7	A table of relevant variables for events past z_{cut} for 100% of the data in the L1L1	
157		category.	152
158	5.8	A table of relevant variables for events past z_{cut} for the full tritrig-wab-beam sample	
159		in the L1L1 category.	153

¹⁶⁰ List of Figures

¹⁶¹	1	This is my current placeholder figure.	v
¹⁶²	1.1	The Standard Model of Particle Physics is a group of the known elementary particles which is composed of six quarks, six leptons, four gauge bosons (which are responsible for the three fundamental forces), and the Higgs Boson (which is the origin of mass of many of the fundamental particles). Find a picture without a watermark	6
¹⁶⁶	2.1	Galactic rotation curves show stars far from the galactic center are orbiting the galactic center far faster than they should gives evidence for invisible matter.	8
¹⁶⁸	2.2	The Bullet Cluster shows visible matter from X-rays (highlighted in blue) and total matter from gravitational lensing (highlighted in pink).	9
¹⁷⁰	2.3	The Cosmic Microwave Background has temperature fluctuations consistent with extra invisible matter in the early universe.	10
¹⁷²	2.4	Left: Big Bang Nucleosynthesis puts an upper bound on the Standard Model matter density in the universe at about 15% of the total energy budget [60]. Right: Measurements from Type 1a supernovae (shaded in blue) together with the CMB and BAO measurements put the total mass in the universe at 30% of the total energy budget along with dark energy at 70% (from the intersection in gray) [14]. A combination of these measurements show that the Standard Model cannot account for most of the matter in the universe.	11
¹⁷⁹	2.5	A one-loop kinetic mixing process where an A' mixes with the SM photon through an interaction of massive fields that couple to both photons.	13
¹⁸¹	2.6	Left: The results from PAMELA, AMS, and Fermi-LAT showing the positron fraction excess (above the expected calculation from cosmic rays in grey) at above ~ 10 GeV [35]. Right: The Feynman diagram for the dark matter annihilation into two A' s which subsequently decay into e^+e^- pairs. This provides an explanation for positron fraction excess. This explanation has since been disfavored.	15

186	2.7	The mechanism of thermal freeze-out in which dark matter and SM matter are in thermal equilibrium in the early universe. As the universe cools (x -axis), the relic abundance of dark matter (y -axis) is depleted by self-annihilation until enough cooling occurs and the dark matter relic abundance is set.	17
187			
188			
189			
190	2.8	The branching ratio for heavy photon decays to SM particles as a function of mass. This assumes no decays into dark sector particles.	21
191			
192	2.9	Existing constraints of heavy photons on the whole parameter space [48]. The constraints come from a variety of sources including astrophysical measurements, precision QED, and particle accelerator-based experiments. The regional labeled “unified DM” is of particular interest to dark matter for reasons described in Sec. 2.4 and Sec. 2.3 and will be the focus. Note that the notation on this plot is such that $\epsilon \rightarrow \chi$ and A' is denoted as γ'	23
193			
194			
195			
196			
197			
198	2.10	A schematic of beam dump experiments SLAC E-137 and E-141 which searched for long-lived particles that decay in a region several hundred meters from the target.	25
199			
200	2.11	The Light Dark Matter eXperiment (LDMX) searches for heavy photon decays to invisibles by measuring the recoil electron momentum and searching for missing momentum. The apparatus includes a tagging tracker, recoil tracker, an Ecal, and an Hcal.	26
201			
202			
203			
204	2.12	The kinematics for heavy photon (A') produced from an electron on a fixed target. In general, A' 's retain most of the incident beam energy, remain close to the beam axis due to a small recoil angle, and have a small opening angle.	28
205			
206			
207	2.13	Left pictures show Feynman diagrams for A' (top), RAD (middle) and BH (bottom) events. Right picture shows WAB process.	30
208			
209	2.14	Positron momentum vs electron momentum comparing Bethe-Heitler tridents and A' 's (and hence radiative tridents). A' 's generally have a large x in comparison to Bethe-Heitler. This is for a beam energy of 1.06 GeV.	31
210			
211			
212	3.1	A 3D rendering of the HPS detector complete with the silicon vertex tracker (SVT), electromagnetic calorimeter (Ecal), and chicane.	33
213			
214	3.2	The rate of electrons in at the first layer of the SVT from the so-called “wall of flame” - beam electrons that lose energy due to bremmstrahlung in the target and bend in the magnetic field. To avoid the radiation damage from the wall of flame, the detector is split into top and bottom halves.	34
215			
216			
217			
218	3.3	A schematic of the upgraded Continuous Electron Beam Accelerator Facility (CE-BAF) at Jefferson Laboratory. The machine is a recirculating linear accelerator designed to send a beam of electrons of different currents and energies to four different experimental halls (Halls A - D).	35
219			
220			
221			

222	3.4 A schematic of Hall B including the CLAS-12 spectrometer and the HPS detector in the Hall B alcove. The electron beam enters the hall from the left in this picture.	36
223		
224	3.5 An example of a scan from the 2H02 wire harp from the 2016 Engineering Run. This provides a measurement of the beam profile that is useful as input to tuning the beam to its optimal profile at the target. The profile shows a width of 92 μm in x and 14 μm in y with minimal beam tails.	38
225		
226		
227		
228	3.6 A schematic of the HPS beamline inside the Hall B alcove.	39
229		
230	3.7 An example of an SVT wire scan measurement from the 2016 Engineering Run. This provides a measurement of the beam profile as close to the target as possible. This scan shows a beam with a 14 μm width in the y -direction with minimal tails and 35 μm from the nominal beam plane. This is an excellent beam profile for HPS.	40
231		
232		
233		
234	3.8 A measurement of the beam halo from 2015 Engineering Run using the occupancy of the first layer of the SVT in a no target run. The beam halo shows a width of 960 μm and 5 orders of magnitude less than the peak of the beam.	40
235		
236		
237		
238	3.9 A schematic of the HPS silicon vertex tracker (SVT) which includes 6 layers of silicon microstrip sensors inside a vacuum and a uniform magnetic field. Maybe find a better picture.	41
239		
240	3.10 A schematic of the APV25 deep submicron readout chip that was originally designed for CMS detectors but is used for the HPS SVT.	43
241		
242	3.11 A picture of the two SVT sensors (end to end) with each sensor. The sensors are readout by APV25 chips which are housed on a hybrid circuit.	44
243		
244	3.12 The APV25 Shaper schematic. The parameters VFS (related to the input voltage) and isha (related to the input current) were optimized for improved time resolution and reduced pileup.	45
245		
246	3.13 A single SVT module which comprises of two silicon microstrip sensors which are axial (front) and stereo (back) to the beam plane. Each sensor is supported by a carbon fiber support structure can be seen protruding from the right of the axial sensor.	46
247		
248		
249	3.14 Layers 1 - 3 modules of the SVT (from left to right) are placed in one of the U-channels. Copper cooling lines and electrical lines can be seen. The wire frames and scan wires can also be seen on the left.	47
250		
251		
252	3.15 A picture inside the SVT vacuum chamber with everything installed except for the target. The frontend boards (FEBs) and FEB cooling plate are on the left. The SVT cooling lines protrude outward in the picture. The first layer of the SVT can be seen in the back behind the wire frames. The SVT is in its closed position and the beam must go through the 1 mm gap between the top and bottom sensors.	48
253		
254		
255		
256		
257	3.16 A schematic of the SVT DAQ system described in Sec. 3.3.3.	49

258	3.17 The FEB cooling plate complete with 10 FEBs fastened to the front and back of the plate.	51
260	3.18 A rendering of the HPS Ecal. Each segment is one of the 442 lead tungstate crystals and the Ecal is split in half to avoid radiation damage from the most intense parts of the beam.	52
263	3.19 A schematic of a PbWO ₄ crystal in the Ecal.	53
264	3.20 A schematic of the trigger for the Ecal. Top and bottom halves of the Ecal are each are readout by FADC readout boards, and then sent to the SSP where a trigger decision is made.	54
267	3.21 A summary for the integrated charge over time for the Top: 2015 Engineering Run and Bottom: 2016 Engineering Run. Replace these figures	56
269	4.1 A schematic of the linear collider tracking parameters 5.17 [52].	58
270	4.2 The run-dependent average position in z for unconstrained vertices fit represented by solid points and a solid line for data and MC simulation, respectively.	66
272	4.3 The run-dependent mean (left) and width (right) in x and y for the unconstrained vertex position in data. The MC is represented as a solid line.	67
274	4.4 Left: The measured SVT layer 1 efficiency for electrons in layer 1 bottom stereo sensor. The MC does not have the correct hit efficiencies. Right: The layer 1 hit efficiency as a function of track slope ($\tan\lambda$) used for the hit killing algorithm described in Sec Section. Replace these figures. Add a positron hit efficiency plot.	68
277	4.5 The target position is found to be -4.3 mm. I actually need to get these plots. Some placeholders are there for now.	70
278	4.6 Preselection and layer 1 requirements for tritrig-wab-beam MC for e^+ and e^- tracks. Left: Purity. Right: Layers with a bad hit. Redo these plots	72
280	4.7 Left pictures show Feynman diagrams for A' (top), RAD (middle) and BH (bottom) events. Right picture shows WAB process.	75
283	4.8 Comparison of 10% Data and tritrig-wab-beam for preselected events.	79
284	4.9 Preselection cutflow for as a function of reconstructed z . Top Right: Run 7800 in data. Top Left: a fraction of the tritrig-wab-beam sample. Bottom Left: 80 MeV displaced A' s. Bottom Right: 100 MeV displaced A' s.	81
287	4.10 Preselection cutflow for reconstructed mass. Top Right: Run 7800 in data. Top Left: a fraction of the tritrig-wab-beam sample. Bottom Left: 80 MeV displaced A' s. Bottom Right: 100 MeV displaced A' s.	82
289	4.11 Preselection cutflow for as a function of reconstructed V0 momentum. Top Right: Run 7800 in data. Top Left: a fraction of the tritrig-wab-beam sample. Bottom Left: 80 MeV displaced A' s. Bottom Right: 100 MeV displaced A' s.	83

294	4.12 Track-cluster match number of σ for electrons (left) and positrons (right). A loose cut 295 is placed at $N\sigma < 10$ for both electrons and positrons to eliminate poor track-cluster 296 matches.	83
297	4.13 Track χ^2 per degrees of freedom (dof) for electrons (left) and positrons (right). A cut 298 is placed at $\chi^2 < 6$ for both electrons and positrons to eliminate poor tracks that can 299 falsely reconstruct downstream of the target.	84
300	4.14 Cluster-track time difference (with the time offset from Table 4.7) for electrons (left) 301 and positrons (right). A cut is placed at a time difference of 4 ns for both electrons 302 and positrons to eliminate out of time tracks. There is significant mismodeling for 303 the track time resolution; however, this is a data-driven cut.	84
304	4.15 Electron momentum (left) and positron momentum (right) both have minimum mo- 305 mentum cuts at 0.4 GeV in order to reduce low momentum particles that have larger 306 multiple scattering. Another maximum momentum cut is placed on electrons only at 307 1.75 GeV to eliminate V0s that reconstruct with elastically-scatter electrons in the 308 target. There is some mismodeling for individual particle momenta particularly at 309 low momentum.	85
310	4.16 Left: A cluster time difference cut between electrons and positrons is placed at 1.45 311 ns to eliminate accidentals from other beam bunches (Hall B bunches are spaced at 312 2 ns). Right: A loose cut on the unconstrained vertex fit χ_{unc} is placed at 10 to 313 eliminate poorly reconstructed V0s that can incorrectly reconstruct downstream of 314 the target. There is some mismodeling for the cluster time resolution, and there is 315 some mismodeling in the vertex quality.	85
316	4.17 A maximum V0 momentum cut is placed at 2.4 GeV since signal is not expected far 317 above the beam energy at 2.3 GeV.	86
318	4.18 Integrated cross section for the RAD (left), Trident-Trig(middle) and WAB(right) 319 samples, separately.	87
320	4.19 Left: The differential cross sections ($d\sigma/dm$) of wab, trident, and radiative trident 321 components from MC as well as the measured cross section from 10% of the data. 322 In principle, one would expect the tridents + wabs (turquoise) to agree with data 323 (blue). The discrepancy is explained in Sec. 4.11.3. Right: The radiative fractions as 324 a function of mass. It is fit to a 5th order polynomial and is used to determine the 325 expected radiative trident rate from the number of e+e- pairs in a mass bin.	89
326	4.20 The invariant mass for 10% of the data with the radiative cut selection. It is fitted 327 to the an exponential to a 5th order polynomial. This is the number of e+e- pairs 328 in a 1 MeV bin used to normalize the expected radiative trident rate, and hence the 329 expected A' rate.	90

330	4.21 Distributions of e^+e^- events with scaling all MC cross-sections by 0.8. Clockwise from top left: positron+electron momentum, e^+e^- invariant mass, positron track slope, electron track slope, electron momentum, positron momentum.	92
333	5.1 Mass slice from 2015 Replace this with the 2016 mass slice.	94
334	5.2 Final event selection for the displaced vertex search in the 2015 Engineering Run for Left: Data and Right: a luminosity-equivalent tritrig-wab-beam MC sample. The z_{cut} is shown in red.	95
337	5.3 Final results for the displaced vertex search for the 2015 Engineering Run. Left: The number of expected A' events after all analysis cuts and z_{cut} as a function of mass and ϵ^2 . Right: The limit on the A' cross section as a function of mass and ϵ^2 . State the minimum and maximum values.	96
341	5.4 From detailed MC studies, it was shown that the backgrounds are due to two main processes. We seek to further mitigate these backgrounds in the 2016 Engineering Run. Left: A vertex is falsely reconstructed downstream of the target due to two large scatters of the e^+e^- pairs away from the beam plane. Right: A vertex is falsely reconstructed downstream of the target due to a track picking up the incorrect layer 1 hit (mis-tracking). These events are usually accompanied by a large scatter in the other particle that is tracked correctly.	96
348	5.5 Fitted e^-e^- spectrum using the Møller selection for Upper Left: Data, Upper Right: MC with track momentum smearing, and Bottom: Møller MC.	100
350	5.6 Upper Left: Fitted reconstructed mass spectrum for a 100 MeV displaced A' . Upper Right: Fitted reconstructed mass spectrum for a 100 MeV displaced A' with track momentum smearing. Lower Left: Reconstructed mass vs truth z decay for a 100 MeV displaced A' . Lower Right: The fitted mass resolution for 100 MeV displaced A' s as in slices of truth z . Mass resolution is approximately independent of decay length. These plots are for the L1L1 category.	101
356	5.7 Upper Left: Fitted reconstructed mass spectrum for a 100 MeV displaced A' . Upper Right: Fitted reconstructed mass spectrum for a 100 MeV displaced A' with track momentum smearing. Lower Left: Reconstructed mass vs truth z decay for a 100 MeV displaced A' . Lower Right: The fitted mass resolution for 100 MeV displaced A' s as in slices of truth z . Mass resolution is approximately independent of decay length. These plots are for the L1L2 category.	102
362	5.8 A' mass resolution as a function of mass comparing A' MC, A' MC scaled using the ratio of the Møller mass resolution in data to MC, and A' MC with smearing for the Left: L1L1 category and the Right: L1L2 category. The mass resolution is fitted to a straight line to the MC with track momenta smearing and is used as an input to the size of the mass bins in the final results.	102

367	5.9 Left: The measured SVT layer 1 efficiency for electrons in layer 1 bottom stereo sensor. The MC does not have the correct hit efficiencies. Right: The layer 1 efficiency used for the hit killing algorithm as a function of track slope ($\tan\lambda$).	105
370	5.10 The product of geometrical acceptance and efficiency for displaced A' 's for the L1L1, L1L2, and L2L2 categories as well as there sums. 80 MeV displaced A' 's are on the left and 100 MeV displaced A' 's are on the right. The top is before hit killing and the bottom is with hit killing and a fit function fit to the sum of the categories. The top plots I still have to make, I have the same plots there as the bottom as a placeholder.	107
375	5.11 The product of geometrical acceptance and efficiency for displaced A' 's for the L1L1, L1L2, and L2L2 categories as well as there sums. These plot are normalized to unity at the target, where the sum is normalized before hit killing and further analysis cuts. 80 MeV displaced A' 's are on the left and 100 MeV displaced A' 's are on the right. The top is without the z_{cut} and the bottom is with the z_{cut} from 10% of the data.	108
380	5.12 The run-dependent mean (left) and width (right) for x and y target projection for the unconstrained vertex in data.	109
382	5.13 Left: Schematic of a relatively short A' decay length in which both daughter particles have a layer 1 hit. Right: Schematic of a relatively long A' decay length in which one of the daughter particles misses layer 1 (but hits layer 2) and the other daughter particle hits layer 1.	111
386	5.14 Left: A schematic of a prompt background process that has a hit inefficiency in layer 1 and is placed in the L1L2 category. Right: A schematic of a prompt background process in which one of the daughter particles scatters away from the beam in the inactive silicon of layer 1 and into the acceptance of the tracker. This process is placed in the L1L2 category and also reconstructs a false vertex downstream of the target.	112
391	5.15 The V0 projection back to the target for Preselection in the L1L1 category. Upper Left: 10% Data with a linear fit to the $x-y$ correlation Lower Left: 10% tritrig-wab- beam with a linear fit to the $x-y$ correlation. The V0 projection back to the target for L1L1 Preselection with rotated $x-y$ coordinates for Upper Right: 10% Data and Lower Right: 10% tritrig-wab-beam. The angle of rotation is $\theta_{data} = 0.0387$ rad in data and $\theta_{MC} = 0.1110$ rad in MC.	115
397	5.16 Left: Example of mistracking from a layer 1 bad hit that falsely reconstructs down- stream of the target. Right: Geometric picture of the isolation cut comparing the distance between the nearest hit away from the beam δ and the track longitudinal impact parameter of the track z_0 where the correct track is in green and the incorrect track found by the tracking algorithm is in red.	116
401	5.17 A schematic of the linear collider tracking parameters.	117

403	5.18 Left: Prompt background that falsely reconstructs at a large z due to an e^- particle 404 with a large scatter away from the beam plane in layer 1 of the SVT. The correspond- 405 ing e^+ does not have a large scatter and the track point back near the primary. A 406 cut on the impact parameter can eliminate such background. Right: A true displaced 407 vertex will have a large impact parameter for both e^+e^- pairs that is correlated with 408 reconstructed z	124
409	5.19 Left: The y -intercept for a linear fit in z_0 vs reconstructed z at various mass points. 410 Each For simplicity, the range is fit with a constant and used as an input to Eq: 5.12 411 ($a_+(m) = a_-(m) = a$) . Right: The slope for a linear fit in z_0 vs reconstructed z as a 412 function of mass for tracks in the top volume of the SVT. The range is fit using Eq: 413 5.13. These plots are ugly, but I can replace them in the future if necessary.	125
414	5.20 Invariant mass vs the momentum sum of a trident sample. The red starts are the 415 optimal momentum sum in slices of mass based on $sig/\sqrt{sig + bck}$ where radiative 416 tridents are signal and tridents are background. Above 60 MeV, the lower mass bound 417 of interest for the displaced vertex search, the optimal value is a momentum sum of 418 about 2.0 GeV.	125
419	5.21 Upper Left: Comparison of 10% Data and tritrig-wab-beam MC for the final event 420 selection in the L1L1 category. Upper Right: Comparison of 10% of the Data for 421 before and after multiple V0 events are removed. Lower Left: Comparison of 80 MeV 422 displaced A's for before and after multiple V0 events are removed. Lower Right: 423 Comparison of 100 MeV displaced A's for before and after multiple V0 events are 424 removed.	128
425	5.22 Upper Left: Comparison of 10% Data and tritrig-wab-beam MC for the final event 426 selection in the L1L1 category. Upper Right: Comparison of 10% of the Data for 427 before and after multiple V0 events are removed. Lower Left: Comparison of 80 MeV 428 displaced A's for before and after multiple V0 events are removed. Lower Right: 429 Comparison of 100 MeV displaced A's for before and after multiple V0 events are 430 removed.	129
431	5.23 Upper Left: Comparison of 10% Data and tritrig-wab-beam MC for the final event 432 selection in the L1L1 category. Upper Right: Comparison of 10% of the Data for 433 before and after multiple V0 events are removed. Lower Left: Comparison of 80 MeV 434 displaced A's for before and after multiple V0 events are removed. Lower Right: 435 Comparison of 100 MeV displaced A's for before and after multiple V0 events are 436 removed.	130

437	5.24 Upper Left: Comparison of 10% Data and tritrig-wab-beam MC for the final event 438 selection in the L1L1 category. Upper Right: Comparison of 10% of the Data for 439 before and after multiple V0 events are removed. Lower Left: Comparison of 80 MeV 440 displaced A's for before and after multiple V0 events are removed. Lower Right: 441 Comparison of 100 MeV displaced A's for before and after multiple V0 events are 442 removed.	131
443	5.25 Plots showing the effect of with and without the isolation cut for the L1L2 category. 444 Upper Left: Comparison of VZ distributions for 10% Data and 100% tritrig-wab- 445 beam MC for all tight cuts except for the isolation cut. Upper Right: Comparison of 446 preselection, tight cuts, and tight cuts without the isolation cut for 10% Data. Middle 447 Left: Electron isolation cut value for 10% Data and tritrig-wab-beam MC using all 448 tight cuts except the isolation cut. Middle Right: Positron isolation cut value for 10% 449 Data and tritrig-wab-beam MC using all tight cuts except the isolation cut. Bottom 450 Left: Comparison of preselection, tight cuts, and tight cuts without the isolation cut 451 for displaced 80 MeV A's. Bottom Right: Comparison of preselection, tight cuts, and 452 tight cuts without the isolation cut for displaced 100 MeV A's.	133
453	5.26 Impact parameter vs. reconstructed z for different mass values of 10% data and A' s 454 in the L1L2 category. The red lines indicate the impact parameter cut at the specified 455 mass value. Upper Left: 10% data in mass range 75-85 MeV. Upper Right: 10% data 456 in the mass range 95-105 MeV. Lower Left: 80 MeV Displaced A' s. Lower Left: 100 457 MeV Displaced A' s.	137
458	5.27 Comparisons of tight cuts for the L1L2 category. Upper Left: Comparison of the 459 tight cutflow for 10% Data and tritrig-wab-beam. Upper Right: Comparison of 10% 460 Data and tritrig-wab-beam for events with tight cuts. Lower Left: Tight cutflow for 461 80 MeV displaced A' 's. Lower Right: Tight cutflow for 100 MeV displaced A' 's.	138
462	5.28 Upper Left: Comparison of 10% Data and tritrig-wab-beam MC for the final event 463 selection in the L1L2 category. Upper Right: Comparison of 10% of the Data for 464 before and after multiple V0 events are removed. Lower Left: Comparison of 80 MeV 465 displaced A's for before and after multiple V0 events are removed. Lower Right: 466 Comparison of 100 MeV displaced A's for before and after multiple V0 events are 467 removed.	139
468	5.29 Upper Left: Comparison of 10% Data and tritrig-wab-beam MC for the final event 469 selection in the L1L1 category. Upper Right: Comparison of 10% of the Data for 470 before and after multiple V0 events are removed. Lower Left: Comparison of 80 MeV 471 displaced A's for before and after multiple V0 events are removed. Lower Right: 472 Comparison of 100 MeV displaced A's for before and after multiple V0 events are 473 removed.	140

474	5.30 Left: 10% Data and full MC comparison in reconstructed z for a slice in mass for L1L1. For both distributions, the fitted mean is shifted to 0. Right: 10% Data and full MC comparison in reconstructed z for a slice in mass for L1L2. For both distributions, the fitted mean is shifted to 0.	140
478	5.31 Top Left: Fitted mean as a function of mass comparing 10% of the data to the full tritrig-wab-beam sample for the L1L1 category. Top Right: Fitted mean as a function of mass comparing 10% of the data to the full tritrig-wab-beam sample for the L1L2 category. Middle Left: Fitted σ as a function of mass comparing 10% of the data to the full tritrig-wab-beam sample for the L1L1 category. Middle Right: Fitted σ as a function of mass comparing 10% of the data to the full tritrig-wab-beam sample for the L1L2 category. Bottom Left: Fitted “tail z ” parameter (the number of σ from the mean the function transitions from Gaussian core to exponential tail) as a function of mass comparing 10% of the data to the full tritrig-wab-beam sample for the L1L1 category. Bottom Right: Fitted “tail z ” parameter (the number of σ from the mean the function transitions from Gaussian core to exponential tail) as a function of mass comparing 10% of the data to the full tritrig-wab-beam sample for the L1L2 category.	141
490	5.32 The final event selection with overlaid z_{cut} from 10% data, the full tritrig-wab-beam sample, and projected to the full dataset for Top Left: 10% data for the L1L1 category, Top Right: full tritrig-wab-beam sample for the L1L1 category, Bottom Left: 10% data for the L1L2 category, and Bottom Right: full tritrig-wab-beam sample for the L1L2 category.	142
495	5.33 Top Left: A comparison of z_{cut} between 10% data and scaled to the full dataset to the maximum z value in a mass bin for the L1L1 category. Top Right: A comparison of z_{cut} between 10% data and scaled to the full dataset to the maximum z value in a mass bin for the L1L2 category. Bottom Left: A comparison of the biased and unbiased (excluding the mass search bin) z_{cut} for the L1L1 category. Bottom Right: A comparison of the biased and unbiased (excluding the mass search bin) z_{cut} for the L1L2 category.	143
502	5.34 Left: The number of A’s produced for each mass and ϵ^2 in prompt acceptance including all efficiencies for 10% of the data. In other words, the term in front of the integral in Eq. 5.20. Right: The number of A’s produced for each mass and ϵ^2 in prompt acceptance including all efficiencies projected for 100% of the data.	144
506	5.35 Left: The expected number of A’ events past zcut including all efficiencies for the L1L1 category for 10% of the data. Right: The expected number of A’ events past zcut including all efficiencies for the L1L1 category projected for the full dataset. . .	145

509	5.36 Left: The expected number of A' events past zcut including all efficiencies for the	
510	L1L2 category for 10% of the data. Right: The expected number of A' events past	
511	zcut including all efficiencies for the L1L2 category projected for the full dataset. . .	145
512	5.37 Left: The number of background events past zcut based on the background model	
513	and the candidate events past z_{cut} for the L1L1 category. Right: The p-value for the	
514	L1L1 category	146
515	5.38 The effects of a single event on the Optimum Interval Method limit for several decay	
516	lengths for an 80 MeV mass bin (left) and a 100 MeV mass bin (right). The relative	
517	limit (relative to the background-free limit) is plotted as a function of reconstructed	
518	z of a single dummy background event. A single background event can result in up	
519	to about a 70% worse limit.	147
520	5.39 Left: The limit from Optimum Interval Method for the L1L1 category. Right: The	
521	limit from Optimum Interval Method for the L1L2 category. Report minimum value	148
522	5.40 Left: The combined expected number of A' events past z_{cut} including all efficiencies	
523	for the L1L1 and L1L2 categories for 10% of the data. Right: The combined ex-	
524	pected number of A' events past z_{cut} including all efficiencies for the L1L1 and L1L2	
525	categories for the full dataset. Report minimum value	149
526	5.41 The combined limit from Optimum Interval Method for the L1L1 and L1L2 categories.	
527	Report minimum value	149
528	6.1 Trident Acceptance L0.	155
529	6.2 VZ Resolution.	155
530	6.3 A' efficiency.	156
531	6.4 A' total efficiency	156
532	6.5 zcut	157
533	6.6 4 weeks projection.	157
534	6.7 Positron Trigger	158
535	6.8 L0 design	159
536	6.9 SVT view.	160
537	6.10 Survey and test box	161
538	6.11 The testing station for the DAQ had a sophisticated humidity monitoring system	
539	which readout a humidity sensor via an arduino which was connected to a Twitter-	
540	based alert system. This picture shows an example of a sudden increase in humidity	
541	in both test boxes which was immediately followed by an alert tweet. In other words,	
542	someone opened the test boxes.	162
543	6.12 Timeline	162
544	6.13 Beam	162
545	6.14 Projections	163

546	6.15 Data 2019	163
547	6.16 A hidden $SU(3)$ symmetry can contain hidden hadrons which include dark pions and	
548	dark vector mesons. These particles could only interact indirectly with the SM via	
549	kinetic mixing between an A' and the SM photon as describe in Sec. 2.2.	165
550	6.17 This mechanism is known as the SIMP Miracle.	166
551	6.18 Left: SIMP p Right: livetime	167
552	6.19 SIMP $\frac{m_\pi}{f_\pi}$ and branching ratio	167
553	6.20 The SIMP reach estimate from the full 2016 Engineering Run dataset shown in ϵ^2 -	
554	$m_{A'}$ space for $\alpha_{dark} = 0.01$ and for Left: $m_\pi/f_\pi = 3$ and Right: $m_\pi/f_\pi = 4\pi$. The	
555	ratio of the masses is kept constant at $m_{A'} : m_\rho : m_\pi = 3.0 : 1.8 : 1.0$ for simplicity.	
556	The dataset is projected to set new limits in previously unprobed territory. These	
557	figures need to be replaced.	168

558 This thesis is dedicated to...

559 **Chapter 1**

560 **Introduction**

561 The Standard Model of Particle Physics (SM) is humanity's best attempt to explain matter, its
562 interactions, and its origin at the most fundamental level possible. Shown in Fig. 1.1, the basic
563 framework of the SM contains a group of six quarks and 6 leptons which compose all the known
564 matter as well as four gauge bosons which are responsible for the three fundamental forces in nature
565 - electromagnetism, strong nuclear force, and weak nuclear force. The last piece of the SM is the
566 Higgs Boson, the explanation of origin of mass of the elementary particles, which was triumphantly
567 discovered in 2012 at the Large Hadron Collider (LHC) - a 17 mile long circular particle accelerator
568 and multi-billion dollar project. This is the largest machine ever built by mankind, and because of
569 the scale and technology required, the SM Higgs Boson prediction and its discovery almost 50 years
570 later remains one of the greatest intellectual accomplishments of humanity. For almost 60 years, the
571 SM has proven to be robust in its agreement with data and has remained the best explanation of
572 elementary particles and their interactions.

573 However, modern cosmology has completely broken our understanding of particle physics. Through
574 detailed astrophysical measurements, it has been shown that the universe contains an invisible type
575 of matter that the SM fails to explain. Not only that, this invisible matter makes up about 85% of
576 the total matter in the universe which dramatically shows the scale in which the SM is incorrect.
577 This invisible matter is often referred to as “dark matter” due to its lack of interactions with light.

578 The concept of dark matter actually dates back well before the advent of the SM to Lord Kelvin in
579 1884 where he established a relationship between the size of the Milky Way Galaxy and the velocity
580 dispersion of its stars by modeling stars as gaseous particles under the influence of gravity. Using this
581 dynamical model, he reported evidence of additional unobservable matter and concluded that many
582 of the stars could be “dark bodies” [50]. Intrigued by this idea, Henri Poincaré applied Lord Kelvin’s
583 idea to the Milky Way, but disagreed with Lord Kelvin’s general conclusions. Though Poincaré
584 coined the term “matière obscure” (French for dark matter), he remained uncertain and concluded
585 that there could be only as much missing matter as observable stellar matter [57]. Fritz Zwicky

586 extended this idea by applying the virial theorem to the Coma Cluster and showed evidence for
 587 extra-galactic missing matter that he called “dunkle Materie” [65]. Quantitatively these estimations
 588 of invisible matter differed significantly from presently understood values, and it wasn’t until Vera
 589 Rubin’s measurements of galactic rotation curves in the 1970s that modern cosmologists and particle
 590 physicists began to understand the scale of the missing matter problem and began to take the idea of
 591 dark matter seriously. A compelling case for dark matter with modern evidence will be constructed
 592 in more detail in Chp. 2.

593 The nature of dark matter is also linked to its origin, and there is a high probability that
 594 there is some interaction, at least indirect interaction, with SM particles that can be exploited in the
 595 laboratory - either with accelerator experiments or so-called direct detection experiments. In fact, for
 596 a simple mechanism of thermal equilibrium, where collisions between dark matter particles annihilate
 597 into SM particles and vice-versa, the amount of dark matter, called the “relic abundance”, is directly
 598 related to its annihilation cross-section. When one computes the expected mass and cross-section
 599 from such a mechanism, it gives rise to a remarkable coincidence in which the particle responsible
 600 for dark matter has a mass and coupling similar to the SM weak-sector particles (W , Z , and Higgs
 601 Bosons). These hypothetical particles are called for Weakly Interacting Massive Particles (WIMPs)
 602 and this coincidence is so extraordinary, that it is referred to as the “WIMP Miracle” and provides
 603 compelling motivation to search for a stable object on the weak scale through both direct detection
 604 experiments.

605 To date of publication, WIMPs have not been discovered and the accessible parameter space will
 606 be probed with next generation direct detection experiments. As an alternative, it is reasonable
 607 to compliment these searches on the mass scale where known stable SM particles exist, such as
 608 electrons and protons. However at this mass scale, the MeV-GeV mass scale (or sub-GeV), the
 609 simplest mechanisms of thermal equilibrium mediated by SM bosons in the early universe gives an
 610 overproduction of dark matter, greater than the observed 85%. That is, assuming these SM-dark
 611 matter interactions are mediated by SM forces, once the mass scale is below than the so-called “Lee-
 612 Weinberg Bound” at 2 GeV, dark matter with a thermal origin always overproduces the observed
 613 relic abundance. In order to circumvent this bound, dark matter models on the sub-GeV scale called
 614 “light dark matter” require at least one additional comparably light mediator. One such natural
 615 candidate is called a heavy photon (or dark photon or A').

616 First derived by Bob Holdom in the 1985, heavy photons arise as the massive mediator from
 617 a model comprised of an additional $U(1)$ symmetry in nature [47]. This model was given new life
 618 by the results of the PAMELA satellite in 2008 that reported an excess in the flux of cosmic ray
 619 positrons originating from the center of the Milky Way Galaxy [6] and was explained by Arkani-
 620 Hamed as dark matter annihilations through a heavy photon mediator [17]. ¹ In this model, heavy

¹Though dark matter annihilations have been ruled out as an explanation the observed anomaly of by PAMELA, heavy photons are still strongly motivated by a variety of models of sub-GeV dark matter as a way to circumvent the Lee-Weinberg bound as well as a variety of other anomalies discussed in Sec. 2.4.

621 photons act like a bridge, or “vector portal”, in which dark matter and SM can indirectly interact
622 in highly dense and energetic regions such as the galactic center and the early universe. In order
623 to probe heavy photons in the parameter space most relevant to dark matter at accelerator-based
624 experiments, Bjorken, Essig, Schuster, and Toro (B.E.S.T.) developed a variety of clever strategies
625 using colliders, beam dumps, and fixed target experiments based on potential signatures of heavy
626 photons [26]. The two main signatures of a heavy photon that can be used as methods of discovery
627 are through a sharp resonance peak in the invariant mass spectra of its daughter particles or, since
628 heavy photons with small couplings can have a finite livetime, searches for secondary vertices are
629 possible. A variety of existing experiments, including both colliders and beam dump experiments,
630 could easily probe large regions of theoretically-favored heavy photon parameter space.

631 However, several models of sub-GeV dark matter highly motivate a region of heavy photon
632 parameter space in which heavy photons have both a low production cross-section and short decay
633 length (on the scale of mm-cm), proving impossible to probe for existing experiments. Probing the
634 short decay lengths of heavy photons on the scale of \sim 1 - 10 cm is the main goal of the Heavy
635 Photon Search Experiment - a precision vertexing fixed target experiment at Jefferson Laboratory.
636 This introduces a variety of technical challenges. For instance, the HPS particle tracker must
637 balance the detector acceptance of the highly boosted heavy photons with excellent mm-scale vertex
638 resolution. As a result, the most sensitive detector material (silicon from the tracker) is placed at
639 an unprecedented $500\ \mu\text{m}$ from the beam plane. Positioning the silicon any closer will result in
640 significant radiation damage to the silicon sensors from a very intense electron beam, while a more
641 conservative placement will render this type of search infeasible. In addition, because of the small
642 production cross-section and large background rates, the analysis will require an understanding of
643 the SM backgrounds to about one part in a 100 million. That is, the ability to differentiate between
644 about 100 million background processes that are prompt (i.e. they originate from the target) and a
645 small number of true long-lived processes from heavy photons is critical but challenging.

646 From HPS and a few other “flagship” experiments specifically designed to search for heavy
647 photons, the field known as “dark sectors” (i.e. the set of particles belonging to dark matter)
648 was born. Over the course of the past decade, dark sector models have become more generalized
649 extending beyond the simple vector portal from heavy photons to a limited set of additional portals
650 (such as Higgs-like, axion-like, and neutrino-like portals) in which the dark sector can indirectly
651 interact with SM particles. These models also allow arbitrary complex structure and interactions
652 amongst particles in the dark sector much like the matter and interactions in the SM sector.

653 Probing short-lived heavy photons through a precision vertexing experiment is the subject of this
654 dissertation and I place emphasis on the method and results of the displaced vertex search for the
655 2016 Engineering Run for HPS. Though this dissertation centers around my specific contributions,
656 my contributions are not specifically mentioned and as a result, they are listed here. I was heavily
657 involved in two data taking runs - the 2016 Engineering Run and 2019 Physics Runs - and served as

658 both a subsystem expert and shift expert. The 2019 Physics Run also included an upgrade to the
659 tracker in which I was responsible for much of the mechanical work including mechanical survey and
660 alignment, and I was a part of the team that installed and commissioned this upgrade. In addition, I
661 was heavily involved in the data quality of three different datasets including the two listed above and
662 the 2015 Engineering Run, and I made improvements to the software, reconstruction, and analysis
663 data formats. However, my main focus over the course of my PhD was significant improvements
664 to the displaced vertex search by attempting to utilize HPS' full potential for this type of search.
665 These specific contributions are summarized in the following:

- 666 1. The completion of the displaced vertexing analysis for the 2016 Engineering Run from start
667 to finish (data taking to final result and publication).
- 668 2. A leadership role in the completion of the displaced vertexing analysis for the 2015 Engineering
669 Run. I made critical advancements in the simulations that led to a more detailed understanding
670 of backgrounds which were mostly due to mistracking and particles scattering in the tracker.
- 671 3. Studying the sensitivity for heavy photons that decay further downstream and are not in the
672 acceptance of the full tracker. This gives rise to more complex backgrounds, such as hit ineffi-
673 ciencies, scattering in dead material, trident production in the tracker. I made advancements
674 in understanding both the signal and backgrounds for these cases and preliminary studies were
675 used as an input to tracker upgrades.
- 676 4. The development of a machine learning approach utilizing a binary classification to more
677 effectively separate a small signal from a large background. Though this was not used in the
678 published analysis, this method guided us to more effective ways to discriminate between signal
679 and background and could lead to an improved method of background rejection in the future.
- 680 5. Extending this analysis to probe other models of interest that contain long-lived particles
681 beyond the heavy photon model and projecting HPS' sensitivity with existing data for such
682 models.
- 683 6. Using simulations to produce the original reach estimates for the upgrade to the tracker showing
684 dramatic improvement to HPS' projected sensitivity for heavy photons.

685 The remainder of this dissertation details the motivations and theory of heavy photons, detector
686 and experimental setup, physics reconstruction process, displaced vertex analysis and results, and
687 future of HPS including generalized displaced vertices and projections of the latest dataset.

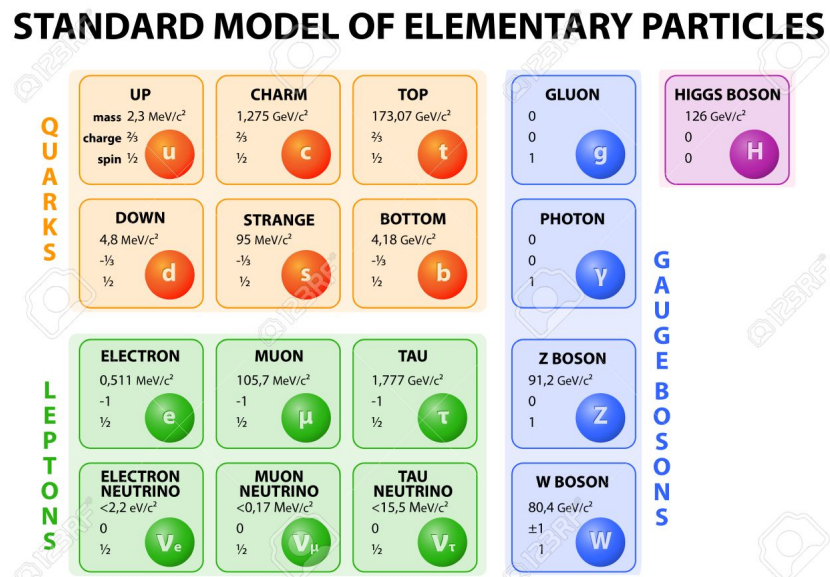


Figure 1.1: The Standard Model of Particle Physics is a group of the known elementary particles which is composed of six quarks, six leptons, four gauge bosons (which are responsible for the three fundamental forces), and the Higgs Boson (which is the origin of mass of many of the fundamental particles). **Find a picture without a watermark**

688 **Chapter 2**

689 **Motivation**

690 The Standard Model of Particle Physics (SM) has remained the best description of elementary parti-
691 cles and their interactions since its formulation. However, there are several observations, particularly
692 measurements from cosmology, that show that the Standard Model description of the universe shown
693 in Fig. 1.1 is incomplete.

694 **2.1 Observations**

695 The modern evidence for invisible matter beyond the SM stems mainly from galactic rotation curves,
696 weak gravitational lensing, the cosmic microwave background (CMB), big bang nucleosynthesis
697 (BBN), and type 1a supernovae.

698 **2.1.1 Galactic Rotation Curves**

699 The first modern evidence for invisible matter comes from Vera Rubin’s measurements of galactic
700 rotation curves (i.e. the velocity at which stars orbit their galactic center) in the 1970s. Based
701 on kinematics and the gravitational inverse square law, in the absence of invisible matter, one
702 expects the speed at which stars orbit their galactic center to scale with the the distance from
703 the center r as $1/\sqrt{r}$. However, Vera Rubin’s measurements show that these velocities were flat
704 with increasing r even for stars far away from the galactic center [59]. This discrepancy between
705 theory and measurements can be explained by the presence of invisible matter that cannot be visibly
706 detected. This effect is shown in Fig. 2.1.

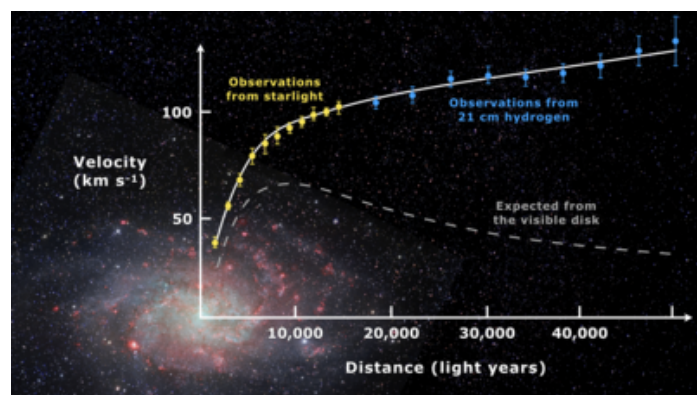


Figure 2.1: Galactic rotation curves show stars far from the galactic center are orbiting the galactic center far faster than they should gives evidence for invisible matter.

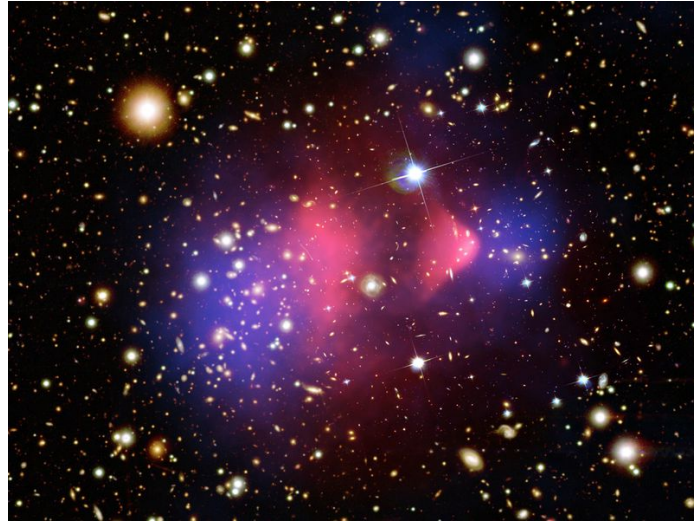


Figure 2.2: The Bullet Cluster shows visible matter from X-rays (highlighted in blue) and total matter from gravitational lensing (highlighted in pink).

707 2.1.2 Weak Gravitational Lensing

708 One could suppose that, since no independent tests of gravity are applied at the galactic scale,
709 gravity could simply be poorly understood at this scale. This is a possibility, in fact throughout the
710 history of astronomy, there is often the tension between a new theory of gravity and the presence of
711 some form of unseen matter as a resolution to an anomaly.

712 However, in addition to galactic rotation curves, measurements from gravitational lensing - the
713 bending of light in the presence of matter - provide evidence for invisible matter that cannot be
714 accounted for by the SM. The amount of bending of light from distant galaxies upon its trajectory
715 before it's measured on earth provides a measurement of the total mass in large regions of galactic
716 clusters. This can be compared with the distribution of X-rays from colliding galactic clusters, which
717 is a clear measurement of the distribution of visible matter in the galactic cluster. In a measurement
718 of two colliding galactic clusters known as the Bullet Cluster shown in Fig. 2.3, the distribution of
719 visible matter from X-ray measurements (reconstructed in pink) does not agree with the distribution
720 of the total amount of matter from weak gravitational lensing (reconstructed in blue) [33]. This is
721 clear indication that there is invisible matter located within the Bullet Cluster that is not described
722 by the SM and cannot be accounted for by a different theory of gravity.

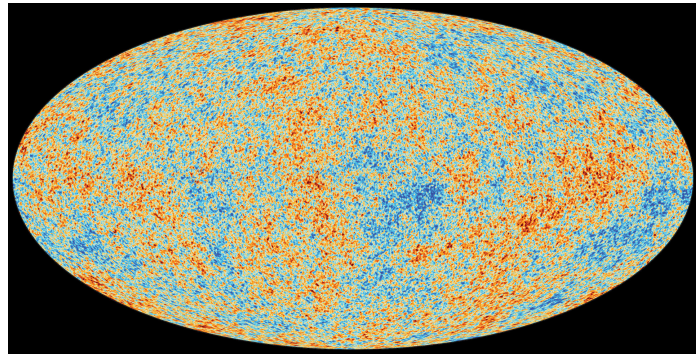


Figure 2.3: The Cosmic Microwave Background has temperature fluctuations consistent with extra invisible matter in the early universe.

2.1.3 Cosmic Microwave Background

An invisible matter hypothesis is favored with the anomalies of both galactic rotation curves and gravitational lensing. However, these evidences alone do not rule out the possibility of a SM explanation of this invisible matter, or being particulate in nature at all. For instance, black holes are a possible form of a non-particulate invisible matter that involves neither new particles beyond the SM or a particle nature of dark matter.

The cosmic microwave background (CMB), the thermal “afterglow” of the Hot Big Bang, shows evidence for invisible matter in the early universe that cannot be explained by the SM shown in the bottom of Fig. 2.3. Specifically, the correlations in the temperature fluctuations in the CMB spectrum, called CMB anisotropies, provide a measurement of sound waves in the early universe (called baryon acoustic oscillations, or simple BAO). This provides a quantitative measurement of both the amount of total matter and the amount of baryonic matter in the early universe. Of the total matter in the early universe, precision BAO measurements gives about $\sim 15\%$ baryonic matter (which is representative of the total SM matter in the early universe) and 85% of an additional type of matter. This matter discrepancy is in agreement with the anomalies described by the galactic rotation curves and gravitational lensing suggesting that the same invisible matter that is observed in the universe today is the same type of invisible matter that existed in the early universe.

This does not explicitly rule out the possibility of primordial black holes, that is those that existed and were formed in the early universe. (Is this true? I remember hearing this at a talk somewhere, I could use a source.). However, these are not favored because they require unnatural fine tuning to get the models to produce observed results are do not explain the next anomaly - the upper bound on baryonic matter set by Big Bang Nucleosynthesis.

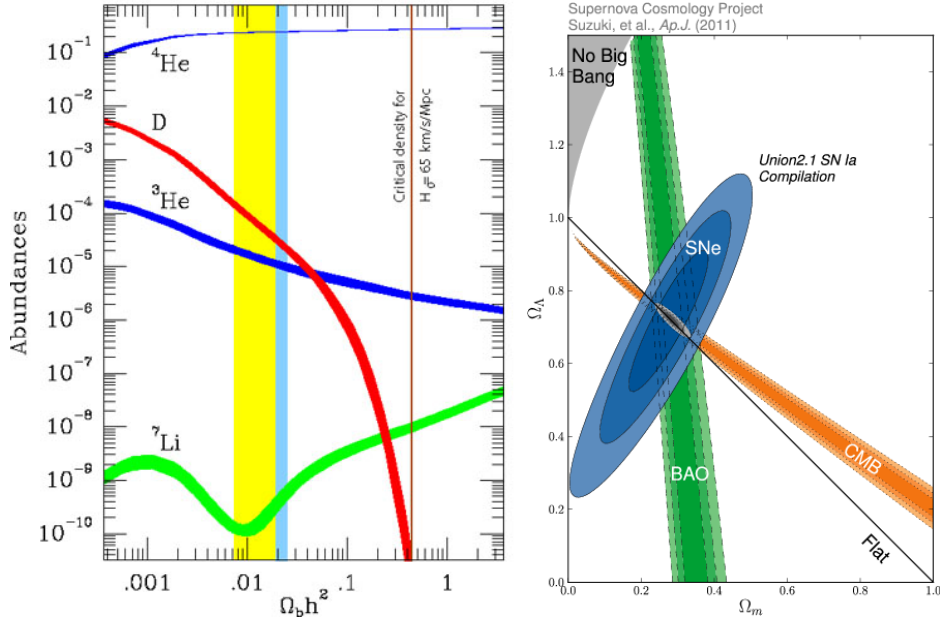


Figure 2.4: Left: Big Bang Nucleosynthesis puts an upper bound on the Standard Model matter density in the universe at about 15% of the total energy budget [60]. Right: Measurements from Type 1a supernovae (shaded in blue) together with the CMB and BAO measurements put the total mass in the universe at 30% of the total energy budget along with dark energy at 70% (from the intersection in gray) [14]. A combination of these measurements show that the Standard Model cannot account for most of the matter in the universe.

745 2.1.4 Big Bang Nucleosynthesis and Type 1a Supernovae

746 Measurements from Type 1a Supernovae, known as a “standard candle” because their well-defined
 747 and easily identifiable light curves, provide a measurement of the total matter in the universe. In
 748 the framework of the Λ CDM Model, a comparison of the redshift and luminosity of these supernovae
 749 gives a measurement of 30% matter of the total energy budget of the universe which is in agreement
 750 with CMB measurements [14].¹

751 On the other hand, Big Bang Nucleosynthesis (BBN), the description of production of hydrogen
 752 and helium nuclei in the early universe, provides an upper bound on baryonic matter at 15% of the
 753 total energy budget of the universe [60]. This is far below the total mass measurement from Type 1a
 754 Supernovae suggesting much of matter in the universe is non-baryonic, and hence beyond the SM.
 755 The measurements from Type 1a Supernovae and BBN are shown in Fig. 2.4

¹The Λ CDM Model (dark energy and cold dark matter) is the standard model of cosmology built on the framework of General Relativity. Dark energy is the energy responsible for the accelerated expansion of the universe as measured by the Type 1a Supernovae and CMB. The fundamental nature and origin of dark energy is also a mystery and will not be discussed further.

2.1.5 Some Properties of Dark Matter

From these measurements, one can provide general constraints to the properties of this missing matter. Any potential explanation of this missing matter must account for the following.

1. Since it has evading all detection mechanisms other than gravitational effects thus far, this missing matter is invisible and does not interact with SM photons. Hence, the common term for this matter is “dark matter.”
2. Measurements of the amount of dark matter from the early universe, particularly from the CMB, agree with present measurements. This indicates that dark matter is stable with a lifetime far greater than the 13.8 billion year age of the universe.
3. Measurements from different regions of the universe are consistent with the idea of missing matter. This, together with the Cosmological Principle, provides compelling evidence that dark matter is present everywhere in the universe, including here on Earth.
4. The density of dark matter in the universe is similar to the density of SM matter (i.e. they have the same order of magnitude). A natural explanation for this unlikely coincidence is that there is some interaction, even indirect, between dark matter and SM matter in the early universe that connects their origins. This is the basis for the concept of “thermal dark matter” in which dark matter and SM matter were in thermal equilibrium in first few nanoseconds of the universe.

These measurements, specifically the CMB and Type 1a Supernovae measurements, together with the Λ CDM Model also provide a quantitative breakdown of the energy budget of the universe. Matter itself only composes about 30% ($\Omega_m = 30\%$) of the energy budget. The remaining 70% is due to dark energy ($\Omega_\Lambda = 70\%$). Within the matter budget, dark matter comprises about 85% of the total mass ($\Omega_{DM} = 26\%$) while SM matter, which includes our everyday atoms and molecules, comprises only 15% of the total mass in the universe ($\Omega_{SM} = 4\%$). Furthermore, any model of dark matter must respect this observed value of Ω_{DM} called the “relic density” (any model that overproduces dark matter can be immediately ruled out).

Double check to make sure these numbers are the latest.

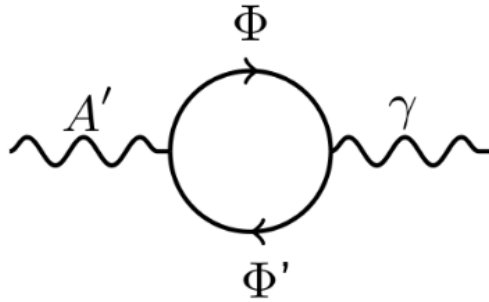


Figure 2.5: A one-loop kinetic mixing process where an A' mixes with the SM photon through an interaction of massive fields that couple to both photons.

783 2.2 Theory Summary

784 Heavy photons are connected to a variety of dark matter models as a method of indirect interactions
 785 with SM matter, and detailed motivations for dark matter with a heavy photon hypothesis will be
 786 described in detail in Sec. 2.3 and Sec. 2.4. But first, it is important to understand the basics of
 787 heavy photon formalism.

788 A theory that has gained interest over the past few years is that of an additional Abelian gauge
 789 symmetry $U'(1)$. This was first proposed by Holdom in 1985 and is the basic assumption behind the
 790 existence of a heavy photon where the additional broken symmetry interacts with the SM hyper-
 791 charge via kinetic mixing [47]. Suppose nature does contain this additional Abelian gauge symmetry
 792 $U'(1)$ which contains a massive gauge boson A' . This would produce the following Lagrangian:

$$\mathcal{L} = \mathcal{L}_{SM} + \frac{1}{4} F'^{\mu\nu} F'_{\mu\nu} + m_{A'}^2 A'^{\mu} A'_{\mu} + \epsilon F^{\mu\nu} F'_{\mu\nu} \quad (2.1)$$

793 where \mathcal{L}_{SM} is the Standard Model Lagrangian, $F_{\mu\nu}$ is the electromagnetic field strength, $F'_{\mu\nu} =$
 794 $\partial_{\mu} A'_{\nu} - \partial_{\nu} A'_{\mu}$ is the heavy photon field strength tensor (SM hypercharge), and ϵ is a dimensionless
 795 coupling constant also called the kinetic mixing parameter. This additional symmetry gives rise
 796 to a kinetic mixing term $\epsilon F^{\mu\nu} F'_{\mu\nu}$ with ϵ as the kinetic mixing parameter where the Standard
 797 Model photon mixes with the a new gauge boson, an A' , through an interactions of massive fields
 798 M_{Φ} and $M_{\Phi'}$ as shown in Fig 2.5. These intermediate particles could be massive far above the
 799 Supersymmetry-breaking scale, but the kinetic mixing will persist down to much lower mass scales.
 800 Due to kinetic mixing, the fields are non-orthogonal, but orthogonality can be restored by redefining
 801 the electromagnetic field as $A^{\mu} \rightarrow A^{\mu} + \epsilon A'^{\mu}$. By removing all the resulting ϵ^2 terms, this diagonalizes
 802 the gauge terms in the Lagrangian in Eq. 2.1 as

$$\mathcal{L}_{gauge} = -\frac{1}{4} F'^{\mu\nu} F'_{\mu\nu} - \frac{1}{4} F^{\mu\nu} F_{\mu\nu} \quad (2.2)$$

803 The redefinition of the gauge field also changes the interaction term of the Lagrangian $\mathcal{L}_{int} =$
 804 $A^\mu J_\mu^{EM}$ to

$$A^\mu J_\mu^{EM} \rightarrow (A^\mu + \epsilon A'^\mu) J_\mu^{EM} \quad (2.3)$$

805 This induces an effective coupling between the heavy photon field and the electromagnetic current
 806 that is proportional to a factor ϵ . Since basic observations require $\epsilon \ll 1$, ϵ suppresses the effective
 807 charge. One loop processes such as the one shown in Fig. 2.5 can be naturally generated by heavy
 808 multiplets that are charged under both the SM electric charge and a dark charge (the charge resulting
 809 from the new symmetry) [18] [26]. This process motivates ϵ to be in the range $\sim 10^{-2} - 10^{-4}$ and
 810 can be related to several parameters by the following:

$$\epsilon \sim \frac{eg_D}{16\pi^2} \log\left(\frac{M_\Phi}{M_{\Phi'}}\right) \sim 10^{-2} - 10^{-4} \quad (2.4)$$

811 where e is the electric charge and g_D is the hypercharge dark coupling. If the theory does not
 812 contain these additional particles that are charged under both $U(1)$ symmetries, the additional loop
 813 processes are possible and motivated by Grand Unification Theories (GUT) generally in the range
 814 $\epsilon \sim 10^{-3} - 10^{-6}$ [18]. Finally, some versions of string theory motivate ϵ as low as 10^{-12} from Eq. 2.11
 815 [44] [43] [32].

816 There is a wide range of theoretically favorable mass for heavy photons. Models of light dark
 817 matter, where the dark matter mass is below the Lee-Wienberg bound as described in Sec. 2.4, as
 818 well as certain models of supersymmetry motivate mass scales of MeV-GeV. String theories connect
 819 ϵ to the mass scale resulting in a motivated mass region down to the meV scale.

820 The existence of a new gauge boson arising from an additional massive $U'(1)$ symmetry that
 821 can couple to charged SM particles leads to interesting possibilities. This idea has gained particular
 822 interest as a potential way for an indirect coupling between SM fermions and a dark sector, that could
 823 lead to a way to probe the possible structure of this dark sector. These heavy photon masses and
 824 coupling ranges can be probed by both current and future experimental programs (including HPS)
 825 and will provide insight on a variety of outstanding mysteries in particle physics and astrophysics
 826 which are described in the following sections.

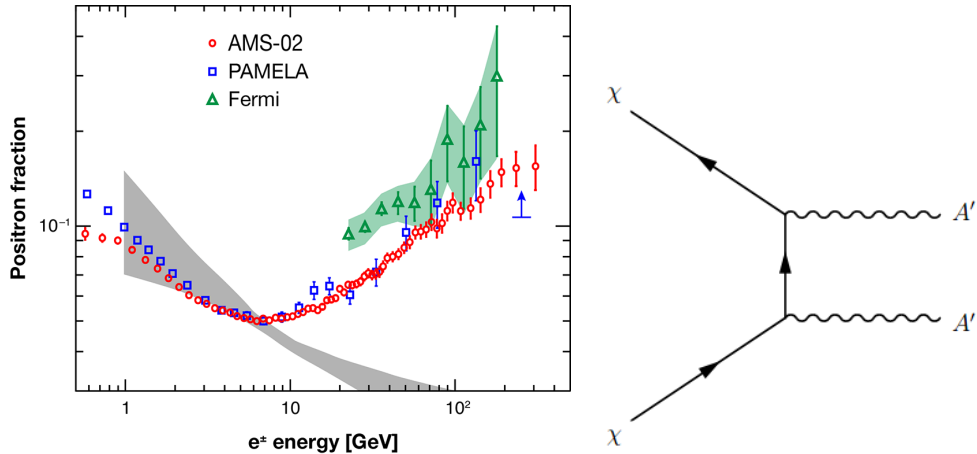


Figure 2.6: Left: The results from PAMELA, AMS, and Fermi-LAT showing the positron fraction excess (above the expected calculation from cosmic rays in grey) at above ~ 10 GeV [35]. Right: The Feynman diagram for the dark matter annihilation into two A' 's which subsequently decay into e^+e^- pairs. This provides an explanation for positron fraction excess. This explanation has since been disfavored.

2.3 Historical Motivations for A' 's

There are two specific historical anomalies that generated much interest in the heavy photon hypothesis among the communities of particle physicists and astrophysicists. In 2008, the Payload for Antimatter Matter Exploration and Light-nuclei Astrophysics (PAMELA) measured an anomalous excess of positron fraction ($\phi(e^+)/(\phi(e^+) + \phi(e^-))$) above ~ 10 GeV at the center of the Milky Way Galaxy that was inconsistent with the expectation from secondary production from cosmic-ray nuclei interactions with interstellar gas [6] [3]. Further measurements from the Fermi Large Area Telescope and the Alpha Magnetic Spectrometer (AMS) not only confirmed this anomaly, but extended it to even higher energies of ~ 200 GeV [9]. These measurements are shown in Fig. 2.6.

Since the implied annihilation cross-section is larger than one would expect from a thermal relic ($\langle\sigma v\rangle \sim 3 \times 10^{-26} \text{ cm}^3 \text{s}^{-1}$), this was interpreted by some as dark matter annihilation through a heavy photon mediator as shown in Fig. 2.6 [17]. Heavy photons are particularly appealing since if dark matter annihilations are mediated by heavy photons, a so-called ‘Sommerfeld enhancement’ can occur in which the cross-section is dependent on the inverse of velocity ($\langle\sigma v\rangle \sim 1/v$). Thus low-velocity interactions (e.g. dark matter collisions in the galactic halo) are enhanced while still preserving the dark matter freeze-out scenario (described in Sec. 2.4) with the observed dark matter relic abundance. In addition, this annihilation cross-section is much larger than observed for hadrons, which motivates heavy photons with $m_{A'} < 2m_p$ where decays to proton-antiproton pairs are kinematically forbidden. Thus, the MeV-GeV heavy photon mass range is highly motivated by both the Sommerfeld enhancement and observations of annihilation into hadrons.

847 This anomaly is now disfavored for several reasons. A larger AMS dataset shows softer positron
848 spectrum that is more consistent with a pulsar origin for cosmic ray positron excess than a heavy
849 photon interpretation; however, this does not exclude the possibility of heavy photons decaying into
850 intermediate states before an e^+e^- final state [31]. In addition, measurements by the Planck satellite
851 put strong constraints on the dark matter annihilation rate at recombination, thus making the heavy
852 photon explanation of the PAMELA anomaly unlikely [18] [5].

853 In addition to the positron cosmic ray excess, heavy photons were originally motivated by the
854 measurement of the magnetic momentum of muons ($a_\mu = (g - 2)/2$, or simply known as $g - 2$)
855 which deviates by more than 3 standard deviations away from the predicted value from the SM.
856 This can be explained by a contribution of the heavy photon to the muon magnetic moment for a
857 heavy photon within a certain range of parameter space shown in green in Fig. 6.14. In addition,
858 the excellent agreement between the corresponding magnetic moment of the electron and the SM
859 excludes the region in red. This favored region for a heavy photon explanation of the anomalous
860 magnetic moment of the muon has since been ruled out by several experiments both for visible and
861 invisible decays.

862 A heavy photon hypothesis for these two anomalies have since been ruled out. Even though
863 some of the original motivations for dark sector searches such as the anomalous positron excess from
864 PAMELA and the muon G-2 anomaly are no longer favored, motivations for searching for such a
865 particle remain particularly in models involving light dark matter.

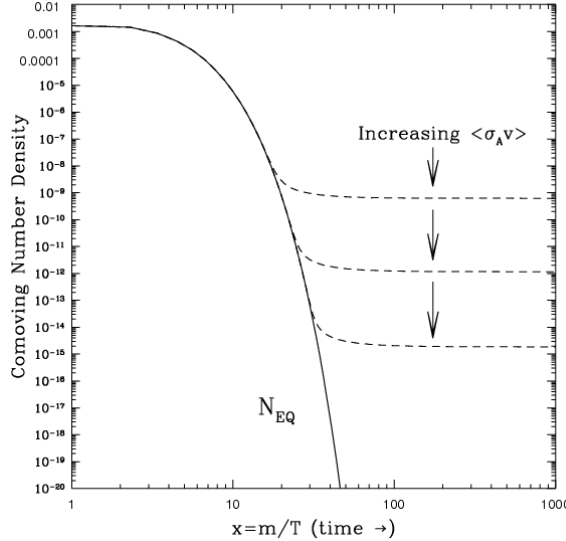


Figure 2.7: The mechanism of thermal freeze-out in which dark matter and SM matter are in thermal equilibrium in the early universe. As the universe cools (x -axis), the relic abundance of dark matter (y -axis) is depleted by self-annihilation until enough cooling occurs and the dark matter relic abundance is set.

866 2.4 Light Dark Matter

867 There are many references missing in this subsection.

868 Heavy photons are connected to a variety of models of light dark matter, that is dark matter
 869 on the MeV-GeV scale (or sub-GeV scale) where stable massive SM particles are known to exist, as
 870 well as self-interacting dark matter. In order to understand the potential connection between light
 871 dark matter and heavy photons, one must first understand the mechanisms of thermal dark matter
 872 and its connection to the amount of dark matter relic abundance. This connection is referred to
 873 as “thermal freeze-out” (which was alluded to in Chp. 1) and the simplest mechanism of thermal
 874 freeze-out as shown in Fig. 2.7 goes as follows.

- 875 1. The whole universe began in a hot dense state with some amount of SM matter (Ω_{SM}) and
 876 some relic density of dark matter (Ω_{DM}) colliding in thermal equilibrium.
- 877 2. Through an unspecified mechanism, dark matter particles annihilate with one another into
 878 SM particles and through the same mechanism SM also annihilate into dark matter particles.
 879 This occurs in thermal equilibrium. For simplicity, dark matter self-interactions are assumed
 880 to have no effect on this mechanism.
- 881 3. Throughout this mechanism, the universe expands and cools which decreases the rate of dark
 882 matter-SM interactions. Eventually, the universe cools enough to stop the SM annihilation

883 into dark matter particles; however, the dark matter annihilation into SM particles persists.
 884 Thus, over this short time the amount of dark matter is continually depleted.

885 4. As the universe continues to cool, eventually these dark matter annihilations stop as dark
 886 matter completely decouples from the SM. At this point, the amount of dark matter called the
 887 “relic abundance” is set at a fixed value. Measurements from a variety of astrophysical sources
 888 described in Sec. 2.1 put the relative relic abundance $\Omega_{DM} = 85\%$ of the total matter in the
 889 universe. In addition, there is an inverse relationship between the annihilation cross-section
 890 and the relic abundance ($\langle\sigma v\rangle \propto \frac{1}{\Omega_{DM}}$) such that the larger the dark matter annihilation
 891 cross-section the longer it will be in thermal equilibrium and the more it will be depleted.

892 From the observed relic abundance, using the inverse relationship the expected annihilation cross-
 893 section can be computed as $\langle\sigma v\rangle \sim 3 \times 10^{-26} \text{ cm}^3 \text{s}^{-1}$. In addition, the annihilation cross-section can
 894 be related to the dark matter particle mass and the mass of mediator (such as the Z boson in this
 895 case) as follows:

$$\langle\sigma v\rangle \propto \frac{m_{DM}^2}{m_Z^4} \quad (2.5)$$

896 One can solve for the dark matter particle mass and see that such a mechanism gives a mass
 897 in the 100 GeV range. This mass scale and cross-section is typical and of what one would expect
 898 from weak sector particles such as W bosons, Z bosons, or Higgs bosons providing a hint that
 899 a dark matter particle could be a particle that interacts weakly with SM particles. These dark
 900 matter candidates are named “Weakly Interacting Massive Particles” (WIMPs), and this mass and
 901 cross-section computation is such a remarkable coincidence that this is famously referred to as the
 902 “WIMP Miracle.” However, a major difference between WIMPs and weak-scale SM particles is that
 903 WIMPs must be stable in order to be a dark matter candidate whereas weak-scale SM particles are
 904 unstable. In addition, in order to resolve the hierarchy problem, models of Supersymmetry (SUSY)
 905 were developed and many models described WIMP-like objects.

906 Because of this, over the past few decades much of the focus of the particle physics and astro-
 907 physics communities has been on both direct detection experiments and colliders such as the Large
 908 Hadron Collider (LHC) searching for WIMP-like dark matter and SUSY on the ~ 100 GeV-scale.
 909 However, to date of publication, neither WIMPs nor SUSY have been discovered and accessible pa-
 910 rameter space for these models is shrinking. Specifically, direct detection experiments are approach-
 911 ing the so-called neutrino floor where the direct detection of neutrino with the detector medium
 912 become indistinguishable from dark matter recoils, thus searches of this type will no longer be pos-
 913 sible, while the LHC will probe the most favorable models of SUSY within the next few years [How
914 do I make this claim more precise?](#).

915 As a way to compliment the SUSY-WIMP dark matter searches, it is reasonable to search for
 916 dark matter at the mass scale where known stable SM particles, such as electrons and protons,

exist. If one naively computes the relic abundance of potential dark matter particles on the MeV - GeV scale with an electroweak mediator using Eq. 2.5, the calculation results in an annihilation cross-section far smaller than is expected from the simplest mechanisms of thermal equilibrium. And because the annihilation cross-section is proportional to the inverse of the relic abundance, this mass scale crosses the threshold of the so-called Lee-Weinberg bound at ~ 2 GeV such that dark matter candidates below this bound will result in an overproduction of dark matter.² Of course, this computation assumes only interactions mediated through SM bosons such as W bosons, Z bosons, and Higgs bosons.

As a way to circumvent the Lee-Weinberg bound, one could postulate an annihilation mechanism through a new, comparably light mediator. This would provide another degree of freedom in Eq. 2.5 and allow for this simple mechanism to produce the observed dark matter relic abundance. Thus, any thermal dark matter model on the MeV-GeV scale, called “light dark matter”, requires an additional boson beyond the SM. A heavy photon is a simple and natural candidate that could mediate dark matter annihilations in the early universe much like PAMELA’s observed positron cosmic ray excess was explained (though collisions in the galactic halo occur at an enhanced rate because of the Sommerfeld enhancement). Beyond this simple mechanism, heavy photons are connected with more complicated models of dark matter that allow for more complex structure and interactions within the so-called “dark sector” - the sector of all particles responsible for the 85% of dark matter. Due to the kinetic mixing between the heavy photon and the SM photon, heavy photons would provide an indirect mechanism to probe the particles and interactions in this dark sector. This mechanism is also called a “vector portal.”

In addition to mechanisms of thermal dark matter and a vector portal, heavy photons are often motivated by a variety of self-interacting dark matter where dark sector particles are allowed to interact with other dark sector particles.³ Excesses in both gamma ray and X-ray spectra can provide hints of dark matter self-interactions potentially mediated by heavy photons. The Fermi-LAT telescope has observed an extended emission in the gamma ray spectrum originating from the galactic center. There are several models that explain this including pulsars, energetic protons accelerated by a super-massive black hole, and dark matter annihilations into SM particles. The dark matter annihilation can be explained through a heavy photon model, much like what was explained for the original observed positron fraction anomaly by PAMELA. An excess in the X-ray spectra at 3.5 keV from several galaxy clusters has been explained in a model called “eXciting Dark Matter” (XDM). In this model, self-interacting dark matter can collide via a heavy photon and excite dark matter ($\chi^* \chi^*$) and its subsequent de-excitation emits an observable 3.5 keV X-ray ($\chi^* \rightarrow \chi\gamma$).

Along the same lines of self-interacting dark matter, collisionless dark matter has historically

²When computing any mechanism of thermal origins of dark matter, and overproduction above the observed relic abundance is never allowed. However, an underproduction of dark matter is allowed since another mechanism can compensate the remaining dark matter relic abundance.

³These dark matter self-interaction can be mediated by heavy photons or by other additional mediators in the dark sector. In contrast, the minimal WIMP model does not allow for additional self-interactions.

951 failed to account for detailed simulations of dark matter of galactic halos. Often these problems
952 can be resolved by self-interacting dark matter with a velocity-dependent cross-section which is
953 consistent with a heavy photon hypothesis which would otherwise be constrained by high-velocity
954 collisions such as the Bullet Cluster shown in Fig. 2.3 [54].

955 For instance, there are observations in which Milky Way dwarf satellite galaxies have smaller
956 rotational velocities than predicted by these simulations for dark matter subhalos. This is called
957 the “too big to fail” problem and it suggests that the rotational velocities are actually smaller
958 than predicted, these massive subhalos fail to create these dwarf galaxies, or these massive subhalos
959 simply do not exist. Self-interacting dark matter provides a solution via the first possibility as it can
960 naturally reduce the central densities of subhalos (and hence reducing their rotational velocities). In
961 addition, collisionless dark matter fails to resolve the so-called “cusp-core problem” in
962 which the observed matter density profiles of galaxies are better modeled with a constant density core
963 from self-interacting dark matter than models from collisionless dark matter. There are, however,
964 other explanations of these phenomena that do not involve self-interacting dark matter such as
965 baryonic outflows in galaxies that may also produce similar cored distributions by transferring energy
966 to dark matter. As these simulations develop and improve over time, these conflicts of collisionless
967 dark matter may be resolved. **Is this still true?**

968 Should I include the anomalies observed from Be8 [53] [40] and Experiment to Detect the Global
969 EoR Signature (EDGES)

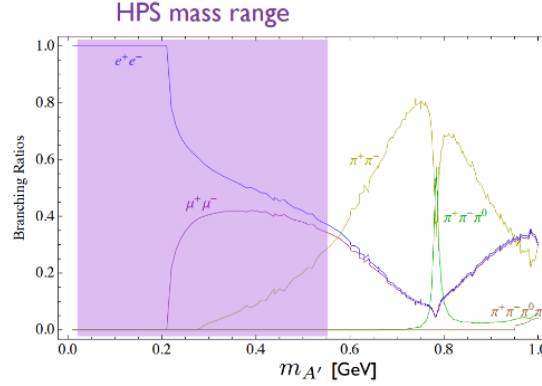


Figure 2.8: The branching ratio for heavy photon decays to SM particles as a function of mass. This assumes no decays into dark sector particles.

970 2.5 Signatures of A's

971 According to the minimal heavy photon model, kinetic mixing is the only coupling to the SM. One
 972 can also assume decays to dark sector particles are forbidden (i.e. $2m_d > m_{A'}$), thus the focus
 973 will be on visible decays (i.e. SM particles).⁴ Under this assumption, the branching ratio of heavy
 974 photon decays to visibles as a function of mass in the MeV-GeV range is shown in Fig. 2.8 which
 975 are derived by the ratio of cross sections as a function of center-of-mass energy for different final
 976 states of e^+e^- interactions.

977 The heavy photon decay width is given by:

$$\Gamma = \frac{N_{eff} m_{A'} \alpha \epsilon^2}{3} \quad (2.6)$$

978 where $N_{eff} = 2 + R(m_{A'})$ and the function $R(Q)$ is given by

$$R(Q) = \frac{\sigma(e^+e^- \rightarrow \text{hadrons}, Q)}{\sigma(e^+e^- \rightarrow \mu^+\mu^-, Q)} \quad (2.7)$$

979 For $m_{A'} < 2m_\mu$, $N_{eff} = 1$ since the only kinematically allowed SM decay is to e^+e^- pairs.⁵
 980 Since the fractional decay width $\Gamma/m_{A'}$ is proportional to $\alpha \epsilon^2$, the small ϵ^2 will result in a very
 981 narrow decay width, and the heavy photon will appear as a sharp resonance.

982 The corresponding product of livetime and the speed of light (the $c\tau$ value) is related to the
 983 inverse of the decay width in Eq. 2.6 by:

⁴If one relaxes this assumption, the possible decay scenarios become more complicated. Decays to invisible particles become possible and searches for missing mass or missing momentum must be performed.

⁵This is true for most of the parameter space covered by HPS, though the mass range at higher beam energies for HPS does cross the dimuon threshold.

$$c\tau = \frac{\hbar c}{\Gamma} = \frac{3\hbar c}{N_{eff} m_{A'} \alpha \epsilon^2} \quad (2.8)$$

984 The decay length in the laboratory frame is related to $c\tau$ value by a factor of relativistic γ but
 985 is not universal as it will depend on the type of experiment (e.g. fixed target experiment vs. a
 986 collider experiment). But, for sufficiently small ϵ , the decay length becomes measureable by both
 987 experiments with excellent vertex resolution and beam dump experiments.

988 Finally, the rate of heavy photon production is directly proportional to the corresponding process
 989 for virtual photons at a given heavy photon mass. Thus, there exist an irreducible background with
 990 identical kinematics for a given heavy photon production. The only directly distinguishable feature
 991 is the fact that the heavy photon is on-shell and can have a finite, and hence measureable, livetime.
 992 The ratio of the A' differential cross-section for a given $m_{A'}$ and ϵ to the cross-section of the
 993 corresponding virtual photon process integrated over the narrow mass range $m_{A'} \pm \frac{\delta m}{2}$ is given by:

$$\frac{d\sigma(X \rightarrow A'Y \rightarrow ZY)}{d\sigma(X \rightarrow \gamma^*Y \rightarrow ZY)} = \left(\frac{3\pi\epsilon^2}{2N_{eff}\alpha} \right) \left(\frac{m_{A'}}{\delta m} \right) \quad (2.9)$$

994 The specific virtual photon process related to HPS is discussed in more detail Sec. 2.8. If an
 995 experiment can directly measure the rate of the corresponding virtual photon process, the expected
 996 rate of heavy photon production can be normalized in a data-driven way.

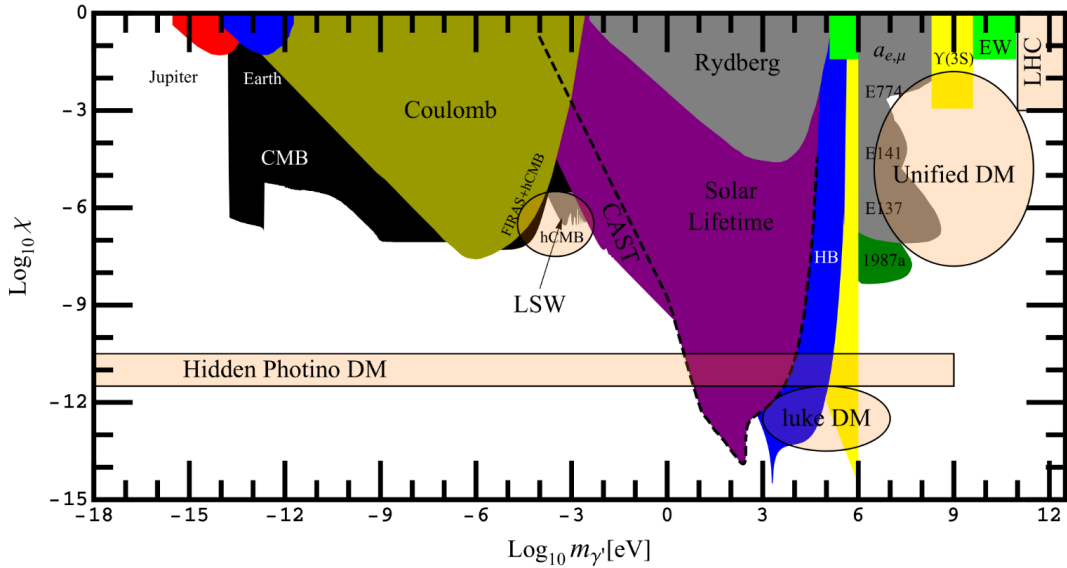


Figure 2.9: Existing constraints of heavy photons on the whole parameter space [48]. The constraints come from a variety of sources including astrophysical measurements, precision QED, and particle accelerator-based experiments. The regional labeled “unified DM” is of particular interest to dark matter for reasons described in Sec. 2.4 and Sec. 2.3 and will be the focus. Note that the notation on this plot is such that $\epsilon \rightarrow \chi$ and A' is denoted as γ' .

2.6 Overview of Searches

997 This subsection still needs a bit of work. Omar and Sho’s thesis were useful, but out of date.

999 The parameter space for heavy photons is large, and current heavy photon constraints from various
1000 astrophysics measurement, precision QED, and accelerator-based experiments are summarized
1001 in Fig. 2.9 [48]. There is a much narrower region of partially unexplored parameter-spaced that is
1002 theoretically favorable with sub-GeV dark matter models. This parameter space is typically probed
1003 by accelerator-based experiments in which a beam of high energy particles (e.g. electron, protons,
1004 etc.) are collided with material or another beam in order to produce heavy photons.

1005 The common production methods are through dark bremsstrahlung ($e^-Z \rightarrow e^-ZA'$), Drell-
1006 Yan ($q\bar{q} \rightarrow \gamma A'$), e^+e^- annihilation ($e^+e^- \rightarrow \gamma A'$), and meson decays (such as $\pi^0 \rightarrow \gamma A' \eta \rightarrow \gamma A' \phi \rightarrow \eta A'$). Once heavy photons are produced, experiments are designed and built to indirectly detect
1008 heavy photons often by measuring their decay products. Common detection signatures include a
1009 mass resonance of the SM decay products, missing mass or momentum (heavy photons decay to
1010 dark sector particles and cannot be detected directly), and displaced vertices from long-lived heavy
1011 photons.

1012 Different types of experiments and facilities are designed to utilize these production and detection
1013 methods. These include complimentary searches from colliders, thin fixed targets, and beam dumps

1014 from facilities that utilize protons beams, ion beams, electron beams, and positron beams. In general,
 1015 fixed targets and beam dump experiments are higher luminosity and able to probe smaller ϵ while
 1016 colliders with a high center-of-mass energy can probe larger masses.

1017 2.6.1 Colliders

1018 Searches for heavy photons at colliders mostly come from flavor factories that produce heavy photons
 1019 through meson decays, but also through e^+e^- annihilation, Drell-Yan, and even displaced vertices.

1020 Among the experiments that utilize high-luminosity e^+e^- colliders to search for heavy photons
 1021 are BaBar, KLOE and KLOE-II, and Belle-II. Each of these experiments were run at different
 1022 center-of-mass energies and thus searched at complimentary masses. BaBar was run at the PEP-II
 1023 B-Factory at SLAC and heavy photon searches were performed using upsilon decays ($\Upsilon \rightarrow \gamma A'$) and
 1024 then heavy photon decays into $\mu^+\mu^-$ final states [19]. KLOE was run at the DAΦNE ϕ factory and
 1025 search for *phi* meson decays ($\phi \rightarrow \eta A'$) and then heavy photon decays into e^+e^- and $\mu^+\mu^-$ final
 1026 states as well as dipion decays [20] [16]. **Belle-II I need to look up because I think this was recent.**
 1027 **Maybe KLOE-II as well.**

1028 Proton colliders such as the Large Hadron Collider (LHC) at CERN which houses experiments
 1029 such as ATLAS, CMS, and LHCb can search for meson decays and forms of “dark showering”. Since
 1030 these experiments are run at a higher center-of-mass energy than any other current experiment, these
 1031 experiments can probe the largest A' mass space.

1032 Specifically, for heavy photon masses below the dimuon threshold LHCb can search for heavy
 1033 photons in the $D^* \rightarrow D^0 A'$ channel decays into e^+e^- final states. For heavy photon masses above
 1034 the dimuon threshold, LHCb can search for heavy photon decays into a $\mu^+\mu^-$ final state. In addition,
 1035 LHCb can perform a displaced vertex search for η decays in a heavy photon and ($\eta \rightarrow \gamma A'$) then for
 1036 a long-lived heavy photon that decays into a $\mu^+\mu^-$ final state. Future upgrades to LHCb, specifically
 1037 a trigger-less readout that allows for online reconstruction, will enable a search for displaced vertices
 1038 with an e^+e^- final state with projected sensitivity competitive with the HPS displaced vertex search.

1039 Lower energy proton colliders such as WASA at COSY searched for neutral pion decays into
 1040 heavy photons ($\pi_0 \rightarrow \gamma A'$) and heavy photon decays into e^+e^- final states. PHENIX at the
 1041 Relativistic Heavy Ion Collider (RHIC) at Brookhaven uses both proton-proton and deuterium-
 1042 gold nuclei ($d+Au$) collisions to produce neutral mesons that decay into heavy photons ($\pi_0 \rightarrow \gamma A'$
 1043 and $\eta \rightarrow \gamma A'$) which then decay into e^+e^- final states [4].

1044 2.6.2 Beam Dumps

1045 As previously stated, heavy photons with sufficiently small couplings will be long-lived. This prop-
 1046 erty can be exploited by beam dump experiments where a high intensity electron or proton beam
 1047 is “dumped” onto a target of thickness comparable to the decay length of the heavy photon, and a
 1048 search for heavy photon decays to visible particles can be performed. If the beam dump is sufficiently

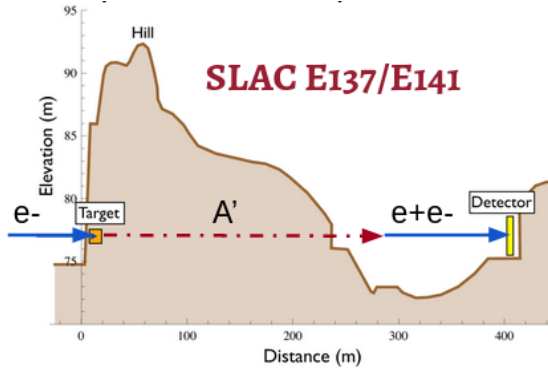


Figure 2.10: A schematic of beam dump experiments SLAC E-137 and E-141 which searched for long-lived particles that decay in a region several hundred meters from the target.

1049 thick enough, this will filter all SM background and any decay within a specific volume would be
 1050 clear evidence for a new long-lived particle. Otherwise, the decay products must be reconstructed
 1051 to measure their decay position to distinguish SM processes from potential new processes.

1052 Several general-purpose electron beam dump experiments that were originally designed and run
 1053 to search for axion-like and Higgs-like particles such as E137 and E141 at SLAC, E774 at Fermilab,
 1054 KEK in Japan, and an experiment at Orsay reinterpreted previously taken data to show constraints
 1055 for heavy photons. NA64 is a future electron beam dump at CERN. These experiments produce
 1056 heavy photons by dark bremmstrahlung, a process related to ordinary photon bremmstrahlung.

1057 Similar constraints can be set from a proton beam dump experiment where heavy photons are
 1058 produced by either the decay of neutral mesons produced at the target or proton bremsstrahlung
 1059 such as the U70 accelerator. Future proton beam dump experiments include a SHiP at CERN [11]
 1060 which is a general-purpose dark sector experiment, or SeaQuest at Fermilab (soon to be SpinQuest
 1061 or DarkQuest) which is typically used for nuclear physics experiments [42].

1062 Other beam dump experiments include BDX [23], MiniBooNE [10], COHERENT at ORNL
 1063 Proton beam dump [36], SBN at Fermilab Proton beam dump [2]

1064 2.6.3 Thin Fixed Target

1065 Fixed target experiments are much like beam dump experiments; however unlike beam dump ex-
 1066 periments, fixed target experiments are designed with a much thinner target which allows for most
 1067 SM particles to interact with the detector that would otherwise be filtered by a beam dump. As a
 1068 result, fixed target experiments must have the ability to reconstruct these SM particles which has
 1069 the advantage of enabling both prompt and long-lived searches for heavy photons.

1070 Fixed target experiments utilize an electron beam to produce A' using the same dark bremm-
 1071 strahlung mechanism as beam dump experiments. A Prime EXperiment (APEX) is a fixed target

1072 experiment at Jefferson Laboratory that uses an electron beam to detect the e^+e^- decay products
 1073 from an electro-produced heavy photon [38] [1]. It uses a septum magnet to separate e^+e^- pairs
 1074 into two calorimeters (HRS spectrometer in Hall A) whose measurements are used to compute the
 1075 invariant mass. In addition the A1 spectrometer at the Mainz Microtron **does something interesting**
 1076 [56]. Several additional electron beam fixed target experiments are planned including DarkLight
 1077 using the Low-Energy Recirculator Facility at JLab and MAGIX at the Mainz Energy-Recovering
 1078 Superconducting Accelerator.

1079 Future experiments such as the Light Dark Matter eXperiment (LDMX) at SLAC search for
 1080 heavy photons through a production of dark bremmstrahlung and a subsequent decay into invisibles
 1081 [66]. The search is for a missing momentum signature by precision measurements of the recoil
 1082 electron momentum. Rare photo-nuclear processes that can mimic a missing momentum signature
 1083 are vetoed by a large hadronic calorimeter. The design of the LDMX apparatus is shown in Fig.
 1084 2.11.

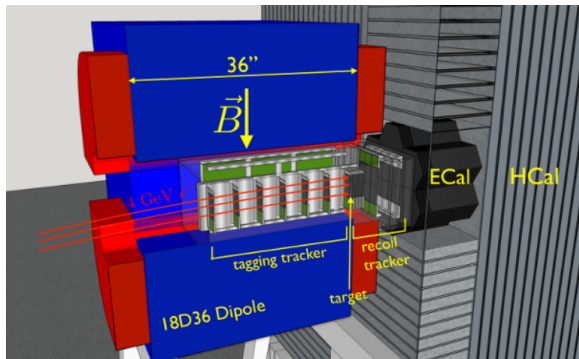


Figure 2.11: The Light Dark Matter eXperiment (LDMX) searches for heavy photon decays to invisibles by measuring the recoil electron momentum and searching for missing momentum. The apparatus includes a tagging tracker, recoil tracker, an Ecal, and an Hcal.

1085 In addition to electron beams, positron beams are also used in fixed target experiments to
 1086 search for heavy photons through e^+e^- annihilation. These searches utilize monophoton final states
 1087 ($\gamma A' \rightarrow \gamma \chi\chi^*$) such that a missing mass search can be performed. Proposed experiments of this
 1088 type include PADME at INFN Frascati and VEPP-3 at the Budker Institute at Novosibirsk [62].
 1089 The proposed Missing Mass A-Prime Search (MMAPS) at Cornell is a similar style missing mass
 1090 search with a $e^+e^-\gamma A'$ [12].

1091 Proton fixed target experiments such as NA48/2 at the Super Proton Synchrotron (SPS) at
 1092 CERN search for meson decays into heavy photons (specifically $K^\pm \rightarrow \pi^\pm\pi^0; \pi^0 \rightarrow A'$), that then
 1093 decay to e^+e^- pairs by utilizing a beryllium target to produce a Kaon beam (K^\pm) [22]. In addition,
 1094 the HADES measures potential heavy photons from meson decays (specifically $\pi_0 \rightarrow \gamma A', \eta \rightarrow \gamma A',$
 1095 $\Delta \rightarrow N A'$) and e^+e^- final states by using a variety of both hydrogen and niobium (Nb) targets

1096 [7].

1097 Finally, the Heavy Photon Search (HPS) utilizes an electron beam to produce A' 's through dark
1098 bremsstrahlung and searches for e^+e^- daughter particles from A' decays. HPS is unique in that it
1099 reconstructs both the mass and vertex positions with excellent precision which enables searches for
1100 both prompt decays and secondary vertices from heavy photons with a short decay length in the
1101 range of 1-10 cm in the laboratory frame.

1102 Also, TREK at J-PARC [15] (using a stopped kaon beam)

1103 Did I miss any other experiments that should be mentioned?

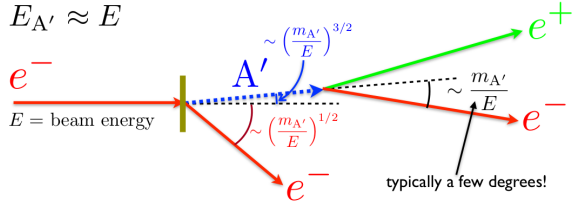


Figure 2.12: The kinematics for heavy photon (A') produced from an electron on a fixed target. In general, A' 's retain most of the incident beam energy, remain close to the beam axis due to a small recoil angle, and have a small opening angle.

1104 2.7 Heavy Photon Fixed Target Kinematics

1105 High luminosity fixed target experiments, that is experiments with a high intensity beam incident
1106 on a thin metal foil, can probe theoretically favored regions of the heavy photon parameter
1107 space. Production mechanisms are analogous to that of regular photon bremsstrahlung, called “dark
1108 bremsstrahlung”, albeit, with suppressed rates due to the weak effective coupling of the A' to elec-
1109 tric charge and significantly different kinematics because of the relatively large mass of the A' . The
1110 kinematics of heavy photons can be calculated from the Weizacker-Williams Approximation (WWA)
1111 where the nucleus is replaced by an effective photon flux. This gives the production differential cross
1112 section for an electron with energy E_0 incident on a fixed target as

$$\frac{d\sigma}{dx d \cos\theta_{A'}} \approx \frac{8Z^2\alpha^3\epsilon^2 E_0^2}{U^2} \frac{\chi}{Z^2} \left(1 - x + \frac{x^2}{2} - \frac{x(1-x)m_{A'}^2(E_0^2 x \theta_{A'}^2)}{U^2} \right) \quad (2.10)$$

1113 where E_0 is the beam energy, $x = E_{A'}/E_0$, $E_{A'}$ is the energy of the A' , and $\theta_{A'}$ is the angle
1114 from the beam in the lab frame. The value χ/Z^2 is related to the electric form factor and is in the
1115 range $\sim 5 - 10$ for the HPS range of interest. The function $U(x, \theta_{A'}) = E_0^2 x \theta_{A'}^2 + m_{A'}^2 \frac{1-x}{x} + m_e^2 x$ is
1116 related to the virtuality of the intermediate electron. The characteristic angle of emission is set by
1117 $U(x, \theta_{A'}) - U(x, 0) \sim U(x, 0)$ which occurs at $\theta_{A'} \sim \frac{m_{A'} \sqrt{1-x}}{xE_0}$.

1118 Integrating over angle $\theta_{A'}$ and neglecting the mass of the electron m_e and assuming that $m_e \ll$
1119 $m_{A'} \ll E_0$ and $x\theta_{A'}^2 \ll 1$, the differential cross section becomes

$$\frac{d\sigma}{dx} \approx \frac{8Z^2\alpha^3\epsilon^2 x}{m_{A'}^2} \frac{\chi}{Z^2} \left(1 + \frac{x^2}{3(1-x)} \right) \quad (2.11)$$

1120 This equation reduces to the photon bremsstrahlung cross section in the limit that $m_{A'} \rightarrow 0$.
1121 Since $U(x, 0)$ is minimized, the A' production rate is maximum at $x \approx 1$, showing that A' 's take most
1122 of the incident electron's energy $E_{A'} \approx E_0$. There is also a cutoff value of $1 - x$ at $\max\left(\frac{m_e^2}{m_{A'}^2}, \frac{m_{A'}^2}{E_0^2}\right)$
1123 and a median of $\max\left(\frac{m_e^2}{m_{A'}^2}, \frac{m_{A'}^2}{E_0^2}\right)$. The A' emission angle cutoff is given by $\max\left(\frac{\sqrt{m_{A'} m_e}}{E_0}, \frac{m_{A'}^{3/2}}{E_0^{3/2}}\right)$
1124 and is much smaller than the opening angle of the decay products $A' \sim m_{A'}/E_0$. The recoil electron

¹¹²⁵ has a recoil angle of about $\theta_R \sim (\frac{m_{A'}}{E_0})^{1/2}$.

¹¹²⁶ The overall A' rate is proportional $\frac{\alpha^3 \epsilon^2}{m_{A'}^2}$, thus decreasing with increasing A' mass, and is reduced
¹¹²⁷ from ordinary photon bremsstrahlung by a factor of $\frac{\epsilon^3 m_e^2}{m_{A'}^2}$. A typical decay length as measured in
¹¹²⁸ the lab frame $\gamma c\tau$ can be calculated from Eq. 2.8.

$$\gamma c\tau = \frac{3\hbar E_0}{N_{eff} m_{A'}^2 \alpha \epsilon^2 c} \quad (2.12)$$

¹¹²⁹ For a fixed target experiment that attempts to reconstruct vertex positions, these kinematics
¹¹³⁰ provide significant challenges particularly from a highly boosted particle with a small opening angle.
¹¹³¹ A schematic of the basic kinematics and A' production from an electron incident on a fixed target
¹¹³² is shown in Fig. 2.12.

¹¹³³ The BEST Paper [26]

¹¹³⁴ Fixed Targets [24]

¹¹³⁵ Pair production bremmstrahlung [61]

¹¹³⁶ 2.8 Fixed Target Backgrounds

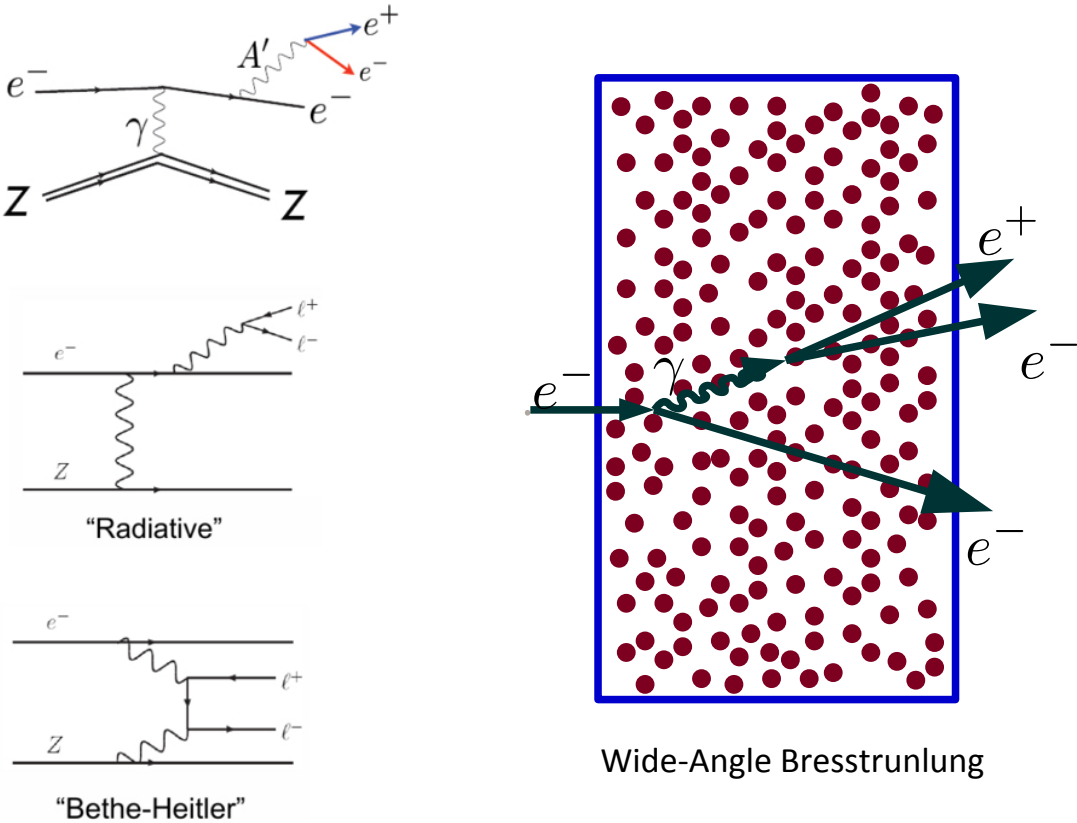


Figure 2.13: Left pictures show Feynman diagrams for A' (top), RAD (middle) and BH (bottom) events. Right picture shows WAB process.

¹¹³⁷ There are three main sources of physics backgrounds that are electro-produced in a fixed target
¹¹³⁸ that have an e^+e^- final state. The first two are prompt QED process ($e^-Z \rightarrow e^+e^-e^-Z$) called “tri-
¹¹³⁹ dents” because of the three-lepton final state. The other main e^+e^- background is bremsstrahlung
¹¹⁴⁰ production followed by pair conversion ($e^-Z \rightarrow e^-\gamma Z$ and then $\gamma Z \rightarrow e^+e^-Z$) which can recon-
¹¹⁴¹ struct as trident-like due to the three-lepton final state. These are not necessarily prompt since the
¹¹⁴² conversion can occur from an on-shell γ in either the target or any material in the detector. Their
¹¹⁴³ Feynman Diagrams are shown shown in Fig. 4.7.

¹¹⁴⁴ The two types of trident processes are called “radiatives” and “Bethe-Heitler” tridents. Radiative
¹¹⁴⁵ tridents have identical kinematics to A' s. Because of this, radiative tridents constitute an irreducible
¹¹⁴⁶ prompt background that can only be distinguished from A' s through either a mass resonance in the
¹¹⁴⁷ e^+e^- invariant mass spectrum or through a finite decay length for sufficiently small ϵ^2 . However,

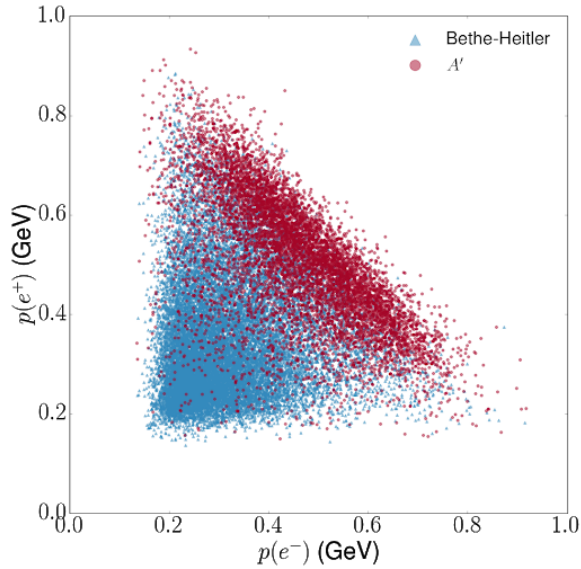


Figure 2.14: Positron momentum vs electron momentum comparing Bethe-Heitler tridents and A' 's (and hence radiative tridents). A' 's generally have a large x in comparison to Bethe-Heitler. This is for a beam energy of 1.06 GeV.

the identical kinematics do provide a way to compute the expected A' rates directly from counting e^+e^- pairs in the data and then using Eq. 2.9.

Bethe-Heitler tridents can be kinematically distinguished from A' 's and radiative tridents and generally have softer daughter e^+e^- pairs (e^+e^- pair is not peaked at high x). This difference in kinematics is illustrated in Fig. 2.14. In addition, there are interference terms between radiative tridents and Bethe-Heitler tridents which make a significant contribution to the overall cross-section, but make it impossible to physically distinguish between recoil and daughter electrons where either particle paired with a positron is a potential background. However, even when selecting only e^+e^- pairs at high x where radiative tridents peak, the Bethe-Heitler tridents and cross terms (altogether called “non-radiative” tridents) still dominate the rate of radiative tridents by nearly an order of magnitude.

The last main background are known as wide-angle bremsstrahlung (WABs) where a photon and electron are both emitted from the target at large angles from the beam axis into the acceptance of HPS. The photon can either convert in the target or a silicon plane in the tracker. There is a very large rate of WABs; however, only a small fraction are in HPS acceptance. The WABs that reconstruct a vertex with the daughter positron and the recoil electron are a background, though it will reconstruct at the primary even though the converted photon itself can be a displaced vertex. The rates of converted WABs with an e^+e^- pair in opposite halves of the detector after reconstruction is comparable to radiative tridents.

1167 2.9 Overview of HPS

1168 The Heavy Photon Search (HPS) is a fixed target experiment at Jefferson Laboratory that searches
1169 for electro-produced heavy photons from a high energy electron beam and utilizes a compact for-
1170 ward acceptance spectrometer to capture the charged-lepton decay products of heavy photons and
1171 reconstruct their vertex positions and masses. The main components of HPS consists of a silicon
1172 vertex tracker (SVT) used for reconstruction of particle trajectories and electromagnetic calorimeter
1173 (Ecal) used for timing and triggering.

1174 HPS searches for heavy photons using two distinct methods. The first method is a basic resonance
1175 search, or “bump hunt”, where a search for a resonance in the invariant mass spectrum of e^+e^-
1176 pairs at the heavy photon mass over a large background of QED processes. HPS is competitive with
1177 other experiments that can perform a similar search offering a relatively wide mass range over e^-
1178 fixed-target competitors.

1179 The second search method is a displaced vertex search where a secondary vertex displaced from
1180 the target is distinguished from a large prompt QED background. The fact that HPS can search
1181 for long-lived heavy photons by actually reconstructing the vertex instead of using a much simpler
1182 beam dump experiment makes HPS uniquely able to probe a region of phase space of particles with
1183 short $c\tau$ values on the order of 1 - 10 mm.

1184 In order to successfully perform these two searches, HPS must accomplish two difficult challenges.
1185 First, the heavy photon kinematics require large acceptance and excellent vertex resolution. This
1186 results in silicon from the first layer of the SVT to be 0.5 mm from an intense electron beam risking
1187 both highly non-linear radiation damage to the sensors and challenges of particle occupancy in the
1188 detector. The second challenge requires separating a large number of prompt QED process on the
1189 order of 10^8 that undergo multiple scattering in the tracker that may reconstruction downstream of
1190 the target from only a few true displaced vertices which are from a long-lived particle off the tail
1191 of its exponential distribution. The remainder of this thesis will focus on the methods and results
1192 from the displaced vertex search.

₁₁₉₃ **Chapter 3**

₁₁₉₄ **The HPS Detector**

₁₁₉₅ The Heavy Photon Search (HPS) is a precision vertexing experiment designed to measure both
₁₁₉₆ prompt and long-lived heavy photons that decay to e^+e^- pairs. The HPS detector is a large, compact
₁₁₉₇ forward acceptance spectrometer with three main components - a silicon vertex tracker (SVT), an
₁₁₉₈ electromagnetic calorimeter (Ecal), and a three-magnet chicane. A rendering of the detector is
₁₁₉₉ shown in Fig. 3.1. The SVT used to measure track particles and measure their momentum, the
₁₂₀₀ Ecal is used for timing and triggering, and the analyzing magnet (the middle magnet of the chicane)
₁₂₀₁ bends charged particles for a momentum measurement and particle identification.

₁₂₀₂ The specific design of the detector components are optimized for the physics goals of HPS.
₁₂₀₃ To maximize A' 's signal yield, particularly low mass and displaced A' 's, the detector must have
₁₂₀₄ acceptance to small angles. The search for displaced vertices is limited by vertex resolution that
₁₂₀₅ is dominated by multiple scattering, thus the first layer must be placed as close to the target as
₁₂₀₆ possible.

₁₂₀₇ Beam electrons that are elastically scattered in the target are the dominate source of background
₁₂₀₈ and can be tolerated with a selective trigger. The beam electrons that lose energy in the target due

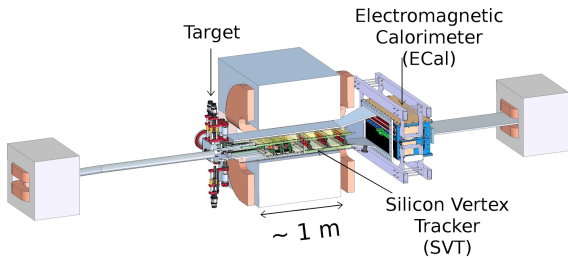


Figure 3.1: A 3D rendering of the HPS detector complete with the silicon vertex tracker (SVT), electromagnetic calorimeter (Ecal), and chicane.

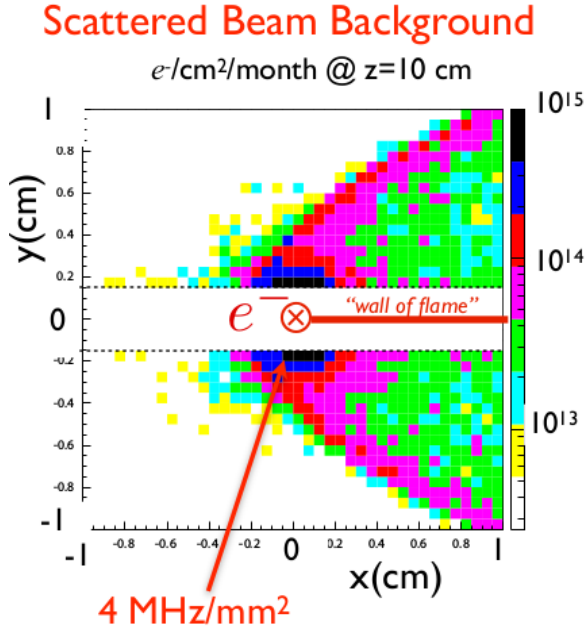


Figure 3.2: The rate of electrons in at the first layer of the SVT from the so-called “wall of flame” - beam electrons that lose energy due to bremmstrahlung in the target and bend in the magnetic field. To avoid the radiation damage from the wall of flame, the detector is split into top and bottom halves.

to Bremsstrahlung bend in the presence of the magnetic field and form the so-called “wall of flame” that would produce too much radiation damage in any detector component as shown in Fig. 3.2. Thus, the SVT and Ecal are both split in top/bottom halves and placed as close to the beam plane as possible. In order to balance between maximizing signal yield, optimal vertexing resolution, and radiation damage, the detector is designed at an opening angle of 15 mrad from the beam plane for both top and bottom halves.

The last major design consideration is due to the fact that there exist a possibility for a beam-gas interaction downstream of the target that will mock a downstream decay and look very signal-like. For this reason, the SVT and Ecal are under vacuum. As a result, all materials must be vacuum compatible (and are tested in a high vacuum test chamber). In addition, all materials must be nonmagnetic because the SVT operates in a high magnetic field.

3.1 The Continuous Electron Beam Accelerator Facility (CEBAF)

The high energy electron beam used for A' production by bremsstrahlung on a thin target is provided by Jefferson Laboratory’s Continuous Electron Beam Accelerator Facility (CEBAF) [49]. CEBAF is

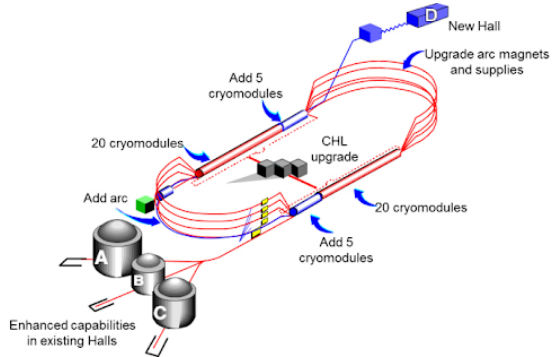


Figure 3.3: A schematic of the upgraded Continuous Electron Beam Accelerator Facility (CEBAF) at Jefferson Laboratory. The machine is a recirculating linear accelerator designed to send a beam of electrons of different currents and energies to four different experimental halls (Halls A - D).

able to simultaneously deliver intense and energetic electron beams of different energies and currents to three different experimental halls (Hall A, Hall B, and Hall C). The recent upgrade allows for CEBAF to deliver beam to four experimental halls (an additional Hall D) in multiples of 2.2 GeV up to 12 GeV [30] [37]. Beyond and including the 2015 Engineering Run, HPS runs have all been in the 12 GeV era - that is with the upgrades.

CEBAF is a recirculating linear accelerator (linac) designed as a “racetrack” configuration where beam bunches are circulated multiple times through the same two linacs by arcs as shown in Fig. 3.3. Each cycle, or pass, around the accelerator adds an additional 2.2 GeV of beam energy for a maximum of 5 passes to Hall A, Hall B, and Hall C and an additional half pass to Hall D. Thus, the energy in a hall will be $0.1 \text{ GeV} + n \times 2.2 \text{ GeV}$ for n passes (the addition 0.1 GeV comes from the energy from the injector). CEBAF can deliver a beam current of up to $85 \mu\text{A}$ to halls A and C and deliver up to $5 \mu\text{A}$ to halls B and D (HPS utilizes a current far less than the maximum).

Electrons in the accelerator originate from the photoemission of a strained GaAs superlattice photocathode with an incident laser of 780 nm wavelength, which is equal to the band gap of the GaAs [55]. The incident laser is pulsed at 499 MHz for ≈ 40 ps. The photoemitted electrons are then brought to the the injector before finally entering the accelerator.

CEBAF accelerates electrons using superconducting radiofrequency (RF) cavities operating at 1500 MHz and by using an RF separator, can deliver beam pulses at either 500 MHz or 250 MHz, essentially a continuous duty cycle, to each of the four experimental halls. The continuous duty cycle is essential to HPS as it reduces pileup effects while maximizing luminosity. The 12 GeV upgrade included a 750 MHz RF separator which allowed the beam to be diverted to the new Hall D.

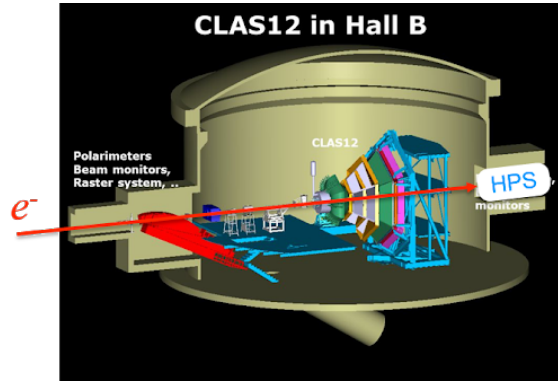


Figure 3.4: A schematic of Hall B including the CLAS-12 spectrometer and the HPS detector in the Hall B alcove. The electron beam enters the hall from the left in this picture.

1245 3.2 Hall B and HPS Beamline

1246 The HPS experiment is located in Hall B in an alcove behind the CLAS12 (CEBAF Large-Acceptance
 1247 Spectrometer) detector, which is typically used for low-current precision nuclear physics. Hall B can
 1248 receive either an electron or photon beam. In order to reduce pileup and beam background for
 1249 the HPS experiment, the Hall B beam from CEBAF is a continuous beam structure with a bunch
 1250 spacing at 2 ns (which is far shorter than the trigger window and comparable to the detector timing
 1251 resolution).

1252 The Hall B beamline begins with a large tagger dipole magnet which is a dipole magnet which,
 1253 when energized, steers the electron beam into the tagger dump below the beamline. The tagger
 1254 magnet is far upstream of HPS and allows for tuning of the beam to an acceptable quality before
 1255 delivering the beam to HPS. This is critical as the low acceptance of the tracker puts the silicon
 1256 within 5 mm of the nominal beam plane even with the SVT fully retracted, thus a poor quality
 1257 beam (one with a large spotsize, beam tails, or other instabilities) could cause unnecessary radiation
 1258 damage to the detector. If a target is placed upstream of the tagger magnet, a photon beam can
 1259 also be produced in Hall B which has been used for test runs for HPS in the past. The nominal
 1260 configuration for HPS physics running is for the tagger magnet to be de-energized so that the electron
 1261 beam can be delivered to HPS.

1262 The beamline between the tagger magnet and HPS consists of several beam position monitors
 1263 (BPMs) which measure the passing beam bunches to provide an estimate of beam current and posi-
 1264 tion. A series of quadrupole magnets and H/V correctors on the beamline are used for fast automatic
 1265 correction to beam trajectories based on the BPM measurements. The quadrupole magnets are also
 1266 used to squeeze the beam spotsize as small as possible at the target.

1267 The Hall B beamline also includes several wire harps to measure the beam position and profile.
 1268 This is used for beam tuning as well as to ensure the beam is safe enough to perform wire scans

1269 with the wires directly connected to the SVT as described below. An example of a harp scan from
1270 the 2H02 harp, which is the closest wire harp to the HPS target at 2.2 m upstream, from the 2016
1271 Engineering Run is shown in Fig. 3.5. The general strategy to achieve a small spot size at the target
1272 is to use the measurements from the 2H02 wire harp as well as several wire harps further upstream
1273 in conjunction with a series of quadrupole magnets along the beamline. The magnetic fields of the
1274 quadrupole magnets can be finely tune such that the waist, that is the minimum beamspot size in
1275 the y -direction, is precisely at the target.

1276 There are several collimators along the beamline to protect both HPS silicon sensors and elec-
1277 tronic components from radiation damage from either a stray beam or particles produced by a
1278 stray beam. When enough of a beam interacts with a collimator, it also produces a bunch of particles
1279 that trip the FSD. The closest collimator to the SVT is a 1 cm thick tungsten plate with machined
1280 slots of different widths connected to a linear shift and placed 2.9 m upstream of target (referred
1281 to as the “SVT collimator”). With the exception of the inner strips of layer 1 of the SVT, this
1282 protects most of the detector from beam tails and beam halo. The collimator can also force an FSD
1283 trip such as when the beam is mis-steered or scrapes the collimator which can produce enough
1284 secondary particles for the FSD counters to cross threshold. For the 2016 Engineering Run, the 4
1285 mm slot was used ([Is this true??](#)).

1286 Downstream of HPS, there are two fluorescent screens and a screen used for optical transition
1287 radiation (OTR) that are useful for viewing the beam position. Finally, the beam is terminated in a
1288 Faraday cup in the Hall B beam dump. The Faraday cup provides the most accurate measurement
1289 of the total beam charge and is used to normalize the data for the analysis. A beam blocker must
1290 be put in front of the Faraday cup at operating beam currents to avoid overheating, and the actual
1291 measurement of integrated charge must be re-scaled.

1292 A schematic of the HPS beamline in the Hall B alcove is shown in Fig. 3.6. The HPS apparatus
1293 is a large, compact forward spectrometer that consists of a three-magnet chicane system, SVT, Ecal,
1294 and a vacuum chamber. On the exterior of HPS, there are several halo counters (plastic scintillators)
1295 that monitor the stability of beam conditions. If these halo counters measure particle rates above
1296 their set threshold, most likely due to an obscured beam, a fast shut down (FSD) is applied to the
1297 Hall B beam within 1 ms to prevent further radiation damage to the HPS detector components.

1298 Thin wires are attached to both the top and bottom of the SVT as described in Sec. 3.3.2 and
1299 are used to measure the beam position and profile with respect to the SVT as close to the target
1300 as possible. Each half the SVT contains a horizontal and a diagonal wire (oriented $\approx 10^\circ$ from
1301 horizontal) for a vertical and horizontal position measurement. These wires move with the SVT
1302 and, as they traverse the beam profile, beam particles are scattered into the halo counters on the
1303 exterior of HPS. The rate of beam particles counted by the halo counters is proportional to the
1304 intensity of the beam, thus through a mapping of the wire position and count rate a beam profile
1305 can be produced. In order to ensure safe operation of the SVT, the beam profile in the y -direction

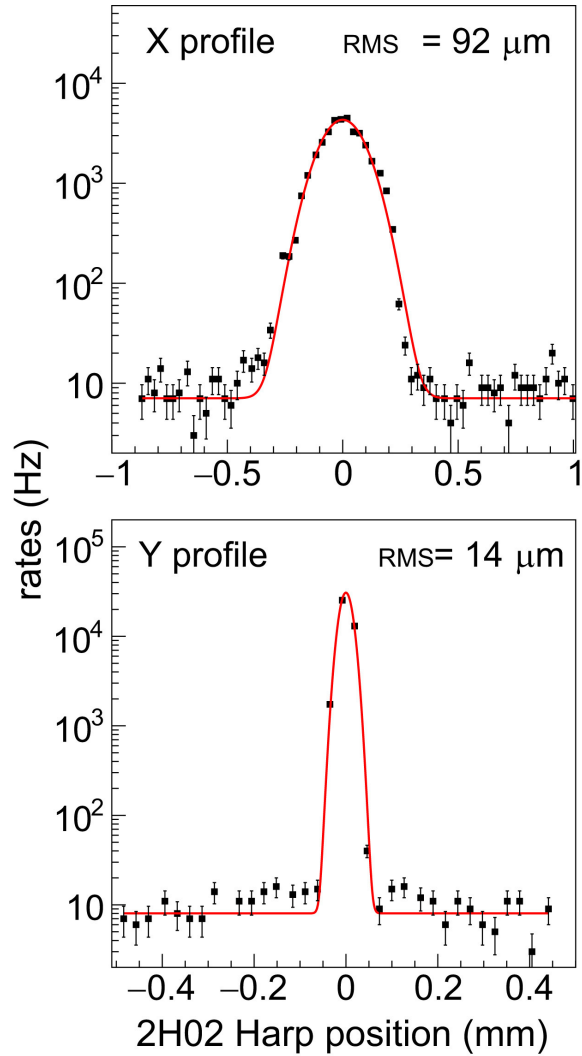


Figure 3.5: An example of a scan from the 2H02 wire harp from the 2016 Engineering Run. This provides a measurement of the beam profile that is useful as input to tuning the beam to its optimal profile at the target. The profile shows a width of $92 \mu\text{m}$ in x and $14 \mu\text{m}$ in y with minimal beam tails.

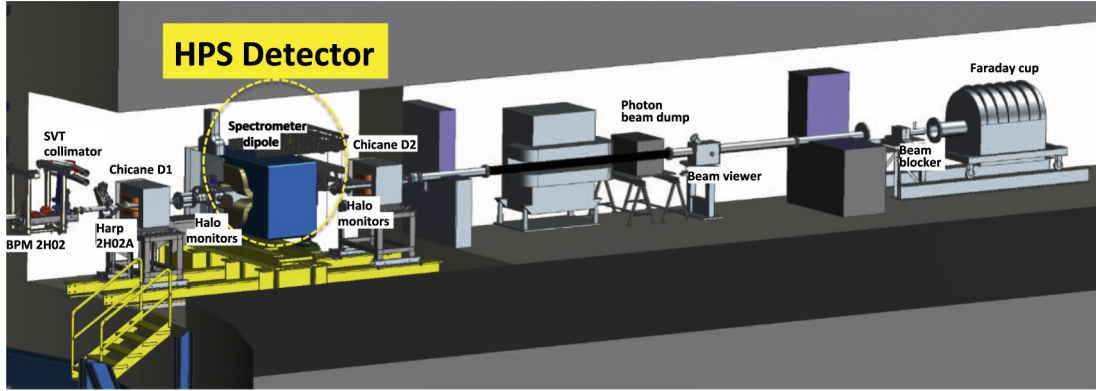


Figure 3.6: A schematic of the HPS beamline inside the Hall B alcove.

is required have a width less than $50\mu\text{m}$ with minimal beam tails and a mean within $50\mu\text{m}$ of the midplane between the top and bottom halves of the SVT. However, a beamspot as small as possible is desired as a smaller spot size will aid the constraint of vertices to the beamspot, thus improving the displaced vertex analysis by more efficiently rejecting tracks and vertices that are inconsistent with the beamspot. The beamspot size and position in the x -direction is less important since the resolution is far worse due to the fact that the SVT strips are oriented horizontally, so a width of less than $150\mu\text{m}$ is sufficient. An example of a wire scan measurement from the 2016 Engineering Run is shown in Fig. 3.7.

The SVT wire scans are unable to effectively measure the beam halo - beam electrons that differ significantly from the standard gaussian beam profile. This is important to understand for the purposes of long term radiation damage in the SVT. A measurement of beam halo from the 2015 Engineering Run by measuring occupancies in layer 1 of the SVT without the target is shown in Fig. 3.8. The beam halo intensity is $\sim 10^5$ which is sufficiently below the rate due to elastically-scattered beam electrons in the target, and thus is acceptable for HPS.

The chicane contains a single 18D36 analyzing magnet (or central magnet of pair spectrometer) with a pole length of 91.44 cm and a gap size of $45.72 \times 15.24\text{ cm}^2$. The analyzing magnet operated with a maximum field strength of 0.24 T for the 2015 Engineering Run and 0.50 T for the 2016 Engineering Run (the field strength scales linearly with beam energy and a maximum field strength of 1.5 T). In addition, two H-dipole Frascati magnets are set on either side of the analyzing magnet such that the total $\int \vec{B} \cdot d\vec{l}$ for the chicane system is 0 (each Frascati magnetic is half the analyzing magnet with opposite sign) which ensures the beam trajectory downstream of the chicane is independent of whether or not the chicane is powered.

The vacuum box has flanges upstream of the analyzing magnet for penetration of linear motion systems, cooling lines, and power and signal cables. The HPS target can be moved remotely by a linear shift from a stepper motor on the vacuum flange and is cantilevered at a ceramic support

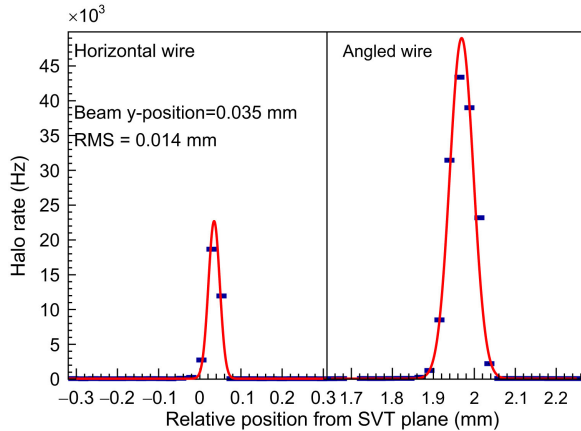


Figure 3.7: An example of an SVT wire scan measurement from the 2016 Engineering Run. This provides a measurement of the beam profile as close to the target as possible. This scan shows a beam with a $14 \mu\text{m}$ width in the y -direction with minimal tails and $35 \mu\text{m}$ from the nominal beam plane. This is an excellent beam profile for HPS.

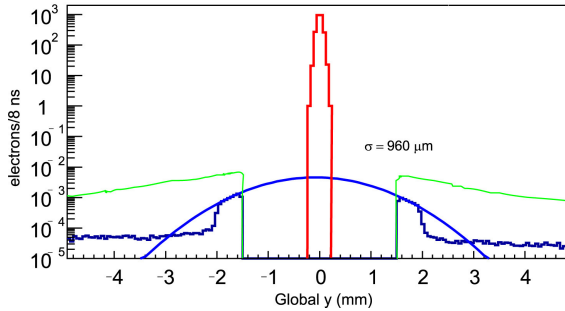


Figure 3.8: A measurement of the beam halo from 2015 Engineering Run using the occupancy of the first layer of the SVT in a no target run. The beam halo shows a width of $960 \mu\text{m}$ and 5 orders of magnitude less than the peak of the beam.

rod. There are several target options that can be selected based on the linear position of the target
 1331 mount - $4 \mu\text{m}$ tungsten (0.125% radiation length design and 0.223% radiation length measured), 8
 1332 μm tungsten (0.25% radiation length design and 0.116% radiation length measured), and a carbon
 1333 target for calibration. The Ecal is downstream of the analyzing magnet. More details of the Hall B
 1334 and HPS beamlines can be found in the HPS Beamlne paper [21].
 1335

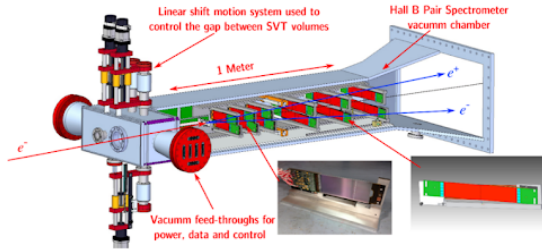


Figure 3.9: A schematic of the HPS silicon vertex tracker (SVT) which includes 6 layers of silicon microstrip sensors inside a vacuum and a uniform magnetic field. **Maybe find a better picture.**

1336 3.3 Silicon Vertex Tracker

1337 The silicon vertex tracker (SVT) provides a momentum measurement from charged particle trajectories
 1338 that bend in the uniform magnetic field that can be used to reconstruct a vertex position.
 1339 The SVT is an array of silicon microstrip sensors consisting of six layers (or measurement stations).
 1340 Microstrips provide a 1D measurement along the direction of the sensor extending away from the
 1341 beam. In order to provide a 3D measurement, each layer contains two components - an axial sensor
 1342 with strips parallel to the beam plane and a stereo sensor rotated at a small angle. A large stereo an-
 1343 gle would provide improved hit resolution in the direction along the axial strip, and hence improved
 1344 momentum resolution.¹ However, a large stereo angle would also cause the stereo sensors to dip
 1345 significantly into the beam plane, lose acceptance, and be prone to ghost hits (falsely reconstructed
 1346 3D hits). Thus, the stereo angle is intentionally small and designed to be 0.100 mrad for the first
 1347 three layers and 0.050 mrad for the last three layers, to provide a compromise between these affects
 1348 and hit resolution. The axial/stereo sensor pairs reconstruct a 3D hit position at each of the six
 1349 layers that are used for track finding.

1350 The SVT is split into top/bottom halves to avoid the very high flux of electrons near the beam
 1351 plane due to the “wall of flame”. Both the top and bottom halves are designed at a 15 mrad
 1352 opening angle with respect to the primary. This opening angle must be as small as possible in order
 1353 to capture as many A' s as possible which are typically highly boosted with a small opening angle.²
 1354 The last three layers of the SVT are double wide (i.e. two sensors end to end) to increase acceptance
 1355 for charged particles that are bending due to the uniform magnetic field.

1356 The six layers are arranged such that the distance between the first and second layer (layer 1
 1357 and layer 2) and the second and third layer is about 10 cm. The distance between the remaining
 1358 layers is about 20 cm. Layer 1 is placed as close to the target as possible at about 10 cm in order
 1359 to provide the best possible vertex resolution, and subsequently the second layer is placed close to
 1360 the first layer to maximize pointing resolutions of tracks back to layer 1. The limiting factor of the

¹The resolution in the bend plane is simply the resolution in the non-bend plane divided by the stereo angle.

²This becomes even more critical for displaced A' 's which, for a given opening angle, lose acceptance rapidly as the decay vertex increases along the beam direction.

1361 first layer placement is the fact that the sensors cannot be closer to 500 μm from the beam plane
 1362 in order to avoid significant radiation damage from both elastically scattered electrons in the target
 1363 and beam tails. Thus for a given opening angle of 15 mrad, the closest the first layer can be placed
 1364 is $\approx 1.5 \text{ mm} / 15 \text{ mrad} = 10 \text{ cm}$.³ This approaches the maximum allowed occupancy for the silicon
 1365 sensors of $\sim 1 - 2\%$. The sensors are designed to be as thin as possible to reduce the material budget
 1366 and hence the effects due to multiple scattering. A summary of the some of the important design
 1367 features of the SVT is shown in Table 3.1.

Layer Number	1	2	3	4	5	6
Distance z from target (mm)	100	200	300	500	700	900
Dead Zone Distance y (mm)	± 1.5	± 3.0	± 4.5	± 7.5	± 10.5	± 13.5
Number of Sensors	4	4	4	8	8	8
Stereo Angle (mrad)	100	100	100	50	50	50
Bend Plane Resolution (μm)	≈ 60	≈ 60	≈ 60	≈ 120	≈ 120	≈ 120
Non-Bend Plane Resolution (μm)	≈ 6	≈ 6	≈ 6	≈ 6	≈ 6	≈ 6
Material Budget (% X_0)	0.7%	0.7%	0.7%	0.7%	0.7%	0.7%
Module Power Consumption (W)	6.9	6.9	6.9	13.8	13.8	13.8

Table 3.1: A summary of the basic parameters for different layers in the SVT.

³The next subsection described a 1 mm inactive part of the sensor, so the active region begins at 1.5 mm from the beam plane.

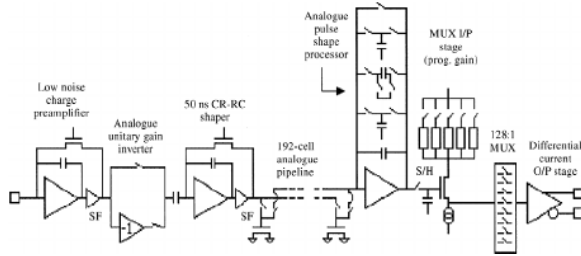


Figure 3.10: A schematic of the APV25 deep submicron readout chip that was originally designed for CMS detectors but is used for the HPS SVT.

3.3.1 Sensors and Readout

HPS utilizes the silicon microstrip sensors originally designed and procured for the upgraded DØ detector at Fermilab for run IIb, which was cancelled in favor of an insertable Layer 0 [34]. The sensor technology was chosen to minimize material budget to mitigate multiple scattering effects and to be highly tolerant to radiation. These sensors are single-sided p+n with AC-coupled readout with a bulk that is lightly doped n-type silicon. The strip implants are strongly p-type doped. The bias of the strips comes from polysilicon resistors at the end of the strips which are capacitively coupled to aluminum readout strips that run on top of the silicon strips.

The sensor cut dimensions are 100 mm × 40.34 mm with an active area of 98.33 mm × 38.34 mm. The silicon strip pitch is 30 μm ; however, only every other strip is readout (i.e. the readout pitch is 60 μm). When a particle is incident on an intermediate strips (a sense strip), the charge will split between the neighboring readout strips and this charge sharing will improve single hit resolution. Each sensor has 640 readout strips.

The useful sensor lifetime is limited by radiation damage where the sensor strips closest to the beam plane are expected to undergo a large electron flux of $> 10^{15}$ electrons per cm^2 over the duration of the experiment. Specifically, incident particles can displace silicon nuclei from their crystal lattice which causes an effective type inversion, where the n-type bulk is converted to p-type. The radiation damage leads to an increase in depletion voltage which means the charge collection efficiency for a given bias voltage will decrease. Thus as a sensor undergoes radiation damage over the course of the run which is highly non-linear and concentrated on the middle beam edge of the sensor (mostly from elastically scattered beam electrons in the target), the bias voltage must be increased to keep the same charge collection efficiency. Eventually, this bias voltage will approach the breakdown voltage and will no longer be usable in the experiment. In addition, radiation damage leads to increased leakage current, and thus sensor heating. For these sensors, the nominal operating bias voltage is 180 V. The design specifications required a breakdown voltage greater than 350 V; however, only sensors with a breakdown voltage greater than 1000 V were used. For the 2015 and 2016 Engineering Runs, radiation was not an issue.

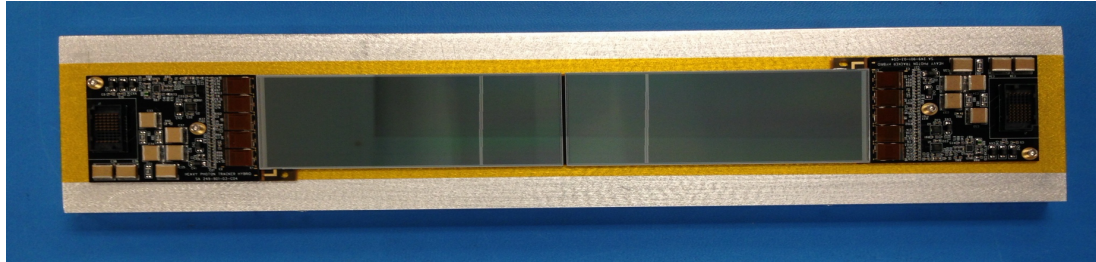


Figure 3.11: A picture of the two SVT sensors (end to end) with each sensor. The sensors are readout by APV25 chips which are housed on a hybrid circuit.

1395 These sensors are readout by the APV25 readout chip which was developed for the silicon mi-
 1396 crostrip sensors in the CMS tracker [58] [41]. A schematic is shown in Fig. 3.10. The APV25 chip
 1397 has high hit time resolution and has the ability to readout multiple consecutive samples of its shaper
 1398 waveform, thus it is useful for pileup rejection - an essential requirement for HPS. The APV25 chip
 1399 has 128 input channels, thus each sensor has $640 / 128 = 5$ readout chips. Each channel contains
 1400 a charge-sensitive preamplifier with an optional inverter, CR-RC shaper, and a 192-cell-deep analog
 1401 pipeline. Only 160 out of 192 of these cells are used to buffer samples and the remaining 32 cells
 1402 buffer the addresses of samples waiting to be readout. A picture of two SVT sensors with APV25
 1403 chips is shown in Fig. 3.11.

1404 The clock is designed for a clock period of 25 ns which is equivalent to the LHC bunch crossing.
 1405 However, HPS adapted this chip to run on a clock period of 24 ns (41.6 MHz) since it is an even
 1406 multiple of the both the JLab and Ecal clocks, which are 2 ns and 4 ns, respectively. Each channel
 1407 samples the shaper output and stores it in a cell of its pipeline on each clock. Once a trigger is
 1408 received, the pipeline cell of each channel is readout, and the chip multiplexes the 128 signals onto a
 1409 single differential current output. A configurable latency (the distance between the read and write
 1410 pointers) setting determines which pipeline cells are readout.

1411 The samples are readout by the Analog Pulse Shape Processor (APSP) which has the ability to
 1412 operate in two distinct modes - deconvolution mode and multi-peak mode. For each trigger signal,
 1413 The deconvolution mode allows for three consecutive pipeline cells to be readout and combined
 1414 into a weight sum whereas the multi-peak readout mode allows for three consecutive pipeline cells
 1415 to be readout without any additional operations. In order to mitigate pile-up effects from large
 1416 occupancy, HPS is operated in multi-peak readout mode and for each trigger, the APV25s are
 1417 sent two consecutive trigger signals for a total of six samples. These six samples are fit to a pulse
 1418 shape predetermined from offline calibration and reconstructed offline in order to obtain the pulse
 1419 amplitude and hit time. This is described in detail in Sec. ??.

1420 During the 2015 Engineering Run, the nominal settings of the APV25 were utilized. For the
 1421 2016 Engineering Run, these same parameters were used with the exception of the input parameters
 1422 of the pulse shaper which were optimized to have a sharp rise time for optimal time resolution and

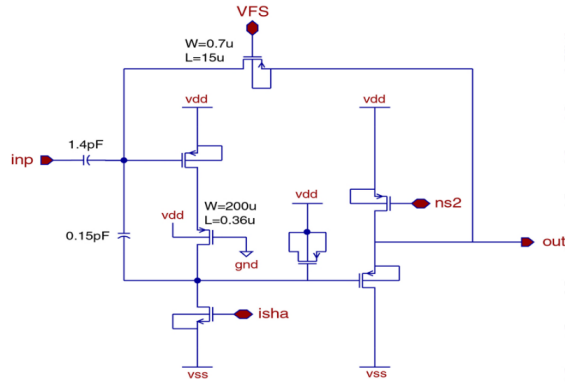


Figure 3.12: The APV25 Shaper schematic. The parameters VFS (related to the input voltage) and isha (related to the input current) were optimized for improved time resolution and reduced pileup.

¹⁴²³ quick fall time to further reduce pileup effects. A schematic of the APV25 shaper and the parameter
¹⁴²⁴ which were optimized is shown in Fig. 3.12.

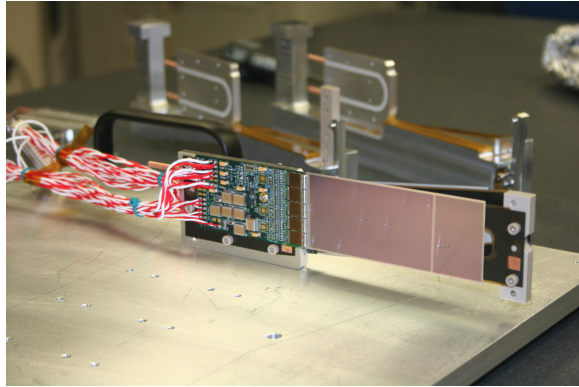


Figure 3.13: A single SVT module which comprises of two silicon microstrip sensors which are axial (front) and stereo (back) to the beam plane. Each sensor is supported by a carbon fiber support structure can be seen protruding from the right of the axial sensor.

3.3.2 SVT Mechanicals

1426 Each sensor is part of a base unit referred to as a “half-module” and is comprised of a single or
 1427 double sensor, carbon fiber support structure, and hybrid readout circuit boards. The first three
 1428 layers 1-3 are composed of a single sensor and hybrid while the last three layers 4-6, since they are
 1429 double wide, are composed of double sensors and hybrids. Each of these half-modules can be used
 1430 as the axial or stereo components of the detector.

1431 The carbon fiber, in addition to support for the sensor, acts as ground plane for the half-module
 1432 while a layer of Kapton insulation isolates the carbon fiber from the back of the sensor which is
 1433 at high voltage. The Kapton and carbon fiber are kept as thin as possible, much thinner than the
 1434 silicon sensors, to avoid adding additional unnecessary material that increases multiple scattering in
 1435 the tracker.⁴

1436 The hybrid circuit boards house the APV25 readout chips, five per half module, and provides
 1437 a connection of the sensor to the rest of the DAQ. The APV25 power, control lines, and output
 1438 channels are wirebonded to the hybrid while the input channels are wirebonded directly to the
 1439 sensor. The hybrid contains temperature sensors and carries filter capacitors for the sensor bias.

1440 Two of these half-modules are paired to create a module with one axial and one stereo half-
 1441 module. The axial half-modules are parallel to the beam plane and the stereo half-modules are
 1442 rotated at a small angle and dips into the beam plane on the positron side (beam left, the side
 1443 opposite to where beam background is bent). These modules are mounted on aluminum support
 1444 modules which hold the half-modules from both sides and, in addition to mechanical support, these
 1445 supports also pull heat generated by the hybrids. The half-modules and the support undergo thermal
 1446 contraction at different rates, thus the module support applies a constant tension from a spring pivot

⁴A window was machined into the carbon fiber support such that the material in the middle of the sensor, where most of the physics of interest is expected, is further minimized.

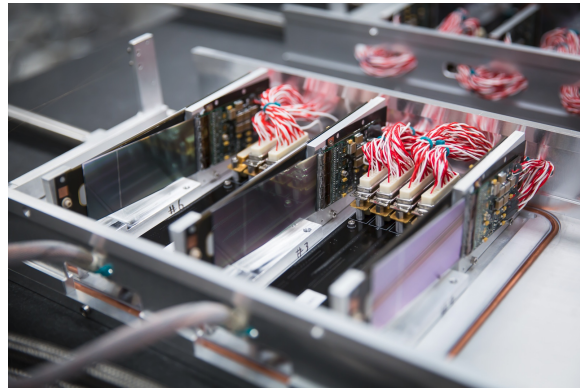


Figure 3.14: Layers 1 - 3 modules of the SVT (from left to right) are place in one of the U-channels. Copper cooling lines and electrical lines can be seen. The wire frames and scan wires can also be seen on the left.

1447 in order to keep the half-modules flat at operating temperature ($\sim 0^\circ \text{ C}$). A picture of a complete
1448 module is shown in Fig. 3.13.

1449 Three of these modules are mounted on an aluminum support structure called a “U-channel”.
1450 The SVT contains a total of four of these U-channel for each top and bottom of L1-3 and L4-6
1451 (which are larger). Each U-channel is supported by the kinematic mounts which guarantee reliable
1452 and repeatable positioning when the U-channels are installed and re-installed. The L1-3 U-channels
1453 rest on two downstream kinematic mounts, which act as a hinge, and is supported at the upstream
1454 end by motion levers which guide the L1-3 U-channels towards and away from beam. Finally, the
1455 L1-3 modules house scan wires as close to the target position as possible to measure the beam
1456 position and profile relative to the SVT to assess beam quality. Each U-channel has two wires -
1457 one parallel to the beam plan and one rotated at a slight angle - in order to obtain 2D position
1458 information. A picture of a L1-3 U-channel is shown in Fig. 3.14.

1459 The SVT underwent a mechanical survey before installation using a coordinate-measuring ma-
1460 chine which utilized both optical and touch probe measurements to locate 3D target points. The
1461 survey ensures the SVT was assembled as designed and allows adjustment for the adjustable com-
1462 ponents if necessary, and it provides an initial alignment for track reconstruction whose quality
1463 depends strongly on precise knowledge of the sensor positions and orientations. This is sufficient
1464 for initial knowledge, but the sensor is later aligned using the data as described in Sec. 4.7. Lastly,
1465 the survey provides a measurement of the edge of the L1 axial sensor relative to the wire on the
1466 U-channel to ensure that the sensor edge is placed at $500 \mu\text{m}$ from the beam plane. A picture of the
1467 SVT installed in the SVT vacuum box is shown in Fig. 3.15.

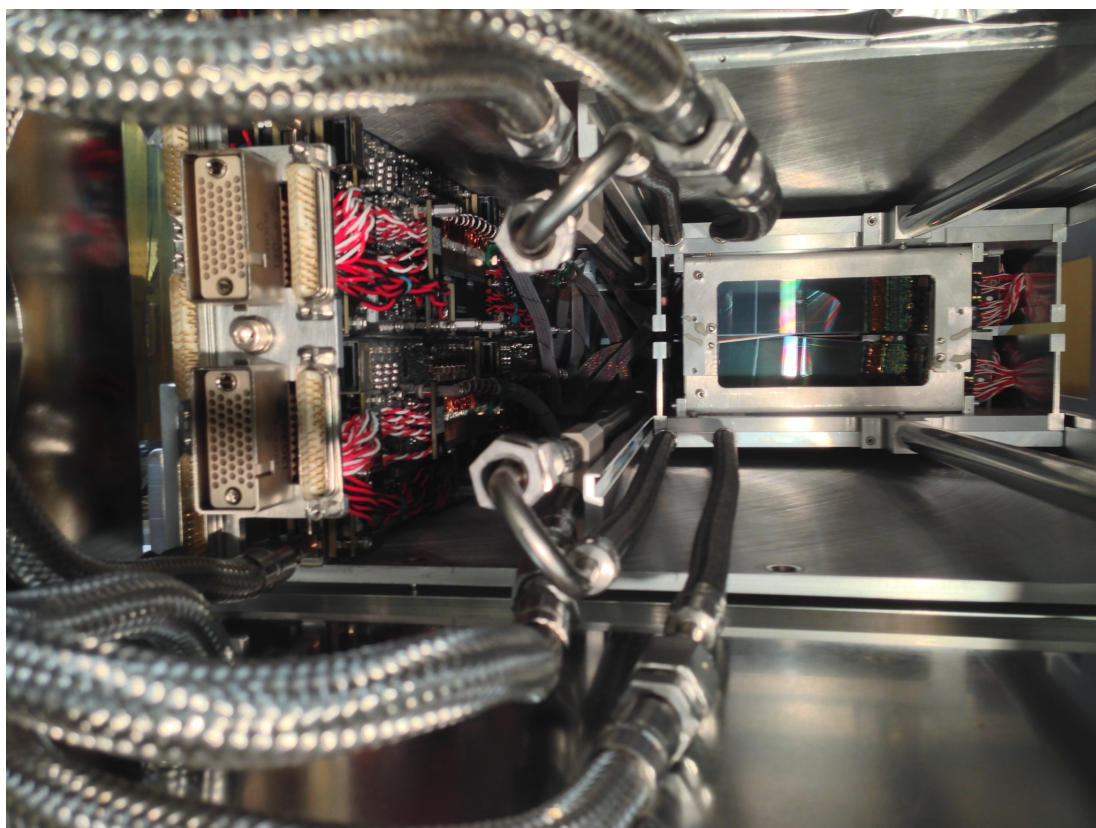


Figure 3.15: A picture inside the SVT vacuum chamber with everything installed except for the target. The frontend boards (FEBs) and FEB cooling plate are on the left. The SVT cooling lines protrude outward in the picture. The first layer of the SVT can be seen in the back behind the wire frames. The SVT is in its closed position and the beam must go through the 1 mm gap between the top and bottom sensors.

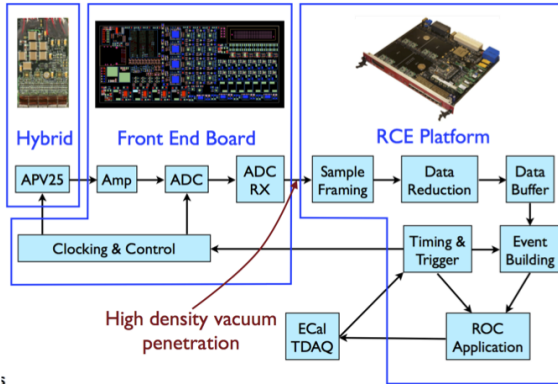


Figure 3.16: A schematic of the SVT DAQ system described in Sec. 3.3.3.

1468 3.3.3 SVT Data Acquisition, Power, and Services

1469 HPS must have a method to pass power and data to the detector given the constraints of the detector
1470 design as described previously. In addition, the nearest rack that can contain the data acquisition
1471 (DAQ) and power supplies is located about 20 m from where HPS is installed thus requiring the
1472 analog signals from the APV25 readout chips to be converted to optical digitized signals. As a
1473 result, the signal digitization and low-voltage regulation is performed inside the vacuum on frontend
1474 boards (FEBs) located on a cooling plate alongside the SVT. And because the SVT and front end
1475 boards (FEBs) are in vacuum, all power and DAQ must pass through a pair of 8-inch vacuum flanges
1476 upstream of the dipole magnet, thus requiring the reduction of the number of signals.

1477 Each of the 10 FEBs can service either a pair of L1-3 modules or a single L4-6 modules totalling
1478 four hybrids which is connected by a single bundle of impedance-controlled twisted pair magnet wire
1479 (which reduces crosstalk and electromagnetic interference between the lines). This carries the analog
1480 APV25 output signals, digital controls, trigger signals, low-voltage power, and high-voltage sensor
1481 bias. The data and control signals are carried by a mini-SAS cable on a high-speed data link. The
1482 FEBs digitize the output signals from 20 APV25 chips (4 hybrids \times 5 APV25 chips). A preamplifier
1483 on the APV25 converts a differential current signal to voltage and is digitized to a value between
1484 0 and 16384 by an AD9252 14-bit analog to digital converter (ADC) which samples the signal at
1485 41.667 MHz.⁵ Each FEB contains a Xilinx Artix-7 FPGA that sends the ADC data upstream to
1486 multi-gigabit receivers and controls and monitors the hybrid state and configuration.

The digitized data, low-voltage power, and high-voltage bias from the FEBs is transferred to electronic boards on the penetration of the vacuum flange (called “flange boards”) through mini SAS cable for data and twisted pair cables for power and bias.⁶ There are two flange boards on

⁵The 14-bit samples for each of the 23040 APV25 channels is too much data to store. The DAQ requires a readout threshold of three out of six samples above a threshold (three times the channel noise above the mean) that is predetermined from offline calibration.

⁶The flange boards are custom-made since the number of required connections is too high for conventional vacuum

1490 the beam right side - one for high voltage and the other for low voltage. The four flange boards
1491 located on the beam left side convert the digitized signal to optical using fiber transceivers so the
1492 signal can be transferred a large distance to the general-purpose Reconfigurable Cluster Elements
1493 (RCE) platform. The RCE plafrom was developed at SLAC and is housed in a standard Advanced
1494 Telecommunications Computing Architecture (ATCA) crate. The data from the FEBs is distributed
1495 on a Cluster on board (COB) between two ATCA blades housed inside the crate. Each COB contain
1496 8 RCE processing nodes which use Xilinx Zynq-7000 series FGPAs to apply data reduction to signals
1497 from the flange boards and build events.

1498 Each COB houses several generic hardware daughterboards common to RCE platforms including
1499 four Data Processing Modules (DPM) and one Data Transport Module (DTM). The DPMs process
1500 and reduce data at high speed while the DTM is responsible for timing and trigger distribution.
1501 The only HPS-specific hardware on the COB is the Rear Transition Module (RTM) which interfaces
1502 the optical fibers from the signal flange boards to the COB. The SVT DAQ utilizes a total of two
1503 COBS and two RTMs. In addition to the core of the DAQ, the rack also contains the low and high
1504 voltage Wiener MPOD power supplies which are commonly used for a variety of JLab experiments.
1505 A schematic of the SVT DAQ system is summarized in Fig. 3.16.

1506 The SVT services - motion, cooling, and power - are supplied from outside the vacuum through
1507 several flanges located upstream of the vacuum chamber. The SVT is cooled through 2 independent
1508 cooling loops one for the silicon sensors and the other for the FEBs. The silicon sensors must be kept
1509 below 0° C in order to avoid further radiation damage due to higher temperature (called reverse
1510 annealing). They are cooled through a hydrofluoroether compound circulating through copper lines
1511 embedded into the U-channels where top and bottom are split and L1-L3 and L4-L6 are connected
1512 in series. The specialized fluid is necessary since its low viscosity maintains high flow rates at low
1513 temperatures.

1514 The FEBs only need to be kept at around room temperature while dissipating only the heat the
1515 produced from operating the FEBs themselves. Thus, distilled water is sufficient as a cooling fluid
1516 and is circulated through copper lines embedded in the FEB cooling plate. The FEBs themselves
1517 are cooled through direct thermal contact with the cooling plate. A picture of the FEBs on the
1518 cooling plate is shown in Fig. 3.17.

1519 In addition to cooling components, there are three linear shift stepper motors that provide
1520 independent motion control of the top and bottom U-channels as well as the target frame. The
1521 motors are powered and controlled by a Newport XPS controller. All three motors have both a
1522 hardware and software safety stop, while the two motors that control the U-channel linear motion
1523 also include a precision limit switch to ensure the SVT is not accidentally driven into the beam.



Figure 3.17: The FEB cooling plate complete with 10 FEBs fastened to the front and back of the plate.

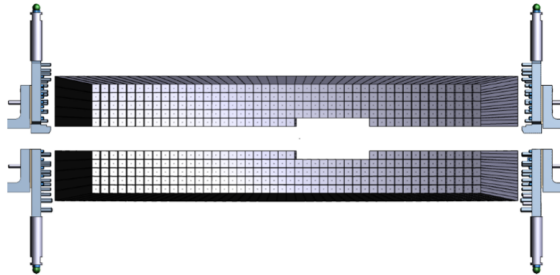


Figure 3.18: A rendering of the HPS Ecal. Each segment is one of the 442 lead tungstate crystals and the Ecal is split in half to avoid radiation damage from the most intense parts of the beam.

3.4 Electromagnetic Calorimeter and Trigger

The electromagnetic calorimeter (ECal) is an array of 442 lead tungstate scintillating crystals (PbWO_4) and is used primarily for precision timing and triggering (cite). The crystals are reused from the CLAS Inner Calorimeter (IC). The crystals have front faces of size $1.3 \times 1.3 \text{ cm}^2$, are 16 cm long, and are tapered such that the back faces have dimensions $1.6 \times 1.6 \text{ cm}^2$ for acceptance purposes. The Ecal itself is split into top and bottom halves much like the SVT to avoid the most intense parts of the beam plane. Each half contains 5 rows of 46 crystals with the exception of the removal of 9 crystals in the innermost row to avoid large occupancy from beam background. This is referred to as the Ecal hole or electron gap. The innermost rows are positioned 2 cm from the beam plane to maintain the 15 mrad design opening angle. The face of the Ecal is positioned 139.3 cm from the target position. Each crystal is readout by an avalanche photodiode (APD) on the back face of the crystal (specifically, a Hamamatsu S8664-1010 APD). One blue and one red LED are positioned on the front face of each crystal and are used for monitoring purposes (specifically radiation damage and stability of readout gain). Since the scintillator response is temperature-dependent, the Ecal is surrounded by a thermal enclosure.

The primary purpose of the Ecal is the main trigger. Jefferson Laboratory has developed general-purpose readout boards called the FADC250 digitizer boards, or simply FADC. Each Ecal crystal contains a preamplifier that outputs signals through a motherboard. Each FADC board has 16 input channels and are continuously digitized at 250 MHz to a 12-bit precision which are then stored in 8 μs deep pipelines to await being readout if a trigger signal is received. There are several readout modes available, but HPS utilizes the readout mode that outputs a window of 100 samples that allows pulse fitting with optimal time resolution.

The FADC boards are located in VXS crates also developed by Jefferson Laboratory as a general-purpose trigger framework. An algorithm that continuously looks for threshold crossings and integrates the digitized signal from the FADC within a fixed window converts the integration to an energy from previously calibrated values from cosmic rays. This gives a crystal position, energy, and

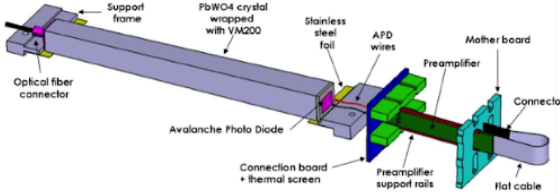


Figure 3.19: A schematic of a PbWO_4 crystal in the Ecal.

time of the threshold crossing which are then passed to the Global Trigger Processor (GTP) every 32 ns. Each Ecal half has a GTP board which clusters hits by looking at a 3×3 block around a center crystal with a least a 50 MeV (Is this number still accurate??) and the surrounding hits within 16 ns of the center hit. This defines a cluster with a center crystal, hit time, number of hits, and total energy. Each GTP reports these clusters to the Single Subsystem Processor (SSP) board.

The SSP uses these clusters to make a decision on the Trigger. For the 2016 Engineering Run, we have 5 triggers. The first is a “pulser” trigger which fires at a fixed rate of 100 kHz. Next, there are two triggers that fire on single clusters that are called “singles1” and its corresponding trigger which has looser requirements “singles0”. Finally, there are two triggers that fire on a pair of top-bottom clusters (at least one cluster in each GTP). These are called “pairs1” and “pairs0” triggers, where pairs0 is the looser version of pairs1. The pairs1 is our nominal trigger that is used for the physics analysis. In order to prevent the other triggers from triggering at a rate higher than the DAQ can handle, the singles triggers and the pairs0 trigger are prescaled such that one trigger in 2^n triggers are accepted where n is in the range of 10 to 13.

Once the SSP makes a trigger decision, if a cluster or pair of clusters meets the requirements above a trigger is sent to the Trigger Supervisor board (TS) and distributes the trigger to the Trigger Interface (TI) boards. The TS can reject the trigger if a subsystem is not ready to accept a trigger or the trigger follows too closely to another trigger.

The livetime of the DAQ, that is the fraction of time the DAQ is willing to receive triggers, must be understood in order to properly normalize the data. One way to measure the livetime is to use the pulser trigger. Since the pulser trigger fires at a constant rate, the ratio of the number of pulser triggers recorded to the number of pulser triggers that should have been recorded based on the 100 Hz rate is a direct measurement of the livetime. Another way to measure the livetime is to combine the measurement of integrated charge from the Faraday cup as described in Sec. 3.2 with a measurement of the integrated charge with the DAQ live. This is called the “gated Faraday cup scaler”, and the ratio of this scalar to the total integrated charge is the DAQ livetime. What do we actually use for 2016?

The HPS physics trigger is designed to maximize efficiency for A' s, or more generally e^+e^- pairs near the beam energy, while sufficiently suppressing backgrounds to avoid overwhelming the DAQ

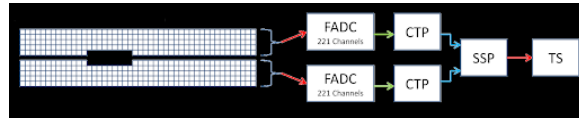


Figure 3.20: A schematic of the trigger for the Ecal. Top and bottom halves of the Ecal are each readout by FADC readout boards, and then sent to the SSP where a trigger decision is made.

systems. The most significant one-cluster background is elastically-scattered electrons in the target. Thus a trigger requiring at least two clusters will eliminate a large fraction of these. The largest source two-cluster backgrounds is elastically-scattered electrons in the target in coincidence with wide-angle bremmstrahlung. These can be eliminated by first requiring top and bottom coincident clusters as well as further timing and energy cuts.

The time coincidence between top and bottom clusters are required to be within 12 ns and is corrected for time walk. In addition to timing requirements, there is a coplanarity requirement that requires two clusters on opposite sides of the beam axis. It is intended to select only e^+e^- coincident pairs which are expected on average to be symmetric about the beam axis. The azimuthal angle ϕ relative to the beam axis of the top and bottom cluster is required to be within $\pm 30^\circ$ of 180° .

Furthermore, the trigger requires some basic energy requirements. First, a maximum energy sum requirement eliminates a large fraction of coincident beam scattered electrons. For the minimum energy requirements, it is important to note that there are substantial energy losses from a variety of sources in the Ecal such as the absorption of energy by the vacuum flange, gaps between crystals, or the back of the Ecal. As stated previously, this is accounted for in the reconstruction by detailed MC studies, but is not accounted for in the trigger. In addition, particles can hit the innermost row of the Ecal and lose energy where much of the shower is lost in the beam gap. This is especially important since a large fraction of signal, particularly at lower mass due to the smaller opening angle, occurs at the beam edge of the calorimeter. For this reason, there are only loose requirements on the minimum energy on individual clusters and minimum energy sum that are below the truth energy threshold of what one would expect from an A' .

Finally, it is expected that the lower energy decay particles from A' 's will have be further from the beam axis due to increased bending of the lower momentum particle from the magnetic field. The energy-distance cut rejects particles that are both low energy and close to the beam axis. This cut has the effect of first rejecting wide-angle bremsstrahlung which is a photon that is typically lower energy and closer to the beam axis and second, rejecting beam electrons that scrape the Ecal edge where most energy is lost. The cut is based on the cluster energy E_{low} and the cluster distance from the beam axis r_{low} and is expressed as $E_{low} + (5.5 \text{ MeV / mm}) r_{low} > 0.7 \text{ GeV}$.

The pairs1 trigger requirements - including the timing, cluster energy, cluster size, energy sum, cluster energy difference, coplanarity, and energy-distance requirements - are summarized in Table 3.2.

Trigger Description	Value
Time Difference	$ t_{top} - t_{bot} \leq 12$ ns
Cluster Energy	$0.15 < E < 1.4$ GeV
Cluster Size	$N_{hits} \geq 1$
Energy Sum	$0.6 < E_{top} + E_{bot} < 2.0$ GeV
Energy Difference	$ E_{top} - E_{bot} < 1.1$ GeV
Coplanarity	$ \phi_{top} - \phi_{bot} - 180^\circ < 35^\circ$
Energy-Distance	$E_{low} + (5.5 \text{ MeV / mm}) r_{low} > 0.7 \text{ GeV}$

Table 3.2: Summary of the pairs1 Trigger Selection from the 2016 Engineering Run.

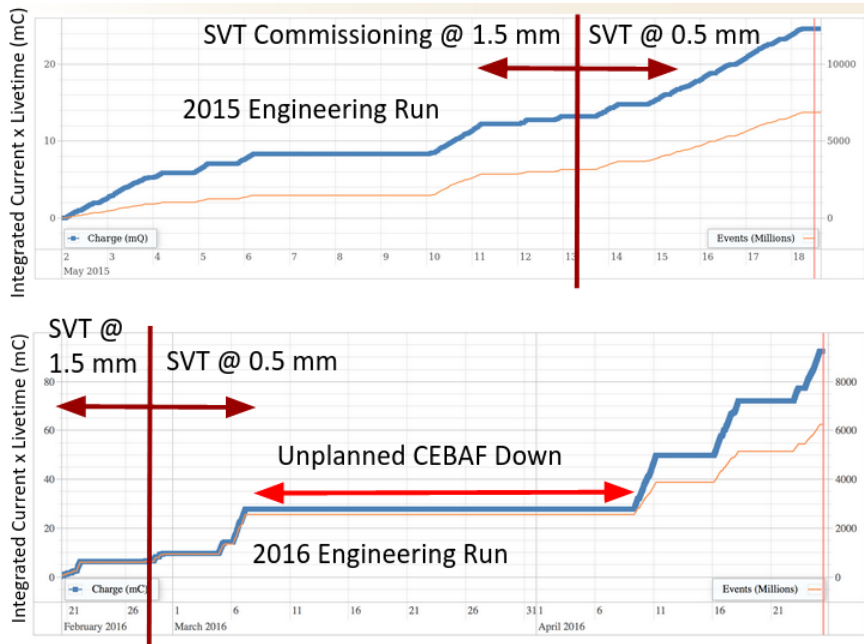


Figure 3.21: A summary for the integrated charge over time for the Top: 2015 Engineering Run and Bottom: 2016 Engineering Run. **Replace these figures**

1610 3.5 Datasets

1611 To date, HPS has three data taking runs - an engineering run in 2015, and engineering run in 2016,
 1612 and a physics run in 2019. The 2015 engineering run was taken with a beam energy of 1.056 GeV
 1613 and beam current of 50 nA incident on a $4 \mu\text{m}$ target. The total luminosity taken over opportunistic
 1614 nights and weekends amount to 74.72 nb^{-1} which corresponds to 0.4671 mC of charge and 0.1
 1615 PAC days. A broken cryogenic helium liquifier (CHL) shortly before the run began resulted in the
 1616 operation of only a single CEBAF linac for this run (as opposed to the usual two linacs). This gave
 1617 HPS a unique opportunity to run at this beam energy equivalent to half a pass which would have
 1618 otherwise been unavailable.

1619 The 2016 Engineering Run was taken with a beam energy of 2.3 GeV and beam current of 200 nA
 1620 incident on a $8 \mu\text{m}$ target. The total luminosity taken over weekends amount to 10753 nb^{-1} which
 1621 corresponds to 0.4671 mC of charge and 5.4 PAC days. **The luminosity need to be checked.** Much
 1622 of the analysis is performed on a blinded $\sim 10\%$ sample (1101 nb^{-1}) before the final results over the
 1623 whole dataset are produced. The data for the 2016 Engineering Run was collected by running on
 1624 weekends over the span of several months.

1625 A summary of the accumulated luminosity over time for the 2015 and 2016 Engineering Runs is
 1626 shown in Fig. 3.21. The focus of this thesis is the displaced vertex analysis from the 2016 engineering
 1627 run. The 2019 Physics Run was take with upgrades and is described in Sec. 6.

1628 **Chapter 4**

1629 **Event Reconstruction & Selection**

1630 Reconstruction is the process in a given event of building actual physics processes, such as an A'
1631 decay, from the raw hits of the detector channels readout by the trigger. The HPS event reconstruc-
1632 tion is based on the lcsim software toolkit [46] and uses both reconstructed clusters from the Ecal
1633 and tracks from the SVT, which are done independently until Ecal clusters and tracks are matched
1634 by extrapolating the track state at the last layer of the SVT to a cluster in the Ecal for particle
1635 identification. These objects, mainly e^+e^- pairs or e^-e^- pairs, are used to reconstruct vertices used
1636 for the physics analysis. The multiple stages of the HPS reconstruction - SVT hit reconstruction,
1637 tracking, vertexing, and Ecal clusters - are as follows in the proceeding sections.

1638 **4.1 HPS Coordinate Systems**

Coordinate System	x	y	z
JLab Coordinates	Beam left	Vertical	Beam direction
Detector/HPS Coordinates	Beam left rot. -30.5 mrad	Vertical	Beam direction rot. -30.5 mrad
Tracking/lcsim Coordinates	Beam direction	Beam left	Vertical

Table 4.1: Basis for several different coordinate systems used in the HPS reconstruction and analysis.

1639 The HPS coordinate system is defined globally by the Hall B beamline where the the x -axis
1640 points beam left in the bend plane, the y -axis points vertically upwards, and the z -axis points along
1641 the direction of the beam. The origin is set at the intersection of the nominal beam and nominal
1642 target position. Due to the asymmetry of HPS with respect to the chicane, where the beam is
1643 rotated 30.5 mrad about the y -axis in the $-x$ -direction to the HPS beam axis. In other words, the
1644 HPS beam axis is rotated by 30.5 mrad beam left from the Hall B beam axis due to the first dipole
1645 magnet in the chicane. This is the natural reference frame for reconstructed particles and, unless

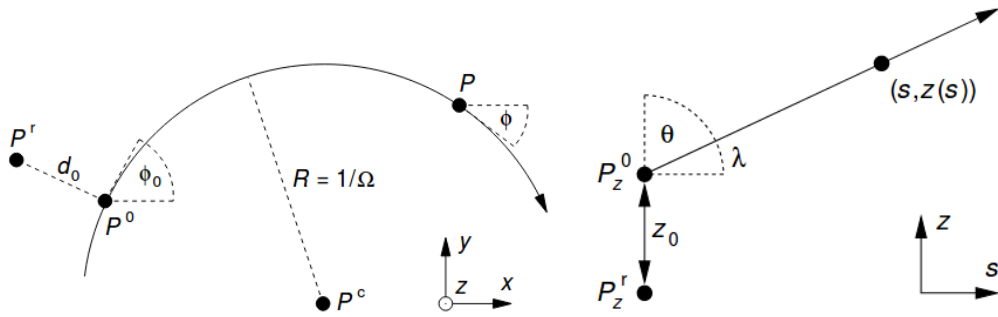


Figure 4.1: A schematic of the linear collider tracking parameters 5.17 [52].

otherwise stated, the physics analysis including positions and momenta will be performed in this frame.

The entire HPS SVT lies within a uniform magnetic field, thus a charged particle will form a helix. Unfortunately, the coordinate systems for track reconstruction and analysis on HPS are different. HPS utilizes perigee parametrization of tracks that fixes a magnetic field along the z -axis (which is the y -axis in HPS coordinates). The tracking coordinates are oriented approximately such that the x -axis points along the direction of the beam, the y -axis points beam left, and the z -axis points vertically upwards. In addition, each track is defined by 5 track parameters - Ω , d_0 , z_0 , $\tan\lambda$, and ϕ - and are briefly described below and shown in Fig. 5.17 [52].

1. Ω is the signed curvature of the track (i.e. the inverse of the radius $C = -q/R$).
2. d_0 is the signed impact parameter in the xy tracking plane. In the HPS detector frame, this translates to the impact parameter along the x (horizontal) direction.
3. z_0 is the tracking z position at the point of closest approach to the reference point. This is the key tracking parameter for the isolation cut. In the HPS detector frame, this approximately corresponds to the impact parameter in the y (vertical) direction.
4. $\tan\lambda$ is the slope of the straight line in the sz tracking plane. In the HPS detector frame, this translates to the slope of the track dy/dz in the yz plane.
5. ϕ is the azimuthal angle of the momentum of the particle at point of closest approach to the reference point.

Due to multiple scattering in the silicon sensors, different segments of the track (between each silicon plane) is describe by a different helix called track states. Thus each track segment will have its own set of unique 5 track parameters, and a track will have 11 or 13 track states depending on the number of hits on track. This process is described in Sec 4.3.3.

1669 4.2 Ecal Reconstruction

1670 The Ecal reconstruction is the process of building particle clusters from the waveforms readout in
1671 single crystals of the Ecal for a given event. Ecal crystals that are readout store 100 samples in 4
1672 ns intervals relative to the trigger time. The pulse shape is fit with a three-pole function

$$F_{3pole}(t) = \frac{t^2}{2\tau^3} e^{-\frac{t}{\tau}} \quad (4.1)$$

1673 The time constant τ is calibrated offline for each channel and is typically ~ 2.4 ns. From this
1674 function, the pedestal, time of the pulse, and amplitude are fit in offline reconstruction and pileup
1675 fits are not considered. From the amplitude, the pulse is converted to energy by two types of channel
1676 calibrations - cosmic rays and elastic scatters in the target ([cite](#)). Cosmic rays are calibrated before
1677 data taking with the beam off through the detection of minimum ionizing particles (MIPs), which
1678 have a known rate of energy loss, passing downwards through the Ecal. After data taking, cluster
1679 energy is calibrated from elastically scattered electrons from the target, which are very near the
1680 beam energy, and the gain constants for every crystal is adjusted until the energies match what is
1681 observed in MC. Both cosmic ray MIPs and elastically scattered electrons populate the full range
1682 of interest in energy.

1683 In order to form clusters in the Ecal, individual hits are formed together using a clustering
1684 algorithm adapted from the CLAS Inner Calorimeter [[cite](#)]. Hits with a local energy maxima are
1685 seeded for clusters, and then the algorithm searches for neighboring crystals with seeds or a hit on
1686 a cluster within 8 ns of the seed. The seed hit time is used as the time of the cluster with larger
1687 energy since higher energy hits have better timing resolution.

1688 The energy of the cluster is initially the sum of the individual hit energies. However, this energy
1689 does not account for electromagnetic showers that are lost on the Ecal edges or energy absorbed
1690 in the vacuum flanges. In addition, particles generally enter an Ecal crystal at an angle off axis
1691 from crystal axis and electromagnetic showers deposit energies at all Ecal depths resulting in the
1692 fact that maximum energy deposition may not occur in the same crystal as the crystal whose
1693 front face the particle has traversed. As a result, energy corrections are based on detailed MC
1694 studies and the energy is corrected as a function of particle type (photon, electron, or positron),
1695 energy, and angle, where the particle type must be determined by track-cluster matching later in the
1696 reconstruction described in Sec. 4.4. In addition, the position of the cluster is initially determined
1697 by a logarithmically weighted centroid. For the same reason as energy, the position must also be
1698 corrected and is done so in the same MC studies as energy. [cite these MC studies](#)

1699 4.3 SVT Reconstruction

1700 The SVT reconstruction is the process of building particle tracks from the waveforms readout in
1701 single strips of the SVT for a given event. These tracks are used to form electron and positron
1702 objects (tracks matched with Ecal clusters), which are then used to form vertices used in the final
1703 analysis.

1704 4.3.1 SVT Hit Reconstruction

1705 For each trigger, SVT channels where at least three of the six samples are above the readout thresh-
1706 old, that was determined by offline calibration before data taking in calibration runs (for reasons
1707 described in Sec. 3.3.3), are readout. For each strip in the SVT that is readout, the APV25 reads
1708 out six samples of 24 ns intervals. The APV25 response is modeled as a four pole filter with three
1709 coincident poles (i.e. three of the poles with the same time constant). This gives the following
1710 transfer function with two time constants τ_1 and τ_2 .

$$\tilde{F}(\omega) = \frac{1}{(1 + i\omega\tau_1)(1 + i\omega\tau_2)^3} \quad (4.2)$$

1711 The inverse Fourier Transform of this transform function is the pulse shape given by

$$F(t, \tau_1, \tau_2) = A \frac{\tau_1^2}{(\tau_1 - \tau_2)^3} \left(e^{-\frac{t-t_0}{\tau_1}} - \sum_{k=0}^2 \left(\frac{\tau_1 - \tau_2}{\tau_1 \tau_2} (t - t_0) \right)^k \frac{e^{-\frac{t-t_0}{\tau_2}}}{k!} \right) \quad (4.3)$$

1712 The time constants are predetermined offline by fitting pulses in calibration runs and have typical
1713 values of $\tau_1 \approx 72$ ns and $\tau_2 \approx 12$ ns. t_0 is defined as the time the fit crosses 0 and is set as the time
1714 of the raw hit. A is related to the amplitude of the pulse in ADC counts. Both of these quantities
1715 are determined by the fit in offline reconstruction.

1716 The pulse is fit to a pileup algorithm where a fit to a single pulse is compared to a fit with a
1717 double pulse. If the single pulse fit has a $\chi^2_{prob} < 0.5$, a refit with two pulses is attempted. If this
1718 produces an improved χ^2_{prob} , the double pulse fit is accepted, else the single pulse fit is accepted.
1719 The time of the pulse is corrected after the fit for several effects including a run-dependent phase
1720 shift, trigger time, and time of flight.

1721 [Add plot of six samples?](#)

4.3.2 SVT Cluster and 3D Hit Reconstruction

After single strip hit reconstruction, the hits are clustered together with neighboring hits using the nearest neighbor RMS Clusterer algorithm [Cite this algorithm](#). The algorithm uses the amplitudes in ADC counts (where it is not necessary to convert amplitude to energy deposition) and seeds hits whose amplitude are at least 4 RMS above the noise of the channel. From there, it appends neighboring strips whose pulse times are within 8 ns of the seed strip and whose amplitudes are at least 3 RMS above the noise of the channel. In addition, each of the strips, whether seed or neighbor channel, must have a χ^2 probability for the fit in Eq. 4.3 greater than 3.20^{-6} . The position of the cluster is the amplitude-weighted centroid of the hits ($\sum x_i A_i / \sum A_i$). Typically, SVT clusters are composed of one or two strips hits in approximately equal proportion. Since time resolution is significantly degraded for hits with low energy deposition, the time of the SVT cluster is weighted by the square of the amplitude ($\sum t_i A_i^2 / \sum A_i^2$).

The 1D strip clusters in each axial sensor in a given layer are then paired together with the corresponding stereo sensor in the same layer to form 3D hits. Only clusters within 12 ns of the trigger time and with at least an amplitude of 400 ADC counts are considered. These clusters must cross physically in space from the perspective of the primary (with some tolerance) and be within a 16 ns coincidence of each other. A 3D hit is reconstructed at the intersection of the two strip clusters. Since this intersection depends on the track angle, the 3D hit position is recalculated every time the hit is used in a track fit to correct for parallax effects.

1741 4.3.3 Track Reconstruction

1742 The SeedTracker algorithm, which was developed for design studies with the SiD detector ([cite](#)), is
 1743 performed as a simple method of track finding for HPS. Seed tracks, that is tracks that result from
 1744 SeedTracker, are found using several different track finding strategies. The tracking strategies are
 1745 as follows.

- 1746 1. A track candidate is found using three 3D hits which forms a helical track.
- 1747 2. This helix is extrapolated to a confirm layer and, if this confirm layer has a 3D hit consistent
 1748 with the helix, this hit is appended to the helical trajectory. Else, the track candidate is
 1749 discarded.
- 1750 3. Lastly this 4-hit track is extrapolated to the remaining two layers called the extend layers. The
 1751 3D hits in those layers that are consistent with the helix are appended. We require at least one
 1752 of the extend layers to have a 3D hit consistent with the helix, thus requiring a minimum of
 1753 five 3D hits on a track. If this extend requirement is not met, the track candidate is discarded.

1754 Four tracking strategies are used because any single strategy using this method will not find
 1755 tracks that miss a seed or confirm layer. The four tracking strategies used in the reconstruction are
 1756 s-345 c-2 e-16, s-456 c-3 e-21, s-123 c-4 e-56, and s-123 c-5 e-46 where s, c, and e are abbreviations
 1757 for seed, confirm, and extend, respectively. As an example, s-345 c-2 e-16 seeds track candidates
 1758 using 3D hits on layers 3, 4, and 5. Then, this helical fit is extrapolated to layer 2, followed by layers
 1759 1 and 6. The seed tracks from 345 that successfully append a hit in layer 2 and either layer 1 or 6
 1760 are stored as a track candidate to be used for the remaining reconstruction.

1761 In addition, there are several other requirements the track must pass. The RMS time of all
 1762 the hits on the track must fall within 8 ns. The track must have a χ^2 less than 100 (including
 1763 an individual hit χ^2 less than 10), a distance of closest approach $d0$ less than 15 mm, an impact
 1764 parameter $z0$ of less than 15 mm, and a minimum transverse momentum of 100 MeV.

1765 The SeedTracker algorithm returns a helical track fit to 3D hits, but fails to take multiple
 1766 scattering into account which results in an artificially worsened momentum resolution. In order to
 1767 account for multiple scattering effects, the helical track fit is refit using the General Broken Lines
 1768 (GBL) algorithm [27] [51]. For HPS, the GBL algorithm treats each sensor plane in the SVT as
 1769 a source of scattering and fits a track segment (defined by 5 parameters described in Sec. 4.1
 1770 that define the track state) between each sensor plane and extrapolates a track segment on the
 1771 first and last SVT sensor plane. For the reconstruction of the 2016 Engineering Run dataset, the
 1772 GBL track is required to have a χ^2 per degrees of freedom less than 12. The GBL fit minimizes
 1773 the hit residuals and scattering angles (called kinks) for each of these track segments and provides
 1774 performance equivalent to a Kalman filter. However, the GBL implementation for HPS requires 3D
 1775 hits from SeedTracker before inputting the track into the GBL algorithm. This 3D hit requirement

1776 results in some efficiency loss due to acceptance for particles that traverse either the axial or stereo
1777 sensor in a given layer. For future track reconstruction for HPS, a Kalman filter will be used to
1778 regain this loss of efficiency.

1779 Add figure for tracking?

1780 4.4 Track Cluster Matching

1781 Tracks are matched to Ecal clusters by extrapolating the track state of the final SVT hit to the face
1782 of the Ecal though a non-uniform magnetic field map and comparing this extrapolated position to
1783 the Ecal cluster position. The track is matched with the cluster with the minimum n_σ , provided
1784 that the match is less than 30σ . Analysis will impose a stricter requirement. Electron objects are
1785 defined as a negatively curved GBL track that is matched to an Ecal cluster in the same detector
1786 volume. Similarly, positron objects are defined as a positively curved GBL track that is matched to
1787 an Ecal cluster in the same detector volume. The electron and positron objects are used as inputs
1788 to the vertex fitter. The remaining Ecal clusters that do not have an associated matching track are
1789 defined as photon objects.

Cut Description	Requirement
Cluster Time Difference	$ t_{e^+Cluster} - t_{e^-Cluster} < 2.5 \text{ ns}$
e^+ Track-Cluster Time Difference	$ t_{e^+Track} - t_{e^+Cluster} - 55 < 10 \text{ ns}$
e^- Track-Cluster Time Difference	$ t_{e^-Track} - t_{e^-Cluster} - 55 < 10 \text{ ns}$
Ecal clusters in opposite volumes	$y_{e^+Cluster} \times y_{e^-Cluster} < 0$
Loose track-cluster match	$\chi^2 < 15$
Beam electron cut	$p(e^-) < 2.15 \text{ GeV}$
Track Quality	$\chi^2/dof < 12$
Maximum Vertex Momentum	$V_{0p} < 2.8 \text{ GeV}$

Table 4.2: Requirements applied to V_0 particles during the reconstruction stage for data (i.e. MOUSE cuts).

Cut Description	Requirement
Cluster Time Difference	$ t_{e^+Cluster} - t_{e^-Cluster} < 5 \text{ ns}$
Track-Cluster Time Difference	$ t_{e^+Track} - t_{e^+Cluster} - 43 < 10 \text{ ns}$
Track-Cluster Time Difference	$ t_{e^-Track} - t_{e^-Cluster} - 43 < 10 \text{ ns}$
Ecal clusters in opposite volumes	$y_{e^+Cluster} \times y_{e^-Cluster} < 0$
Loose track-cluster match	$\chi^2 < 15$
Beam electron cut	$p(e^-) < 2.15 \text{ GeV}$
Track Quality	$\chi^2/dof < 6$
Maximum Vertex Momentum	$V_{0p} < 2.8 \text{ GeV}$

Table 4.3: Requirements applied to V_0 particles during the reconstruction stage for MC (i.e. MOUSE cuts).

4.5 Vertexing

Every pair of e^+ and e^- objects in an event is fitted to a Billior vertex fitter [25]. The Billior vertex fit is a fast vertex fit that finds the best-fit vertex position and track parameters based on the individual track parameters and covariance matrices of the e^+e^- pair. This provides a vertex with a reconstructed 3D position based on the distance of closest approach between the two tracks as well as a reconstructed mass and momentum that are determined based on the fitted track parameters at the fitted vertex position.

The Billior Vertex fit allows for additional vertex constraints. If the e^+ and e^- objects are in the same hemisphere of the detector (most likely converted bremsstrahlung), they are placed in the Unconstrained Vc Collection and not considered for this analysis. If the e^+ and e^- objects are in opposite hemispheres of the detector and they pass the MOUSE cuts (reconstruction cuts) described in Tables 4.2 and 4.3, then they are placed in the Unconstrained V0 Particle Collection and considered for the analysis. In addition, a target constraint (x , y , and z positions) and a beamspot (x and y components of the V0 momentum) are placed on the V0 particle and placed in separate collections with a one-to-one-to-one mapping between the three collections. Specifically, the target

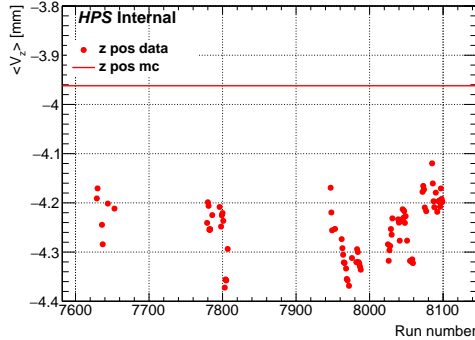


Figure 4.2: The run-dependent average position in z for unconstrained vertices fit represented by solid points and a solid line for data and MC simulation, respectively.

constraint requires the vertex to be consistent with the z position of the target and the x and y positions and sizes of the beamspot while the beamspot constraint requires the vertex momentum to point back to the beamspot at the target z position. Unconstrained vertices are used for the displaced vertex analysis while target constrained vertices are used for the resonance search.

In addition, all electron object pairs are also fit with a Billior Vertex and placed in the unconstrained Møller Candidate Vertex Collection. Møller candidates are also fit with target and beamspot constraints in separate collections and mapped in the same way. The Møller candidates are used for the studying the data/MC comparison of the mass resolution as described in Sec. 5.2.

The beamspot and target constrained Billior Vertex both takes use the beam position and size along with the target position in z as an input. For data, a run-by-run beam parameters were selected based on the fits of distributions. Plots for these beam parameters are shown in Fig. 4.2 and Fig. 4.3 where the data is shown as points and the MC is shown as a solid line. For MC, for simplicity and the parameters chosen to be constant and are $b_x = -0.224$ mm, $\sigma_x = 0.125$ mm, $b_y = -0.08$ mm, and $\sigma_y = 0.030$ mm. These parameters were used for both the actual simulated beam position and profile as well as inputs to the Billior Vertexer. These parameters are also used as inputs to the event selection described in Sec. 5.

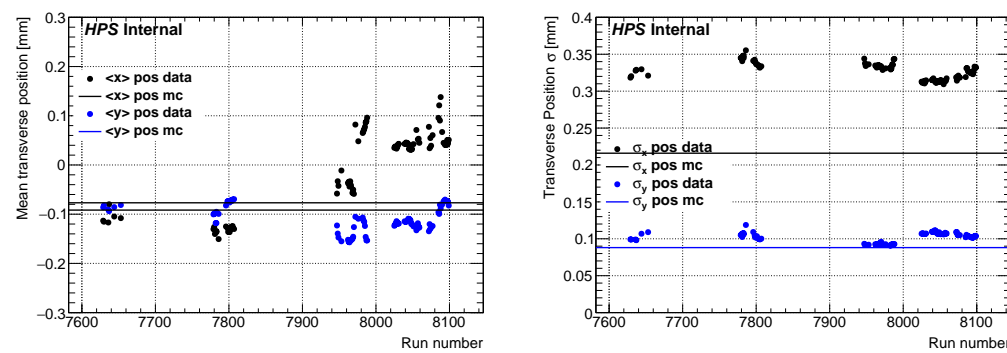


Figure 4.3: The run-dependent mean (left) and width (right) in x and y for the unconstrained vertex position in data. The MC is represented as a solid line.

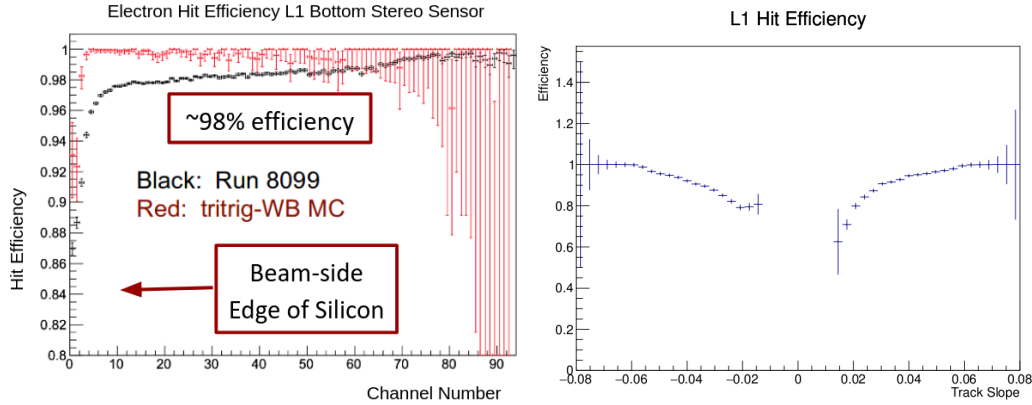


Figure 4.4: Left: The measured SVT layer 1 efficiency for electrons in layer 1 bottom stereo sensor. The MC does not have the correct hit efficiencies. Right: The layer 1 hit efficiency as a function of track slope ($\tan\lambda$) used for the hit killing algorithm described in Sec [Section.Replace these figures. Add a positron hit efficiency plot.](#)

4.6 Hit Efficiency

The HPS detector has hit efficiency effects that must be properly accounted for, particularly in the first layer of the SVT where occupancies are significantly higher than the other layers of the tracker. The main source of hit inefficiencies are wide angle bremsstrahlung conversions (WABs) in layer 1 of the SVT. Positrons from converted WABs are less likely to deposit sufficient energy into a silicon strip to pass readout threshold. This could result in a track that extrapolates to the active area of a layer 1 sensor that lacks a reconstructed hit, and thus will appear as a hit inefficiency in the method described below. This can be seen in a comparison of the hit efficiencies in layer 1 for positrons and electrons in Fig. 5.9 where the difference in efficiency between electrons and positrons can be attributed to converted WABs.

The remaining sources of hit inefficiencies are mostly unknown and are still under exploration. One hypothesis is some of the channels are readout, but the corresponding waveforms fail the fit requirements of the hit reconstruction stage described in Sec. 4.3. There is evidence of this from the fact that hit efficiencies are dominant in layer 1 at the strips nearest to the beam plane which have the highest occupancies due to elastically-scattered beam in the target and x-ray emissions from the target.

Hit efficiencies are measured using a track refit to a layer of interest, and an unbiased extrapolation to that layer to see if a hit lies within a certain window of the extrapolated position. As an example, in order to measure layer 1 efficiencies, the standard track reconstruction is performed on all layers except for layer 1. The tracks that meet basic quality requirements are extrapolated to both the axial and stereo sensor planes in layer 1. For the tracks that extrapolate to the active area of the sensor of interest, if a 1D hit is not found within 5σ of the extrapolation error it is counted as

1843 a hit inefficiency. The hit efficiency is defined as the ratio of the number of tracks with a hit within
1844 the defined extrapolation window to the total number of tracks sampled.

1845 Due to the highly non-linear nature of occupancies on the sensors, the hit efficiencies are separated
1846 by channel number using the position of the extrapolated track at each sensor¹. A sample of
1847 measured hit efficiency in data in comparison with MC as a function of channel number for the layer
1848 1 bottom stereo sensor is shown in Fig. 5.9. In addition, there are multiple scattering effects that
1849 result in a reduced measured hit efficiency on the edge of the sensors due to the fact that particle
1850 trajectories that don't traverse the active sensor area reconstruct a track that extrapolates to the
1851 active sensor area due to resolution effects (and thus counted as a hit inefficiency). This is most
1852 visible in MC which does not contain any hit efficiencies yet has a rapidly decreasing measured
1853 hit efficiency along the edge of the sensor. In principle, this can be corrected if errors on track
1854 extrapolations are computed correctly.

1855 Unfortunately hit efficiencies are not present in the MC, and methods of incorporating these
1856 effects are under investigation. However, this effect that will affect the signal rate and distributions
1857 for a variety of variables of interest. To account for hit efficiencies in both a simple and reasonable
1858 way, a post-reconstruction hit killing algorithm based on track slope is applied to signal MC (and
1859 some background distributions). This method is described in detail in Sec. 5.3.2.

¹The extrapolated track must be used since for an inefficiency. One cannot assign an inefficiency to a specific channel.



Figure 4.5: The target position is found to be -4.3 mm. I actually need to get these plots. Some placeholders are there for now.

1860 4.7 Tracker Alignment

1861 An initial mechanical survey is applied to the SVT as described in Sec. 3.3.2 which defines sensor
 1862 positions to within a precision of $50 - 100 \mu\text{m}$. This level of imprecision will create systematic shifts
 1863 in track parameters and artificially degrade tracking and vertexing resolutions, thus is insufficient
 1864 to meet the HPS physics goals. In order to mitigate alignment-related effects, an offline alignment
 1865 using particle trajectories to find the sensor positions and orientations as close as possible to their
 1866 true values is performed.

1867 Detector alignment comes in two steps - internal alignment and global alignment. The internal
 1868 alignment finds the sensor positions relative to each other using the top and bottom volumes of the
 1869 SVT separately with the goal of minimizing the track χ^2 . The internal alignment utilizes Millepede-
 1870 II which was developed for fast alignment of large tracking detectors such as CMS [28] [29]. Each
 1871 sensor can be corrected by translation along or rotation about the three coordinate axis for a total
 1872 of six possible alignment corrections.

1873 These corrections are not equally important. For instance, track parameters are sensitive to
 1874 translations along the measurement direction in a given sensor but completely insensitive to trans-
 1875 lations along the non-measurement direction (other than minor acceptance affects for track on the
 1876 sensor edge). For simplicity for this alignment, only translations along the measurement direction
 1877 and beam direction as well as rotations about the sensor normal were aligned **Is this true?**. The
 1878 sensor position and orientations were found by iterating with different alignment configurations that
 1879 float a single sensor position or orientation until the optimal alignment constant is found.

1880 Global alignment involves fixing the so-called “weak modes” where sensors move in together in

such a way that the track parameters and track quality are unaffected. Since there are 5 track parameters there are 5 weak modes - translating in the horizontal ($d0$) and vertical directions ($z0$), rotating tracks horizontally (ϕ) and vertically ($\tan\lambda$), and the horizontal quadratic shear (Ω).

Elastically-scattered electrons from the target ($e^-Z \rightarrow e^-Z$) have a known momentum at the beam energy, a known origin at the beam spot on the target, and sufficiently populate the full HPS angular acceptance making them ideal to study various weak modes. First the known curvature, provides a way to study the horizontal quadratic shear. Second, the known origin provides a way to study the translational weak modes as well as the z position of the target z_{targ} . In the yz -plane the extrapolated y position of any track can be parametrized as follows:

$$y(z) = y_{beam} + \tan\lambda \times (z - z_{targ}) \quad (4.4)$$

where $\tan\lambda$ is the track slope defined in Sec. 4.1. The equation contains two unknowns - the target position in z and the beam position in y y_{beam} . This can be resolved by using both the top and bottom halves of the SVT by moving in the vertical direction until their measurements are in agreement. Similarly, the x position of the beamspot x_{beam} can be found using the same method.

Include the target position.

Møller-scattered electron pairs, that is beam electrons that scatter off of a target electron, have a known momentum equal to the momentum of the beam, including both magnitude and direction. This can be used to measure the beam angle deviation from the nominal beam axis. In addition, the two-body kinematics of Møller scattering is identical to Compton scattering and has the following relation:

$$m_e c^2 (1/E - 1/E_{beam}) = 1 - \cos \theta \quad (4.5)$$

where θ is the angle from the beam axis and E is the energy of the e^-e^- pair. As a result, all Møllers at a specific energy will scatter at the same angle from the beam axis which can be used to constrain both the rotational weak modes. Møller-scattered electrons are also useful as a “standard candle” for determining the mass scale and mass resolution as described in Sec. 5.2.

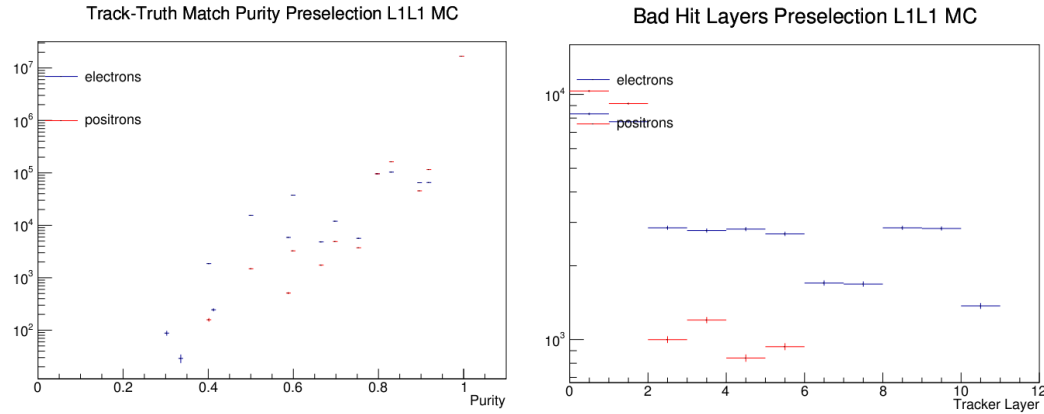


Figure 4.6: Preselection and layer 1 requirements for tritrig-wab-beam MC for e^+ and e^- tracks. Left: Purity. Right: Layers with a bad hit. **Redo these plots**

1904 4.8 Track-Truth Matching

1905 Due to the nature of backgrounds due to mistracking as described in Sec [Section](#), it is useful in the
 1906 displaced vertex search for tracks to be matched to truth particles in the MC. This will enable a
 1907 detailed study of mistracked backgrounds that can falsely reconstruct downstream of the target and
 1908 appear signal-like. A simple track-truth matching algorithm is performed after reconstruction, and
 1909 the algorithm is as follows:

- 1910 1. In the reconstruction process, the hits on track (i.e. the tracker hits) are each mapped to a
 1911 list of truth particles (called MCParticles) that contribute to the hit.
- 1912 2. For each MCParticle, the number of tracker hits that the MCParticle contributes to on a given
 1913 track is added.
- 1914 3. The MCParticle with the highest score, that is the highest number of tracker hits, is considered
 1915 to be the truth match.

1916 If there is a tie in this score, the MCParticle with the inner most hits (closer to the target)
 1917 is considered the to be the truth match. More precisely, a loop is performed over the tracker
 1918 hits in order from first sensor to last sensor, and the MCParticle that does not contribute to
 1919 a tracker hit first in this loop is no longer considered for the truth match.

1920 If there is still a tie, the higher momentum MCParticle is considered to be the truth
 1921 match. This last tie breaker is arbitrary and its occurrence is exceedingly rare, if ever.

1922 Once an MCParticle is matched to a track, the quality of the match can be quantified by com-
 1923 puting the purity of the match - which is defined as the ratio of hits the truth-matched MC particle
 1924 contributes to the track to the total number of hits on track (a fraction of 10 for 5-hit tracks and a

¹⁹²⁵ fraction of 12 for 6-hit tracks). The purity of the preselection with layer one requirements of tritrig-
¹⁹²⁶ wab-beam for positrons and electrons is shown in Fig. 4.6. In this sample, about 0.002% of e^+ and
¹⁹²⁷ e^- tracks do not have a MCParticle match to track where the most likely explanation are particles
¹⁹²⁸ with truth information that is not propagated to the reconstruction level. These truth-matched
¹⁹²⁹ tracks are used to study backgrounds due to mistracking in detail.

1930 4.9 Monte Carlo Samples

Sample	Generator	Statistics
RAD	MadGraph5	~2.9M
Tritrig	MadGraph5	~8.0M
WABs	MadGraph4	~32k
A' prompt	MadGraph4	~3.8M
A' displaced	MadGraph4	~56k
Møller	EGS5	~500k
Beam	EGS5	Background

Table 4.4: Event generators and statistics for MC samples.

1931 In order to be confident with the results from the analysis that it is well-understood, realistic
1932 Monte Carlo (MC) samples are run that specifies particular physics processes. Specifically for
1933 the background studies, we are most interested in correctly simulating trident physics processes
1934 and converted bremsstrahlung as well as multiple and single Coulomb scattering of particles in the
1935 tracker. Both prompt and displaced A' s are also simulated for signal kinematics.

1936 For event generation and cross-section computation, the HPS MC chain uses several generators
1937 depending on the specific physics process of interest including EGS5 [Cite EGS5](#) and MadGraph4 [13].
1938 Trident processes, wide-angle bremsstrahlung (wabs), and A' 's are generated using MadGraph4. The
1939 Feynman diagrams are shown in Fig. 4.7. Beam background, Møllers, and scattering in the target
1940 are simulated using EGS5. All prompt processes are passed through EGS5 to properly simulate the
1941 scattering in the target which produces EGS5 final state particles. From EGS5 final state particles,
1942 a package called Stdhep is used in order to persist truth information rotate and difuse the beam,
1943 offset the target, and build beam bunches using a Poisson distribution for beam backgrounds.

1944 The detector response is then simulated using a GEANT4-based package [8] called Slic (Simulator
1945 for the Linear Collider) [45]. The detector response, specifically for the SVT and the Ecal, is
1946 converted into raw hits with time stamps and energy deposition information.

1947 Next, the raw hit information must pass through the readout simulation which emulates that
1948 trigger response including digitization and readout. Finally, the digitization from the readout sim-
1949 ulation is used as input in the physics reconstruction software in hps-java in the same way the real
1950 experimental data is reconstructed. This provides a way for data and simulation to be directly
1951 compared, with MC able to be separated into different background components.

1952 The MC samples produced as shown in Table 4.4 are background samples of RAD, tritrig, WAB,
1953 Møller, and beam background. The A' samples come in two different types - prompt and displaced
1954 from the target. Prompt A' samples are used for the resonance search and for an estimate of the mass
1955 resolution described in Sec. 5.2 (mass resolution is independent of displacement). The displaced
1956 A' 's are used to estimate the z -dependence of efficiency and geometrical acceptance. The detailed

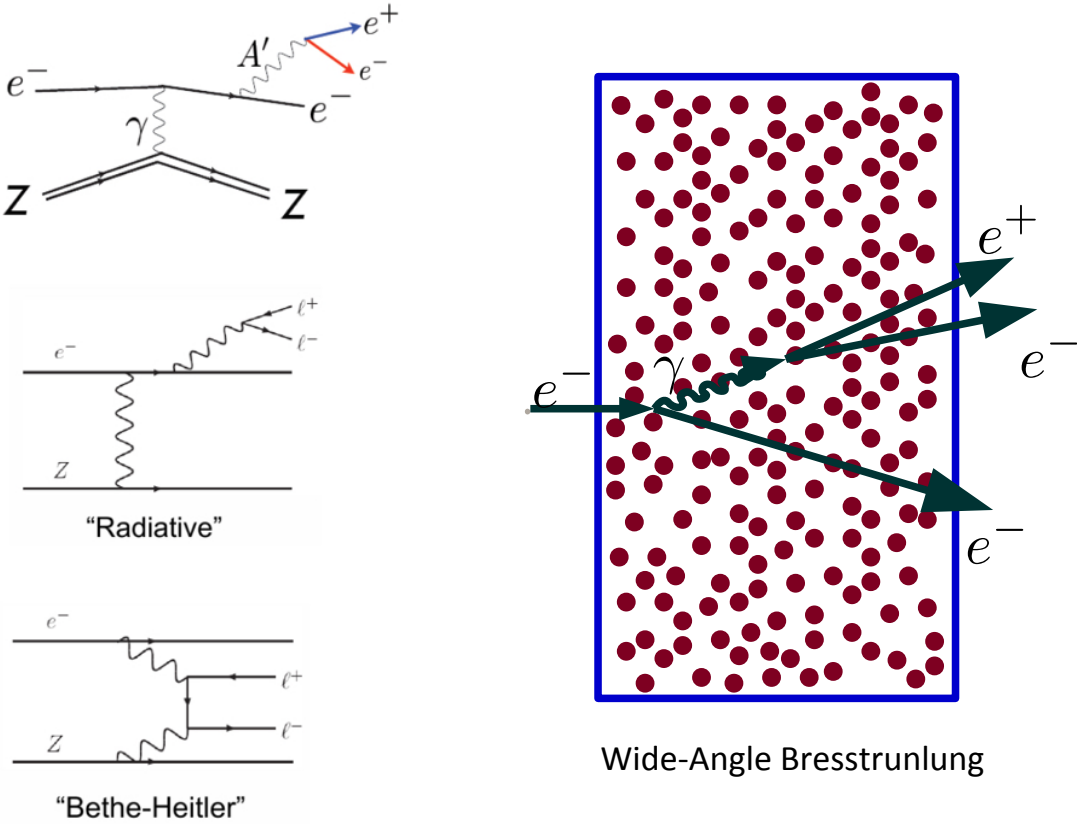


Figure 4.7: Left pictures show Feynman diagrams for A' (top), RAD (middle) and BH (bottom) events. Right picture shows WAB process.

generator level requirements for each MC sample are shown in Table 4.5.

Both prompt and displaced A' samples are generated at specific mass points over the range of interest determined by the acceptance at a specific beam energy, and with close enough spacing such that interpolation of acceptance between mass points contains minimal error. The mass points generated are between 50 MeV and 150 MeV in increments of 5 MeV as well as a high mass point at 175 MeV. The displaced A' samples must populate the decay range of interest ($\sim 0 - 150$ mm) with sufficient statistics. These samples are produced with a constant livetime at $c\tau = 10$ mm, which is a larger decay length than HPS is sensitive to for A' 's, and then reweighted at a later step to reflect actual signal shapes.

Detailed steps on the production of beam particles are as follows:

1. Beam particles are produced in EGS5.
2. Beam rotation, diffusion, and the target offset are all applied via stdhep. Beam particles are

¹⁹⁶⁹ sampled and beam bunches are built in stdhep.

¹⁹⁷⁰ 3. The beam bunches are passed through Slic.

¹⁹⁷¹ Detailed steps on the remaining MC - RAD, tritrig, WAB, Møllers, and A' with beam overlay -
¹⁹⁷² are as follows:

¹⁹⁷³ 1. Particles are produced in MadGraph. The exception is that Møllers are produced in EGS5.

¹⁹⁷⁴ 2. Final state particles from MadGraph are passed through the target via EGS5. Because dis-
¹⁹⁷⁵ placed A' have no interaction with the target, only the recoil electron for these samples is
¹⁹⁷⁶ passed through the target.

¹⁹⁷⁷ 3. Parent particles are added into each event of the EGS5 output.

¹⁹⁷⁸ 4. Beam rotation, diffusion, and the target offset are all applied via stdhep.

¹⁹⁷⁹ 5. The events are passed through Slic.

¹⁹⁸⁰ 6. The output events from Slic are spaced apart by a fixed interval equal to the event window in
¹⁹⁸¹ the trigger system.

Sample	Cut Description	Cut Requirement
RAD	Min energy of daughter particles	$E_{e+} > 50 \text{ MeV}$ and $E_{e-} > 50 \text{ MeV}$
RAD	Min for y -direction of e^+e^- particles	$p_{e+,y}/p_{e+} > 0.005$ and $p_{e-,y}/p_{e-} > 0.005$
RAD	Min total energy of e^+e^- pair	$E_{e+} + E_{e-} > 500 \text{ MeV}$
RAD	Min invariant mass of e^+e^- pair	$m_{e^+e^-} > 10 \text{ MeV}$
Tritrig	Min energy of e^+	$E_{e+} > 100 \text{ MeV}$
Tritrig	Min for y -direction of e^+	$p_{e+,y}/p_{e+} > 0.005$
Tritrig	Min total energy of a e^+e^- pair ²	$E_{e+} + E_{e-} > 1000 \text{ MeV}$
Tritrig	Min invariant mass of a e^+e^- pair ³	$m_{e^+e^-} > 10 \text{ MeV}$
WABs	Min photon energy	$E_\gamma > 400 \text{ MeV}$
WABs	Min for y -direction of e^+e^- particles	$p_{\gamma,y}/p_\gamma > 0.005$
Møller	Min energy of final state particles	$E > 10 \text{ MeV}$
Møller	Min for transverse direction for f.s. particles	$\sqrt{(p_x/p)^2 + (p_y/p)^2} > 0.005$
Beam	Min energy of beam particles	$E_{e-} > 0.005E_{beam}$
Beam	Min for transverse direction for f.s. particles ⁴	$\sqrt{(p_x/p)^2 + (p_y/p)^2} > 0.005$
Photon	Min for y -direction of γ	$p_{\gamma,y}/p_\gamma > 0.004$
Photon	Max for y -direction of γ ⁵	$p_{\gamma,y}/p_\gamma < 0.005$
A' 's Prompt	None	—
A' 's Displaced	None	—

Table 4.5: Basic generator level physics requirements for different physics processes.

- 1982 7. The sample is mixed with the beam sample or a WAB sample if desired.
1983 8. Readout and reconstruction is processed.

1984 Lastly, since the displaced vertex analysis is mostly concerned with a near-zero background region
1985 far beyond the target, the background shapes at the extreme tails of the reconstructed z distributions
1986 must be understood. In order to do this, a sample of tridents overlaid with beam and wabs, with
1987 the trident luminosity equivalent to the luminosity of the dataset, is generated. This gives some
1988 indication of the high z background due to both mistracking and large scatterings in the tracker and
1989 is used as a direct comparison to data in Sec. 5.

1990 In addition a sample of pure tridents with about three times the luminosity in data is used to
1991 further understand the tails of the z distributions due to prompt processes that undergo significant
1992 multiple scattering or single Coulomb scattering and reconstruct far downstream of the target. The
1993 pure trident sample is used for the high luminosity sample because overlaying a sample with beam
1994 is computationally expensive.

Cut Description	Requirement
Trigger	Pair1
Track-cluster match	$\chi^2 < 10$
Cluster Time Difference	$ t_{e^+Cluster} - t_{e^-Cluster} < 1.45$ ns
Track-Cluster Time Difference	$ t_{e^+Track} - t_{e^+Cluster} - \text{offset} < 4$ ns
Track-Cluster Time Difference	$ t_{e^-Track} - t_{e^-Cluster} - \text{offset} < 4$ ns
Beam electron cut	$p(e^-) < 1.75$ GeV
Track Quality	$\chi^2/\text{dof} < 6$
Vertex Quality	$\chi^2_{unc} < 10$
Minimum e^+ Momentum	$p(e^+) > 0.4$ GeV
Minimum e^- Momentum	$p(e^-) > 0.4$ GeV
Maximum Vertex Momentum	$V_{0p} < 2.4$ GeV

Table 4.6: Requirements applied to V_0 after reconstruction as an initial set to study. The time offset for data is 56 ns and the time offset for MC is 43 ns.

1995 4.10 e^+e^- Preselection

1996 After reconstruction, analysis can be performed. The goal of the displaced vertex analysis is to
 1997 search for long-lived A' 's produced in a fixed target that decay to e^+e^- pairs in the range $\sim 1 - 10$
 1998 cm in the lab frame. These rare signal processes must be distinguished from a large number of
 1999 prompt QED tridents, and this search is limited by the vertex resolution of HPS. In this energy
 2000 range, the vertex resolution is dominated by multiple scattering in the tracker, particularly in the
 2001 first layer. In order to perform the search most effectively, a series of analysis cuts are utilized to
 2002 separate the prompt background that reconstructs falsely downstream of the target from true long-
 2003 lived particles. Because the expected relative signal rate is very low, a near-zero background region
 2004 is required to make this search possible. Thus, these cuts aimed to eliminate nearly all background
 2005 in a signal region that is sufficiently downstream of the target without sacrificing too much signal
 2006 efficiency.

2007 This section presents and describes the cuts from the reconstruction quality requirements to the
 2008 quality cuts applied to define kinematic regions used for the background normalization and shape
 2009 corrections evaluation and signal selection optimization. The reconstruction is run on V_0 skims on
 2010 the pass 4 dataset - which have at least one V_0 candidate in the event (at least one e^+e^- pair in
 2011 opposite halves of the detector). The cut flow is separated into three parts - reconstruction selection
 2012 (shown in Table 4.2 and Table 4.3), preselection, and tight selection (described in Chp. 5) - each
 2013 successive part contains stricter requirements to further eliminate backgrounds.

2014 The physics trigger used by HPS was tuned to accept time coincident e^+e^- pairs, where the
 2015 and e^- reside in opposite detector volumes. Therefore, as an initial requirement, the Ecal clusters
 2016 associated with the e^+ and e^- are required to be in opposite halves of the detector, i.e. have a y

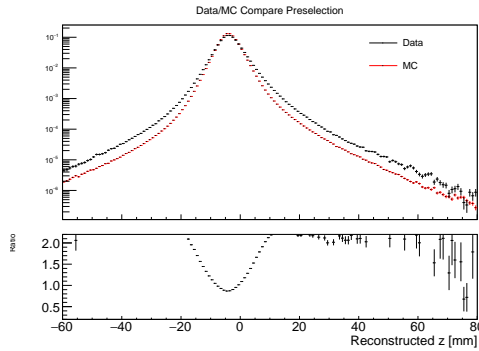


Figure 4.8: Comparison of 10% Data and tritrig-wab-beam for preselected events.

²⁰¹⁷ position which satisfies the following relation:

$$y_{Cluster} \times y_{e^-Cluster} < 0. \quad (4.6)$$

²⁰¹⁸ In addition, several loose cuts are required at the reconstruction stage, the so-called MOUSE
²⁰¹⁹ cuts which are shown in Table 4.2 for data and Table 4.3 for MC. Since this analysis only considers
²⁰²⁰ pairs formed using tracks that are matched to Ecal clusters, a loose cut is placed on the track-cluster
²⁰²¹ matching χ^2 to guard against the case where a track is grossly mismatched to an Ecal cluster. To
²⁰²² further reduce those events, a loose cut is placed on the time difference between e^+e^- clusters and
²⁰²³ the time difference between the track and the matched cluster to eliminate out of time events. In
²⁰²⁴ addition, we require a loose track quality. Finally, we place a loose cut on the maximum electron
²⁰²⁵ momentum to further reduce elastically scattered electrons in the target and on the maximum V0
²⁰²⁶ momentum. Each of these MOUSE cuts - cluster-track time difference, cluster time difference, track-
²⁰²⁷ cluster matching, electron momentum, track quality, and momentum V0 cut - will have a tighter
²⁰²⁸ cut at the Preselection stage.

Cut Description	Requirement
Trigger	Pair1
Track-cluster match	$\chi^2 < 10$
Cluster Time Difference	$ t_{e+Cluster} - t_{e-Cluster} < 1.45 \text{ ns}$
Track-Cluster Time Difference	$ t_{e+Track} - t_{e+Cluster} - \text{offset} < 4 \text{ ns}$
Track-Cluster Time Difference	$ t_{e-Track} - t_{e-Cluster} - \text{offset} < 4 \text{ ns}$
Beam electron cut	$p(e^-) < 1.75 \text{ GeV}$
Track Quality	$\chi^2/\text{dof} < 6$
Vertex Quality	$\chi^2_{unc} < 10$
Minimum e^+ Momentum	$p(e^+) > 0.4 \text{ GeV}$
Minimum e^- Momentum	$p(e^-) > 0.4 \text{ GeV}$
Maximum Vertex Momentum	$V_{0p} < 2.4 \text{ GeV}$

Table 4.7: Requirements applied to V_0 after reconstruction as an initial set to study. The time offset for data is 56 ns and the time offset for MC is 43 ns.

2029 The vertices contained in the events that pass the trigger requirement are selected by a set of
 2030 cuts, tighter with respect to the reconstruction quality cuts but still loose enough to select signal-like
 2031 higher-quality vertices with large statistics. This set of cuts is referred to as *Preselection*. Preselected
 2032 events are used as a way to study trident rates and as a way to study the need for tighter cuts
 2033 (described in the next section). At this stage only vertices reconstructed by an unconstrained fit
 2034 are considered. In general, the preselection cuts have shown to be effective in the past or are shared
 2035 with the resonance search, thus further study is unnecessary. The selection starts by requiring that
 2036 the distance between the tracks and the matched electromagnetic clusters is lower than 10σ , where
 2037 σ is the error associated to the cluster position as reported in ?? [PF::Refer to Sebou's/Holly's thesis to make a reference to this number](#). This is shown in Fig. 4.12. The time difference between the
 2038 calorimeter clusters matched to SVT tracks and where they are in opposite top and bottom volumes
 2039 is required to be less than 1.45 ns (the Hall B bunches are separated by 2 ns). This cut aims to reduce
 2040 the contamination due to accidentals to less than 1% [PF::Cite Old BH analysis](#), and is studied in
 2041 detail in the current resonance search ([cite current BH](#)). The cluster time difference cut is shown in
 2042 Fig. 4.16.
 2043

2044 In addition, the difference between the track time and the cluster time is required to be less
 2045 than 4 ns. Before applying this cut, the track time distribution is shifted to zero by correcting the
 2046 offset, which is approximately 56 ns in data and 43 ns in MC simulation⁶. The cut is loose enough
 2047 such that is possible to use the same offset correction for each run in data without introducing
 2048 run-by-run systematic effects and also eliminates e^+e^- pairs where one of the tracks is mismatched
 2049 to the corresponding cluster. This is the same cut value for cluster-track time difference that was

⁶The discrepancy in for the offset between data and MC can be attributed to the different conditions used. The is also a difference between the offsets in data for MOUSE cuts in Table 4.2 (55 ns) and Preselection cuts in Table 4.7 (56 ns). The correct offset is 56 ns; however, the window of 10 ns used for the MOUSE cuts is significantly wider than the 4 ns in the Preselection.

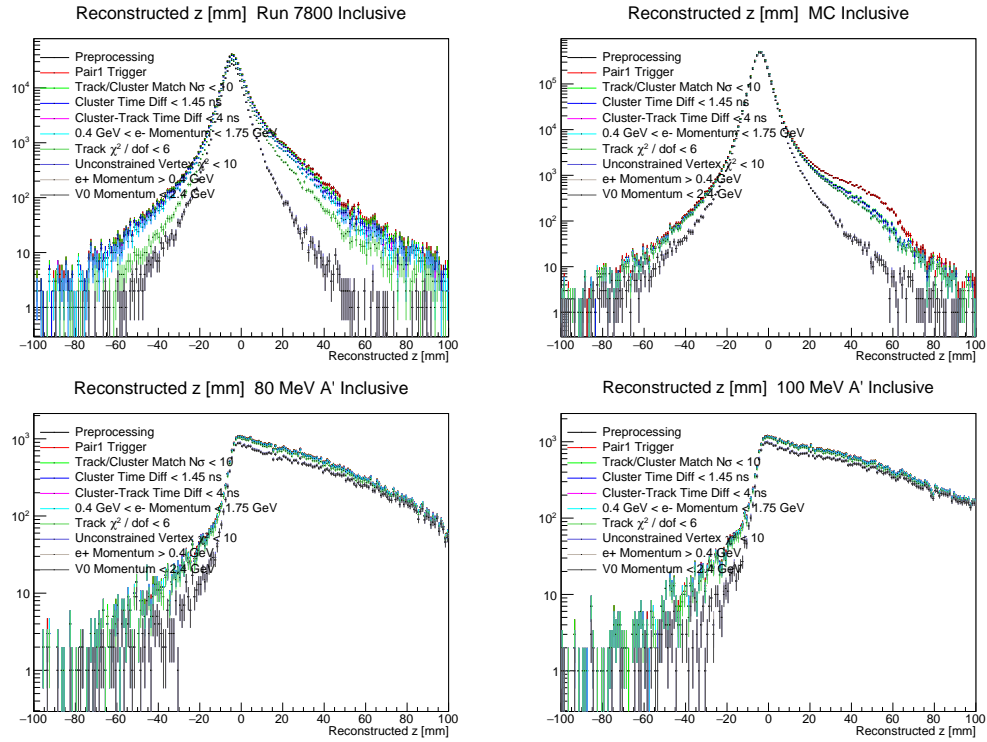


Figure 4.9: Preselection cutflow for as a function of reconstructed z . Top Right: Run 7800 in data. Top Left: a fraction of the tritrig-wab-beam sample. Bottom Left: 80 MeV displaced A' s. Bottom Right: 100 MeV displaced A' s.

used in previous displaced vertexing and resonance search ([cite this](#)) and is shown in Fig. 4.14.

Electrons are required to have a momentum magnitude less than 1.75 GeV in order to remove the contribution from full energy electrons, which are electrons that scatter elastically on the nucleus of the tungsten target [PF::Cite Current BH analysis](#). In addition, loose cuts on the minimum particle momentum at 0.4 GeV, to eliminate low momentum particles which could have large multiple scattering, and maximum V_0 momentum 2.4 GeV (above which no signal is expected) are also shared with the resonance search. The particle momentum cuts are shown in Fig. 4.15 and the maximum V_0 momentum cut is shown in Fig. 4.17.

Poorly fit tracks and vertices can lead to falsely reconstructed vertices downstream of the target. Both tracks are required to have a track quality of χ^2/dof (degrees of freedom) less than 6 which was used for the 2015 Displaced Vertex Search ([cite 2015 vertex search](#)). Each vertex is required to a vertex fit quality on the unconstrained vertex of at least have a $\chi^2_{\text{unc}} < 10$ which is a loose requirement. A summary of the *Preselection* cuts applied to the reconstructed vertices is presented in Table 4.7 while in Table 4.8 the cutflow and the cut efficiency on various samples for MC simulation are shown.

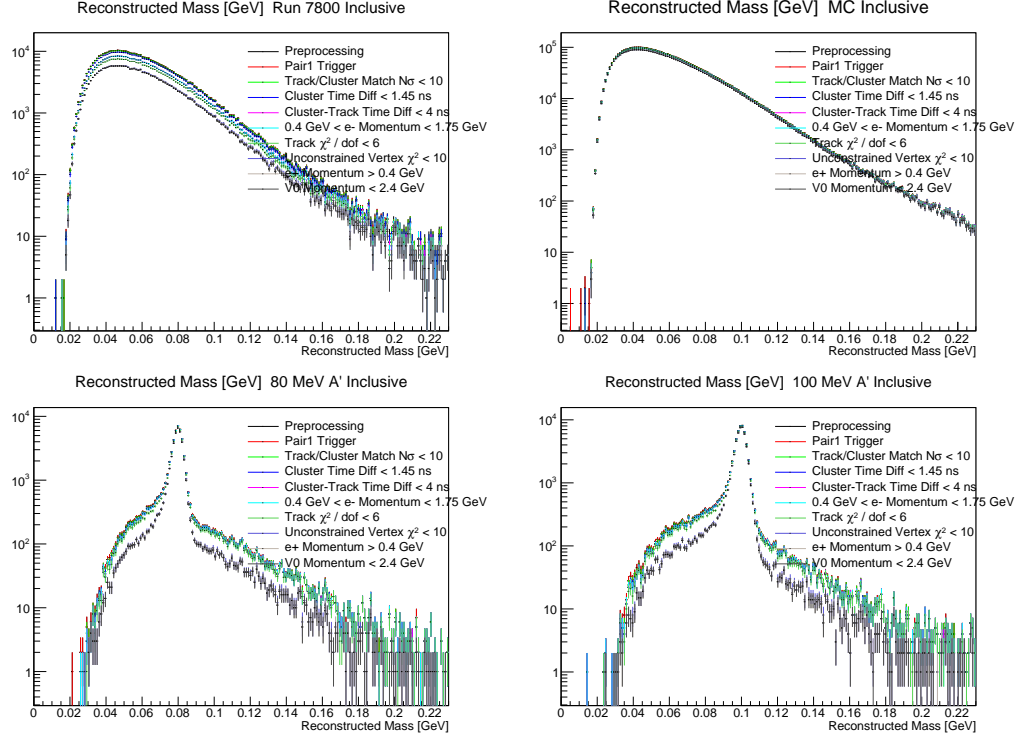


Figure 4.10: Preselection cutflow for reconstructed mass. Top Right: Run 7800 in data. Top Left: a fraction of the tritrig-wab-beam sample. Bottom Left: 80 MeV displaced A' s. Bottom Right: 100 MeV displaced A' s.

	data ϵ_{tot}	tridents ϵ_{tot}	WAB ϵ_{tot}	AP ϵ_{tot}
no-cuts	2.65672e+07	–	8.05260e+06	–
Trigger Pair1	2.65022e+07	0.998	0 0.0	0 0.0
$e^- \Delta_d(trk, clu) < 10\sigma$	2.63041e+07	0.99	7.96627e+06 0.989	31702 0.993 55363 0.989
$e^+ \Delta_d(trk, clu) < 10\sigma$	2.62441e+07	0.988	7.94766e+06 0.987	31473 0.986 55251 0.987
$\Delta_t(clue_-, clue_+) < 2\text{ns}$	2.49811e+07	0.94	7.83282e+06 0.973	31002 0.971 54665 0.977
$e^- \Delta_t(trk, clu) < 4\text{ns}$	2.26414e+07	0.852	7.78389e+06 0.967	30882 0.967 54463 0.973
$e^+ \Delta_t(trk, clu) < 4\text{ns}$	2.15004e+07	0.809	7.7633e+06 0.964	30440 0.954 54293 0.97
$p_e^- < 1.75\text{GeV}$	2.14217e+07	0.806	7.75548e+06 0.963	30379 0.952 54201 0.969
$e^- Track\chi^2 < 6$	2.06244e+07	0.776	7.58028e+06 0.941	29735 0.932 52652 0.941
$e^+ Track\chi^2 < 6$	1.9464e+07	0.733	7.42088e+06 0.922	27139 0.85 50983 0.911
$\chi^2_{unc} < 10$	1.53681e+07	0.578	6.9479e+06 0.863	13226 0.414 42929 0.767
$p_e^- > 0.4\text{GeV}$	1.5204e+07	0.572	6.88443e+06 0.855	13194 0.413 42474 0.759
$p_e^+ > 0.4\text{GeV}$	1.5204e+07	0.572	6.88443e+06 0.855	13194 0.413 42474 0.759
$p_{vtx} < 2.4\text{GeV}$	1.51465e+07	0.57	6.8777e+06 0.854	13128 0.411 42205 0.754

Table 4.8: Table showing the efficiency of each cut on 10% of the 2016 data sample and on MC simulation for tridents, WABs and 80 MeV A' displaced samples. The trident sample contains both Bethe-Heitler and radiative events.

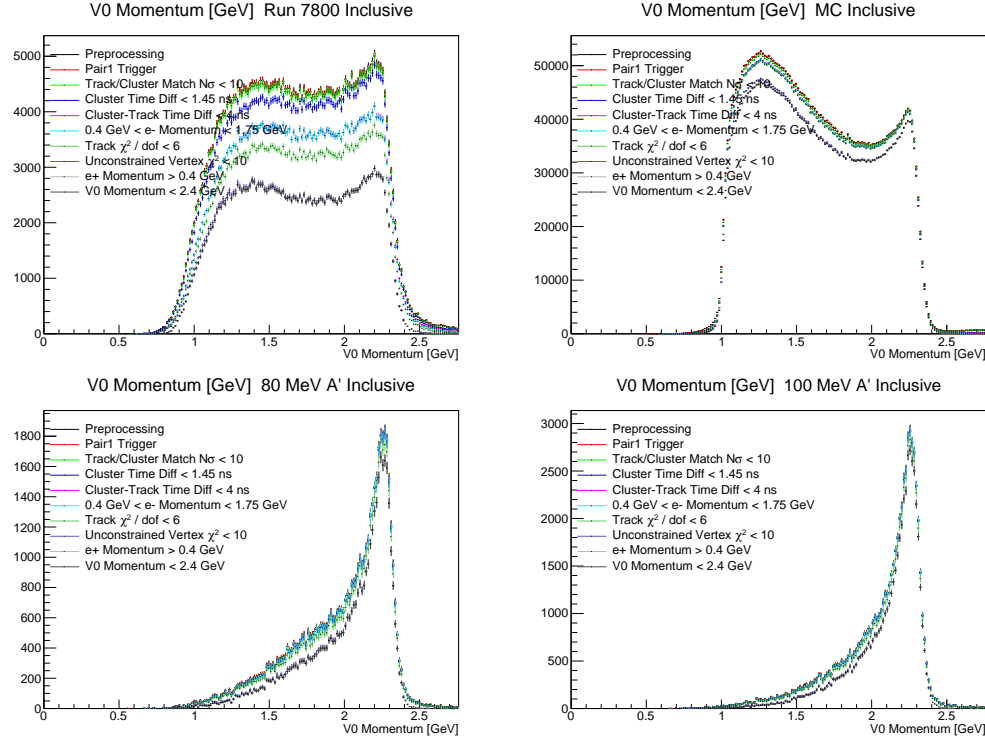


Figure 4.11: Preselection cutflow for as a function of reconstructed V0 momentum. Top Right: Run 7800 in data. Top Left: a fraction of the tritrig-wab-beam sample. Bottom Left: 80 MeV displaced A' s. Bottom Right: 100 MeV displaced A' s.

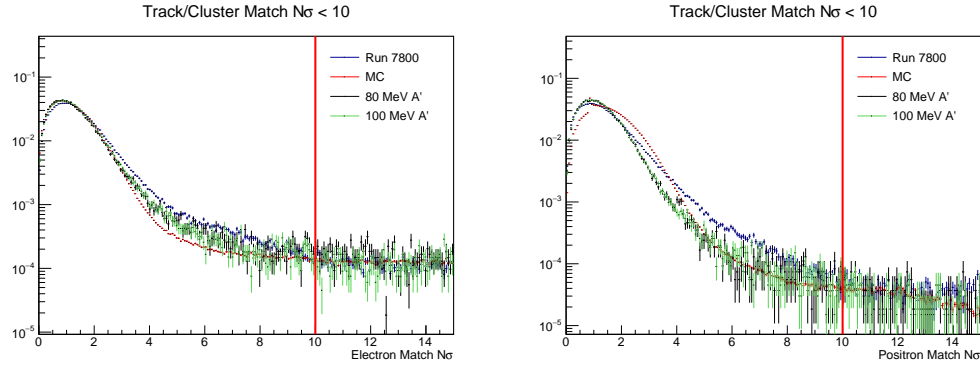


Figure 4.12: Track-cluster match number of σ for electrons (left) and positrons (right). A loose cut is placed at $N\sigma < 10$ for both electrons and positrons to eliminate poor track-cluster matches.

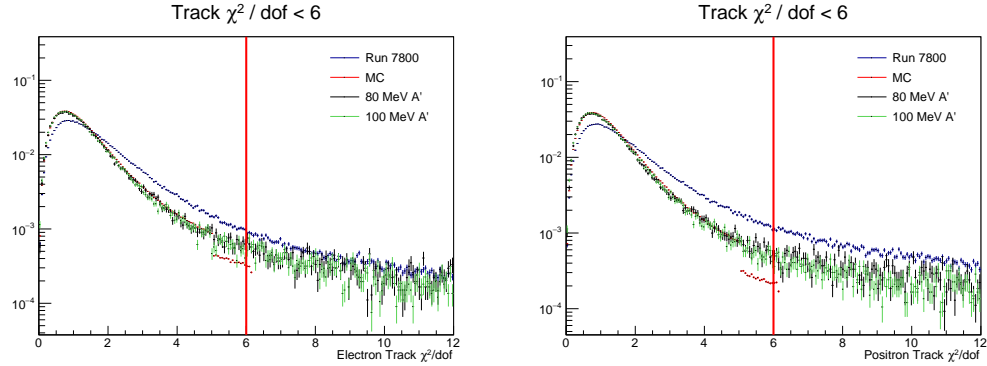


Figure 4.13: Track χ^2 per degrees of freedom (dof) for electrons (left) and positrons (right). A cut is placed at $\chi^2 < 6$ for both electrons and positrons to eliminate poor tracks that can falsely reconstruct downstream of the target.

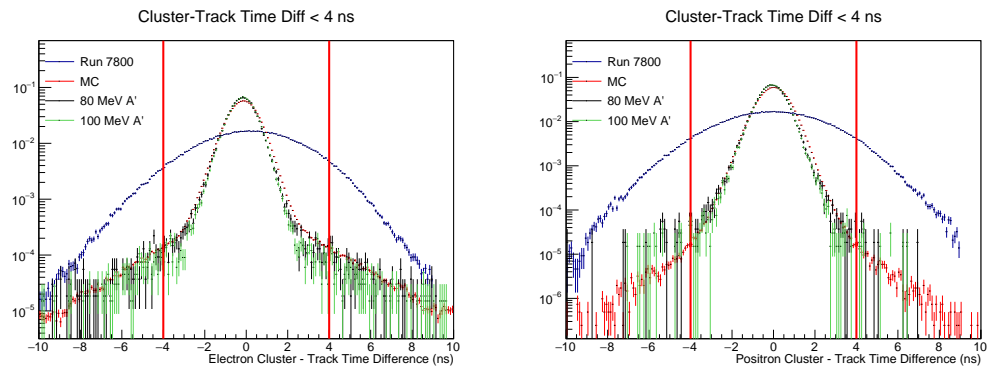


Figure 4.14: Cluster-track time difference (with the time offset from Table 4.7) for electrons (left) and positrons (right). A cut is placed at a time difference of 4 ns for both electrons and positrons to eliminate out of time tracks. There is significant mismodeling for the track time resolution; however, this is a data-driven cut.

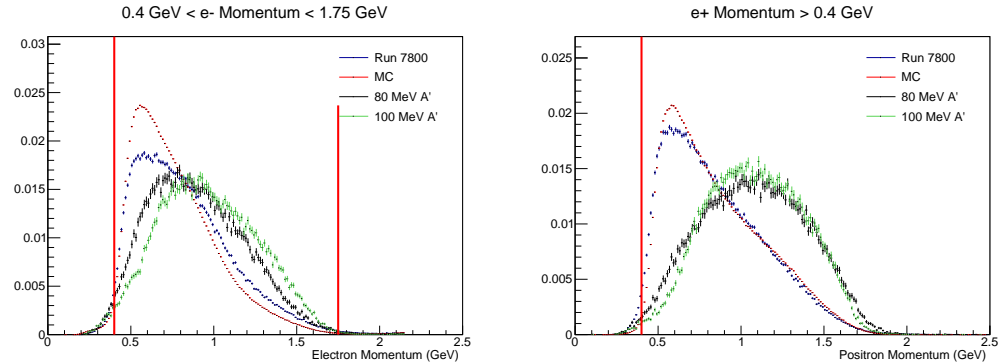


Figure 4.15: Electron momentum (left) and positron momentum (right) both have minimum momentum cuts at 0.4 GeV in order to reduce low momentum particles that have larger multiple scattering. Another maximum momentum cut is placed on electrons only at 1.75 GeV to eliminate V0s that reconstruct with elastically-scatter electrons in the target. There is some mismodeling for individual particle momenta particularly at low momentum.

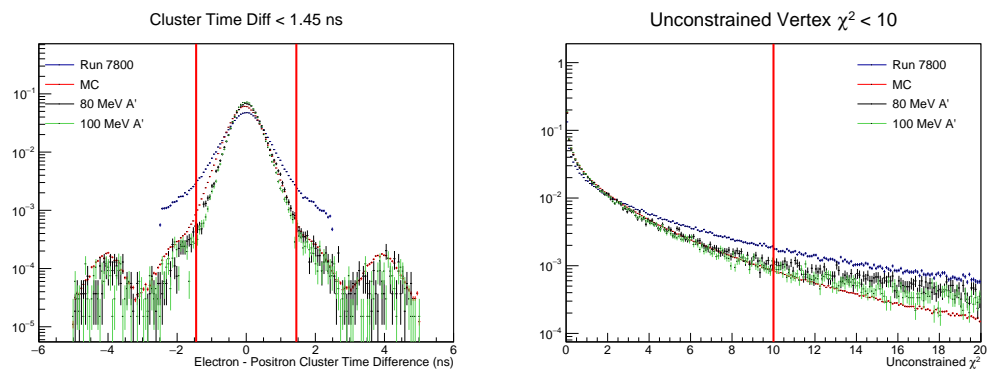


Figure 4.16: Left: A cluster time difference cut between electrons and positrons is placed at 1.45 ns to eliminate accidentals from other beam bunches (Hall B bunches are spaced at 2 ns). Right: A loose cut on the unconstrained vertex fit χ_{unc}^2 is placed at 10 to eliminate poorly reconstructed V0s that can incorrectly reconstruct downstream of the target. There is some mismodeling for the cluster time resolution, and there is some mismodeling in the vertex quality.

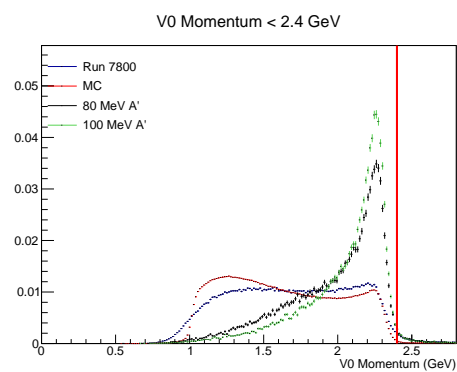


Figure 4.17: A maximum V0 momentum cut is placed at 2.4 GeV since signal is not expected far above the beam energy at 2.3 GeV.

2065 4.11 Composition of the e^+e^- Sample & Normalization

2066 Understanding the normalization of the data is imperative to correctly computing the expected
 2067 number of detectable A 's as a function of mass and ϵ . In addition to the overall rate, a detailed
 2068 understanding of the composition of the e^+e^- pairs, mainly separating by background components
 2069 into as radiative, tridents, and converted WAB processes, are necessary to computing the expected
 2070 A' rate.

2071 **4.11.1 MC Normalization**

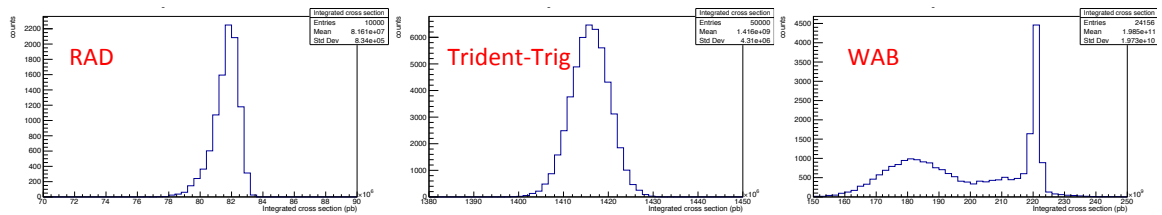


Figure 4.18: Integrated cross section for the RAD (left), Trident-Trig(middle) and WAB(right) samples, separately.

Sample	μ of ICS	σ of ICS	# of good files	# of generated events per file
RAD	81.61 μ b	0.08340 μ b	9940	10k
Trident-Trig	1.416 mb	0.004310 mb	9853	50k
WAB	0.1985 b	0.01973 b	9956	100k

Table 4.9: Normalization parameters for the RAD, Tritrig, and WAB samples

2072 Normalization for MC is computed by using the mean of the integrated cross section for each
 2073 sample produced as shown in Fig. 4.18 and the total number of events generated (Luminosity =
 2074 Events Generated / Mean Integrated Cross-section). The results are shown in Table 4.9 and are
 2075 used to separate the rate of different e^+e^- production processes and as a comparison to the overall
 2076 e^+e^- rate in data.

2077 **4.11.2 Radiative Fraction**

2078 **I think this section needs a little bit more detail.**

2079 A key component to translating the number of signal events to the coupling epsilon is the fraction
 2080 of reconstructed events in our sample, after all selection requirements, that come from radiative
 2081 tridents. This fraction, the so-called radiative fraction, is defined as a function of mass:

$$f_{rad}(m) = \frac{d\sigma_{rad}/dm(m)}{d\sigma_{tri}/dm(m) + d\sigma_{cWAB}/dm(m)} \quad (4.7)$$

2082 While the total number of tridents can be taken from data (from the maximum likelihood fit, as
 2083 a function of mass), the radiative fraction must be computed using Monte Carlo. Therefore it is
 2084 important that we understand the composition of our data sample, namely, the relative contributions
 2085 of trident events to converted WAB (cWAB) events.

2086 The method of determining the radiative fraction is the same as used in the resonance search.
 2087 The actual e^+e^- daughter pairs from the γ^* for the radiative events (i.e. the numerator in the
 2088 radiative fraction) are truth-matched to avoid including events that are falsely reconstructed with
 2089 the recoil electron. The total number of tridents and wabs (i.e. the sum of the expected e^+e^-
 2090 backgrounds) are used in the denominator of the radiative fraction. Since physics does not enable
 2091 us to differentiate between trident events that are reconstructed with the true daughter electron
 2092 as opposed to the recoil electron (even using truth information from MC due to the cross terms
 2093 between the Bethe-Heitler and radiative diagrams), these events cannot be truth-matched and the
 2094 reconstructed mass is used in a mass bin in the denominator.

2095 The two notable differences between the displaced vertex search and the resonance search with
 2096 respect to the radiative fraction are the event selection and the use of unconstrained vertices as
 2097 opposed to target constrained in the resonance search. The selection that is used for the radiative
 2098 fraction for the displaced vertex search are the preselection cuts from Sec. ?? as well as the layer
 2099 2 requirement, and the radiative cut (V0 momentum) is shown in Table 4.10. When deriving the
 2100 expected A' rate, the added complication of the displaced vertex search is the fact that the analysis
 2101 is divided into several mutually exclusive categories based on the first layer with a hit on track, and
 2102 each of these categories has a different selection. The motivation for these specific cuts is to use only
 2103 the cuts that are shared between these categories. The isolation cut, impact parameter cut, and V0
 2104 projection back to the target are applied in a later step.

Cut Description	Requirement
Preselection	-
Layer 2 Requirement	e^+ and e^- have L2 hit
Radiative Cut	$V_{0p} > 1.85$ GeV

Table 4.10: A list of cuts that are used to determine the radiative fraction and the number of e^+e^- events within a mass bin. The cuts are composed of the preselection cuts from Sec. ?? as well as the common cuts shared between L1L1, L1L2, and L2L2.

2105 From these selections, the radiative fraction is computed as the number of truth-matched ra-
 2106 diative tridents in a narrow bin of truth mass divided by the sum of trident and wab process in
 2107 the same narrow bin of reconstructed mass, and normalized by their cross sections, as a function of
 2108 mass as in Eq. 4.7. Both the radiative fraction and differential cross sections of various background
 2109 components and data are shown in Fig. 4.19. The radiative fraction is parametrized using a 5th
 2110 order polynomial.

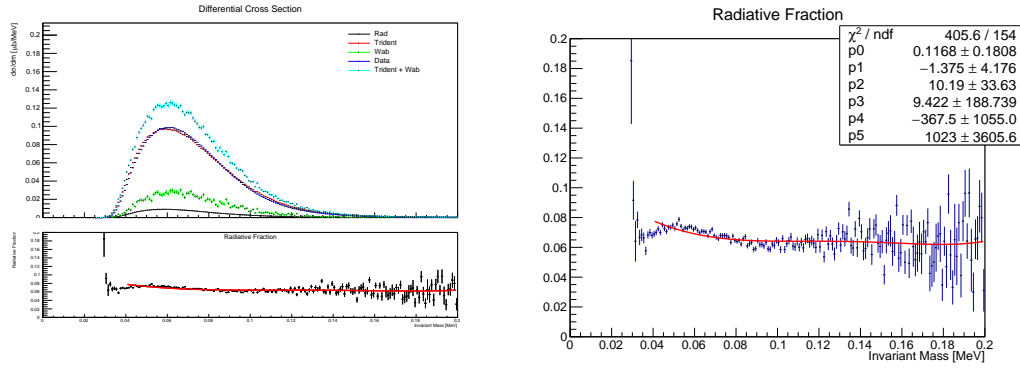


Figure 4.19: Left: The differential cross sections ($d\sigma/dm$) of wab, trident, and radiative trident components from MC as well as the measured cross section from 10% of the data. In principle, one would expect the tridents + wabs (turquoise) to agree with data (blue). The discrepancy is explained in Sec. 4.11.3. Right: The radiative fractions as a function of mass. It is fit to a 5th order polynomial and is used to determine the expected radiative trident rate from the number of e+e- pairs in a mass bin.

$$f_{rad}(m[\text{GeV}]) = 0.1168 - 1.375m + 10.19m^2 + 9.422m^3 - 367.5m^4 - 1023m^5 \quad (4.8)$$

Using the radiative fraction and the number of e+e- pairs in a given mass bin will give the expected number of radiative tridents in that mass bin, the N_{bin} in Eq. 5.20 ($N_{rad}(m) = f_{rad}(m)N_{bin}(m)$). The invariant mass plot using the radiative fraction selection from Table 4.10 using 1 MeV bins which gives the number of e+e- events in that bin is shown in Fig. 4.20. This is parametrized as using an exponential to a 5th order polynomial.

$$N_{bin}(m[\text{GeV}]) = e^{4.903 + 208.3m - 1880m^2 - 1868m^3 + 6.870e4m^4 - 1.980e5m^5} \quad (4.9)$$

Using this equation and the radiative fraction, the expected number of radiative tridents in a given mass bin can be computed. From there, the expected A' production rate at the target, as a function of mass and ϵ can be computed. These A's must then be properly accounted for based on which of the mutually exclusive categories they fall in or if they are eliminated due to hit efficiencies or further cuts. This is discussed in detail in Sec. ??.

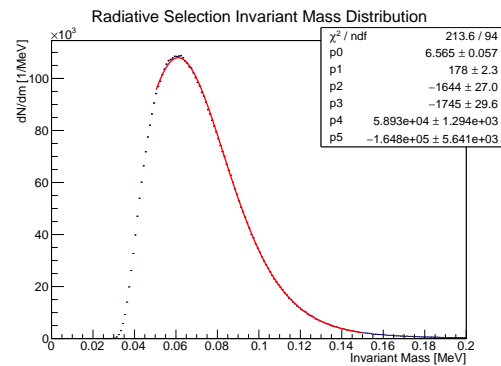


Figure 4.20: The invariant mass for 10% of the data with the radiative cut selection. It is fitted to the an exponential to a 5th order polynomial. This is the number of e+e- pairs in a 1 MeV bin used to normalize the expected radiative trident rate, and hence the expected A' rate.

2121 4.11.3 HPS Rates

2122 A dedicated study of the HPS sample composition and comparison of what we see in a data to our
2123 Monte Carlo was performed and documented in the 2016 sample composition note [?]. The study
2124 looked at both (dominated by WABs) and e^+e^- (both tridents and cWABs) final states. The MC
2125 used for this are summarized in ?? and we used 10% of run 7963 for the data. The selection used
2126 for the composition study were chosen to be (very close to) the same as those used the pre-selection
2127 defined in this note. There were three primary conclusions from this study:

- 2128 • it appears that the MC overestimates the overall rates of all MC samples by ~ 0.80
2129 • the SVT hit inefficiency is underestimated in MC, most importantly in module 1

2130 Figure 4.21 shows the distributions of some kinematic variables for the e^+e^- events from the com-
2131 position study. The events shown in these distributions have the radiative cut but do not require
2132 that the tracks have both L1 and L2 hits. There are a few features in these plots (e.g. skew in track
2133 momentum, some differences in track slope) but generally the agreement between data and MC for
2134 these distributions is quite good. The overall scale difference could have a few sources. While the
2135 MC is generated at a single set of conditions, there is some run-to-run scatter seen in the e^+e^- rates
2136 of order 5%. Also, this MC does not account for data/MC tracking efficiencies which are of the
2137 order of $\sim 10\%$.

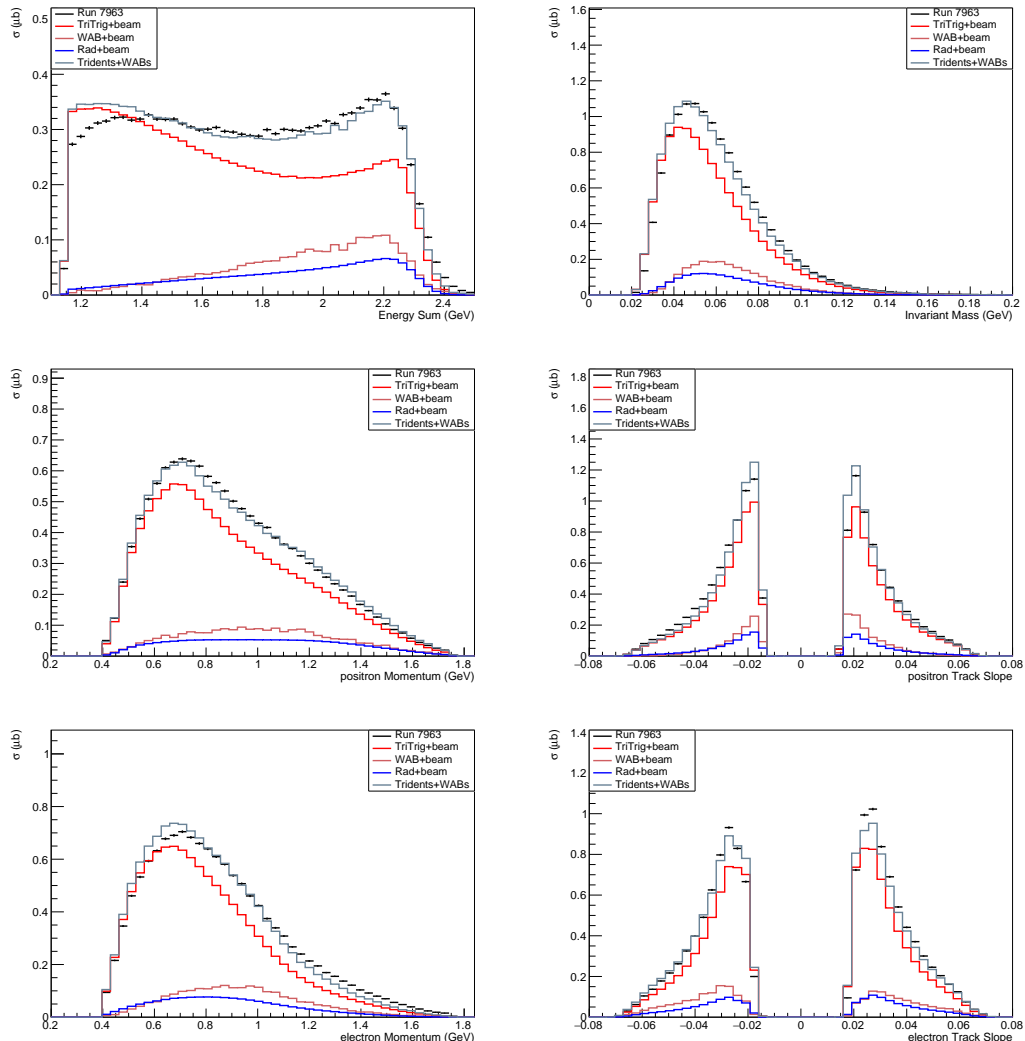


Figure 4.21: Distributions of e^+e^- events with scaling all MC cross-sections by 0.8. Clockwise from top left: positron+electron momentum, e^+e^- invariant mass, positron track slope, electron track slope, electron momentum, positron momentum.

2138 **Chapter 5**

2139 **Search for A' Displaced Vertices**

2140 I copied most of this chapter from the analysis note. It should be checked as a basic outline only. I
2141 was too lazy to put most of the figures in this chapter because I expect them to change.

2142 As stated previously, the basic premise of the displaced vertex search is to search for long-lived
2143 A 's that reconstruct far enough away from the target to distinguish from prompt processes. The
2144 expected rate of A 's is on the order of $\sim 10^{-7} - 10^{-8}$ relative to the large prompt trident background
2145 rate requiring a search in a near-0 background region.

2146 Since the expected decay shape is exponential, a larger signal region closer to the target dra-
2147 matically improves the expected number of detectable A 's. Thus, the effectiveness of the search is
2148 limited by the detector vertex resolution, which itself is limited by multiple scattering of particles
2149 in the tracker (particularly layer 1 of the SVT). There are key differences, both kinematically and
2150 with features of the tracks and vertices, between the signature of an A' and prompt backgrounds
2151 that falsely reconstruct downstream of the target. These features can be exploited to effectively
2152 distinguish between signal and background and are described in the sections that follow.

2153 After utilizing these distinguishing features, the remaining prompt background can be character-
2154 ized in such a way that the expected background at a given z position downstream of the target can
2155 be predicted. This can be used to define a z -value that delineates a region downstream of which a
2156 near-0 background is expected. This value is denoted as z_{cut} and the signal region is defined as the
2157 reconstructed $z > z_{cut}$. Even though a near-0 background region is defined, it is often the case that
2158 much larger backgrounds appear in these regions than predicted by the background characterization
2159 in both data and MC. These events are call “high z events” and their study is important to the
2160 current and future success of this type of search. These high z backgrounds must be understood
2161 and mitigated by orders of magnitude in order to see a signal.

2162 The proceeding sections describe a summary of the results from the 2015 Engineering Run,
2163 the details of analysis cuts used to distinguish between signal and background, a procedure of
2164 determining z_{cut} and the signal region, the final results of the 2016 Engineering Run, and a detailed

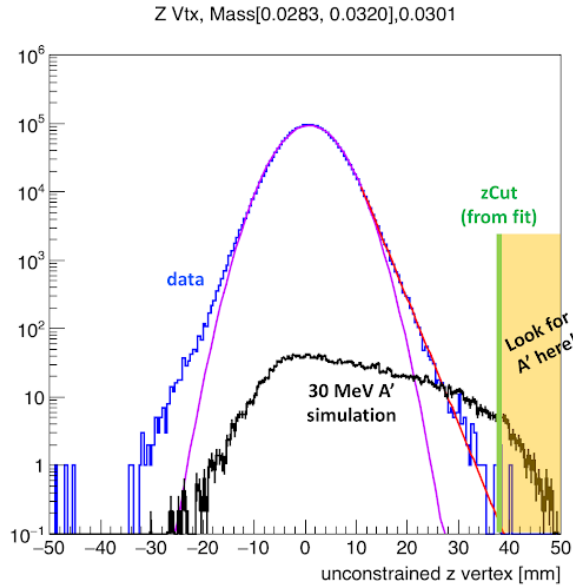


Figure 5.1: Mass slice from 2015 Replace this with the 2016 mass slice.

2165 discussion on high z events in both data and MC.

2166 5.1 Previous Results from 2015 Engineering Run

2167 The first displaced vertex search for A' 's on HPS was performed on the 2015 Engineering Run (Cite
2168 Sho, Holly, and ICHEP proceedings). As previously described, events were selected to eliminate
2169 prompt backgrounds that reconstruct downstream from the target where signal is expected, and the
2170 final event selection that was used in this analysis is shown in Fig. 5.2.

2171 The final results of this analysis consist of estimating the expected number of signal events in
2172 the signal region and setting a limit on the A' model. The maximum number of expected A' events
2173 is 0.1 events at 40 MeV and $\epsilon^2 = 10^{-9}$ (insert correct numbers here). Unfortunately, this signal
2174 expectation is insufficient to set a limit on the canonical A' model. However, the best limit is at
2175 50 MeV and $\epsilon^2 = 10^{-9}$ (insert correct numbers here) in which an A' -like model with 36 times the
2176 cross-section is excluded with 90% confidence at this point in parameter space.¹ Though there is
2177 no known motivation for such a model, this provides an estimate for expected sensitivity for future
2178 runs. These final results are shown in Fig. 5.3.

2179 Even though the displaced vertex search from the 2015 Engineering Run did not provide a
2180 physically meaningful result, it provided essential information about backgrounds, particular those

¹One may be tempted to interpret this result as a simple scaling in luminosity. However, scaling luminosity also changes the signal region such that the expected A' rate does not scale linearly. The exclusion of the A' model times a certain factor of the cross-section is the better interpretation of this exclusion.

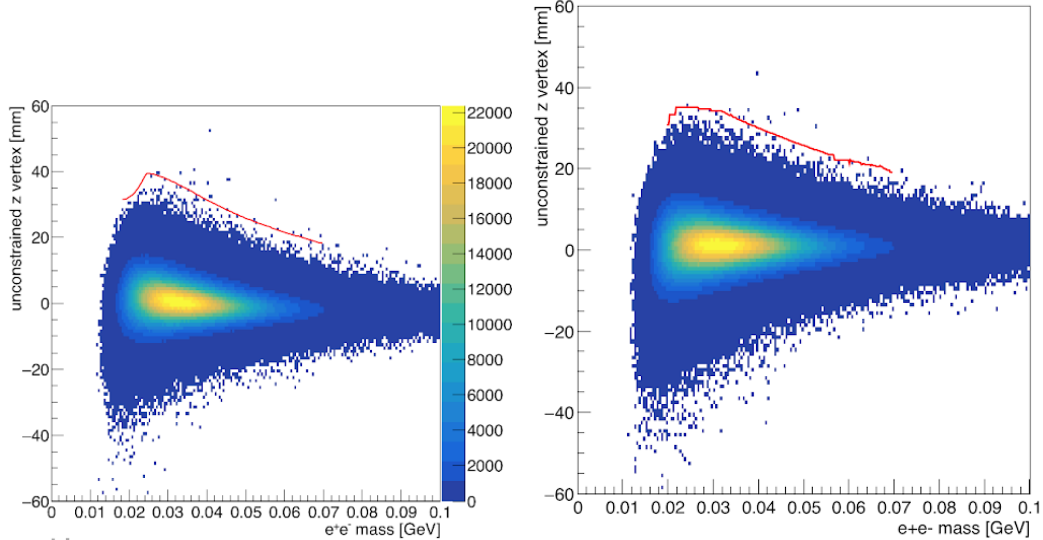


Figure 5.2: Final event selection for the displaced vertex search in the 2015 Engineering Run for Left: Data and Right: a luminosity-equivalent tritrig-wab-beam MC sample. The z_{cut} is shown in red.

at high z . Through a detailed analysis of both the full dataset and in MC at truth level, it was determined that there were two main sources of high z events. The first are due to large scatters in layer 1 of the tracker in which both e^+e^- particles each have a large scatter away from the beam plane. This can either be a result of multiple Coulomb scattering, which dominates the cores and tails of the distribution, or from single Coulomb scattering which has an even longer tail. This process can reconstruct a vertex far downstream from the target with a small error, and though most of these can be mitigated, a few of these processes are indistinguishable from a true displaced signal. Coulomb scattering in the first layer of the tracker remains the fundamental limit of the experiment.

The second main source of high z backgrounds are due to mis-tracking in which the tracking algorithms pick up an incorrect hit in layer 1, usually from a scattered beam particle, which pulls the vertex downstream. This situation is usually accompanied by a large scatter away from the beam plane in the other particle (even though it is tracked correctly) which results in a vertex reconstruction even further downstream. A schematic of these two backgrounds is shown in Fig. 5.4. The knowledge obtained from this dataset was used to further improve the displaced vertex analysis for the 2016 Engineering Run.

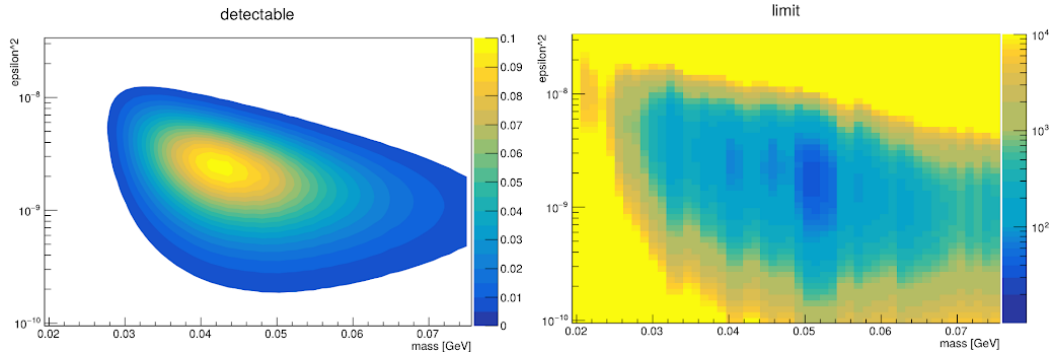


Figure 5.3: Final results for the displaced vertex search for the 2015 Engineering Run. Left: The number of expected A' events after all analysis cuts and z_{cut} as a function of mass and ϵ^2 . Right: The limit on the A' cross section as a function of mass and ϵ^2 . **State the minimum and maximum values.**

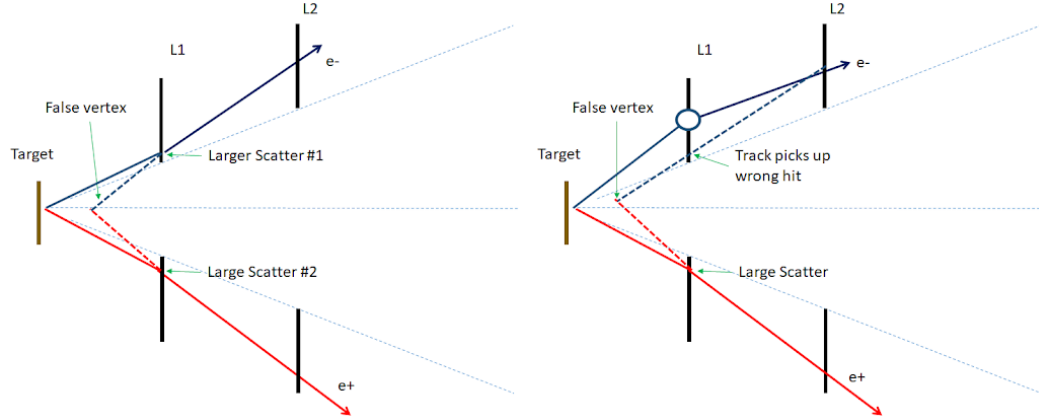


Figure 5.4: From detailed MC studies, it was shown that the backgrounds are due to two main processes. We seek to further mitigate these backgrounds in the 2016 Engineering Run. Left: A vertex is falsely reconstructed downstream of the target due to two large scatters of the e^+e^- pairs away from the beam plane. Right: A vertex is falsely reconstructed downstream of the target due to a track picking up the incorrect layer 1 hit (mis-tracking). These events are usually accompanied by a large scatter in the other particle that is tracked correctly.

5.2 Mass Resolution

The displaced vertex search will be performed in bins of reconstructed mass for a given A' mass hypothesis. In order to accurately estimate the expected A' yield in a given mass bin, it is important to have an accurate estimate of the mass resolution as a function of mass in order to compute the amount of signal lost by searching in a finite mass window. The uncertainty of the mass resolution is a source of systematic uncertainty and is described in Sec. 5.13.

In order to provide a standard mass point directly from data, the known mass of scattered e^-e^- Møller pairs are used. However, unfortunately, comparing the mass resolution for Møllers between data and MC shows dramatically difference results. This can be attributed to the discrepancy in the momentum resolutions. In order to account for this, the momentum of the tracks is smeared and the mass resolution is re-scaled. Lastly, the mass resolution is shown to be independent of decay length, thus the mass resolution for a given A' mass can be kept constant. More details on the mass resolution are shown in the 2016 Resonance Search note ([cite BH note](#)).

5.2.1 Møller Event Selection

Møllers, that is elastically-scattered e^-e^- pairs, provide a convenient standard mass point for HPS. The invariant mass of Møllers is a function of beam energy and can be computed from the total energy in the center of mass frame at a beam energy of 2.3 GeV.

$$M(e^-e^+) = \sqrt{S_{\text{cm}}} = \sqrt{2m_{e^-}^2 + 2E_{\text{beam}}m_{e^-}} \approx \sqrt{2E_{\text{beam}}m_{e^-}} = 48.498 \text{ MeV} \quad (5.1)$$

The Møller event selection is shared with the resonance search and more details are discussed in the analysis note ([cite BH note](#)). Similar to how V0 candidates are constrained differently between the resonance search and the displaced vertex search, the main difference for the vertex formed by electron pairs is the target constraint for the resonance search and unconstrained for the displaced vertex search.

The basic selections involve selecting on e^-e^- pairs in opposite detector volumes within a small time window and in a fiducial region of the Ecal. These selections reduce the backgrounds due to out of time electrons and elastically-scattered electrons off a target nuclei. However, the moller mass is on the edge of the HPS acceptance at a beam energy of 2.3 GeV such that it is rare for both electrons to fall within the acceptance of the Ecal (although one electron must interact with the Ecal for the trigger). Despite this, both electrons can be within the tracker acceptance since the tracker acceptance still covers the acceptance over the so-called Ecal hole (where the other electron usually ends up).

Thus, the Møller event selection must be track-based using both the track times and the extrapolation of the track to the face of the Ecal. Both of the track extrapolation resolution and timing resolutions are difference between data and MC, thus a different set of cuts is utilized between the

Cut Description	Requirement
Time Difference Min	$\Delta t > -2.94$ ns
Time Difference Max	$\Delta t < 1.69$ ns
P_{sum} Min	$P_{sum} > 2.0$ GeV
P_{sum} Max	$P_{sum} < 2.45$ GeV
Δx_{top} Min	$\Delta x_{top} > -4.72$ mm
Δx_{top} Max	$\Delta x_{top} < 6.15$ mm
Δx_{bot} Min	$\Delta x_{bot} > -7.51$ mm
Δx_{bot} Max	$\Delta x_{bot} < 2.98$ mm

Table 5.1: Møller event selection for data on e^-e^- pairs. Since electron tracks are not required to match to Ecal clusters, the time difference is between track times and position differences are based on track extrapolations to the Ecal.

Cut Description	Requirement
Time Difference Min	$\Delta t > -1.44$ ns
Time Difference Max	$\Delta t < 1.54$ ns
P_{sum} Min	$P_{sum} > 2.15$ GeV
P_{sum} Max	$P_{sum} < 2.42$ GeV
Δx_{top} Min	$\Delta x_{top} > -4.89$ mm
Δx_{top} Max	$\Delta x_{top} < 4.82$ mm
Δx_{bot} Min	$\Delta x_{bot} > -4.98$ mm
Δx_{bot} Max	$\Delta x_{bot} < 4.52$ mm

Table 5.2: Møller event selection for MC on e^-e^- pairs. Since electron tracks are not required to match to Ecal clusters, the time difference is between track times and position differences are based on track extrapolations to the Ecal.

2230 two. The Møller event selection for data is summarized in Table 5.1 and for MC is summarized
 2231 in Table 5.2. The Møller mass resolution for data, MC, and MC with track momentum smearing
 2232 (described in the next section) using the unconstrained e^-e^- vertex is shown in Fig. 5.5.

5.2.2 Mass Resolution

As stated previously, there is a discrepancy in the Møller mass resolution between data and MC that can be attributed to the difference in momentum resolution of individual tracks. To approximate the effect of a momentum resolution difference on the mass resolution, a small-angle approximation for the opening angle can be used. The invariant mass and mass resolution is given by

$$m \sim \frac{1}{\sqrt{2}}\theta\sqrt{p_{e^+}p_{e^-}} \quad (5.2)$$

$$\sigma_m = \frac{1}{\sqrt{2}}\left(\theta\frac{\sqrt{p_{e^+}p_{e^-}}}{2}\left(\frac{\sigma_{p_{e^+}}}{p_{e^+}} + \frac{\sigma_{p_{e^-}}}{p_{e^-}}\right) + \sigma_\theta\sqrt{p_{e^+}p_{e^-}}\right) \quad (5.3)$$

From equation 5.3, it can be seen that a 20 % increase in momentum resolution results in an increase in the mass resolution of $\sim 20\%$, which would largely account for the mass resolution discrepancy.

In order to account for this, a smearing technique on the track momentum is utilized and the mass resolution is re-scaled. The detail method is described in the resonance search analysis note [cite bump hunt](#). [Add more detail on momentum smearing](#).

An example of a 100 MeV displaced A' in the L1L1 category comparing the MC with and without momentum smearing as well as the decay length dependence is shown in Fig. 5.6. An example of a 100 MeV displaced A' in the L1L2 category comparing the MC with and without momentum smearing as well as the decay length dependence is shown in Fig. 5.7. In general, there is very little dependence of the mass resolution on the decay length. This is because the precision of the momentum measurement, and hence the mass resolution, is a result of the back layers of the SVT where the curvature of charged particles can be more precisely measured. Thus, mass resolution is general a function of the number of layers hit, not of the decay position or which layer the particles hit first.

Because of this, the prompt A' s can be used which offer an advantage of more statistics particularly at low mass. In addition, for simplicity, the same cuts as the radiative fraction in Table 4.10 with the appropriate layer requirements are used to determine the mass resolution as any further cuts are used to eliminate falsely reconstructed vertices downstream of the target and has little effect on the core.

The mass resolution for both the L1L1 and L1L2 categories comparing MC, MC scaled by the Møller mass resolution in data and MC, and MC with track momentum smearing is shown in Fig. 5.8. [Note that the L1L2 category is not final. What is shown here is the results from the displaced in the L1L2 category. The plan is to still use prompt, but it will be different than L1L1 due to different proportions of 5-hit and 6-hit tracks, and I have to take that proportion into account. I of course have to show this.](#)

Lastly, the mass resolution is parametrized as a function of mass using a straight line fit to the mass resolution with track momentum smearing. This parameterization is used as an input to the

²²⁶⁶ size of the mass search windows. For L1L1, the parametrization is

$$\sigma_m(m) = 0.9348 \text{ MeV} + 0.05442 m - 5.784 \times 10^{-3} \text{ MeV}^{-1} m^2 + 5.852 \times 10^6 \text{ MeV}^{-2} m^3 - 1.724 \times 10^{-8} \text{ MeV}^{-3} m^4 \quad (5.4)$$

²²⁶⁷ and for L1L2, the parametrization is

$$\sigma_m(m) = 0.04906 \text{ MeV} + 0.04694 m \quad (5.5)$$

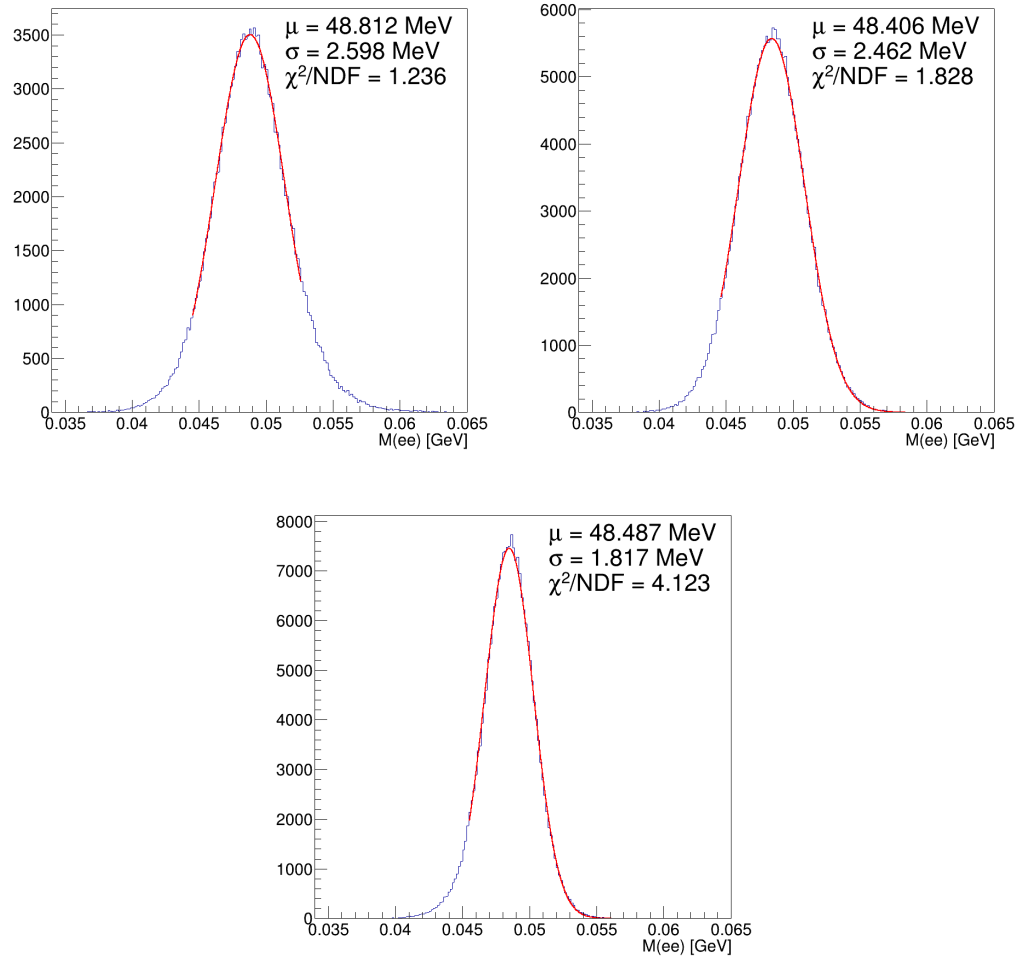


Figure 5.5: Fitted e^-e^- spectrum using the Møller selection for Upper Left: Data, Upper Right: MC with track momentum smearing, and Bottom: Møller MC.

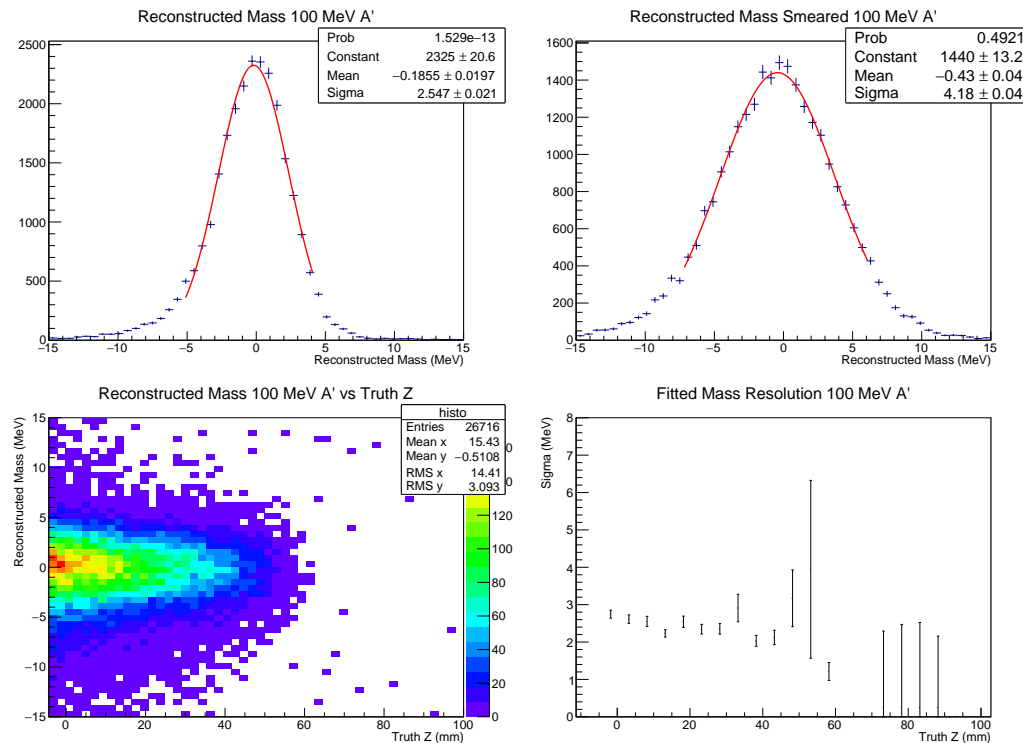


Figure 5.6: Upper Left: Fitted reconstructed mass spectrum for a 100 MeV displaced A' . Upper Right: Fitted reconstructed mass spectrum for a 100 MeV displaced A' with track momentum smearing. Lower Left: Reconstructed mass vs truth z decay for a 100 MeV displaced A' . Lower Right: The fitted mass resolution for 100 MeV displaced A' 's as in slices of truth z . Mass resolution is approximately independent of decay length. These plots are for the L1L1 category.

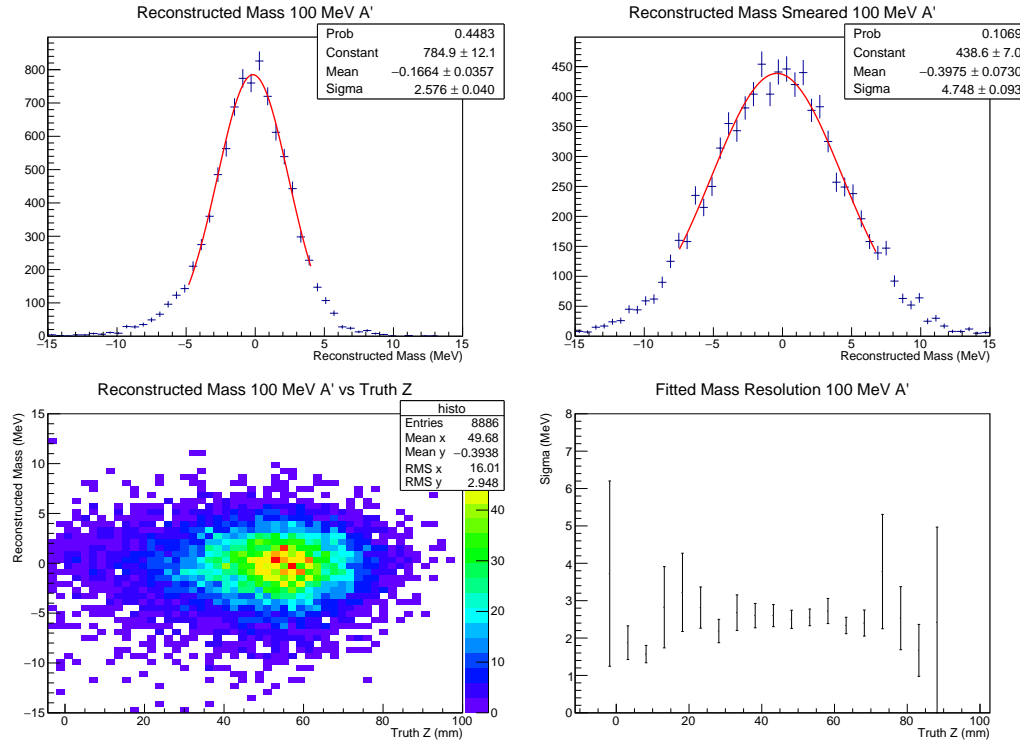


Figure 5.7: Upper Left: Fitted reconstructed mass spectrum for a 100 MeV displaced A' . Upper Right: Fitted reconstructed mass spectrum for a 100 MeV displaced A' with track momentum smearing. Lower Left: Reconstructed mass vs truth z decay for a 100 MeV displaced A' . Lower Right: The fitted mass resolution for 100 MeV displaced A' 's as in slices of truth z . Mass resolution is approximately independent of decay length. These plots are for the L1L2 category.

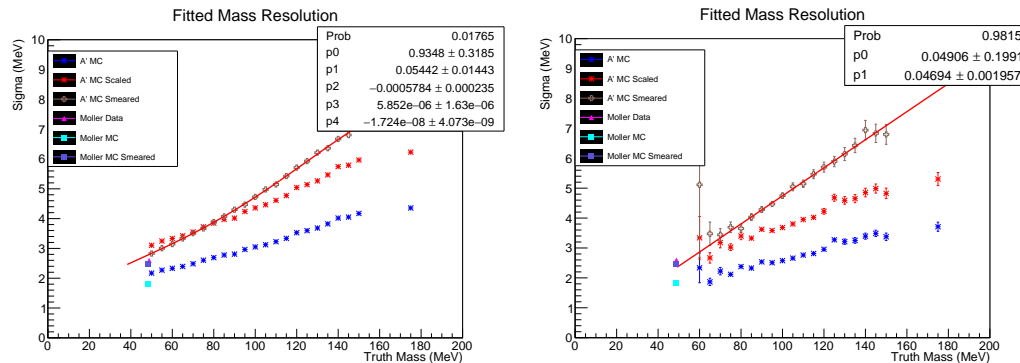


Figure 5.8: A' mass resolution as a function of mass comparing A' MC, A' MC scaled using the ratio of the Møller mass resolution in data to MC, and A' MC with smearing for the Left: L1L1 category and the Right: L1L2 category. The mass resolution is fitted to a straight line to the MC with track momenta smearing and is used as an input to the size of the mass bins in the final results.

2268 5.3 Hit Killing

2269 Finding the expected number of radiative events was shown in Sec. ?? as the product of the radiative
 2270 fraction f_{rad} and the number of e+e- events in a given mass bin N_{bin} . The number of expected A's
 2271 as a function of mass and ϵ can be easily computed by

$$S(m_{A'}, \epsilon) = f_{rad} N_{bin} \frac{3\pi\epsilon^2}{2N_{eff}\alpha} \frac{m_{A'}}{\delta m_{A'}} \quad (5.6)$$

2272 where N_{eff} is the number of possible A' decay channels (1 for the parameter space of interest)
 2273 and $\delta m_{A'}$ is the narrow mass bin width of width 1 MeV. Now that we have the production rate, we
 2274 must do the proper accounting for the fact that the parameter space of interest for the displaced
 2275 vertex search are actually downstream decays.

2276 5.3.1 A' Acceptance Effects

2277 The SVT is designed to have a geometrical acceptance of 15 mrad for prompt decays. However,
 2278 downstream decays must have a larger opening angle to remain in the acceptance of the SVT, and
 2279 the further downstream the decay, the more likely the daughter particles will miss the SVT. Thus,
 2280 the geometrical acceptance drops dramatically with increasing decay length. Based on geometrical
 2281 acceptance, there are several possibilities for a long-lived A'.

- 2282 1. The A' has a finite, but relatively short decay length, and both of the A' daughter particles
 2283 have layer 1 hits. This category is denoted as L1L1 (where the 1's denote the first layer of the
 2284 SVT that the A' daughter particles hit).
- 2285 2. The A' has a slightly longer decay length than the L1L1 category causing exactly one of the
 2286 A' daughter particles to miss layer 1 but hits layer 2, whereas the other particle hits layer 1.
 2287 This category is denoted as L1L2.
- 2288 3. The A' has a longer decay length than the L1L2 category causing both of the A' daughter
 2289 particles to miss layer 1, but both particles have hits in layer 2. This category is denoted as
 2290 L2L2.
- 2291 4. The A' has a relatively long decay length or a small opening angle where at least one of the
 2292 A' daughters misses both layer 1 or layer 2. In these cases, the A' is not reconstructed.

2293 Since we require 5 hit tracks with a 6 layer SVT, these three categories are the only viable
 2294 categories. The product of the geometrical acceptances and efficiencies of these three categories as
 2295 well as their sum is shown in Fig. 5.10. Once the displaced A's are placed in the correct category and
 2296 the geometrical acceptances are properly accounted for, the last steps to do are to properly account
 2297 for hit efficiencies in the SVT, where events can migrate into other categories or be eliminated, and

2298 the remaining event selections (isolation cut, impact parameter cut, and V0 extrapolation to the
2299 target cut) for each of the individual categories. The hit killing method and algorithm are described
2300 in the following subsection in Sec. 5.3.2.

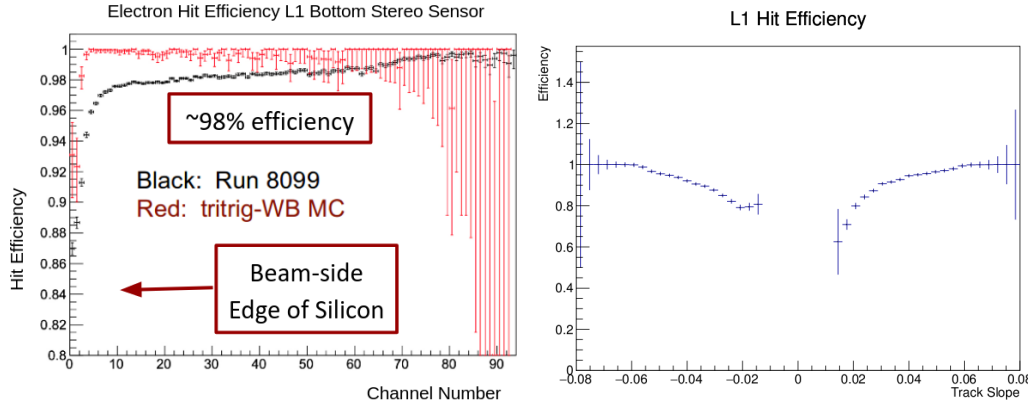


Figure 5.9: Left: The measured SVT layer 1 efficiency for electrons in layer 1 bottom stereo sensor. The MC does not have the correct hit efficiencies. Right: The layer 1 efficiency used for the hit killing algorithm as a function of track slope ($\tan\lambda$).

5.3.2 Hit Killing

The HPS detector has hit efficiency effects, particularly in the first layer of the SVT, that must be accounted for in the A' efficiencies. Hit efficiencies are measured using a track refit to a layer of interest, and an unbiased extrapolation to the layer to see if a hit lies within a certain window. A sample of measured hit efficiency in data in comparison with MC for the layer 1 bottom stereo sensor is shown in Fig. 5.9.

Unfortunately hit efficiencies are not present in the MC, although this is on the future agenda. However, this is an effect that will affect the signal rate, particularly in which of the categories the signal lies in. To account for hit efficiencies in a reasonable way, a post-reconstruction hit killing algorithm is applied as a function of track slope shown in Fig. 5.9. If a track passes the hit killing algorithm, nothing changes. However, if a track fails the hit killing algorithm, the layer 1 hit is removed and the A' can either migrate into another category or be eliminated. Details on what happens to an A' with the hit killing algorithm is as follows:

1. Begin with the L1L1 category. Based on track slope, decide if each positron and electron track pass the electron efficiency cut. There are 4 possible scenarios.
 - (a) If both pass, the event remains in the L1L1 category.
 - (b) If either track fails to pass the cut and has 5 hits on track, the event is removed.
 - (c) If exactly one track fails to pass the cut and has 6 hits on track, the event is moved to the L1L2 category.
 - (d) If both tracks fail to pass the cut and both tracks have 6 hits on track, the event is moved to the L2L2 category.

- 2322 2. Next move to the L1L2 category. For this category, since we are dealing with only one track
2323 with a layer 1 hit, we only consider the track with the layer 1 hit. Again based on track
2324 slope, decide if the positron or electron track passes the hit efficiency cut. There are 3 possible
2325 scenarios.
- 2326 (a) The track with the layer 1 hit passes the hit efficiency cut, it remains in the L1L2 category.
2327 (b) The track with the layer 1 hit fails the hit efficiency cut and has 5 hits on track. This
2328 event is removed.
2329 (c) The track with the layer 1 hit fails the hit efficiency cut and has 6 hits on track. This
2330 event is moved to the L2L2 category.
- 2331 3. Finally, no events are removed from the L2L2 category since only layer 1 efficiencies are
2332 considered and L2L2 events have no layer 1 hit by definition. However, L2L2 gains the additions
2333 from L1L1 and L1L2. As previously explained, L2L2 is not considered for this analysis.
- 2334 4. Lastly for this category, add the events that have migrated from L1L2 from L1L1, and add
2335 the events that have migrated from L1L1 and L1L2 into L2L2.

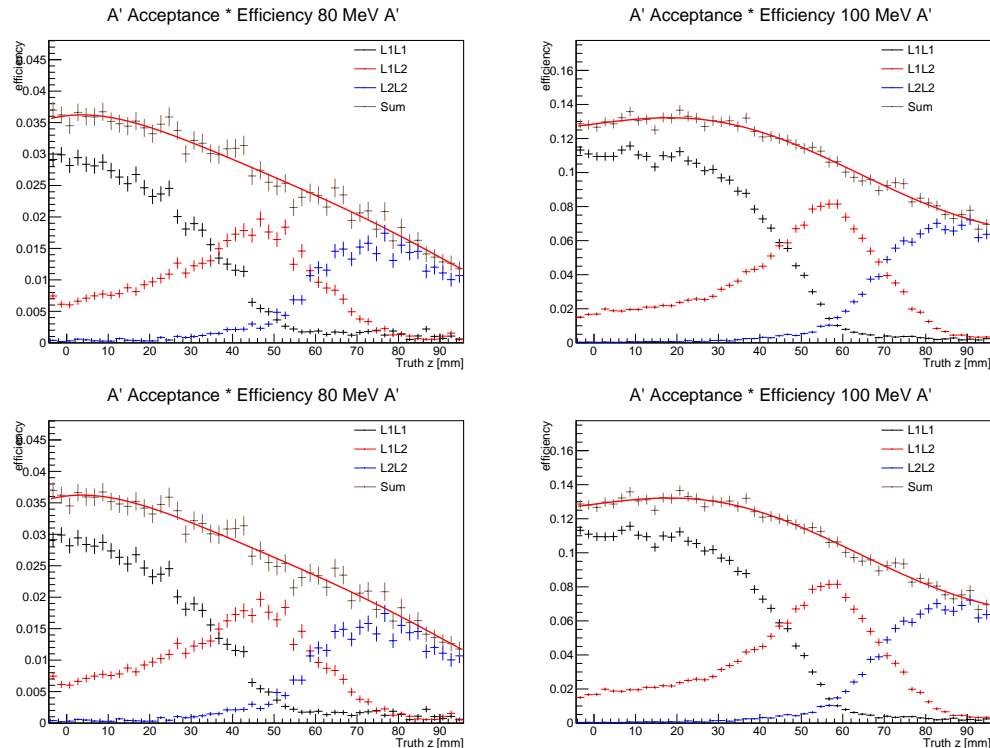


Figure 5.10: The product of geometrical acceptance and efficiency for displaced A' 's for the L1L1, L1L2, and L2L2 categories as well as there sums. 80 MeV displaced A' 's are on the left and 100 MeV displaced A' 's are on the right. The top is before hit killing and the bottom is with hit killing and a fit function fit to the sum of the categories. **The top plots I still have to make, I have the same plots there as the bottom as a placeholder.**

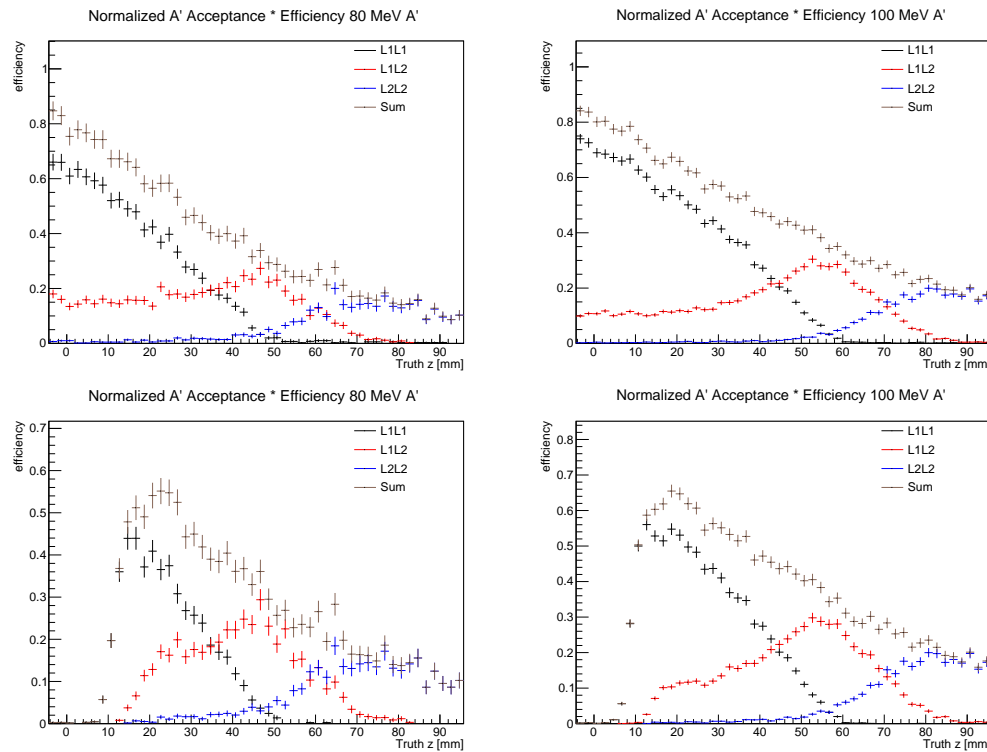


Figure 5.11: The product of geometrical acceptance and efficiency for displaced A' 's for the L1L1, L1L2, and L2L2 categories as well as there sums. These plot are normalized to unity at the target, where the sum is normalized before hit killing and further analysis cuts. 80 MeV displaced A' 's are on the left and 100 MeV displaced A' 's are on the right. The top is without the z_{cut} and the bottom is with the z_{cut} from 10% of the data.

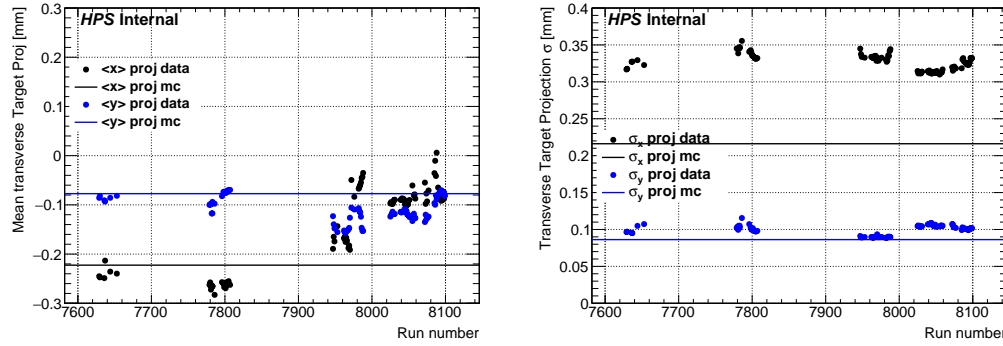


Figure 5.12: The run-dependent mean (left) and width (right) for x and y target projection for the unconstrained vertex in data.

2336 5.4 Vertex Cuts

2337 Normalization is done by the area under the curve.

2338 5.5 L1L1

2339 The goal of the displaced vertexing analysis is to find long-lived A 's beyond a background of prompt
2340 QED tridents. In order to achieve this, tighter cuts must be utilized such that the prompt background
2341 that reconstructs at large z , the so-called “high z background”, is reduced to manageable level such
2342 that A 's can be potentially discovered. Thus, beyond the Preselected events, we must utilize several
2343 more cuts in order to further reduce backgrounds at high z that appear otherwise signal-like.

2344 A majority of the large z backgrounds result from multiple scattering in layer 1 of the tracker
2345 (both the active and dead detector material) or mis-reconstructed tracks. Because of this, there are
2346 a variety of handles that can be utilized to efficiently distinguish between a true displaced signal
2347 and a prompt background. In general, a true displaced signal will have a downstream reconstructed
2348 position with small error, will have a momentum point back to the beam spot, and be composed
2349 of clean tracks with large vertical impact parameters. This is not necessarily true for background.
2350 Thus, cuts on impact parameters, projections of the V0 momentum back to the target, and vertex
2351 quality are utilized. In addition, to guard against high z background due to mistracking the so-called
2352 “isolation cut” is implemented as well as a minimum V0 momentum cut to kinematically separate
2353 A 's from Bethe-Heitler tridents.

2354 These cuts are fairly easy to demonstrate the qualitative effectiveness of reducing background
2355 without sacrificing too much signal efficiency. Unfortunately, the current understanding of the
2356 background shapes and uncertainties in the background model are not known in detail. In order
2357 to tune actual cut values beyond the initial qualitative justification, we must rely on only 10% of
2358 the data, a luminosity-equivalent MC sample of tridents overlaid with simulated beam background

2359 and wabs, and a three times luminosity-equivalent sample of pure tridents. Although these samples
2360 are all informative, this limitation makes it difficult to specify some of the cut values in a rigorous
2361 quantitative manner. For those cuts that can't be demonstrated quantitatively, the number of events
2362 past z_{cut} (as defined in 10% of the data) in each sample as well as signal efficiencies are compared for
2363 a reasonable decision, where the number of events past z_{cut} are scaled to 10% of the data (divided
2364 by 10 for tritrig-wab-beam and divided by 30 for tritrig).



Figure 5.13: Left: Schematic of a relatively short A' decay length in which both daughter particles have a layer 1 hit. Right: Schematic of a relatively long A' decay length in which one of the daughter particles misses layer 1 (but hits layer 2) and the other daughter particle hits layer 1.

2365 L1L1 Layer Requirements

2366 A' 's with a relatively short decay length will have layer 1 hits for both daughter particles, while A' 's
 2367 with longer decay lengths may have one or both of these particles miss layer 1 due to geometrical
 2368 acceptance as shown in Fig. 5.13. For prompt background, even though SVT is designed to
 2369 maintain the same acceptance in all layers at 15 mrad, several “real world” effects cause particles
 2370 to sometimes miss a layer in the detector. First, hit efficiencies in layer 1 may cause particles to
 2371 miss layer one even though the particle traverses the active sensor plane. In addition, daughter
 2372 particles (or photon conversions) can interact with the dead material in layer 1 and force the
 2373 particle to scatter into the acceptance of the detector. These effects are shown in Fig. 5.14.
 2374 Thus, the analysis is divided into several mutually exclusive categories based on the first hits on
 2375 track of the two daughter particles. If both particles have a layer 1 hit, the event is placed in the
 2376 so-called L1L1 category. If exactly one particle hits layer 1 and the other particle misses layer 1,
 2377 the event is placed in the L1L2 category. If both particles miss layer 1, event is placed in the L2L2
 2378 category. These are the only three categories since tracking algorithms require 5 hit tracks in a 6
 2379 layer detector. For the purposes of this analysis, only the L1L1 and L1L2 categories are used since
 2380 the probability of even further downstream decays drops exponentially such that the L2L2
 2381 category adds very little significance to the analysis.
 2382 Performing the analysis on these categories separately instead of together is done for several
 2383 reasons. First, the vertex resolution is highly dependent on which layer is hit first. The closer the
 2384 first hit to the target the better the vertex resolution (i.e. L1L1 has better vertex resolution than

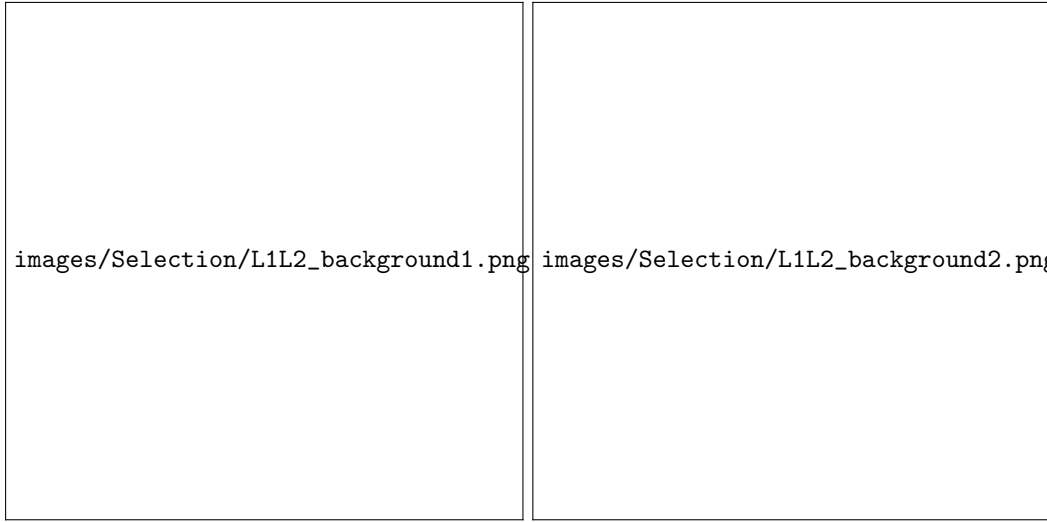


Figure 5.14: Left: A schematic of a prompt background process that has a hit inefficiency in layer 1 and is placed in the L1L2 category. Right: A schematic of a prompt background process in which one of the daughter particles scatters away from the beam in the inactive silicon of layer 1 and into the acceptance of the tracker. This process is placed in the L1L2 category and also reconstructs a false vertex downstream of the target.

2385 L1L2 which has better resolution than L2L2). Second, the nature of the backgrounds between the
 2386 categories are different. The L1L1 category high z backgrounds are typically due to multiple
 2387 scattering in the active region of L1 sensors and mistracking. While backgrounds in the L1L2 and
 2388 L2L2 categories are typically due to hit efficiency effects, multiple scattering in both active and
 2389 inactive regions of layer 1, and mistracking.
 2390 For the L1L1 category, layer 1 hits on both tracks are required. In addition to requiring layer 1 hits,
 2391 layer 2 hits are also required in order to reduce mistracking which can result in high z backgrounds
 2392 (see isolation cut subsection). Requiring layer 2 hits improves the resolution for extrapolating
 2393 tracks to the correct hit in layer 1. Layer 3 hits are not explicitly required by the analysis, rather
 2394 they are implicitly required by the tracking algorithms. Thus, all events in this category have hits
 2395 in layers 1-3. The effect of requiring layer 1 and layer 2 hits is shown in Fig. ???. A summary of the
 2396 cuts in the L1L1 category is shown in Table 5.3 and described in the following subsections.

Cut Description	Requirement
Layer 1 Requirement	e^+ and e^- have L1 hit
Layer 2 Requirement	e^+ and e^- have L2 hit
Radiative Cut	$V_{0p} > 1.85$ GeV
V0 projection to target	Fitted 2σ cut
Isolation Cut	Eq. 5.11
Impact Parameters	Eq. 5.14

Table 5.3: A summary of the tight cuts for the L1L1 category.

2397 Projection of the vertex to the target

2398 As mentioned previously, in order to reduce the number of downstream background events at
2399 high- z it is required that vertices project back to the beam spot position. The vertex projection to
2400 the target in the $x - y$ plane is computed by taking the direction of the vertex momentum,
2401 computed as the vector sum of the momenta of the e^-e^+ pair, and extrapolated the vertex
2402 position to the target location (at -4.3 mm in detector coordinates). While in MC simulation the
2403 beamspot is generated in a fixed position, the position of the unconstrained vertices in the $x - y$
2404 plane depends in data depends on the beam conditions and position, leading to run-by-run biases
2405 that need to be corrected before applying the target projection cut.

2406 The longitudinal and transverse spatial distributions of the vertices that pass the *Preselection* cuts
2407 are used to estimate the run-by-run position of the beamspot in data and MC simulation. The
2408 spatial distributions are fit with a gaussian function in the interval [-1.5RMS, 1.5RMS], where
2409 RMS is the root mean square of the distributions. The same procedure is applied to the
2410 distributions for the transverse projections of the vertex to the target surface.

2411 The transverse projections show correlation between the x and y coordinates in Fig. 5.15 in both
2412 data and MC, although different correlations. The linear correlation was fit in the interval [-0.5
2413 mm, 0.5 mm] in order to fit the correlation in the core of the distribution. The angle in data,
2414 across all 10%, is $\theta_{data} = 0.0387$ rad and in a subset of tritrig-wab-beam $\theta_{MC} = 0.1110$ rad. The
2415 rotation is also shown Fig. 5.15. The new rotated coordinates are then refit using the method
2416 above to determine the rotated x and y fitted means and sigmas in MC and on a run-by-run basis
2417 for data. These values are used to form an elliptical cut on the rotated x and y coordinates in
2418 units of n_σ from the mean.

2419 In Figure 4.2 the mean of the longitudinal position for data and MC simulation is shown. In
2420 Figure 4.3 and in Figure 5.12 the mean and width of the transverse position and of the transverse
2421 projection to the target surface, with rotations for the x and y coordinates, for data and MC
2422 simulation are shown, respectively. The elliptical cuts at 2σ are shown in Fig. ??.

2423 The actual cut value is difficult to demonstrate quantitatively. Table ?? and Table ?? show the
2424 effect of the V0 projection cut on high z events (events past z_{cut} from the 10% data) on 10% data,
2425 100% tritrig-wab-beam sample, and x3 tritrig sample as well as 80 MeV and 100 MeV displaced
2426 A's. From this data, a circular cut on the rotated projections is set to 2σ from the mean and is
2427 shown in Fig. ???. The effect of the V0 projection cut is shown in Fig. ???. The effect of floating
2428 the value of the V0 projection cut is shown in Fig. ??.



Figure 5.15: The V0 projection back to the target for Preselection in the L1L1 category. Upper Left: 10% Data with a linear fit to the x - y correlation Lower Left: 10% tritrig-wab-beam with a linear fit to the x - y correlation. The V0 projection back to the target for L1L1 Preselection with rotated x - y coordinates for Upper Right: 10% Data and Lower Right: 10% tritrig-wab-beam. The angle of rotation is $\theta_{data} = 0.0387$ rad in data and $\theta_{MC} = 0.1110$ rad in MC.



Figure 5.16: Left: Example of mistracking from a layer 1 bad hit that falsely reconstructs downstream of the target. Right: Geometric picture of the isolation cut comparing the distance between the nearest hit away from the beam δ and the track longitudinal impact parameter of the track z_0 where the correct track is in green and the incorrect track found by the tracking algorithm is in red.

2429 Isolation Cut

2430 Mis-reconstructed tracks, or mistracking, are tracks that contain at least one hit on track that is
 2431 not associated with the particle responsible for the other hits on track. For instance, a track can
 2432 reconstruct using an additional hit from a beam electron, recoil electron, photon, or noise hit. This
 2433 incorrect hit is also called a “bad hit”. And when this additional hit is in layer 1 and is closer to
 2434 the beam than the true hit (or if the true hit doesn’t exist), this can falsely reconstruct a
 2435 downstream vertex, often significantly downstream, that appears signal-like as shown in Fig. 5.16.
 2436 Often this occurs as a result of scattering in the second layer causing the track to extrapolate to
 2437 the incorrect hit in layer 1 and occurs at a significant enough rate that it needs to be mitigated.
 2438 The isolation cut is performed on tracks, and unfortunately, the coordinate systems for track
 2439 reconstruction and analysis on HPS are different. In the analysis, as previously stated, the x
 2440 direction is beam left, the y direction is vertical upwards, and the z direction is the direction of the
 2441 beam. The tracking coordinates are oriented approximately such that the x direction is the
 2442 direction of the beam, the y direction is beam left, and the z direction is the vertically upwards. In
 2443 addition, each track is defined by 5 track parameters - Ω , d_0 , z_0 , $\tan\lambda$, and ϕ - and are briefly
 2444 described below and shown in Fig. 5.17, as well as described in more detail here ([cite this paper:](#))

- 2445 1. Ω is the signed curvature of the track (i.e. the inverse of the radius).
- 2446 2. d_0 is the signed impact parameter in the xy tracking plane. In the HPS detector frame, this
 2447 translates to the impact parameter along the x (horizontal) direction.



Figure 5.17: A schematic of the linear collider tracking parameters.

- 2448 3. z_0 is the tracking z position at the point of closest approach to the reference point. This is
 - 2449 the key tracking parameter for the isolation cut. In the HPS detector frame, this
 - 2450 approximately corresponds to the impact parameter in the y (vertical) direction.
 - 2451 4. $\tan\lambda$ is the slope of the straight line in the sz tracking plane. In the HPS detector frame, this
 - 2452 translates to the slope of the track dy/dz in the yz plane.
 - 2453 5. ϕ is the azimuthal angle of the momentum of the particle at point of closest approach to the
 - 2454 reference point.
- 2455 The isolation cut is designed to eliminate high z backgrounds due to mistracking from bad hits in
- 2456 layer 1. In particular, tracks that misreconstruct the 3D hit in the first layer of the SVT where the
- 2457 hit is closer to the beam than the true hit can reconstruct a downstream vertex that appears to be
- 2458 signal-like. The isolation cut offers a simple strategy to test if fitting a track with another hit in
- 2459 layer 1 is more consistent with the track coming from the primary than the secondary vertex
- 2460 without re-running track reconstruction (even if the original track would have better track
- 2461 quality). If the track is more consistent with the primary, the event is eliminated.
- 2462 The most basic form of this cut is a simple geometric cut that compares the distance of the next
- 2463 closest hit in the sensor, called the isolation value δ , to the track longitudinal impact parameter z_0
- 2464 (tracking z is in the vertical direction y in the detector frame). First, since the track parameter z_0
- 2465 is recorded at the origin and the target position is upstream from the origin at $z_{targ} = -4.3$ mm,
- 2466 the value of z_0 is corrected to the impact parameter at the target z_0_{corr} using a simple linear
- 2467 extrapolation.

$$z0_{corr} = (z0 - z_{targ} \frac{P_Y}{P}) \text{ sign}(P_Y). \quad (5.7)$$

2468 The isolation value δ is the distance along the measurement direction for each sensor between the
 2469 1D cluster hit on track and the next nearest 1D cluster hit in the direction away from the beam
 2470 plane. By sign convention, δ is always positive, and the 1D cluster hits towards to the beam plane
 2471 are not considered since these will reconstruct the vertex further downstream (and we are testing if
 2472 another hit causes the track to be more consistent with the primary). Furthermore, only the
 2473 minimum isolation value between the axial and stereo sensor in a given layer is considered.
 2474 Comparing this value to the impact parameter, the geometrical condition of the isolation cut is
 2475 such that, for the track to pass the cut, the isolation value must be greater than the impact
 2476 parameter times the ratio of the distance between first 2 measurement points and the distance
 2477 between the second measurement and the primary (i.e. $\frac{z_{L2}-z_{L1}}{z_{L2}-z_{targ}}$). In the case of a layer 1 isolation
 2478 cut, since the ratio of the distance between layer 2 and layer 1 and layer 2 and the target is about
 2479 one half, the ratio used in this condition is $\frac{1}{2}$. Otherwise, this “refitted” track is more consistent
 2480 with the primary and the event is eliminated. This concept is shown in Figure 5.16, and this
 2481 condition can be expressed with the following inequality.

$$\delta + \frac{1}{2}z0_{corr} > 0 \quad (5.8)$$

2482 It has been shown in the previous displaced vertexing analysis from the 2015 engineering run that
 2483 this simple geometric cut eliminates a large fraction of high z evens due to mistracking, but fails to
 2484 account for multiple scattering in layer 1 [cite 2015 note]. Thus, the high z backgrounds of this
 2485 nature were not mitigated to the full potential in previous analysis. In other words, there were
 2486 high z background events observed in both data and MC that were near the edge of this basic
 2487 isolation cut, and shifting the cut by even a small amount would have further reduced high z
 2488 background. Extending the simple geometric cut by incorporating an error on the impact
 2489 parameter $z0_{corr}$ accounts for the multiple scattering in the tracker. In order to take multiple
 2490 scattering into account, the $z0_{corr}$ term in Equation 5.8 is modified by adding the estimate of its
 2491 error at the target position, effectively shifting the value of the isolation cut.

$$z0_{corr} \longrightarrow z0_{corr} + \Delta z0_{corr} \quad (5.9)$$

2492 As stated above, in reconstruction the impact parameter $z0$ and error $\Delta z0$ is given with respect to
 2493 the origin of the reference system. Thus, the error on the impact parameter must also be
 2494 propagated to the target position. Propagating the error requires the use of the track slope $\tan\lambda$
 2495 and track curvature Ω as well as their errors. Assuming the track parameter errors are
 2496 uncorrelated, $\Delta z0_{corr}$ can simplify to

$$\Delta z_{0corr} = \Delta z_0 + |z_{targ}| (\Delta \tan \lambda + 2 |\tan \lambda \frac{\Delta \Omega}{\Omega}|) \quad (5.10)$$

2497 This corrected error at the target results in an increase in error of about 10% with respect to Δz_0 .
 2498 Typically, the errors of the impact parameter at the target are ≈ 0.1 mm. In order to take into
 2499 account large scatters in the L1 material, the isolation cut takes into account the errors in the
 2500 track extrapolation on a track-by-track basis by shifting the cut value up to a specified n_σ on z_0
 2501 leading to a final isolation cut value given by I refer to the entire left side of the equation as the
 2502 “isolation cut value”. This may be confusing, but I didn’t have time to change the name on the
 2503 plots so I’ll find a better way to denote it later.

$$\delta + \frac{1}{2} (z_{0corr} - n_\sigma \Delta z_{0corr}) > 0 \quad (5.11)$$

2504 The last step in finalizing the isolation cut is to select the number n_σ to use in the cut. In general,
 2505 the signal efficiency is fairly insensitive to (since $\Delta z_{0corr} \approx 100\mu\text{m}$) as shown in Fig. ?? where $n\sigma$
 2506 is varied as 2.5, 3, and 3.5. A reasonable value on the error is 3σ which eliminates all high z
 2507 background due to mistracking according to MC. The effect of the cut on 10% data, 100%
 2508 tritrig-wab-beam, and 80 MeV and 100 MeV displaced A' s is shown in Fig. ??.
 2509 In order to better understand the effect of the isolation cut, it is important to see its effect on both
 2510 good tracks (those with a purity of 1) and bad tracks (or mistracks, those with a purity of less
 2511 than 1) which can be determined by truth matched tracks in MC. For more details on the
 2512 procedure of the truth matching in MC, see Sec. ???. For preselected events with a layer 1 hit, the
 2513 reconstructed z positions vs the isolation cut value in eq. 5.11 for 10% of the data, 100% the
 2514 tritrig-wab-beam MC sample separating good and bad tracks, and displaced A' MC at two
 2515 different mass points are shown in Fig. ??, Fig. ??, and Fig. ??, respectively. Efficiency as a
 2516 function of reconstructed z for two different A' masses for preselection with layer 1 requirements
 2517 both with and without the isolation cut is shown in Fig. ???. A comparison of the isolation value δ
 2518 and the isolation cut value for 10% data and 100% tritrig-wab-beam are shown in Fig. ???. Finally,
 2519 a comparison of the reconstructed z distribution for 100% tritrig-wab-beam for V0 particles with
 2520 100% pure e^+ and e^- tracks and V0 particles with at least one e^+ or e^- track with a bad hit in L1
 2521 is shown in Fig. ???. For tritrig-wab-beam, 98.8% of the V0 particles have 100% pure tracks for
 2522 both e^+ and e^- tracks while 0.95% of the V0 particles have either e^+ or e^- with a bad L1 hit. The
 2523 remaining fraction of V0 particles have either an e^+ or e^- bad hit in a layer other than L1 (with
 2524 good hits in L1) or have no track to truth match for either the e^+ or e^- particle. The fraction of
 2525 V0 particles for 80 MeV displaced A' s are XX% and XX%, respectively. The fraction of V0
 2526 particles for 100 MeV displaced A' s are XX% and XX%, respectively These numbers need to be
 2527 recorded after I have the new A' MC with truth info.
 2528 The isolation cut is not sensitive to sensor inefficiencies as it has been developed under the

2529 assumption that a real 3D has been formed, reconstructed, and associated to a track. Therefore
2530 tracks that are formed by picking a wrong 3D hit because the true hit has failed the reconstruction
2531 cannot be eliminated by this cut.

Impact Parameters

For signal, a true displaced vertex to have large impact parameters (z_0) in the vertical direction for both electron and positron tracks. Furthermore, these impact parameters are correlated with z , where both electron and positron impact parameters increase with increasing z in well-defined bands. For prompt background that reconstructs at large z , this is not always the case. Instead, it is possible for one particle to have a large scatter (and thus a large impact parameter) and the corresponding particle to either be consistent with the primary or have a smaller impact parameter than is expected from signal. With a cut on impact parameter of both e^+e^- tracks, we can eliminate such backgrounds. This concept is illustrated in Fig. 5.18.

In order to fully utilize an impact parameter as a method to discriminate between background and signal, this cut is performed as a function of z in order to fit the signal bands shown in the z_0 vs. reconstructed z plots of Fig. ???. This figure also shows the same plot in 10% of the data with preselection and layer 1 requirements. This correlation in signal is approximately linear for the masses of interest (which can be seen for 80 MeV and 100 MeV), so there is a requirement for the cut be linear in z .

$$z_{0+}(m, z) > a_+(m) + b_+(m) z \text{ or } z_{0-}(m, z) < a_-(m) + b_-(m) z \quad (5.12)$$

Both the electron and positron are required to satisfy this condition of being above or below this line. The difference in slope between the positive and negative functions is large enough such that they are fit to different constants. Since the opening angle of A' 's is mass-dependent, the slopes of these cuts (and also the z -independent term) also depends on mass. Thus, the constants a_{\pm} and b_{\pm} must be parametrized as a function of mass which will be done below.

In order to obtain these constants for a given A' mass, we begin with a single A' mass and perform a linear fit the inner bands of the z_0 vs z distributions, combining both the electron and positron distributions. Specifically, the z_0 distributions are sliced in overlapping bins of z and the point at which a certain fraction of the signal will be eliminated on the side closer to the beam plane (i.e. the “inner” portion of the z_0 distribution) is determined. This fraction of the signal that is chosen to be eliminated is a tuneable parameter denoted as α . This defines the constants a_{\pm} and b_{\pm} at a specific mass. This process is repeated for each mass point in the range 60 MeV - 150 MeV and a linear fit using the same α is performed at each mass.

As stated previously, each of these parameters that are linear in z must be parametrized as a function of mass. The fits show that the a_{\pm} parameter is generally within 25 μm across all masses including both the positive and negative fit. Thus, this parameter is fit to a constant across all masses such that $a_+ = a_- = a$. The relationship between the mass and the slope is non-linear and increases asymptotically with increasing with mass.

$$b_{\pm}(m) = b_{0\pm} + \frac{b_{1\pm}}{m} \quad (5.13)$$

2565 These two assumptions are justified in Fig. 5.19. Finally, the cut equations can be summed up
 2566 with 5 parameters a , $b_{+\pm}$, and $b_{-\pm}$ that are set with a single tuneable parameter α .

$$z0_+(m, z, \alpha) > a(\alpha) + b_{0+}(\alpha) z + b_{1+}(\alpha) \frac{z}{m} \text{ or } z0_-(m, z, \alpha) < a(\alpha) + b_{0-}(\alpha) z + b_{1-}(\alpha) \frac{z}{m} \quad (5.14)$$

2567 In addition, since there is a mass-dependent target position for data (but not for MC) as shown in
 2568 Fig. 5.31, and these constants must be determined from MC, the reconstructed z for this cut in
 2569 data is shifted by a value dz determined by the difference in fitted mean between 10% data and
 2570 MC preselection.

$$dz = -0.377 + 13.79m - 55.84m^2 + 84.00m^3 \quad (5.15)$$

2571 In addition to the shift in z , there are shifts in the y -direction due to changing beam conditions.
 2572 The beam position in y can shift by as much as $50\mu\text{m}$ which can have a significant impact on the
 2573 signal efficiency of the impact parameter cut as shown in Fig. ???. To mitigate this effect, a
 2574 run-dependent beam y position is utilized in the same way that the V0 projection back to the
 2575 target is run-dependent.
 2576 Next, the parameter α must be chosen. Table ?? and Table ?? show the number of high z
 2577 backgrounds (past the z_{cut} of the 10% of the data) in 10% of the data, 100% of the
 2578 tritrig-wab-beam sample, and x3 tritrig sample as well as the efficiency for 80 MeV and 100 MeV
 2579 displaced A' 's. Based on this data, $\alpha = 15\%$ was selected as it eliminates a significant amount of
 2580 background in all categories, with minimal affect on signal efficiency. At this α , the value of the 5
 2581 parameters are: $a = -2.018e10^{-1}$, $b_{0+} = 5.199e10^{-2}$, $b_{1+} = -2.301e10^{-3}$, $b_{0-} = 4.716e10^{-2}$, and
 2582 $b_{1-} = -1.086e10^{-3}$. The effect of floating the cut about different values of α is shown in Fig. ???.
 2583 The effect of the impact parameter cut is shown in Fig. ??.

2584 Radiative Cut

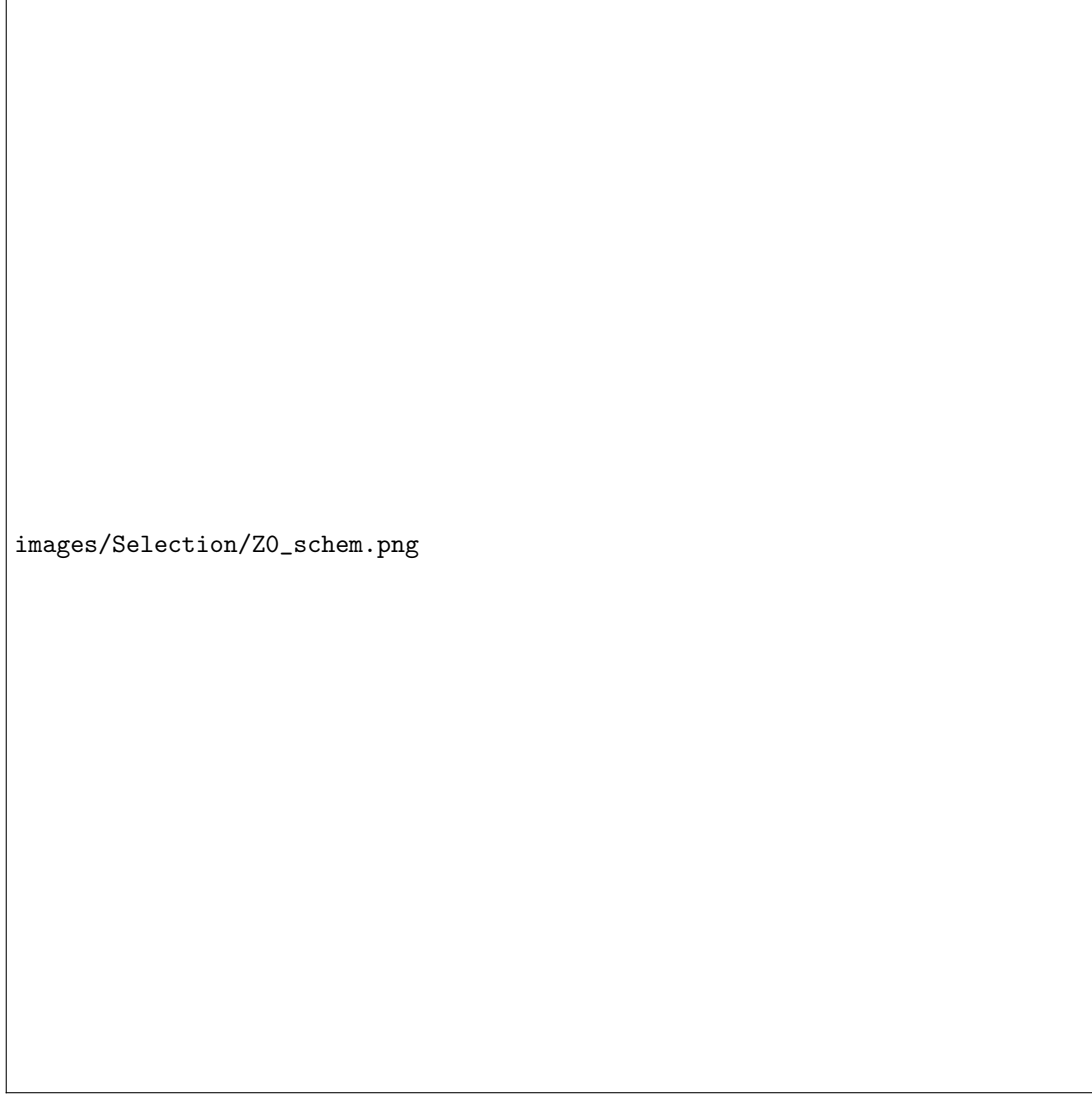
2585 As stated previously, the kinematics of A' 's are such that the recoil electron is generally soft while
 2586 A' 's take most of the beam energy (i.e. have a large $x = E_{A'}/E_{beam}$). Thus, only V0s with
 2587 momentum near the beam energy are selected, and a minimum V0 momentum cut (in addition to
 2588 the maximum V0 momentum cut from preselection), the so-called radiative cut, is necessary. Since
 2589 radiative tridents have identical kinematics to A' 's, this cut can be optimized based on radiative
 2590 trident kinematics against Bethe-Heitler tridents and wabs. And because this is true regardless of
 2591 whether or not A' 's are prompt or displaced, it can be optimized in a similar method to the
 2592 resonance search.
 2593 The resonance search uses the ratio $sig/\sqrt(sig + bck)$ where the signal expectation comes from
 2594 radiative tridents and the total expectation comes from the sum of tridents and wabs. The
 2595 optimum value is generally insensitive to the cut value between the momentum sum ranges from

2596 1.6 GeV to 2.2 GeV, and was found to be 1.88 GeV across all mass ranges. The value of 1.9 GeV
2597 was selected for convenience for the resonance search.

2598 There are two key differences between the resonance search and the displaced vertex search with
2599 respect to the radiative cut. The first is the fact that the search for displaced vertices is in a low
2600 background region, thus the same ratio doesn't necessarily apply. Secondly, there is a
2601 mass-dependence for this cut optimization shown in Fig. 5.20 which skews the optimization for
2602 this figure of merit toward low mass (40 GeV - 60 GeV) and favors a looser radiative cut. For the
2603 displaced vertex search with a 2.3 GeV beam energy, the mass range of interest begins at $\tilde{60}$ MeV,
2604 which has an optimal value at around 2.0 GeV.

2605 However, in a low background region, the ratio $sig/\sqrt{(sig + bck)}$ may not be a sufficient figure of
2606 merit for cut optimization. As a better figure of merit, one can use ratio sig/bck . In order to
2607 provide sufficient statistics for the background term, the entire mass range of interest is used for
2608 the background (from 50 MeV - 150 MeV). For this exercise, there are typically 15-20 background
2609 events, and a new z_{cut} is fit for each x_{cut} point. It is an assumption that the entire mass range is
2610 representative of each individual mass slice. These results for two signal points are shown in Fig.
2611 5.20 and a radiative cut of 1.85 GeV ($x \approx 0.8E_{beam}$) is selected.

2612 The effect of the radiative cut on 10% of the data, signal MC, and background MC is shown in
2613 Fig. ?? while the effect of floating the cut value about its nominal value is shown in Fig. ??.



images/Selection/Z0_schem.png

Figure 5.18: Left: Prompt background that falsely reconstructs at a large z due to an e^- particle with a large scatter away from the beam plane in layer 1 of the SVT. The corresponding e^+ does not have a large scatter and the track point back near the primary. A cut on the impact parameter can eliminate such background. Right: A true displaced vertex will have a large impact parameter for both e^+e^- pairs that is correlated with reconstructed z .

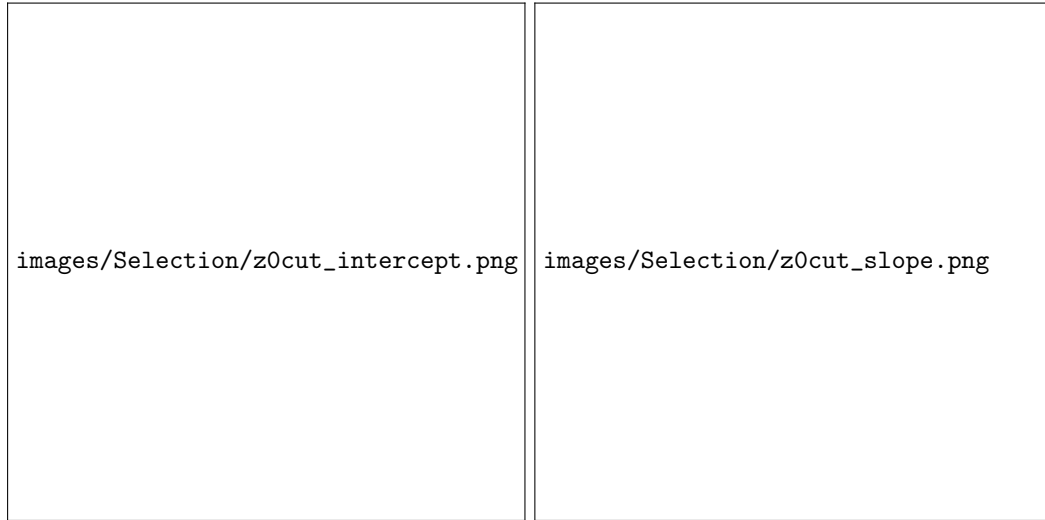


Figure 5.19: Left: The y -intercept for a linear fit in z_0 vs reconstructed z at various mass points. Each For simplicity, the range is fit with a constant and used as an input to Eq: 5.12 ($a_+(m) = a_-(m) = a$) . Right: The slope for a linear fit in z_0 vs reconstructed z as a function of mass for tracks in the top volume of the SVT. The range is fit using Eq. 5.13. **These plots are ugly, but I can replace them in the future if necessary.**



Figure 5.20: Invariant mass vs the momentum sum of a trident sample. The red stars are the optimal momentum sum in slices of mass based on $\text{sig}/\sqrt{(\text{sig} + \text{bck})}$ where radiative tridents are signal and tridents are background. Above 60 MeV, the lower mass bound of interest for the displaced vertex search, the optimal value is a momentum sum of about 2.0 GeV.

	data	ϵ_{tot}	tridents	ϵ_{tot}	WAB	ϵ_{tot}	AP	ϵ_{tot}
Preselection	- -	- -	- -	- -	- -	- -	- -	- -
L1L1 + L2 Requirements	- -		0 0.0	0 0.0	0 0.0	0 0.0	0 0.0	0 0.0
V_0 Projection to Target $< 2\sigma$	- -		- -	- -	- -	- -	- -	- -
$\chi^2_{unc} < 4$	- -		- -	- -	- -	- -	- -	- -
$V_{0p} > 2.0\text{GeV}$	- -		- -	- -	- -	- -	- -	- -
Isolation Cut	- -		- -	- -	- -	- -	- -	- -
Impact Parameter Cut	- -		- -	- -	- -	- -	- -	-

Table 5.4: Table showing the efficiency of each cut on 10% of the 2016 data sample and on MC simulation for tridents, WABs and 80 MeV A' displaced samples for the L1L1 category. **TODO:** Update the cuts and numbers

2614 Selecting Single V0s

2615 A table of the effect of each tight cut in the L1L1 category for data and different MC components
 2616 is shown in Table 5.4 and the effect on the reconstructed z vs mass 2D plots are shown in Fig. ??.
 2617 Finally, after the tight selection, the last step is to remove both duplicate tracks and events with
 2618 multiple V0 particles. Tracks can share hits with other tracks, and these shared hits can be from
 2619 hits from another particle such as a recoil electron, beam electron, or photon or be a noise hit.
 2620 There is evidence shown in Fig. ?? in both data and MC that tracks with shared hits produce a
 2621 small number of high z background events. Because of the possibility of producing high z events,
 2622 tracks with shared hits are eliminated.
 2623 The final requirement is each event to have exactly one V0 candidate that passes all cuts. This will
 2624 prevent duplicate V0s in an event which is not expected for signal. Those events that have more
 2625 than one V0 candidate that passes all cuts is eliminated. A comparison of the cut between 10%
 2626 data, 100% MC, and displaced A 's is shown in Fig. 5.24. The final selection for the L1L1 category
 2627 plotted as reconstructed z vs mass is shown in Fig. 5.23. The total effect of removing tracks with
 2628 shared hits and selecting single V0s eliminates about 10.3% of V0s in data and 8.4% of V0s in both
 2629 signal and background MC. Simply selecting single V0s while allowing tracks with shared hits
 2630 removes a total of about 6% of V0s in both data and MC which corresponds to about 3% of events
 2631 (since nearly all events with multiple V0s that pass all selection cuts contain exactly 2 V0s).

2632 5.6 L1L2

2633 As described in L1L1 section, longer-lived A 's often have one or more daughter particles miss layer
 2634 1 of the SVT, and thus will be eliminated by requiring layer 1 hits. The strategy is to divided the
 2635 analysis into several mutually exclusive categories by the first hit of the daughter particles - L1L1,
 2636 L1L2, and L2L2. For this analysis, only L1L1 and L1L2 are utilized, and the proceeding
 2637 subsections describe the tight cuts in the L1L2 category where exactly one daughter particle is
 2638 required to have a layer 1 hit.

2639 Similar to the L1L1 category, in addition to the L1L2 requirement, layer 2 hits are also required to
2640 reduce mistracking and layer 3 hits are implicitly required by tracking algorithms. The effect of
2641 requiring either a layer 1 hit for the electron or positron (but not both) and requiring layer 2 is
2642 shown in Fig. ???. A summary of the cuts in the L1L2 category is shown in Table 5.5 and described
2643 in the following subsections.

Cut Description	Requirement
Layer 1 Requirement	e^+ xor e^- have L1 hit
Layer 2 Requirement	e^+ and e^- have L2 hit
Radiative Cut	$V_{0p} > 1.85$ GeV
V0 projection to target	Fitted 2σ cut
Isolation Cut	Eq. 5.11 or Eq. 5.16
Impact Parameters	Eq. 5.14

Table 5.5: A summary of the tight cuts for the L1L2 category.

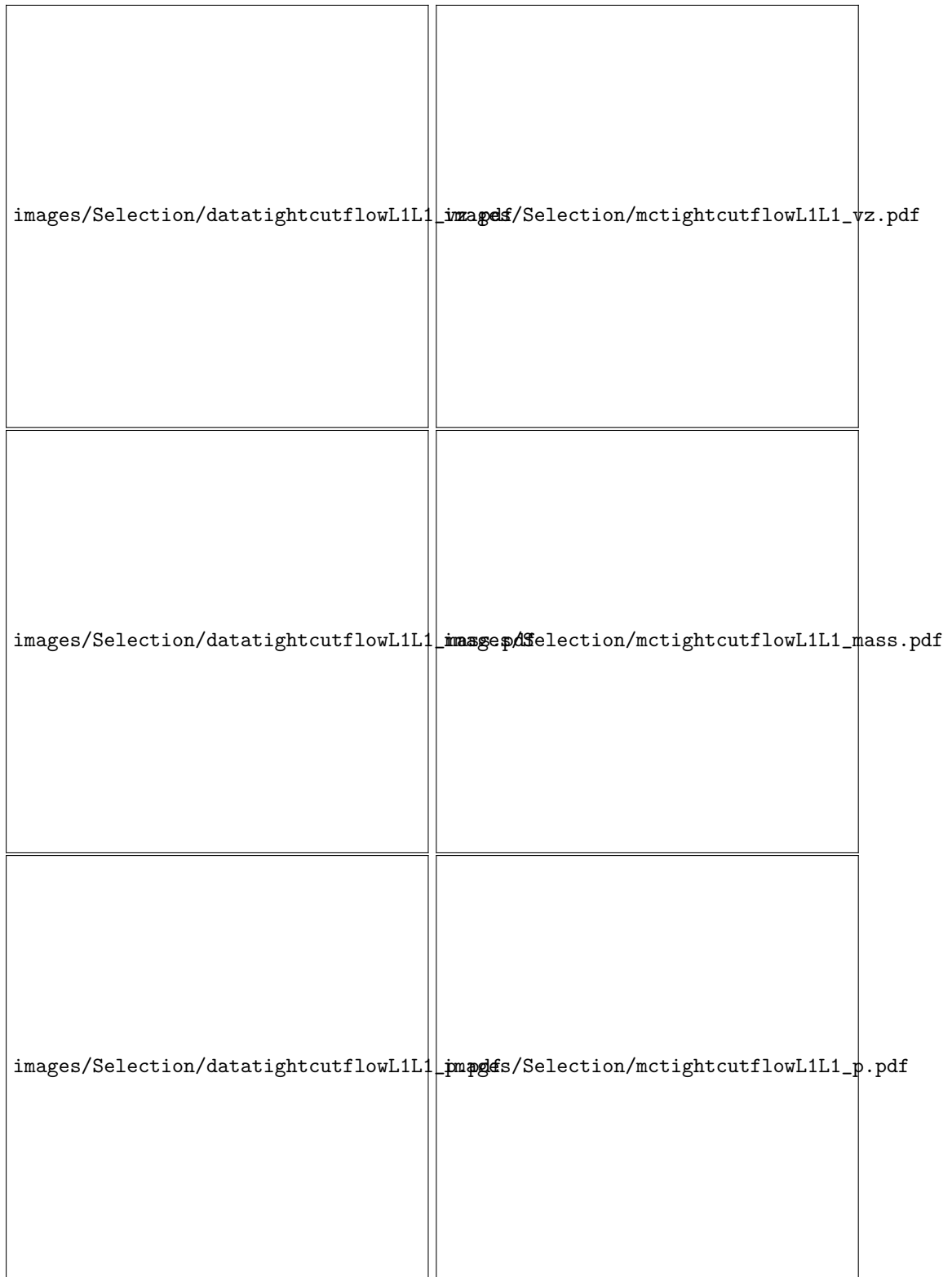


Figure 5.21: Upper Left: Comparison of 10% Data and tritrig-wab-beam MC for the final event selection in the L1L1 category. Upper Right: Comparison of 10% of the Data for before and after multiple V0 events are removed. Lower Left: Comparison of 80 MeV displaced A 's for before and after multiple V0 events are removed. Lower Right: Comparison of 100 MeV displaced A 's for before and after multiple V0 events are removed.



Figure 5.22: Upper Left: Comparison of 10% Data and tritrig-wab-beam MC for the final event selection in the L1L1 category. Upper Right: Comparison of 10% of the Data for before and after multiple V0 events are removed. Lower Left: Comparison of 80 MeV displaced A's for before and after multiple V0 events are removed. Lower Right: Comparison of 100 MeV displaced A's for before and after multiple V0 events are removed.



Figure 5.23: Upper Left: Comparison of 10% Data and tritrig-wab-beam MC for the final event selection in the L1L1 category. Upper Right: Comparison of 10% of the Data for before and after multiple V0 events are removed. Lower Left: Comparison of 80 MeV displaced A 's for before and after multiple V0 events are removed. Lower Right: Comparison of 100 MeV displaced A 's for before and after multiple V0 events are removed.

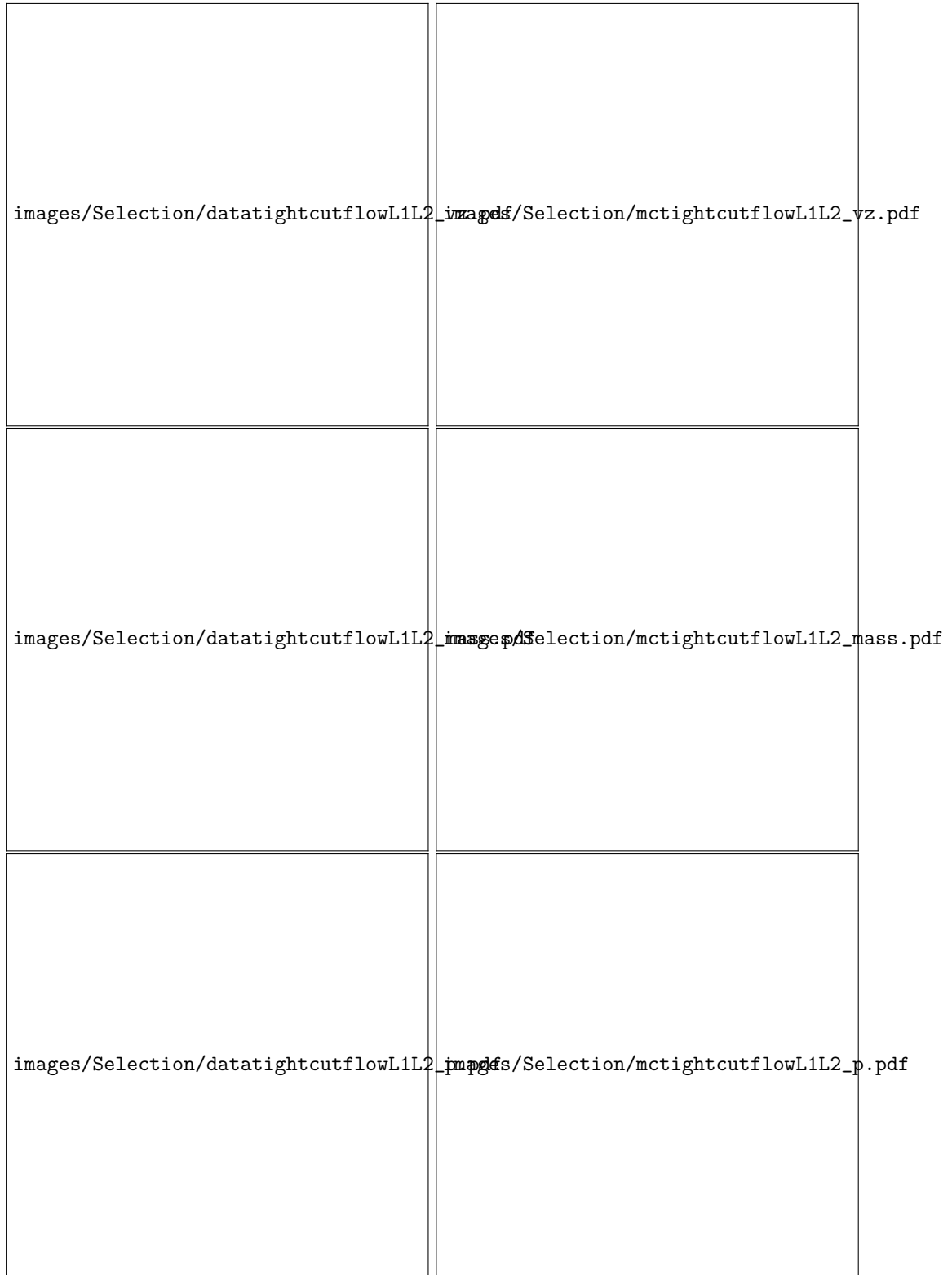


Figure 5.24: Upper Left: Comparison of 10% Data and tritrig-wab-beam MC for the final event selection in the L1L1 category. Upper Right: Comparison of 10% of the Data for before and after multiple V0 events are removed. Lower Left: Comparison of 80 MeV displaced A 's for before and after multiple V0 events are removed. Lower Right: Comparison of 100 MeV displaced A 's for before and after multiple V0 events are removed.

2644 Projection of the vertex to the target

2645 Similar to signal events in the L1L1 category, signal events in the L1L2 category point back to the
2646 beamspot. Thus, a cut on the projection to the target is warranted. The projection is shown in
2647 Fig. ??.

2648 The procedure for the cut on the V0 projection is similar to the L1L1 category, in that there is a
2649 run-by-run fit for the transverse projection for the data, but the degraded resolution due to a
2650 missing layer 1 hit must accounted for. However, since the position and projection resolutions are
2651 further degraded due to interactions with inactive material or active material (with hit
2652 inefficiencies), deriving the resolution in the L1L2 category directly from data or background MC
2653 will artificially inflate the position and projection resolutions from that of a true displaced vertex.
2654 Thus, the best way to obtain the resolutions in the L1L2 category is to compare the resolutions
2655 from A' MC in the L1L1 and L1L2 category. For both categories, the projection resolution are
2656 independent of reconstructed z , but the L1L2 category has about a 25% worse resolution in the x
2657 direction and 50% worse resolution in y . This is shown in Fig. ??.

2658 For data, the run-by-run fitted means and sigmas for the rotated projection back to the target are
2659 used from the L1L1 category and a single value is used for MC. However, for both data and MC,
2660 the fitted sigmas are scaled by 1.25 for the x direction and 1.5 for the y direction, and an elliptical
2661 cut at 2σ from the mean is cut. The cut is shown in Fig. ?? and the effect of the cut is shown in
2662 Fig. ???. The effect of floating the cut value is shown in Fig. ?? and the effect on high z events
2663 (those events greater than z_{cut} from 10% of the data) in data and MC is shown in Table ?? and
2664 Table ??.

2665 Isolation Cut

2666 Similar to the L1L1 category, the L1L2 category also has high Z events due to mistracking.
2667 Specifically, when a track reconstructs with an incorrect hit, a so-called “bad hit”, in the first layer
2668 that the particle hits. However by construction, for the L1L2 category, exactly one particle has its
2669 first hit in layer 1 and the other particle has its first hit in layer 2. Thus, the isolation cut that is
2670 applied to the particle with a layer 1 hit is the same as both the particles in the L1L1 category
2671 using Eq. 5.11.
2672 However, the assumption in this equation is that layer 2 is about twice the distance from the target
2673 from as layer 1 is. This is not true when the first hit is in layer 2. Layer 2 is about 2/3 the distance
2674 from the target than layer 3. Thus the factor of 1/2 in Eq. 5.11 must be replaced by 1/3 to get

$$\delta + \frac{1}{3} (z_{0corr} - 3 \Delta z_{0corr}) > 0 \quad (5.16)$$

2675 For the L1L2 category, if the track has its first hit in layer 2, then Eq. 5.16 is applied.

2676 Similar to L1L1, the cut is selected at 3σ .

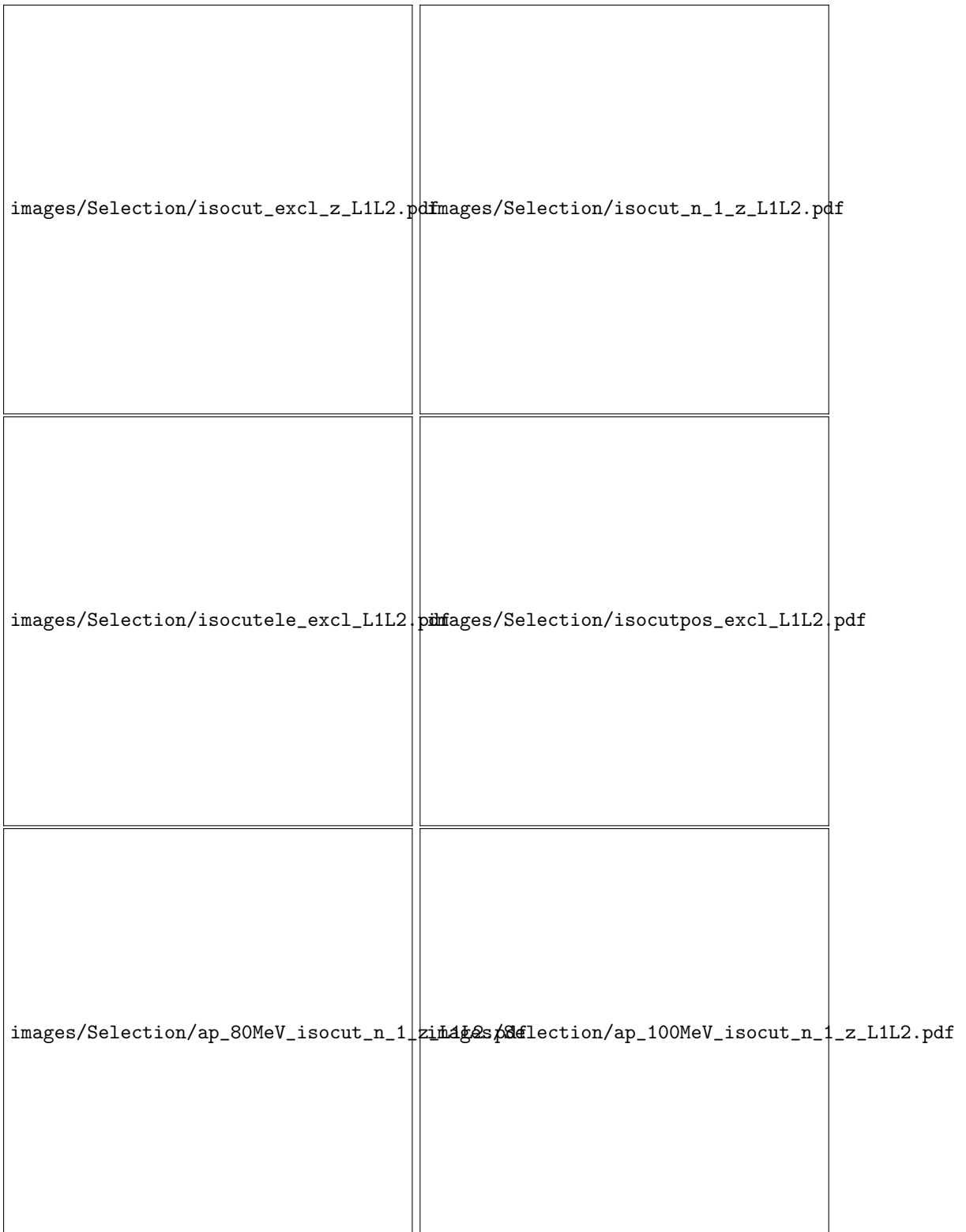


Figure 5.25: Plots showing the effect of with and without the isolation cut for the L1L2 category. Upper Left: Comparison of VZ distributions for 10% Data and 100% tritrig-wab-beam MC for all tight cuts except for the isolation cut. Upper Right: Comparison of preselection, tight cuts, and tight cuts without the isolation cut for 10% Data. Middle Left: Electron isolation cut value for 10% Data and tritrig-wab-beam MC using all tight cuts except the isolation cut. Middle Right: Positron isolation cut value for 10% Data and tritrig-wab-beam MC using all tight cuts except the isolation cut.

2677 Impact Parameters

2678 As with the L1L1 category, true displaced A' 's will have large vertical impact parameters z_0 that
 2679 are correlated within well-defined band with reconstructed z . On the other hand, a prompt
 2680 background that has a large reconstructed z may have only one of the e^+e^- tracks with a large
 2681 impact parameter. Thus, a similar cut on the track impact parameters can be applied to events in
 2682 the L1L2 category.

2683 The method for the impact parameter cut in the L1L2 category is the same as the L1L1 category
 2684 where a tuneable parameter α is chosen to eliminate a certain fraction of signal events as a
 2685 function of z and fit to a linear function as in Eq. 5.12. An example of two mass slice in both 10%
 2686 of the data and signal MC is shown in Fig. 5.26. The linear constants are both parametrized in the
 2687 same way such that Eq. 5.14 is used. The value of reconstructed z for data is also shifted by the
 2688 same value dz from Eq. 5.15 to eliminate the mass-dependent target position in data.

2689 Table ?? and Table ?? show the number of high z events (events past z_{cut} for 10% data in the
 2690 L1L2 category) for 10% data, 100% tritrig-wab-beam, and x3 tridents as well as 80 MeV and 100
 2691 MeV displaced A' 's for varying values of α . From there a determination of α can be made based on
 2692 the amount of high z background it eliminates without reducing too much of the signal efficiency.
 2693 A value of $\alpha = 15\%$ was chosen as a reasonable value and is consistent with the L1L1 α value. The
 2694 corresponding constants are $a = -0.167438502208$, $b_{0+} = 0.016762652862$,

2695 $b_{1+} = 0.00033162637213$, $b_{0-} = 0.0207347770085$, and $b_{1-} = 0.000331699098944$.

2696 The effect of the impact parameter cut is shown in Fig. ?? and the effect of floating the α value is
 2697 shown in Fig. ??.

2698 Radiative Cut

2699 As stated previously, the kinematics of A' 's are such that A' 's generally take most of the beam
 2700 energy and are accompanied by a soft recoil electron. The momentum sum distribution is
 2701 independent of the decay length. Because of this, the radiative cut (i.e. the minimum momentum
 2702 sum cut) in the L1L2 category can simply be the same as the L1L1 category and is set at 1.85
 2703 GeV. The effects of the radiative cut in the L1L2 category are shown in Fig. ??, while the effects
 2704 of floating this cut are shown in Fig. ??.

2705 Selecting Single V0s

2706 A table of the effect of each tight cut in the L1L2 category for data and different MC components
 2707 is shown in Table ?? and the effect on the reconstructed z vs mass 2D plots are shown in Fig. ??.
 2708 Similar to the events in the L1L1 category, the final selection in L1L2 requires only one remaining
 2709 V0 candidate that passes all cuts. That is, any event that has two or more remaining V0
 2710 candidates after all cuts is eliminated. This is about XX% of events. The effect of removing tracks
 2711 with shared hits and removing duplicate V0 candidates is shown in Fig. ??.

2712 5.7 L2L2

2713 L2L2 isn't part of the standard analysis, but I will include it in my thesis. Understanding the
 2714 backgrounds here will be important for future analysis.

2715 5.8 Characterizing the Background

2716 The main goals for this analysis are to understand backgrounds, estimate our expected signal yield
 2717 in a zero-background region (or a small well-characterized background), determine a method for
 2718 signal significance, and set a limit. First, we must define a signal region which will be everything
 2719 downstream of some large z value where we expect very little background. Specifically, this is done
 2720 as a function of mass since we expect a signal at a specific mass value and vertex resolution is a
 2721 function of mass. With this in mind, we divide up the z vs mass distribution in overlapping bins
 2722 equal to $1.9\sigma_m(m)$ for a mass m in the bin center. We fit each mass slice using the following
 2723 continuous and differentiable function consisting of Gaussian core and exponential tail.

$$F\left(\frac{z - \mu_z}{\sigma_z} < b\right) = Ae^{-\frac{(z - \mu_z)^2}{2\sigma_z^2}} \quad F\left(\frac{z - \mu_z}{\sigma_z} \geq b\right) = e^{-\frac{b^2}{2} - b\frac{z - \mu_z}{\sigma_z}} \quad (5.17)$$

2724 The parameter b is the number of standard deviations from the mean that the fit function changes
 2725 from a gaussian to an exponential tail. The function is fit on the range from 2σ upstream of the
 2726 mean to some maximum z where an initial mean and standard deviation are determined by fitting
 2727 the core (and then refit with Eq. 5.17). This is the same fit used in the 2015 displaced vertexing
 2728 analysis (cite note). Previous work used a similar function, but with an additional free parameter
 2729 in the slope of the tail such that the function was no longer differentiable (cite Sho's thesis). This
 2730 fit method was abandoned in favor of Eq. 5.17) since large z events often pulled the tails
 2731 unnaturally such that it resulted in kinks in the transition from the gaussian core to the
 2732 exponential tail. A comparison of 10% of the data and 100% of the tritrig-wab-beam sample in a
 2733 mass slice as well as a sample tail fit for both the L1L1 and the L1L2 category is shown in Fig.
 2734 5.31 (Add example of fit function). A comparison between the fit function parameters from Eq.
 2735 5.17 is shown in Fig. 5.31.

2736 Using the results of the fit function, the z value at which the background fit function predicts half
 2737 a background event is the definition of the z_{cut} . Or more precisely defined

$$0.5 = \int_{z_{cut}}^{\infty} F(z) dz \quad (5.18)$$

2738 In order to roughly predict a z_{cut} for unblinding, the fit function can also be scaled to 100% of the
 2739 data and the z_{cut} is solved for 0.5 background events in the same way. This is just a projection;
 2740 however, the final z_{cut} values will be determined by a fit to 100% of the data. The z_{cut} for 10%

2741 data and the projection to the full dataset as well as for the full tritrig-wab-beam sample is
2742 projected over the final samples for both data and MC for both the L1L1 and L1L2 categories in
2743 Fig. 5.32. The z_{cut} from data is used as the cut in the A' efficiency from Sec ?? and in Fig. 5.11.
2744 To be nearly unbiased, the final fit will be performed without the points in the mass bin of interest
2745 A comparison of the biased and unbiased (i.e. using the mass sidebands) for the 10% data is shown
2746 in Fig. 5.33. This unbiased z_{cut} is used to determined the candidate events in each mass bin.
2747 As described in Sec. ??, the expected rate of A 's produced at the target within prompt acceptance
2748 S as a function of mass and ϵ is given by Eq. 5.6. Further details of normalizing the A' rate directly
2749 from the radiative cross section and the number of e^+e^- pairs in a small mass window of 1 MeV is
2750 described in Sec. ???. These expected rates are also shown in Fig. 5.34 for both 10% of the data
2751 and the expected full dataset. Within a finite mass bin, the amount of expected signal S_{bin} needs
2752 to be corrected by an efficiency factor ϵ_{bin} for an expected Gaussian distribution $S_{bin} = \epsilon_{bin} S$.



Figure 5.26: Impact parameter vs. reconstructed z for different mass values of 10% data and A' 's in the L1L2 category. The red lines indicate the impact parameter cut at the specified mass value. Upper Left: 10% data in mass range 75-85 MeV. Upper Right: 10% data in the mass range 95-105 MeV. Lower Left: 80 MeV Displaced A' 's. Lower Left: 100 MeV Displaced A' 's.



Figure 5.27: Comparisons of tight cuts for the L1L2 category. Upper Left: Comparison of the tight cutflow for 10% Data and tritrig-wab-beam. Upper Right: Comparison of 10% Data and tritrig-wab-beam for events with tight cuts. Lower Left: Tight cutflow for 80 MeV displaced A's. Lower Right: Tight cutflow for 100 MeV displaced A's.



Figure 5.28: Upper Left: Comparison of 10% Data and tritrig-wab-beam MC for the final event selection in the L1L2 category. Upper Right: Comparison of 10% of the Data for before and after multiple V0 events are removed. Lower Left: Comparison of 80 MeV displaced A's for before and after multiple V0 events are removed. Lower Right: Comparison of 100 MeV displaced A's for before and after multiple V0 events are removed.



Figure 5.29: Upper Left: Comparison of 10% Data and tritrig-wab-beam MC for the final event selection in the L1L1 category. Upper Right: Comparison of 10% of the Data for before and after multiple V0 events are removed. Lower Left: Comparison of 80 MeV displaced A 's for before and after multiple V0 events are removed. Lower Right: Comparison of 100 MeV displaced A 's for before and after multiple V0 events are removed.

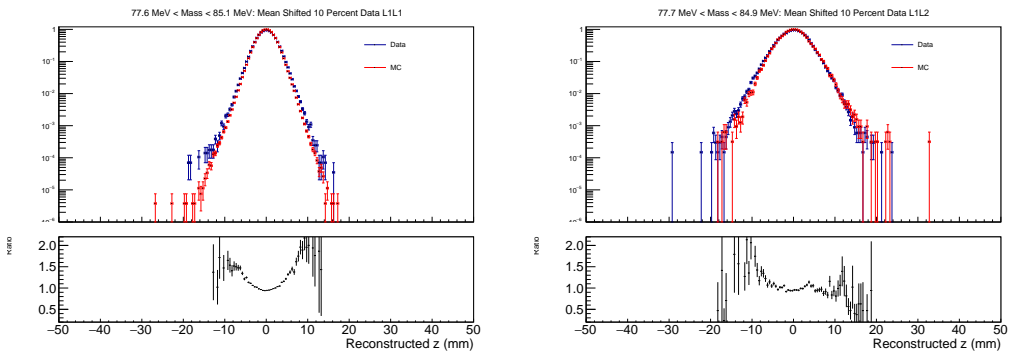


Figure 5.30: Left: 10% Data and full MC comparison in reconstructed z for a slice in mass for L1L1. For both distributions, the fitted mean is shifted to 0. Right: 10% Data and full MC comparison in reconstructed z for a slice in mass for L1L2. For both distributions, the fitted mean is shifted to 0.

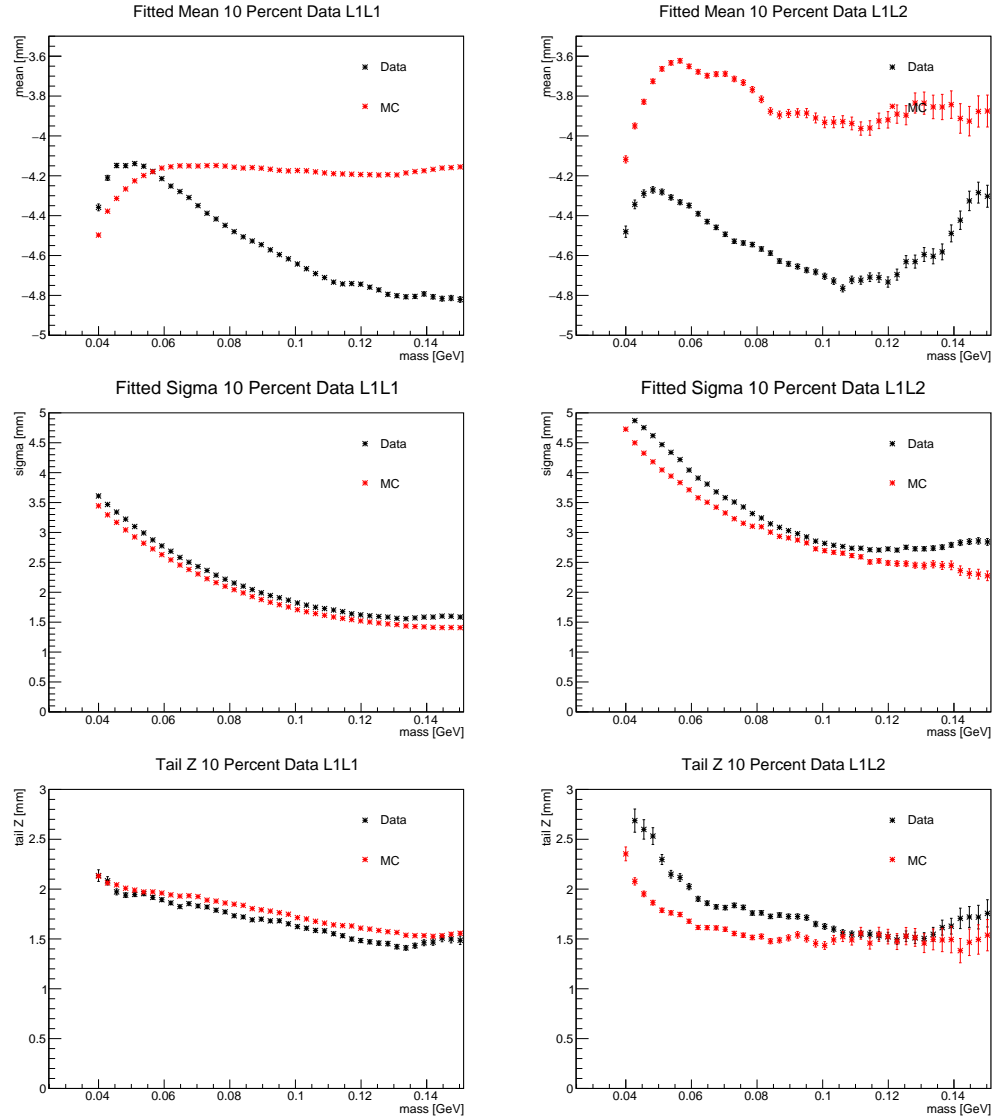


Figure 5.31: Top Left: Fitted mean as a function of mass comparing 10% of the data to the full tritrig-wab-beam sample for the L1L1 category. Top Right: Fitted mean as a function of mass comparing 10% of the data to the full tritrig-wab-beam sample for the L1L2 category. Middle Left: Fitted σ as a function of mass comparing 10% of the data to the full tritrig-wab-beam sample for the L1L1 category. Middle Right: Fitted σ as a function of mass comparing 10% of the data to the full tritrig-wab-beam sample for the L1L2 category. Bottom Left: Fitted “tail z” parameter (the number of σ from the mean the function transitions from Gaussian core to exponential tail) as a function of mass comparing 10% of the data to the full tritrig-wab-beam sample for the L1L1 category. Bottom Right: Fitted “tail z” parameter (the number of σ from the mean the function transitions from Gaussian core to exponential tail) as a function of mass comparing 10% of the data to the full tritrig-wab-beam sample for the L1L2 category.

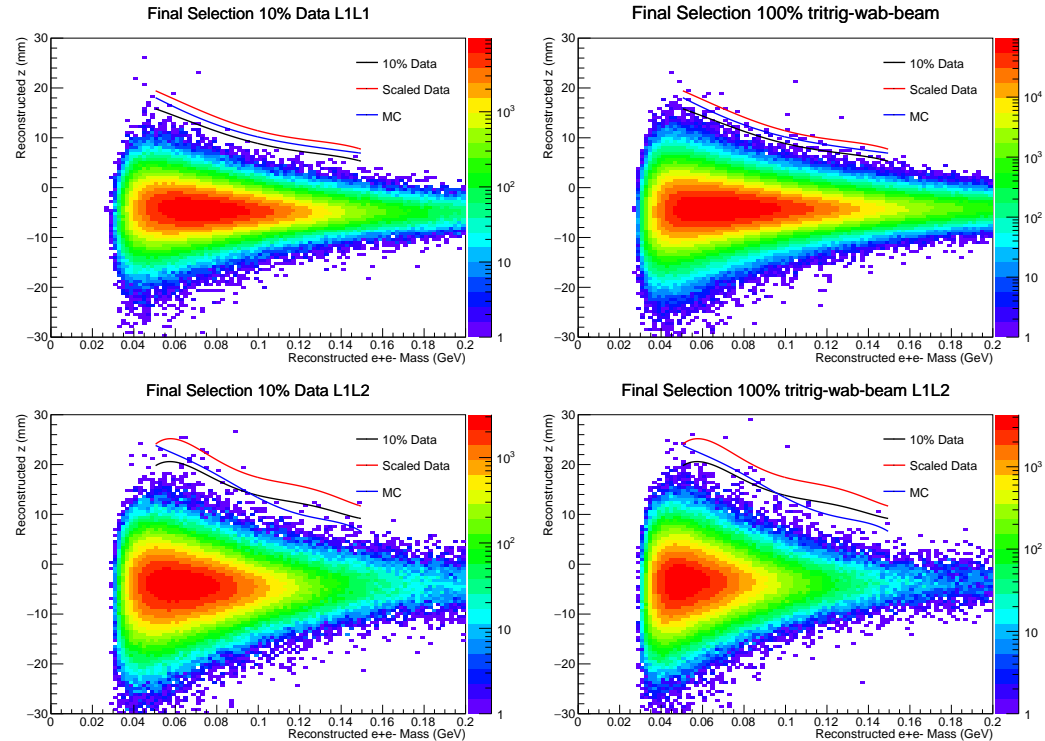


Figure 5.32: The final event selection with overlaid z_{cut} from 10% data, the full tritrig-wab-beam sample, and projected to the full dataset for Top Left: 10% data for the L1L1 category, Top Right: full tritrig-wab-beam sample for the L1L1 category, Bottom Left: 10% data for the L1L2 category, and Bottom Right: full tritrig-wab-beam sample for the L1L2 category.

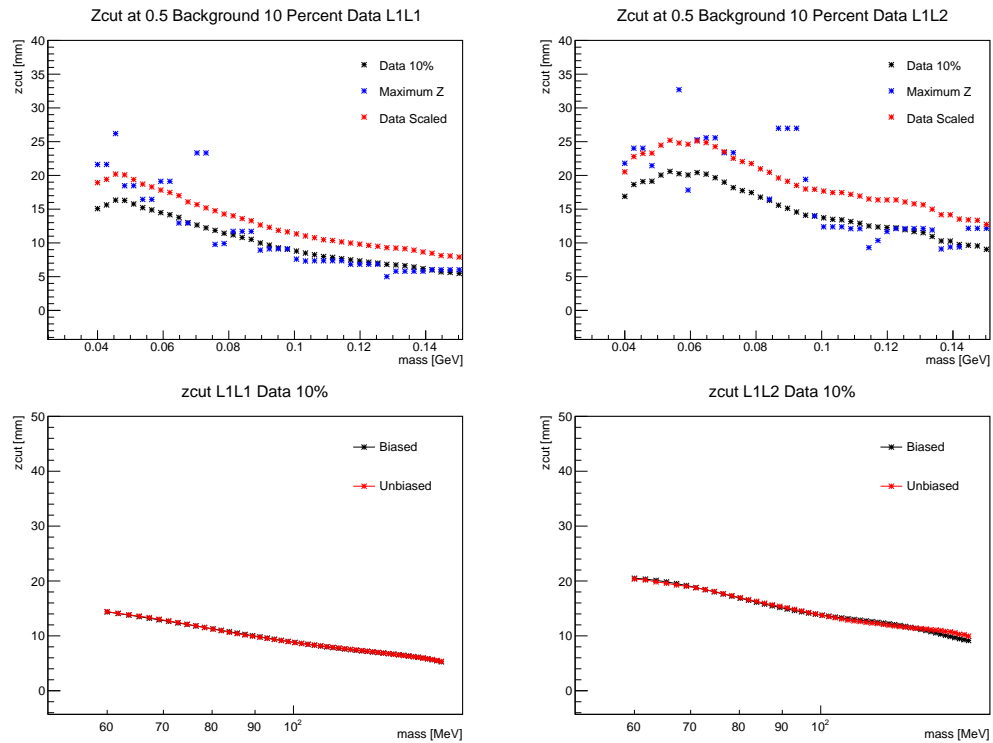


Figure 5.33: Top Left: A comparison of z_{cut} between 10% data and scaled to the full dataset to the maximum z value in a mass bin for the L1L1 category. Top Right: A comparison of z_{cut} between 10% data and scaled to the full dataset to the maximum z value in a mass bin for the L1L2 category. Bottom Left: A comparison of the biased and unbiased (excluding the mass search bin) z_{cut} for the L1L1 category. Bottom Right: A comparison of the biased and unbiased (excluding the mass search bin) z_{cut} for the L1L2 category.

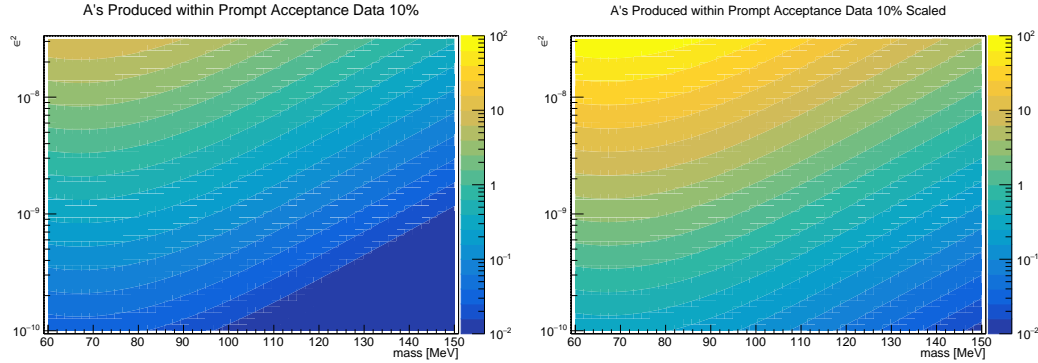


Figure 5.34: Left: The number of A' 's produced for each mass and ϵ^2 in prompt acceptance including all efficiencies for 10% of the data. In other words, the term in front of the integral in Eq. 5.20. Right: The number of A' 's produced for each mass and ϵ^2 in prompt acceptance including all efficiencies projected for 100% of the data.

5.9 Results

The expected A' production rate at the target must be correctly “spread out” in the z -direction in order to obtain the truth signal distributions. The normalized truth signal shape as a function of $c\tau$ (which of course is computed from mass and ϵ) is an exponential given by

$$S_{truth}(z, m_{A'}, \epsilon) = \frac{e^{-(z_{targ} - z)/c\tau}}{\gamma c\tau} \quad (5.19)$$

This function is normalized such that integral from z_{targ} to infinity is unity (i.e.

$\int_{z_{targ}}^{\infty} S_{truth}(z, m_{A'}, \epsilon) dz = 1$) so that it gives the expected signal density distribution. $\gamma = \frac{E}{m_{A'}}$ is the relativistic constant where the A' energy is assumed to be $E = 0.965 E_{beam}$. This assumption is justified in Fig. ?? where the mean to the $E_{A'}/E_{beam}$ distribution is shown to be about 0.965.

At each point in reconstructed z , the truth signal shape must be multiplied by acceptance and

efficiency affects. The details of incorporating these effects is explained in Sec. ?? where hit killing, further analysis cuts, and dividing events into mutually exclusive categories are taken into account.

From this section, $\epsilon_{vtx,sum}(z, m_{A'})$ denotes the efficiency due to acceptance and preliminary analysis cuts and is normalized to unity at the target. While $\epsilon_{vtx,LiLj}(z, m_{A'})$ denotes further efficiency affects due to the hit killing algorithm, further analysis cuts and z_{cut} , and the separation due to the mutually exclusive categories. For this variable, i and j denote to the individual categories L1L1, L1L2, and L2L2.

Finally, bringing this all together and integrating the signal shape across the range of interest in z (note the z_{cut} is already applied in the $\epsilon_{vtx,LiLj}(z, m_{A'})$ term) gives the formula for the expected signal past z_{cut} as a function of mass and ϵ .

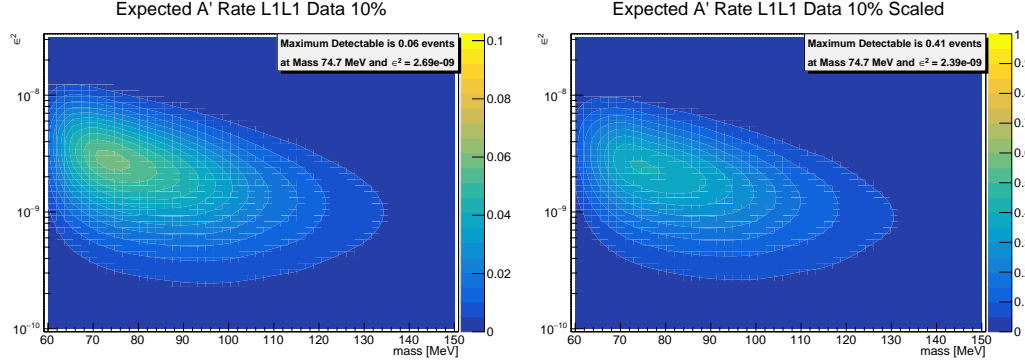


Figure 5.35: Left: The expected number of A' events past z_{cut} including all efficiencies for the L1L1 category for 10% of the data. Right: The expected number of A' events past z_{cut} including all efficiencies for the L1L1 category projected for the full dataset.

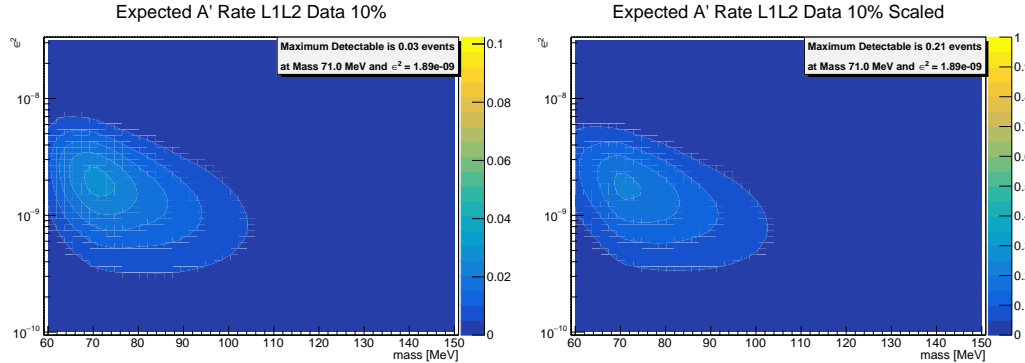


Figure 5.36: Left: The expected number of A' events past z_{cut} including all efficiencies for the L1L2 category for 10% of the data. Right: The expected number of A' events past z_{cut} including all efficiencies for the L1L2 category projected for the full dataset.

$$S_{bin,zCut,LiLj}(m_{A'}, \epsilon) = S_{bin}(m_{A'}, \epsilon) \int_{z_{targ}}^{z_{max}} S_{truth}(z, m_{A'}, \epsilon) \epsilon_{vtx,sum}(z, m_{A'}) \epsilon_{vtx,LiLj}(z, m_{A'}) dz \quad (5.20)$$

2772 The amount of signal expected for the L1L1 category for 10% data and scaled to the full dataset is
 2773 shown in Fig. 5.35 and has a maximum value of [Show max value](#). The scaling takes into account
 2774 both the increase in e^+e^- pairs and the projected z_{cut} . The amount of signal expected for the
 2775 L1L2 category for 10% of the data and scaled to the full dataset is shown in Fig. 5.36 and has a
 2776 maximum value of [Show max value](#).

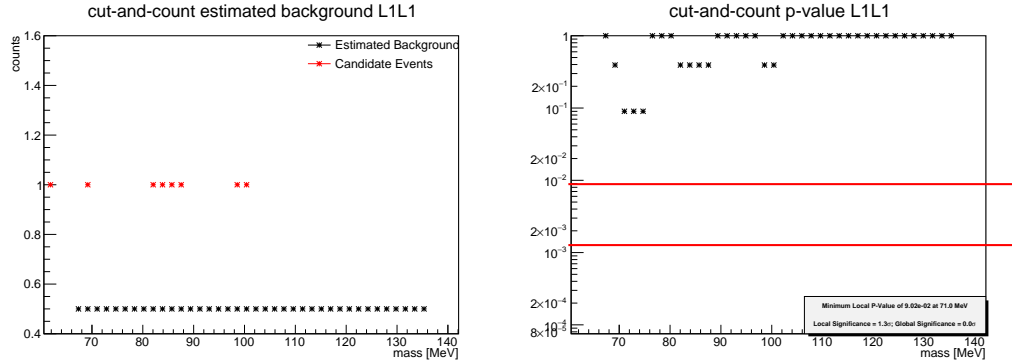


Figure 5.37: Left: The number of background events past z_{cut} based on the background model and the candidate events past z_{cut} for the L1L1 category. Right: The p-value for the L1L1 category

2777 5.10 Finding Signal Significance

2778 I am still working on this part. Feel free to skip. This still needs to be explored.

2779 Previous work in finding signal significance is best described in Sho's thesis ([cite Sho's thesis](#)). For
2780 each mass slice with n events past z_{cut} and the number of expected background events b , the
2781 probability (i.e. the p -value) of having at least n events from Poisson statistics is

$$P(n, b) = \sum_{k=n}^{\infty} \frac{b^k}{k!} e^{-b} \quad (5.21)$$

2782 From the definition of z_{cut} , we should expect the background b to be 0.5 events in each bin;
2783 however, we have backgrounds above this value and this must be estimated for data. In a similar
2784 way to how z_{cut} was determined, we can use the mass sidebands with a background model to fit
2785 and interpolate the model to the mass bin of interest. [Sho used a quadratic function, but we need](#)
2786 [to explore this..](#)

2787 Once this p -value is determined in each mass slice, we need to correct for the look-elsewhere effect.

2788 Finally, we need to convert the p -value to a significance.

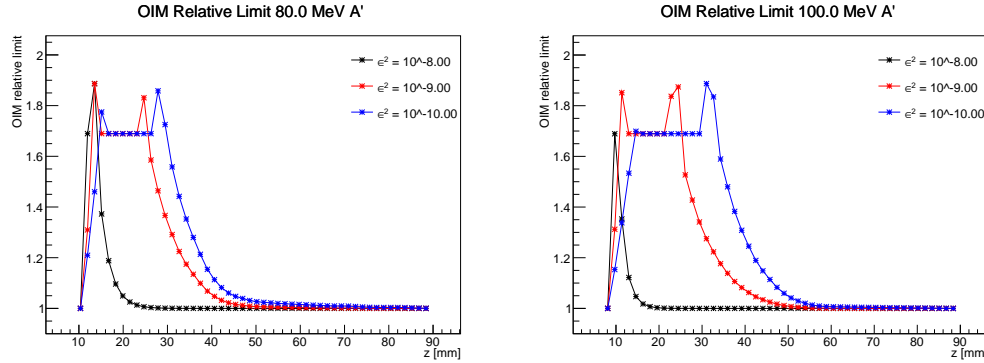


Figure 5.38: The effects of a single event on the Optimum Interval Method limit for several decay lengths for an 80 MeV mass bin (left) and a 100 MeV mass bin (right). The relative limit (relative to the background-free limit) is plotted as a function of reconstructed z of a single dummy background event. A single background event can result in up to about a 70% worse limit.

5.11 Setting Limits

In order to set a limit, we use the Optimum Interval Method (OIM) shown here ([cite OIM paper](#)). This was developed for direct detection experiments where one expects a small signal where the signal shape in one variable (z in our case) is known and there is a small, but not necessarily understood, background. The OIM is an extension of the Maximum Gap Method, which looks for the largest gap in signal space which has no background events (i.e. $x_i = \int_{z_i}^{z_{i+1}} S(z) dz$) in order to set a limit. The OIM generalizes this method to an arbitrary number of background events between any two events in signal space and sets a limit based on the optimum interval. In addition, the absolute cross-section of the signal does not need to be known, instead the OIM finds the optimum interval and sets a limit at the smallest cross section at a specified confidence interval C_0 , 90% in our case.

In order to understand how a single event can potentially impact a limit, a dummy background was placed in an otherwise background-free signal region. The z position of the background event was varied from the z_{cut} to an arbitrarily large z value and the OIM limit relative to the background-free region is recorded. With a single background event, the optimum interval can either be the interval from z_{cut} to the background event, the background event to the maximum z , or the entire interval. A single background event can result in about a maximum of a 70% worse limit compared to the background-free region. These results for an 80 MeV and a 100 MeV displaced A' for several difference values of ϵ^2 are shown in Fig. 5.38.

The result for the OIM for the L1L1 and L1L2 categories on 10% of the data are shown in Fig.

[5.39. Report minimum value](#) The interpretation of this value...

OIM [63]

Feldman Cousins [39]

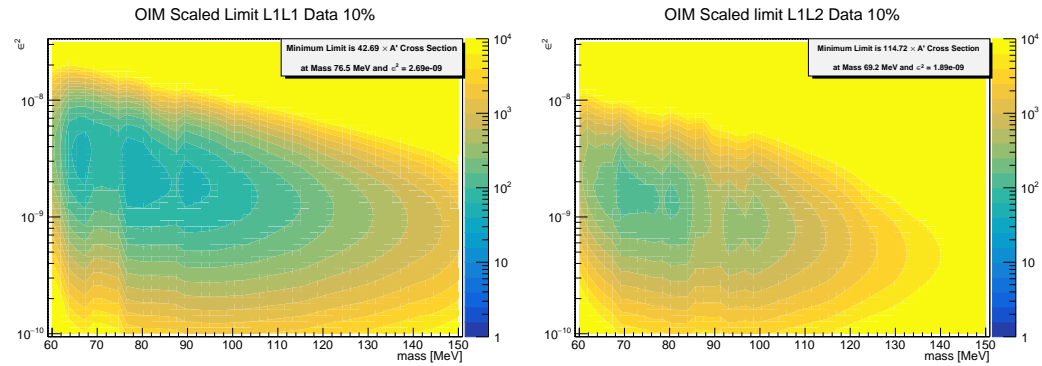


Figure 5.39: Left: The limit from Optimum Interval Method for the L1L1 category. Right: The limit from Optimum Interval Method for the L1L2 category. [Report minimum value](#)

2812 Combining OIM [64]

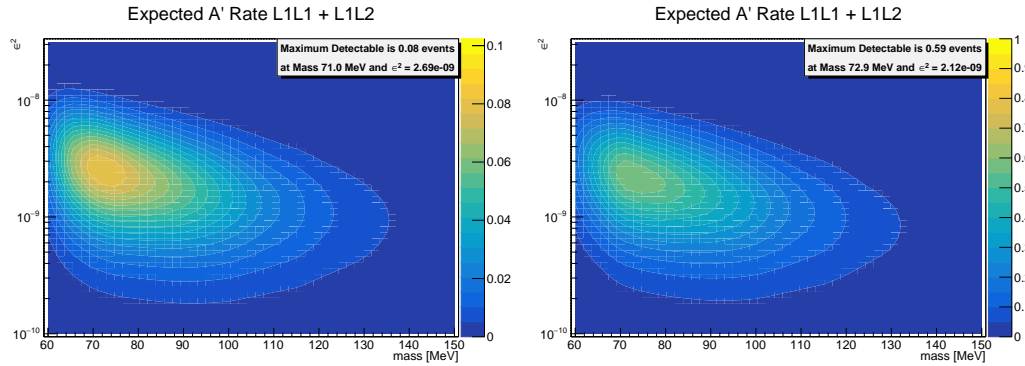


Figure 5.40: Left: The combined expected number of A' events past z_{cut} including all efficiencies for the L1L1 and L1L2 categories for 10% of the data. Right: The combined expected number of A' events past z_{cut} including all efficiencies for the L1L1 and L1L2 categories for the full dataset.
Report minimum value

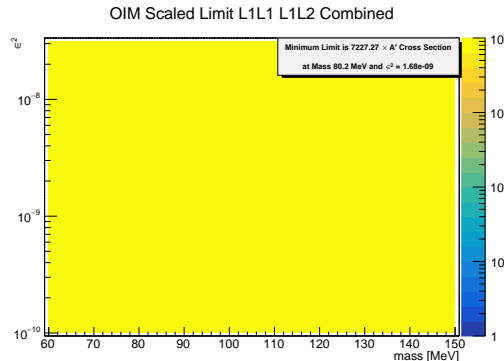


Figure 5.41: The combined limit from Optimum Interval Method for the L1L1 and L1L2 categories.
Report minimum value

2813 5.12 Combining Datasets

2814 I am still exploring these methods.

2815 Once we have results for both the L1L1 and L1L2 datasets, we can combine the results. First the
2816 expected signal yield can be trivially combined for both L1L1 (Fig. ??) and L1L2 (Fig. (XX)) by
2817 simply adding the results which is shown in Fig. (XX).

2818 In order to combine the limits set individually by the Optimum Interval Method, we can treat
2819 them like two different experiments or the same experiment but with limits set with two different
2820 parts of the detector. There are six methods for providing a combined limit from the Optimum
2821 Interval Method shown here (<https://arxiv.org/pdf/1105.2928.pdf>).

5.13 Systematics

- The systematics to be considered are currently listed below.
1. The mass resolution affects the size of the search windows and the fraction of signal with a bin. If the mass resolution is overestimated by say 10% (this number needs to be estimated). In a $1.9\sigma_m$ window, the signal yield would be overestimated by about 3.2%.
 2. There is a systematic associated with the e^+e^- composition, particularly with the radiative fraction. This method will be shared with the resonance search, since the same method is used. Most likely the largest source of uncertainty will be the wab rates.
 3. The target position is estimated to be known within ± 0.5 mm from the nominal position. The most major impact will be on the truth distributions of displaced A' 's. For instance, if the target is 0.5 mm more upstream than assumed, the signal yield will be less than assumed and will depend significantly on ϵ . This can be calculated by simply recomputing the signal yield at a different target position.
 4. There are systematics associated with every analysis cut, the most major sources of systematics are the tight cuts - radiative cut, V0 projection cut, impact parameter cut, and isolation cut. Of these cuts, the impact parameter cut and isolation cut are z -dependent, while the remainder are roughly independent of z . To get a general idea of the systematic associated with each tight cut, Fig. ?? - Fig. ?? show the effect of floating the cut by a small value about its nominal value for the L1L1 category. The same idea is presented in Fig. ?? - Fig. ?? for the L1L2 category.
- A preliminary estimate for the impact parameter cut systematic is about 1% - 2% as illustrated in Fig. ?? and Fig. ???. This is estimated by both shifting and smearing the MC z_0 distributions to match what is seen in data.
- A preliminary estimate of the systematic due to smearing of the momentum resolution (as done in the mass resolution) is shown in Fig. ??.
5. There is a potential systematic associated with the fit to the z distribution in mass bins as from Eq. 5.17. Doing a $\pm 1\sigma$ fit is shown in Fig. ?? for L1L1 and Fig. ?? for L1L2, and the corresponding change in z_{cut} is shown in Fig. ?? for L1L1 and Fig. ?? for L1L2. For the 1σ change in fit, the z_{cut} is changed by a minuscule amount (less than 0.1 mm). The difference in signal yield can be estimated using this change in z_{cut} , but it will likely change by less than 1%.
 6. There is a systematic associated with the A' acceptance times efficiency specifically with the fit function that normalizes the distributions to unity at the target.

2855 In addition, many of the systematics depend on both mass and livetime of the A' , particularly the
 2856 systematics that have a z -dependence. Thus, the systematics that do have a z -dependence will
 2857 have to be expressed as a function of mass and ϵ . The z -dependent systematics include the target
 2858 position and the analysis cuts that depend on z , such as the impact parameter cuts and the
 2859 isolation cut. A summary of all systematics used in this analysis is listed in Table 5.6.

Systematic Description	Value
e^+e^- Composition	X%
Mass Resolution	X%
Analysis Cuts	X%
Vertex Z Fits	X%
Target position	X%

Table 5.6: Summary of systematics found to impact the displaced vertex search.

2860 5.14 Discussion of High z Backgrounds

2861 An important piece of information from the displaced vertex analysis is an understanding of high z
 2862 backgrounds, those that are past z_{cut} , in both data and MC. The high z events from 10% of the
 2863 data, the 100% tritrig-wab-beam sample, and x3 tritrig sample for the L1L1 category is shown in
 2864 Table ??, Table 5.8, and Table ??, respectively. The high z events from 10% of the data, the 100%
 2865 tritrig-wab-beam sample, and x3 tritrig sample for the L1L2 category is shown in Table ??, Table
 2866 ??, and Table ??, respectively. The z_{cut} from 10% of the data is used for the data tables and the
 2867 z_{cut} from the 100% tritrig-wab-beam is used for both the large MC samples.
 2868 The description of the table values, from left to right, are as follows:

- 2869 1. The difference between reconstruction z and the z_{cut} ($V_z - z_{cut}$).
- 2870 2. The reconstructed z of the vertex.
- 2871 3. The reconstructed mass of the vertex.
- 2872 4. For data, the run number. For MC, the truth scattering angle away from the beam plane
 2873 projected on the y -axis for the particle in the top hemisphere. The angle is taken as the
 2874 maximum scattering angle between the axial and stereo sensor in layer 1.
- 2875 5. For data, the event number. For MC, the truth scattering angle away from the beam plane
 2876 projected on the y -axis for the particle in the bottom hemisphere. The angle is taken as the
 2877 maximum scattering angle between the axial and stereo sensor in layer 1.
- 2878 6. The unconstrained vertex quality

Δz_{cut}	VZ (mm)	Mass (MeV)	Run	Event	χ^2_{unc}	V0 Proj Y (n_σ)	VY (n_σ)	$\Delta e^- z0$ (mm)	$\Delta e^+ z0$ (mm)
0.08	12.62	89.95	7780	68384585	0.49	1.37	1.22	0.88	0.43
3.80	20.03	68.19	7781	138205858	4.63	0.28	0.55	0.74	1.10
3.54	15.05	98.57	7796	26862757	4.55	0.61	0.06	0.88	0.64
2.22	15.62	84.02	7800	134296298	8.65	0.68	1.04	0.90	0.60
0.32	11.12	105.89	7803	62089760	1.76	0.58	1.82	0.41	1.05
0.44	17.67	63.17	7803	105453502	8.55	0.65	0.18	0.84	0.74
0.28	13.62	84.37	7805	149492432	1.63	0.80	0.50	0.76	0.42
3.35	20.58	63.19	7947	47657629	2.25	1.78	0.54	0.78	1.26
0.50	17.12	66.21	7970	25752733	7.90	1.71	1.41	1.11	0.47
1.08	13.92	87.78	7988	97203933	1.92	0.79	0.17	1.03	0.66
7.75	23.33	71.48	8029	4393084	1.52	1.24	2.95	1.07	1.38
0.74	10.97	112.86	8040	62210614	2.24	0.78	0.51	0.71	0.43
11.74	27.27	71.71	8046	81085838	0.12	0.34	2.49	1.09	2.31
4.51	20.72	68.24	8055	9714720	0.13	1.08	3.61	0.67	1.25
2.24	14.27	93.91	8095	17884977	0.00	0.03	1.13	0.56	1.17

Table 5.7: A table of relevant variables for events past z_{cut} for 100% of the data in the L1L1 category.

- 2879 7. The projection back to the target in the y direction expressed in the number of unsigned σ
 2880 from the mean.
- 2881 8. The reconstructed y of the vertex expressed in the number of unsigned σ from the mean.
- 2882 9. The positive difference between the electron impact parameter $z0$ and the impact parameter
 2883 cut from Eq. 5.14 at the vertex mass and z .
- 2884 10. The positive difference between the positron impact parameter $z0$ and the impact parameter
 2885 cut from Eq. 5.14 at the vertex mass and z .
- 2886 These tables are informative because they display all the relevant information that can potentially
 2887 distinguish between the large Coulomb scatters and a true displaced signal for a small number of
 2888 events.

2889 **5.15 A Machine Learning Approach**

Δz_{cut}	VZ (mm)	Mass (MeV)	θ_1 (mrad)	θ_2 (mrad)	χ^2_{unc}	V0 Proj	Y (n_σ)	VY (n_σ)	$\Delta e^- z0$ (mm)	$\Delta e^+ z0$ (mm)
0.01	13.62	70.13	2.92	5.07	2.94	1.41		0.99	0.70	0.36
1.00	10.03	108.39	6.37	2.04	1.94	1.28		1.16	0.29	0.54
1.12	10.54	103.89	1.70	1.84	0.12	0.48		0.24	0.30	0.52
0.92	10.06	107.01	8.18	1.71	3.90	0.88		1.34	0.58	0.62
0.90	13.02	80.15	6.03	4.98	1.47	0.34		0.26	0.47	0.48
0.43	8.67	119.19	6.87	6.86	0.82	0.34		0.24	0.42	0.35
1.91	16.09	66.55	8.96	4.55	0.22	1.43		1.22	0.83	0.49
12.08	21.38	105.27	15.71	10.54	0.14	0.23		1.48	1.70	1.48
5.10	18.90	68.91	8.45	3.23	0.00	0.86		1.32	0.99	0.71
0.18	10.81	91.95	3.70	3.35	3.97	1.90		0.38	0.46	0.40
1.09	15.39	65.78	6.42	2.93	0.99	1.47		1.05	0.71	0.38
0.58	15.40	62.68	10.12	1.82	3.95	1.85		1.82	0.80	0.32
0.63	11.48	90.07	5.63	4.32	3.29	1.34		1.01	0.59	0.49

Table 5.8: A table of relevant variables for events past z_{cut} for the full tritrig-wab-beam sample in the L1L1 category.

2890 **Chapter 6**

2891 **Upgrades & the Future of HPS**

2892 The first involves several simple upgrades. The second involves searching for other models that can
2893 be probes by HPS.

2894 **6.1 Layer 0 & Other Upgrades**

2895 In order to achieve the full effectiveness of HPS, several simple upgrades were implemented for the
2896 most recent physics run in 2019. Informed by analysis from the previous two engineering runs,
2897 three simple upgrades were added - an additional tracking layer between the current layer 1 and
2898 the target, a hodoscope for the implementation of a positron trigger, and moving in the current
2899 L2-L3 more towards the beam.

2900 Adding an additional tracking layer, approximately halfway between the current layer 1 and the
2901 target (hence the name “layer 0” or “L0”), improves the vertex resolution by about a factor of two.
2902 This is because L0 cuts the lever arm in half, thus the vertex resolution due to multiple scattering
2903 is improved by a factor of two. The improvement of vertex resolution allows for increased displaced
2904 vertex acceptance (beyond zcut), and thus a dramatic improvement of physics potential for the
2905 displaced vertex search.

2906 There are several technical challenges associated with adding another tracking layer. In order to
2907 maintain the same geometrical acceptance for prompt processes at 15 mrad, the active edge of the
2908 axial L0 sensor must be placed at half the distance from the current location of L1 (from 1.5 mm
2909 to 0.75 mm). The acceptance of this configuration is shown in Fig. Acceptance. However, this
2910 places the guard ring (i.e. the inactive silicon) directly into the beam plane which is obviously not
2911 feasible due to radiation. To account for this, a slim...

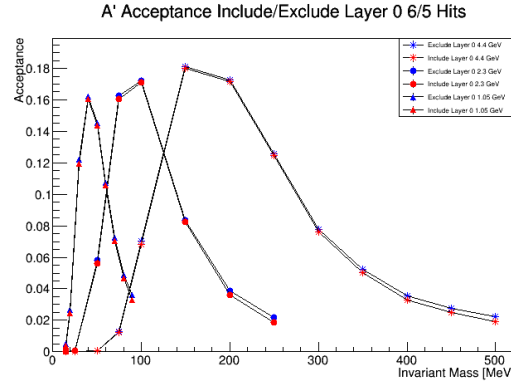


Figure 6.1: Trident Acceptance L0.

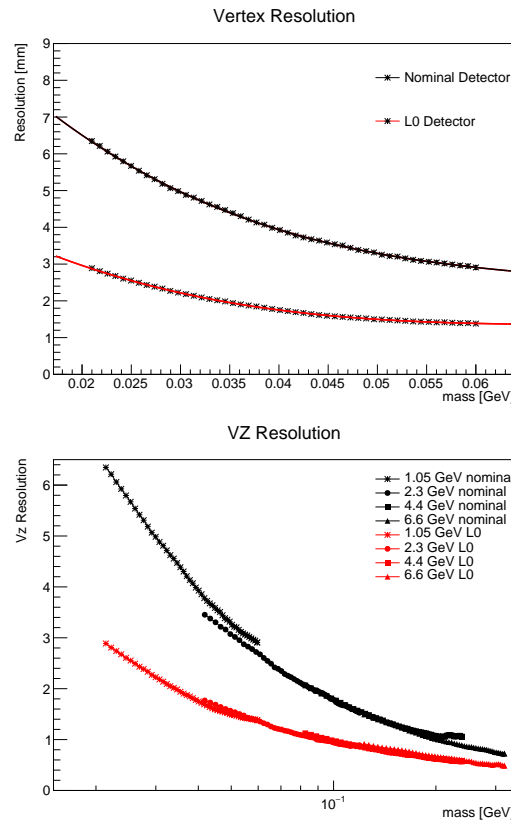


Figure 6.2: VZ Resolution.

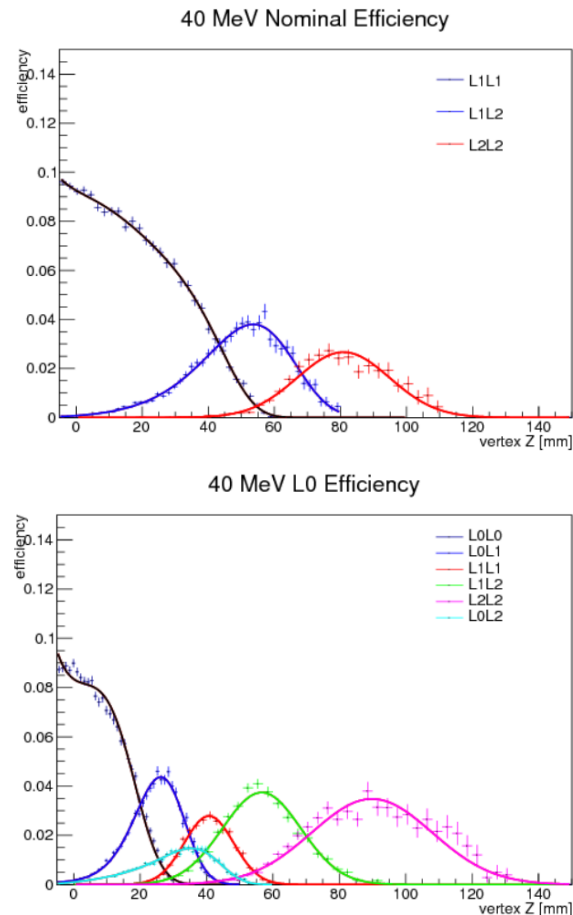


Figure 6.3: A' efficiency.

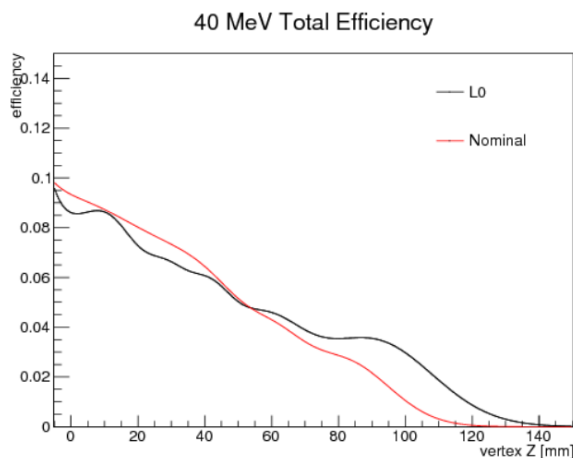


Figure 6.4: A' total efficiency

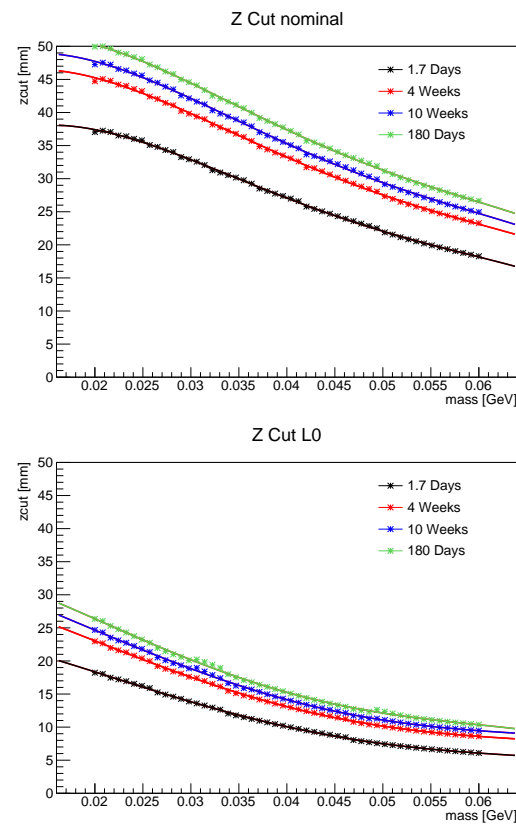


Figure 6.5: zcut

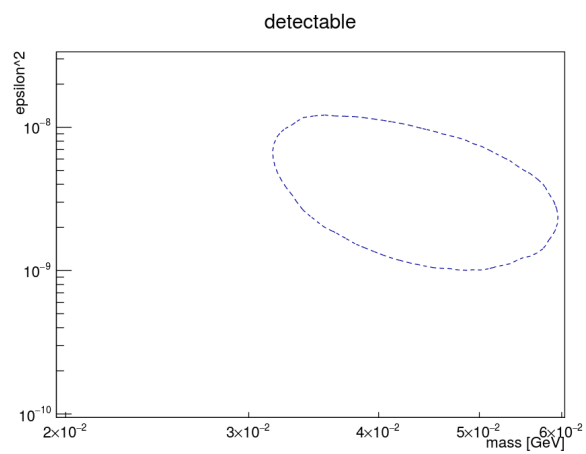


Figure 6.6: 4 weeks projection.

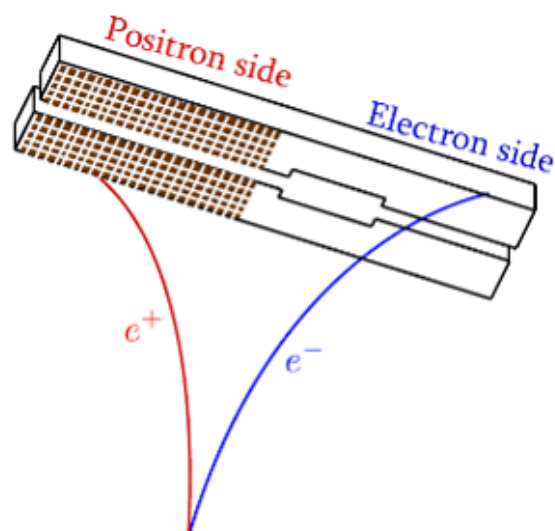


Figure 6.7: Positron Trigger

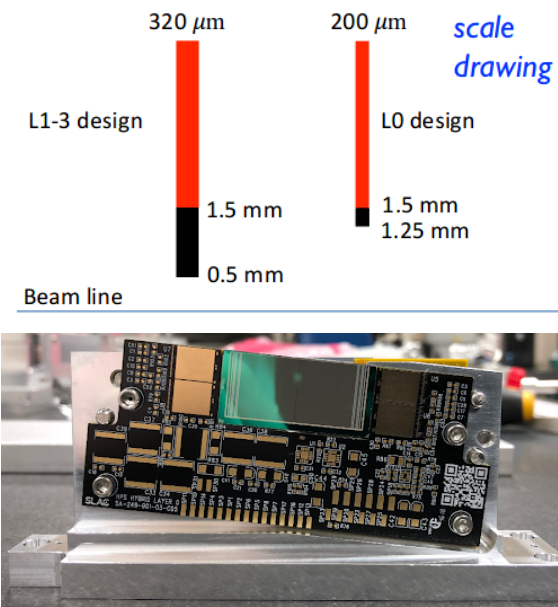


Figure 6.8: L0 design

2912 6.2 Upgrade Performance

2913 The upgrades in 2019 performed well

2914 6.3 Preliminary 2019 Data

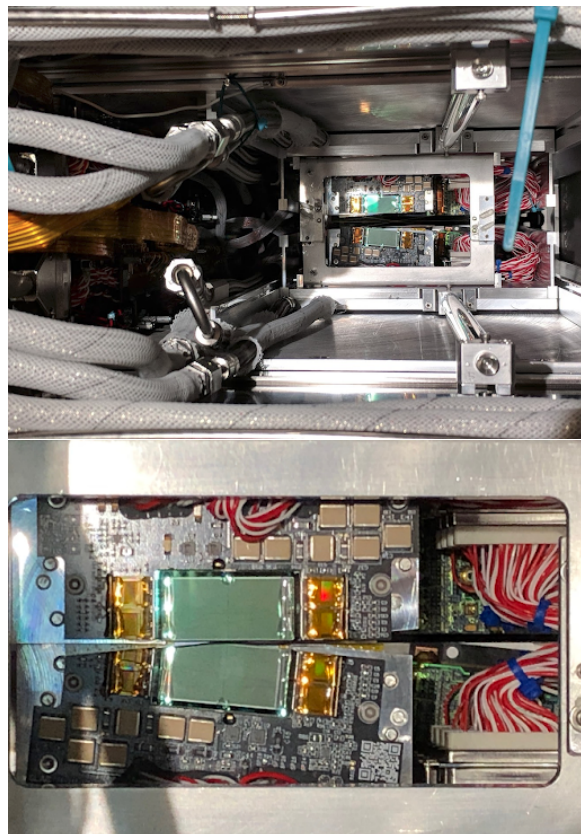


Figure 6.9: SVT view.

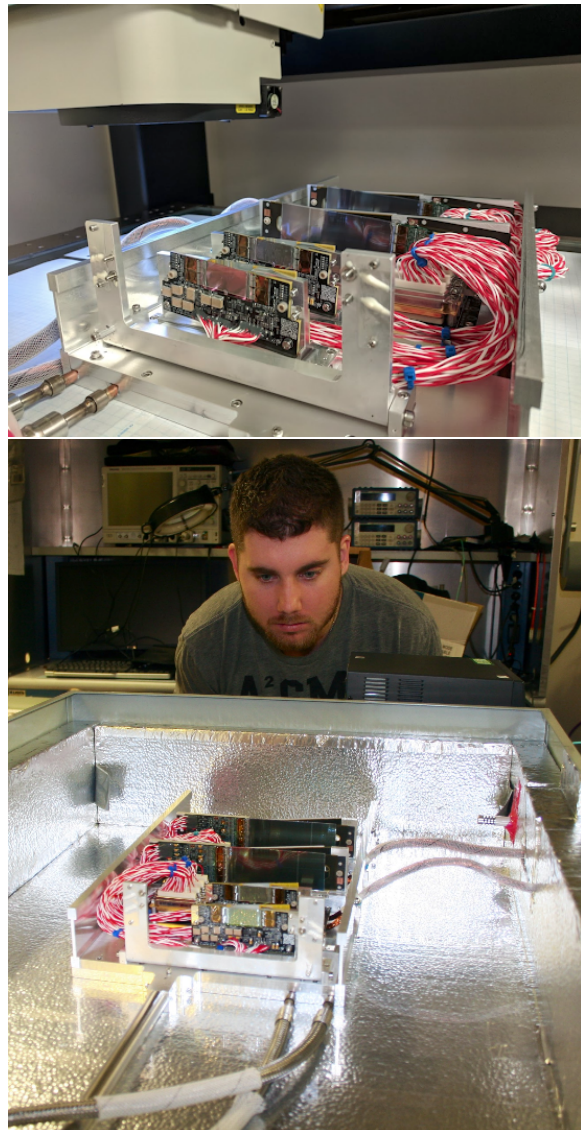


Figure 6.10: Survey and test box

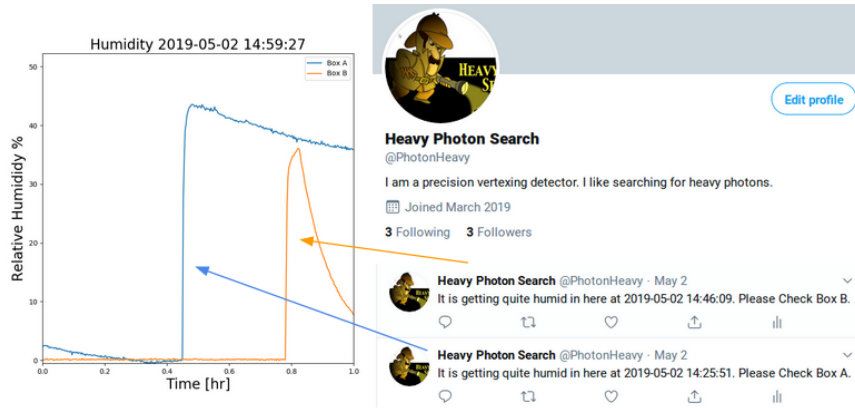


Figure 6.11: The testing station for the DAQ had a sophisticated humidity monitoring system which readout a humidity sensor via an arduino which was connected to a Twitter-based alert system. This picture shows an example of a sudden increase in humidity in both test boxes which was immediately followed by an alert tweet. In other words, someone opened the test boxes.

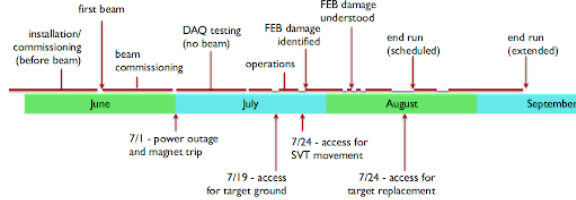


Figure 6.12: Timeline

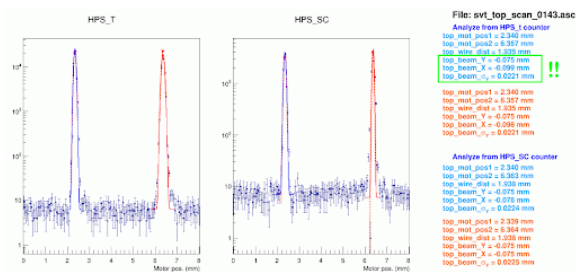


Figure 6.13: Beam

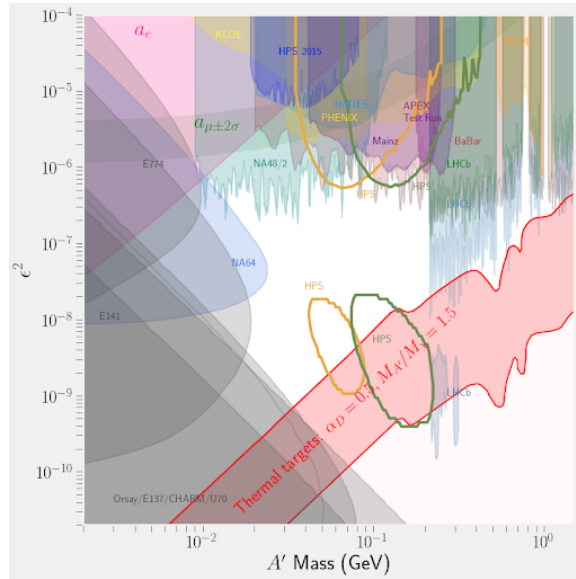


Figure 6.14: Projections

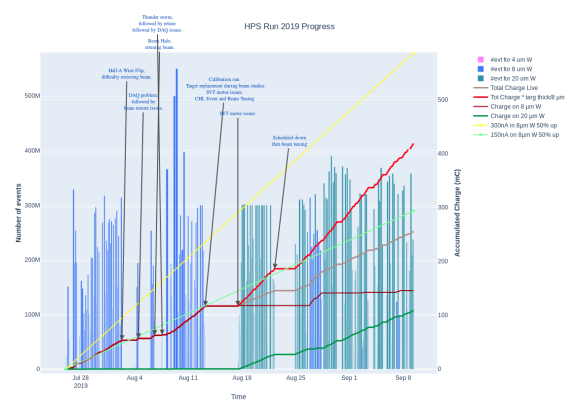


Figure 6.15: Data 2019

²⁹¹⁵ **6.4 Reach Estimates**

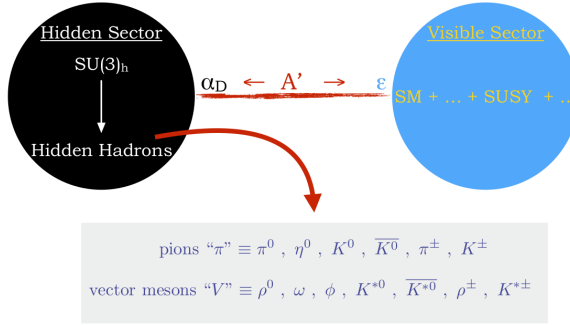


Figure 6.16: A hidden $SU(3)$ symmetry can contain hidden hadrons which include dark pions and dark vector mesons. These particles could only interact indirectly with the SM via kinetic mixing between an A' and the SM photon as described in Sec. 2.2.

2916 6.5 Generalized Displaced Vertices

2917 In addition to the minimal A' model described in Sec. 2.2, HPS can potentially probe any model
2918 with an electro-produced long-lived mediator that decay to e^+e^- pairs and set limits on the mass,
2919 livetime, and cross sections of long-lived particles that decay in the range $\sim 1\text{-}10$ cm.

2920 6.5.1 Strongly Interacting Massive Particles (SIMPs)

2921 Currently, the most appealing model for HPS beyond the minimal A' model are called Strongly
2922 Interacting Massive Particles (SIMPs) which includes an additional $SU(3)$ symmetry to the SM
2923 $SU(3)$ symmetry in addition to an additional $U(1)$ symmetry as shown in Fig. 6.16. This leaves
2924 room for dark quark sector with dark mesons and dark vectors.

2925 The prime motivation for SIMPs are dark matter. There is an annihilation...

2926 The SIMP model contains six parameters, an additional four from the minimal A' model. As one
2927 will see in the proceeding paragraphs, the additional parameters decouple the cross-section from
2928 the livetime of the long-lived particle, thus producing a high rate of long-lived particles which is
2929 ideal for HPS. The six parameters are as follows:

- 2930 1. $m_{A'}$ - The mass of the A' . For the parameter space of interest, A' 's are prompt.
- 2931 2. m_ρ - The mass to the dark ρ which is the particle that is actually long-lived.
- 2932 3. m_π - The mass of the dark pion. This particle is not detected by HPS and shows up as
missing energy. This particle is a candidate for dark matter.
- 2933 4. ϵ - The kinetic mixing parameter from the A' model.
- 2934 5. α_{dark} - The dark sector $U(1)$ gauge coupling constant (analogous to the SM α).

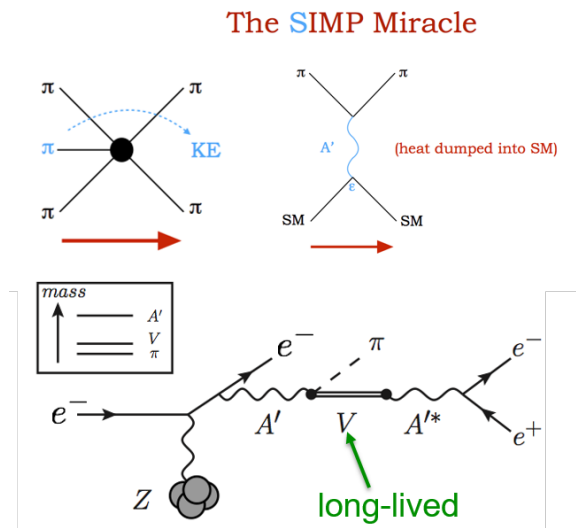


Figure 6.17: This mechanism is known as the SIMP Miracle.

²⁹³⁶ 6. m_π/f_{pi} - The dark sector pion decay constant.

²⁹³⁷ Constraints on the SIMP theory

²⁹³⁸ Mass hierarchy and choice of mass ratios.

²⁹³⁹ 6.5.2 SIMP Projections

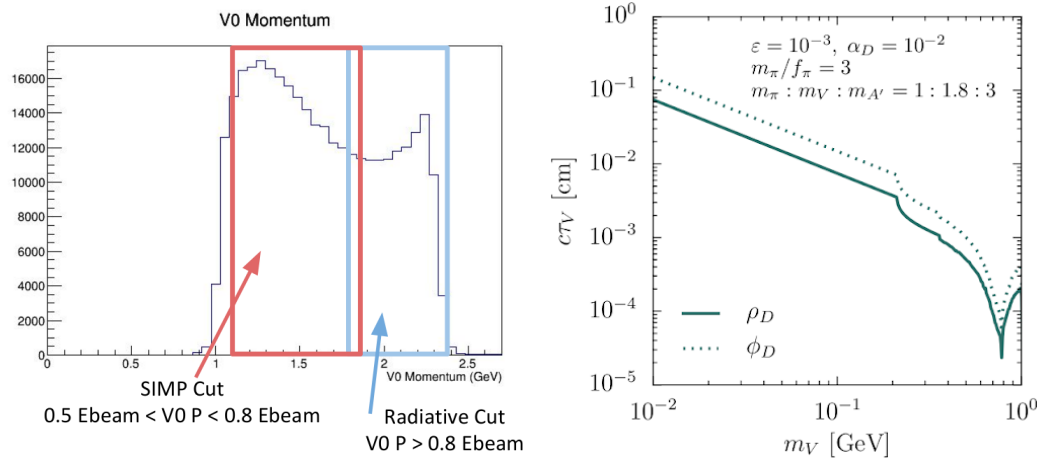
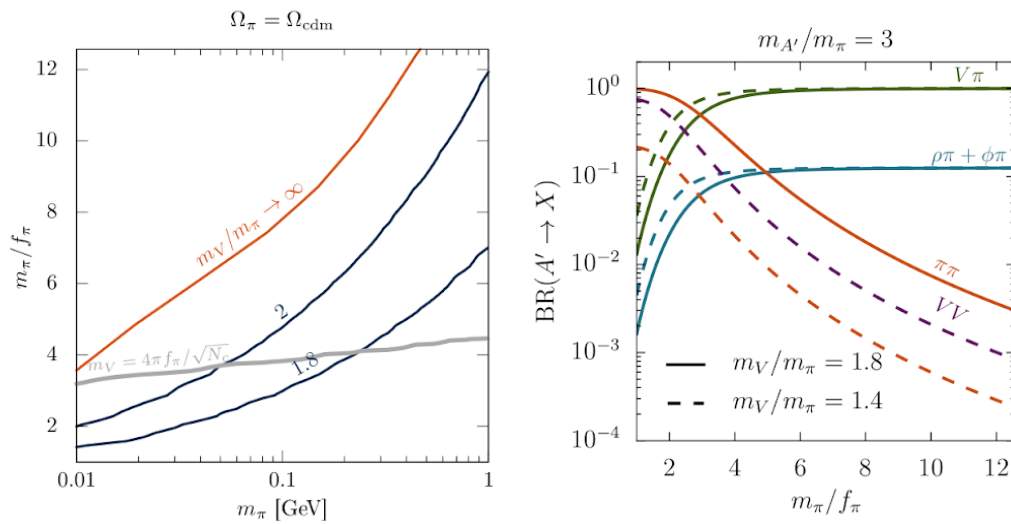


Figure 6.18: Left: SIMP p Right: livetime

Figure 6.19: SIMP $\frac{m_\pi}{f_\pi}$ and branching ratio

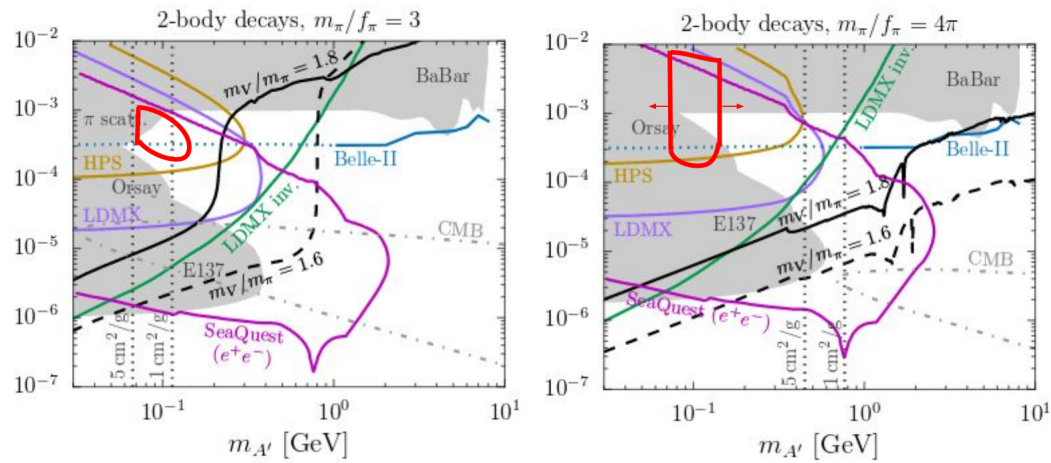


Figure 6.20: The SIMP reach estimate from the full 2016 Engineering Run dataset shown in ϵ^2 - $m_{A'}$ space for $\alpha_{dark} = 0.01$ and for Left: $m_{\pi}/f_{\pi} = 3$ and Right: $m_{\pi}/f_{\pi} = 4\pi$. The ratio of the masses is kept constant at $m_{A'} : m_{\rho} : m_{\pi} = 3.0 : 1.8 : 1.0$ for simplicity. The dataset is projected to set new limits in previously unprobed territory. **These figures need to be replaced.**

²⁹⁴⁰ Chapter 7

²⁹⁴¹ Conclusions

²⁹⁴² We tried really hard but found nothing.

²⁹⁴³ **Bibliography**

- ²⁹⁴⁴ [1] S. Abrahamyan et al. Search for a New Gauge Boson in Electron-Nucleus Fixed-Target
²⁹⁴⁵ Scattering by the APEX Experiment. *Phys. Rev. Lett.*, 107:191804, 2011.
- ²⁹⁴⁶ [2] R. Acciarri, C. Adams, R. An, C. Andreopoulos, A. M. Ankowski, M. Antonello, J. Asaadi,
²⁹⁴⁷ W. Badgett, L. Bagby, B. Baibussinov, B. Baller, G. Barr, N. Barros, M. Bass, V. Bellini,
²⁹⁴⁸ P. Benetti, S. Bertolucci, K. Biery, H. Bilokon, M. Bishai, A. Bitadze, A. Blake, F. Boffelli,
²⁹⁴⁹ T. Bolton, M. Bonesini, J. Bremer, S. J. Brice, C. Bromberg, L. Bugel, E. Calligarich,
²⁹⁵⁰ L. Camilleri, D. Caratelli, B. Carls, F. Cavanna, S. Centro, H. Chen, C. Chi, E. Church,
²⁹⁵¹ D. Cianci, A. G. Cocco, G. H. Collin, J. M. Conrad, M. Convery, G. De Geronimo,
²⁹⁵² A. Dermenev, R. Dharmapalan, S. Dixon, Z. Djurcic, S. Dytmar, B. Eberly, A. Ereditato,
²⁹⁵³ J. Esquivel, J. Evans, A. Falcone, C. Farnese, A. Fava, A. Ferrari, B. T. Fleming, W. M.
²⁹⁵⁴ Foreman, J. Freestone, T. Gamble, G. Garvey, V. Genty, M. Geynisman, D. Gibin,
²⁹⁵⁵ S. Gninenko, D. Glidi, S. Gollapinni, N. Golubev, M. Graham, E. Gramellini, H. Greenlee,
²⁹⁵⁶ R. Gross, R. Guenette, A. Guglielmi, A. Hackenburg, R. Hnni, O. Hen, J. Hewes, J. Ho,
²⁹⁵⁷ G. Horton-Smith, J. Howell, A. Ivashkin, C. James, C. M. Jen, R. A. Johnson, B. J. P. Jones,
²⁹⁵⁸ J. Joshi, H. Jostlein, D. Kaleko, L. N. Kalousis, G. Karagiorgi, W. Ketchum, B. Kirby,
²⁹⁵⁹ M. Kirby, M. Kirsanov, J. Kisiel, J. Klein, J. Klinger, T. Kobilarcik, U. Kose, I. Kreslo, V. A.
²⁹⁶⁰ Kudryavtsev, Y. Li, B. Littlejohn, D. Lissauer, P. Livesly, S. Lockwitz, W. C. Louis, M. Lthi,
²⁹⁶¹ B. Lundberg, F. Mammoliti, G. Mannocchi, A. Marchionni, C. Mariani, J. Marshall,
²⁹⁶² K. Mavrokordidis, N. McCauley, N. McConkey, K. McDonald, V. Meddage, A. Menegolli,
²⁹⁶³ G. Meng, I. Mercer, T. Miao, T. Miceli, G. B. Mills, D. Mladenov, C. Montanari,
²⁹⁶⁴ D. Montanari, J. Moon, M. Mooney, C. Moore, Z. Moss, M. H. Mouhai, S. Mufson,
²⁹⁶⁵ R. Murrells, D. Naples, M. Nessi, M. Nicoletto, P. Nienaber, B. Norris, F. Noto, J. Nowak,
²⁹⁶⁶ S. Pal, O. Palamara, V. Paolone, V. Papavassiliou, S. Pate, J. Pater, Z. Pavlovic, J. Perkin,
²⁹⁶⁷ P. Picchi, F. Pietropaolo, P. Poski, S. Pordes, R. Potenza, G. Pulliam, X. Qian, L. Qiuqiang,
²⁹⁶⁸ J. L. Raaf, V. Radeka, R. Rameika, A. Rappoldi, G. L. Raselli, P. N. Ratoff, B. Rebel,
²⁹⁶⁹ M. Richardson, L. Rochester, M. Rossella, C. Rubbia, C. Rudolf von Rohr, B. Russell, P. Sala,
²⁹⁷⁰ A. Scaramelli, D. W. Schmitz, A. Schukraft, W. Seligman, M. H. Shaevitz, B. Sippach,
²⁹⁷¹ E. Snider, J. Sobczyk, M. Soderberg, S. Sldner-Rembold, M. Spanu, J. Spitz, N. Spooner,

- 2972 D. Stefan, J. St. John, T. Strauss, R. Sulej, C. M. Sutera, A. M. Szczelc, N. Tagg, C. E. Taylor,
 2973 K. Terao, M. Thiesse, L. Thompson, M. Thomson, C. Thorn, M. Torti, F. Tortorici,
 2974 M. Toups, C. Touramanis, Y. Tsai, T. Usher, R. Van de Water, F. Varanini, S. Ventura,
 2975 C. Vignoli, T. Wachala, M. Weber, D. Whittington, P. Wilson, S. Wolbers, T. Wongjirad,
 2976 K. Woodruff, M. Xu, T. Yang, B. Yu, A. Zani, G. P. Zeller, J. Zeniamo, and C. Zhang. A
 2977 proposal for a three detector short-baseline neutrino oscillation program in the fermilab
 2978 booster neutrino beam, 2015.
- 2979 [3] M. Ackermann et al. Measurement of separate cosmic-ray electron and positron spectra with
 2980 the fermi large area telescope. *Phys. Rev. Lett.*, 108:011103, 2012.
- 2981 [4] A. Adare et al. Search for dark photons from neutral meson decays in $p + p$ and $d + \text{Au}$
 2982 collisions at $\sqrt{s_{NN}} = 200$ GeV. *Phys. Rev.*, C91(3):031901, 2015.
- 2983 [5] P. A. R. Ade et al. Planck 2015 results. XIII. Cosmological parameters. 2015.
- 2984 [6] Oscar Adriani et al. An anomalous positron abundance in cosmic rays with energies 1.5-100
 2985 GeV. *Nature*, 458:607–609, 2009.
- 2986 [7] G. Agakishiev et al. Searching a Dark Photon with HADES. *Phys. Lett.*, B731:265–271, 2014.
- 2987 [8] S. Agostinelli, J. Allison, K. Amako, J. Apostolakis, H. Araujo, P. Arce, M. Asai, D. Axen,
 2988 S. Banerjee, G. Barrand, F. Behner, L. Bellagamba, J. Boudreau, L. Broglia, A. Brunengo,
 2989 H. Burkhardt, S. Chauvie, J. Chuma, R. Chytracek, G. Cooperman, G. Cosmo,
 2990 P. Degtyarenko, A. Dell’Acqua, G. Depaola, D. Dietrich, R. Enami, A. Feliciello, C. Ferguson,
 2991 H. Fesefeldt, G. Folger, F. Foppiano, A. Forti, S. Garelli, S. Giani, R. Giannitrapani, D. Gibin,
 2992 J.J. [Gmez Cadenas], I. Gonzlez, G. [Gracia Abril], G. Greeniaus, W. Greiner, V. Grichine,
 2993 A. Grossheim, S. Guatelli, P. Gumplinger, R. Hamatsu, K. Hashimoto, H. Hasui,
 2994 A. Heikkinen, A. Howard, V. Ivanchenko, A. Johnson, F.W. Jones, J. Kallenbach, N. Kanaya,
 2995 M. Kawabata, Y. Kawabata, M. Kawaguti, S. Kelner, P. Kent, A. Kimura, T. Kodama,
 2996 R. Kokoulin, M. Kossov, H. Kurashige, E. Lamanna, T. Lampn, V. Lara, V. Lefebure, F. Lei,
 2997 M. Liendl, W. Lockman, F. Longo, S. Magni, M. Maire, E. Medernach, K. Minamimoto,
 2998 P. [Mora de Freitas], Y. Morita, K. Murakami, M. Nagamatu, R. Nartallo, P. Nieminen,
 2999 T. Nishimura, K. Ohtsubo, M. Okamura, S. O’Neale, Y. Oohata, K. Paech, J. Perl, A. Pfeiffer,
 3000 M.G. Pia, F. Ranjard, A. Rybin, S. Sadilov, E. [Di Salvo], G. Santin, T. Sasaki, N. Savvas,
 3001 Y. Sawada, S. Scherer, S. Sei, V. Sirotenko, D. Smith, N. Starkov, H. Stoecker, J. Sulkimo,
 3002 M. Takahata, S. Tanaka, E. Tcherniaev, E. [Safai Tehrani], M. Tropeano, P. Truscott, H. Uno,
 3003 L. Urban, P. Urban, M. Verderi, A. Walkden, W. Wander, H. Weber, J.P. Wellisch,
 3004 T. Wenaus, D.C. Williams, D. Wright, T. Yamada, H. Yoshida, and D. Zschiesche. Geant4a
 3005 simulation toolkit. *Nuclear Instruments and Methods in Physics Research Section A:*
 3006 *Accelerators, Spectrometers, Detectors and Associated Equipment*, 506(3):250 – 303, 2003.

- 3007 [9] M. Aguilar et al. First result from the Alpha Magnetic Spectrometer on the International
 3008 Space Station: Precision measurement of the positron fraction in primary cosmic rays of
 3009 0.5-350 gev. *Phys. Rev. Lett.*, 110:141102, 2013.
- 3010 [10] A.A. Aguilar-Arevalo, M. Backfish, A. Bashyal, B. Batell, B.C. Brown, R. Carr,
 3011 A. Chatterjee, R.L. Cooper, P. deNiverville, R. Dharmapalan, and et al. Dark matter search
 3012 in a proton beam dump with miniboone. *Physical Review Letters*, 118(22), May 2017.
- 3013 [11] Sergey Alekhin et al. A facility to Search for Hidden Particles at the CERN SPS: the SHiP
 3014 physics case. 2015.
- 3015 [12] J. Alexander. *Baltimore lectures on molecular dynamics and the wave theory of light*, 2016.
 3016 <https://indico.cern.ch/event/507783/contributions/2150181/attachments/1266367/1874844/SLAC->
 3017 MMAPS-alexander.pdf.
- 3018 [13] Johan Alwall, Pavel Demin, Simon de Visscher, Rikkert Frederix, Michel Herquet, Fabio
 3019 Maltoni, Tilman Plehn, David L Rainwater, and Tim Stelzer. Madgraph/madevent v4: the
 3020 new web generation. *Journal of High Energy Physics*, 2007(09):028028, Sep 2007.
- 3021 [14] R. Amanullah, C. Lidman, D. Rubin, G. Aldering, P. Astier, K. Barbary, M. S. Burns,
 3022 A. Conley, K. S. Dawson, S. E. Deustua, and et al. Spectra and hubble space telescope light
 3023 curves of six type Ia supernovae at 0.511 \pm 1.12 and the union2 compilation. *The*
 3024 *Astrophysical Journal*, 716(1):712738, May 2010.
- 3025 [15] M. Amaryan, E. Chudakov, C. Meyer, M. Pennington, J. Ritman, and I. Strakovsky, editors.
 3026 *Mini-Proceedings: Workshop on Physics with Neutral Kaon Beam at JLab (KL2016): Newport*
 3027 *News, VA, USA, February 1-3, 2016*, 2016.
- 3028 [16] F. Archilli et al. Search for a vector gauge boson in ϕ meson decays with the KLOE detector.
 3029 *Phys. Lett.*, B706:251–255, 2012.
- 3030 [17] Nima Arkani-Hamed, Douglas P. Finkbeiner, Tracy R. Slatyer, and Neal Weiner. A Theory of
 3031 Dark Matter. *Phys. Rev.*, D79:015014, 2009.
- 3032 [18] Nima Arkani-Hamed and Neal Weiner. LHC Signals for a SuperUnified Theory of Dark
 3033 Matter. *JHEP*, 12:104, 2008.
- 3034 [19] Bernard Aubert et al. Search for Dimuon Decays of a Light Scalar Boson in Radiative
 3035 Transitions $\Upsilon \rightarrow \gamma A_0$. *Phys. Rev. Lett.*, 103:081803, 2009.
- 3036 [20] D. Babusci et al. Limit on the production of a light vector gauge boson in phi meson decays
 3037 with the KLOE detector. *Phys. Lett.*, B720:111–115, 2013.

- 3038 [21] N. Baltzell, H. Egiyan, M. Ehrhart, C. Field, A. Freyberger, F.-X. Girod, M. Holtrop,
 3039 J. Jaros, G. Kalicy, T. Maruyama, B. McKinnon, K. Moffeit, T. Nelson, A. Odian,
 3040 M. Oriunno, R. Paremuzyan, S. Stepanyan, M. Tiefenback, S. Uemura, M. Ungaro, and
 3041 H. Vance. The heavy photon search beamline and its performance. *Nuclear Instruments and*
 3042 *Methods in Physics Research Section A: Accelerators, Spectrometers, Detectors and Associated*
 3043 *Equipment*, 859:69 – 75, 2017.
- 3044 [22] J. R. Batley et al. Search for the dark photon in π^0 decays. *Phys. Lett.*, B746:178–185, 2015.
- 3045 [23] M. Battaglieri, A. Bersani, B. Caiffi, A. Celentano, R. De Vita, E. Fanchini, L. Marsicano,
 3046 P. Musico, M. Osipenko, F. Panza, M. Ripani, E. Santopinto, M. Taiuti, V. Bellini, M. Bond,
 3047 M. De Napoli, F. Mammoliti, E. Leonora, N. Randazzo, G. Russo, M. Sperduto, C. Sutera,
 3048 F. Tortorici, N. Baltzell, M. Dalton, A. Freyberger, F. X. Girod, V. Kubarovský, E. Pasyuk,
 3049 E. S. Smith, S. Stepanyan, M. Ungaro, T. Whitlatch, E. Izaguirre, G. Krnjaic,
 3050 D. Snowden-Ifft, D. Loomba, M. Carpinelli, V. Sipala, P. Schuster, N. Toro, R. Essig, M. H.
 3051 Wood, M. Holtrop, R. Paremuzyan, G. De Cataldo, R. De Leo, D. Di Bari, L. Lagamba,
 3052 E. Nappi, R. Perrino, I. Balossino, L. Barion, G. Ciullo, M. Contalbrigo, P. Lenisa,
 3053 A. Movsisyan, F. Spizzo, M. Turisini, F. De Persio, E. Cisbani, F. Garibaldi, F. Meddi, G. M.
 3054 Urciuoli, D. Hasch, V. Lucherini, M. Mirazita, S. Pisano, G. Simi, A. D’Angelo, L. Lanza,
 3055 A. Rizzo, C. Schaerf, I. Zonta, A. Filippi, S. Fegan, M. Kunkel, M. Bashkanov, P. Beltrame,
 3056 A. Murphy, G. Smith, D. Watts, N. Zachariou, L. Zana, D. Glazier, D. Ireland, B. McKinnon,
 3057 D. Sokhan, L. Colaneri, S. Anefalos Pereira, A. Afanasev, B. Briscoe, I. Strakovsky,
 3058 N. Kalantarians, L. Weinstein, K. P. Adhikari, J. A. Dunne, D. Dutta, L. El Fassi, L. Ye,
 3059 K. Hicks, P. Cole, S. Dobbs, and C. Fanelli. Dark matter search in a beam-dump experiment
 3060 (bdx) at jefferson lab, 2016.
- 3061 [24] T. Beranek, H. Merkel, and M. Vanderhaeghen. Theoretical framework to analyze searches for
 3062 hidden light gauge bosons in electron scattering fixed target experiments. *Phys. Rev.*,
 3063 D88:015032, 2013.
- 3064 [25] P. Billoir and S. Qian. Fast vertex fitting with a local parametrization of tracks. *Nuclear*
 3065 *Instruments and Methods in Physics Research Section A: Accelerators, Spectrometers,*
 3066 *Detectors and Associated Equipment*, 311(1):139 – 150, 1992.
- 3067 [26] James D. Bjorken, Rouven Essig, Philip Schuster, and Natalia Toro. New Fixed-Target
 3068 Experiments to Search for Dark Gauge Forces. *Phys. Rev.*, D80:075018, 2009.
- 3069 [27] V. Blobel. A new fast track-fit algorithm based on broken lines. *Nuclear Instruments and*
 3070 *Methods in Physics Research Section A: Accelerators, Spectrometers, Detectors and Associated*
 3071 *Equipment*, 566(1):14 – 17, 2006. TIME 2005.

- 3072 [28] V. Blobel. Software alignment for tracking detectors. *Nuclear Instruments and Methods in*
3073 *Physics Research Section A: Accelerators, Spectrometers, Detectors and Associated*
3074 *Equipment*, 566(1):5 – 13, 2006. TIME 2005.
- 3075 [29] Volker Blobel, Claus Kleinwort, and Frank Meier. Fast alignment of a complex tracking
3076 detector using advanced track models. *Computer Physics Communications*, 182(9):1760 –
3077 1763, 2011. Computer Physics Communications Special Edition for Conference on
3078 Computational Physics Trondheim, Norway, June 23-26, 2010.
- 3079 [30] Volker D. Burkert. The JLab 12 GeV upgrade and the initial science program - Selected
3080 topics. *Proc. Int. Sch. Phys. Fermi*, 180:303–332, 2012.
- 3081 [31] Ilias Cholis and Dan Hooper. Dark Matter and Pulsar Origins of the Rising Cosmic Ray
3082 Positron Fraction in Light of New Data From AMS. *Phys. Rev.*, D88:023013, 2013.
- 3083 [32] Michele Cicoli, Mark Goodsell, Joerg Jaeckel, and Andreas Ringwald. Testing String Vacua in
3084 the Lab: From a Hidden CMB to Dark Forces in Flux Compactifications. *JHEP*, 07:114, 2011.
- 3085 [33] Douglas Clowe, Anthony Gonzalez, and Maxim Markevitch. Weak lensing mass reconstruction
3086 of the interacting cluster 1e 0657558: Direct evidence for the existence of dark matter. *The*
3087 *Astrophysical Journal*, 604(2):596603, Apr 2004.
- 3088 [34] D0 Collaboration. Layer 2-5 silicon sensor specifications for D0 SMTII. *Internal Note*, 2003.
- 3089 [35] S. Coutu. Positrons galore. *Phys. Online J.*, 6, 40:1-40:3, 2013.
- 3090 [36] Patrick deNiverville, Maxim Pospelov, and Adam Ritz. Light new physics in coherent
3091 neutrino-nucleus scattering experiments. *Phys. Rev. D*, 92:095005, Nov 2015.
- 3092 [37] Jozef Dudek et al. Physics Opportunities with the 12 GeV Upgrade at Jefferson Lab. *Eur.*
3093 *Phys. J.*, A48:187, 2012.
- 3094 [38] Rouven Essig, Philip Schuster, Natalia Toro, and Bogdan Wojtsekhowski. An Electron Fixed
3095 Target Experiment to Search for a New Vector Boson A' Decaying to e+e-. *JHEP*, 02:009,
3096 2011.
- 3097 [39] Gary J. Feldman and Robert D. Cousins. Unified approach to the classical statistical analysis
3098 of small signals. *Phys. Rev. D*, 57:3873–3889, Apr 1998.
- 3099 [40] Jonathan L. Feng, Bartosz Fornal, Iftah Galon, Susan Gardner, Jordan Smolinsky, Tim M.P.
3100 Tait, and Philip Tanedo. Particle physics models for the 17 mev anomaly in beryllium nuclear
3101 decays. *Physical Review D*, 95(3), Feb 2017.
- 3102 [41] M. J. French et al. Design and results from the APV25, a deep sub-micron CMOS front-end
3103 chip for the CMS tracker. *Nucl. Instrum. Meth.*, A466:359–365, 2001.

- 3104 [42] S. Gardner, R. J. Holt, and A. S. Tadepalli. New Prospects in Fixed Target Searches for Dark
3105 Forces with the SeaQuest Experiment at Fermilab. 2015.
- 3106 [43] Mark Goodsell, Joerg Jaeckel, Javier Redondo, and Andreas Ringwald. Naturally Light
3107 Hidden Photons in LARGE Volume String Compactifications. *JHEP*, 11:027, 2009.
- 3108 [44] Mark Goodsell and Andreas Ringwald. Light Hidden-Sector U(1)s in String
3109 Compactifications. *Fortsch. Phys.*, 58:716–720, 2010.
- 3110 [45] Norman Graf and Jeremy McCormick. Simulator for the linear collider (slic): A tool for ilc
3111 detector simulations. *AIP Conference Proceedings*, 867(1):503–512, 2006.
- 3112 [46] Norman A Graf. org.lcsim: Event reconstruction in java. *Journal of Physics: Conference
3113 Series*, 331(3):032012, dec 2011.
- 3114 [47] Bob Holdom. Two U(1)’s and Epsilon Charge Shifts. *Phys. Lett.*, B166:196–198, 1986.
- 3115 [48] Joerg Jaeckel and Andreas Ringwald. The low-energy frontier of particle physics. *Annual
3116 Review of Nuclear and Particle Science*, 60(1):405437, Nov 2010.
- 3117 [49] Reza Kazimi, John Hansknecht, Michael Spata, and Haipeng Wang. Source and Extraction
3118 for Simultaneous Four-hall Beam Delivery System at CEBAF. In *Proceedings, 4th
3119 International Particle Accelerator Conference (IPAC 2013)*, page WEPFI085, 2013.
- 3120 [50] B. Kelvin. *Baltimore lectures on molecular dynamics and the wave theory of light*, 1904.
3121 <https://archive.org/details/baltimorelecture00kelviala>.
- 3122 [51] Claus Kleinwort. General broken lines as advanced track fitting method. *Nuclear Instruments
3123 and Methods in Physics Research Section A: Accelerators, Spectrometers, Detectors and
3124 Associated Equipment*, 673:107110, May 2012.
- 3125 [52] T. Kraemer. Track Parameters in LCIO. *LC-Notes*, 2006.
- 3126 [53] A.J. Krasznahorkay, M. Csatls, L. Csige, Z. Gcsi, J. Gulys, M. Hunyadi, I. Kuti, B.M. Nyak,
3127 L. Stuhl, J. Timr, and et al. Observation of anomalous internal pair creation inbe8: A
3128 possible indication of a light, neutral boson. *Physical Review Letters*, 116(4), Jan 2016.
- 3129 [54] M. Markevitch, A. H. Gonzalez, D. Clowe, A. Vikhlinin, W. Forman, C. Jones, S. Murray, and
3130 W. Tucker. Direct constraints on the dark matter selfinteraction cross section from the
3131 merging galaxy cluster 1e 065756. *The Astrophysical Journal*, 606(2):819824, May 2004.
- 3132 [55] T. Maruyama et al. A systematic study of polarized electron emission from strained
3133 gaas/gaasp superlattice photocathodes. *Appl. Phys. Lett.*, 85:2640, 2004.

- 3134 [56] H. Merkel et al. Search at the Mainz Microtron for Light Massive Gauge Bosons Relevant for
3135 the Muon g-2 Anomaly. *Phys. Rev. Lett.*, 112(22):221802, 2014.
- 3136 [57] H. Poincaré. The Milky Way and the Theory of Gases. *Popular Astronomy*, 14:475–488,
3137 October 1906.
- 3138 [58] M. Raymond et al. The CMS tracker APV25 0.25-mu-m CMOS readout chip. *Conf. Proc.*,
3139 C00091111:130–134, 2000. [,130(2000)].
- 3140 [59] V. C. Rubin, N. Thonnard, and W. K. Ford, Jr. Rotational properties of 21 SC galaxies with
3141 a large range of luminosities and radii, from NGC 4605 /R = 4kpc/ to UGC 2885 /R = 122
3142 kpc/. *Astrophys. J.*, 238:471, 1980.
- 3143 [60] David N. Schramm and Michael S. Turner. Big-bang nucleosynthesis enters the precision era.
3144 *Reviews of Modern Physics*, 70(1):303–318, January 1998.
- 3145 [61] Yung-Su Tsai. Pair Production and Bremsstrahlung of Charged Leptons. *Rev. Mod. Phys.*,
3146 46:815, 1974. [Erratum: Rev. Mod. Phys.49,521(1977)].
- 3147 [62] B. Wojtsekhowski, D. Nikolenko, and I. Racheck. Searching for a new force at VEPP-3. 2012.
- 3148 [63] S. Yellin. Finding an upper limit in the presence of an unknown background. *Phys. Rev. D*,
3149 66:032005, Aug 2002.
- 3150 [64] S. Yellin. Some ways of combining optimum interval upper limits, 2011.
- 3151 [65] F. Zwicky. Die Rotverschiebung von extragalaktischen Nebeln. *Helv. Phys. Acta*, 6:110–127,
3152 1933.
- 3153 [66] Torsten kesson, Asher Berlin, Nikita Blinov, Owen Colegrove, Giulia Collura, Valentina Dutta,
3154 Bertrand Echenard, Joshua Hiltbrand, David G. Hitlin, Joseph Incandela, John Jaros, Robert
3155 Johnson, Gordan Krnjaic, Jeremiah Mans, Takashi Maruyama, Jeremy McCormick, Omar
3156 Moreno, Timothy Nelson, Gavin Niendorf, Reese Petersen, Ruth Pttgen, Philip Schuster,
3157 Natalia Toro, Nhan Tran, and Andrew Whitbeck. Light dark matter experiment (ldmx), 2018.